Ludwig–Maximilians–Universität München
Fakultät für Physik

Dissertation

Investigation of $ZnWO_4$ and $CaMoO_4$ as Target Materials for the CRESST–II Dark Matter Search

Irina Bavykina
aus Russland

München
September 2009

Erstgutachter : Prof. Dr. O. Biebel

Zweitgutachter : PD. Dr. P. Thirolf

Tag der mündlichen Prüfung: 08.12.2009

Zusammenfassung

Diese Arbeit beschäftigt sich mit der Untersuchung von szintillierenden Kalziummolybdat ($CaMoO_4$) und Zinkwolframat ($ZnWO_4$) Kristallen und deren Entwicklung als Phonondetektoren für die direkte Suche nach Dunkler Materie mit CRESST-II (Cryogenic Rare Event Search with Superconducting Thermometers). CRESST-II sucht nach elastischen Streuprozessen von WIMPs (Weakly Interacting Massive Particles) an den Kernen der Kristalldetektoren (Kapitel 1). Man erwartet eine WIMP-Streurate von weniger als 0.1 pro Kilogramm Detektormaterial und Tag, während die Hintergrundraten selbst in einem stark abgeschirmten Aufbau um vieles größer sind. Die Reduzierung jenes Hintergrundes, der ein potentielles WIMP Signal überdeckt oder imitiert, ist daher von zentraler Wichtigkeit (Kapitel 2).

Die CRESST–II Detektoren können aktiv zwischen Kernrückstößen (verursacht durch Neutronen und erwartet durch WIMPs) und α-, β- und γ-Radioaktivität unterscheiden. Dies wird durch simultane Messung von Phononen sowie von Szintillationslicht, entstehend durch die Wechselwirkung eines Teilchens mit dem Kristall, erreicht (Kapitel 2 und 3). Die Schwierigkeit einer solchen Messung liegt in der geringen Menge an freigegebenem Szintillationslicht (Kapitel 4). In einem Kalziumwolframat ($CaWO_4$) Kristall (Standardmaterial für CRESST-II) werden typischerweise nur ca. 1% der gesamten deponierten Energie in Form von γ/β-Strahlung detektiert. Um eine bessere Detektionsschwelle bei niedrigen Rückstoßenergien (unter 40 keV) zu erreichen, muss die Menge an emittiertem Szintillationslicht möglichst groß sein.

In dieser Arbeit werden die Szintillationseigenschaften von $CaMoO_4$ und $ZnWO_4$ Kristallen bei Zimmertemperatur (Kapitel 5) sowie bei kryogenischen Temperaturen (Kapitel 6) untersucht und mit denen von $CaWO_4$ Kristallen verglichen. Im Besonderen werden erstmals die Lichtemissionsfähigkeit und die Szintillationszeitskalen von $CaMoO_4$ und $ZnWO_4$ im milli-Kelvin (mK) Bereich gemessen.

Des weiteren wurde im Zuge dieser Arbeit ein 10 g $ZnWO_4$ Phonondetektor zu einem 400 g Prototypen skaliert und 200 g $CaMoO_4$ Phonondetektoren (Kapitel 7). Für den $ZnWO_4$ Phonondetektor wird ein neues Design mit separatem Thermometer-Träger untersucht. Diese Detektoren wurden auch im CRESST–II Versuchsaufbau im Gran Sasso-Untergrundlaboratorium erstmals in Betrieb genommen (Kapitel 8). Zusätzlich zu einer allgemeinen Studie über das neuartige Detektordesign ermöglichen die gemessenen Daten eine detaillierte Untersuchung der radioaktiven Kontamination der Kristalle. Aufgrund der guten Eigenschaften des $ZnWO_4$ Prototypen wird eine zusätzliche Detektoreinheit aus diesem Material im CRESST–II Aufbau zum Einsatz kommen (Kapitel 9).

Abstract

This work reports on the investigation of calcium molybdate ($CaMoO_4$) and zinc tungstate ($ZnWO_4$) scintillating crystals and the development of prototype phonon detectors based on these new target materials for CRESST–II (Cryogenic Rare Event Search with Superconducting Thermometers). The CRESST–II direct dark matter search experiment seeks the detection of WIMPs (Weakly Interacting Massive Particles) via their elastic scattering off nuclei (Chapter 1). The WIMP event rate is expected to be less than 0.1 event per kg of the target and per day while the background rate is orders of magnitude higher, even after placing the detector in a well–shielded facility. Therefore, suppression of background that would hide or mimic a potential WIMP signal is of the central importance (Chapter 2).

CRESST–II detectors can actively discriminate nuclear recoils (caused by neutrons and expected from WIMPs) from radioactive α-, β-, and γ–backgrounds while simultaneously measuring phonon and light signals caused by a particle interaction in the scintillating crystal (Chapter 2 and 3). The challenge of such a measuring technique is the small amount of scintillation light generated (Chapter 4). Typically, only 1% of the total energy deposited into calcium tungstate ($CaWO_4$) crystals (standard target for CRESST–II) by γ/β particles is detected. In order to achieve a better discrimination threshold down to lower recoil energies (below 40 keV), the amount of emitted scintillation light has to be maximized.

In this work scintillation properties of $CaMoO_4$ and $ZnWO_4$ crystals have been investigated at room temperature (Chapter 5) and at cryogenic temperatures (Chapter 6) and compared with those ones of $CaWO_4$. In particular, the light output and scintillation decay time constants of $CaMoO_4$ and $ZnWO_4$ crystals at mK temperatures have been measured for the first time.

Furthermore, a 10 g $ZnWO_4$ phonon detector was scaled up to a full 400 g prototype and 200 g $CaMoO_4$ phonon detectors were developed (Chapter 7). The $ZnWO_4$ detector has been integrated into the CRESST–II setup at Gran Sasso where it has been operated in a well–shielded facility for the first time (Chapter 8). Besides allowing for performance studies of the new detector design, data taken with this detector made a detailed investigation of radioactive contaminations of the $ZnWO_4$ crystal possible. Due to the excellent characteristics obtained with the prototype $ZnWO_4$ phonon detector this material will be used as an additional target unit for the CRESST–II experiment (Chapter 9).

Acknowledgments

First of all, I would like to express my gratitude towards my research advisor Dr. Franz Pröbst at the Max Planck Institute for Physics (MPI) for giving me the opportunity to conduct my Ph.D. within the CRESST group. I am grateful for his continuous support, kindness, and advice. I am thankful to the MPI and to the Cluster of Excellence initiative for financial support and for providing optimal research possibilities.

I am grateful to my university supervisor Prof. Otmar Biebel for his support during the final stages of my PhD and for providing the academic framework to my Ph.D. studies.

To all the members of the CRESST group I am thankful for a stimulating atmosphere. I would like to thank Federica for taking the great effort of proofreading my thesis. I am also grateful to Dieter, Mr. Jens Bond and Patrichek for proofreading, fruitful discussions, and comments. Thanks to my office mate Rafael. Special thanks to Emilija for teaching me not to give up. Gode, Michael, Hans, Wolfgang, Peter, Leo, Antonio, Quirin, Christoph, Rafael2, and Karo thank you all very much. Vielen Dank! I really enjoyed the discussions about our work and beyond.

I am further grateful to Eugenij N. Galashov and Yan. V. Vasiliev from NIIC for providing crystals which were crucial for my Ph.D. studies. I am deeply thankful to Alexander F. Novikov for his advise, given many years ago.

Finally, I am indebted to all my friends. Simon Eidelman, Andrej and Larisa Kiryuniny, Anna, Stas, Mitja, a takzhe bolshoe semejstvo dyatlov vo glave s Ilonkoj spasibo chto byli ryadom vse jeti gody i podderzhivali menya. I also would like to thank the Pradler family for just being so great to me.

Last but not least, I would like to thank my parents, grandfather and brother for their unconditional love and support, spasibo Vam.

To Josef Pradler, bolshoe spasibo.

Contents

Chapter 1

Introduction to dark matter

The question of what constitutes the mass density of the Universe is practically as old as extragalactic astronomy. The kinematics of galaxies and galaxy clusters early suggested that the dynamic mass involved is far greater than the observable luminous mass [1]. Considerable experimental effort is in progress throughout the world to elucidate the yet unknown nature of the missing matter of the Universe, the so-called dark matter. It is with no doubt one of the most stunning astrophysical mysteries.

This chapter provides a cursory overview of the dark matter problem by reviewing the standard cosmological model. Potential dark matter candidates and the basics of direct detection of dark matter are discussed.

1.1 Dark matter problem

Our present understanding of the Universe is based on a fundamental picture, the Hot Big Bang Scenario in which the Universe once has been in a highly compressed state. Since then (from about 14 billion years) the Universe has been expanding. In its earliest stages it contained an extremely hot and dense plasma of elementary particles, frequently reacting among each other. As during expansion of the Universe the density of these particles and also their energy (or simply the temperature of the Universe) became lower, reactions among particles froze out. The course and the outcome of these reactions in the early Universe therefore determined in what form particles and thus matter survived. Small fluctuations in particle density were the seeds for the formation of the first stars and subsequently galaxies, galaxy clusters, and of all the other structure in the Universe.

Historically, one of the most convincing arguments for the existence of large amounts of non-luminous matter in the Universe comes from observations of

rotation curves of galaxies. A typical galaxy such as our Milky Way contains in the order of 10^{11} stars, together with clouds of gas and dust. Various forms of galaxies are observed, the most common being elliptical or spiral galaxies. In spiral galaxies a central spherical hub (or bulge) is surrounded by a flattened structure or disk in the form of spiral arms. The latter are moving in roughly circular orbits. The total number of observable galaxies is enormous ($\sim 10^{11}$) and they gather together in clusters and superclusters of galaxies. The latter are the largest observed structures on cosmological scales.

The orbital velocities of stars and gas as a function of their distance from the galactic center are inferred from Doppler shifts of spectral lines.

Given that the observed surface luminosity of the disk falls off exponentially with radius r from the galactic centre as

$$I(r) = I_0 e^{-r/r_D}, \tag{1.1}$$

one would expect that most of the galactic mass is concentrated within a few r_D, where r_D is the disk length scale [2]. Thereby, under the assumption that centrifugal forces are balanced by gravity, the rotation velocity at large radii should be given by

$$v_{rot} \simeq \sqrt{\frac{G_N M}{r}} \propto r^{-1/2} \tag{1.2}$$

with M denoting the total mass of the galactic nucleus. However, such a behaviour is not observed. The orbital speed of stars and hydrogen clouds does not decrease with r. It rises roughly linearly from the center outward until it reaches a typical value of around 200 $\mathrm{km\,s^{-1}}$. The rotation curve then stays flat out to the largest measured radii. Figure 1.1 shows the rotation curve for the exemplary galaxy M81. The difference between the measured values of v_{rot} and the expected ones from Equation 1.2 is ascribed to the gravitational effect of Dark Matter. Indeed, an overall consistent picture of spiral galaxies only emerges when the bulge and disk are gravitationally subdominant components immersed in a larger spherical halo of Dark Matter.

1.1.1 The standard cosmological picture

Galactic rotation curves are not the only observational evidence for the existence of dark matter. The discovery of the cosmic microwave background (CMB) radiation has not only put the Hot Big Bang Model on firm footing but has recently also allowed to infer the (cold) dark matter content of the Universe on comological scales to great accuracy.

When electrons recombined with the light elements (mainly protons and alpha particles) roughly 380.000 years after the Big Bang gravity driven accoustic oscillations of the formerly tightly coupled baryon-photon fluid became imprinted on the subsequently free streaming CMB photons. With the measurements of the

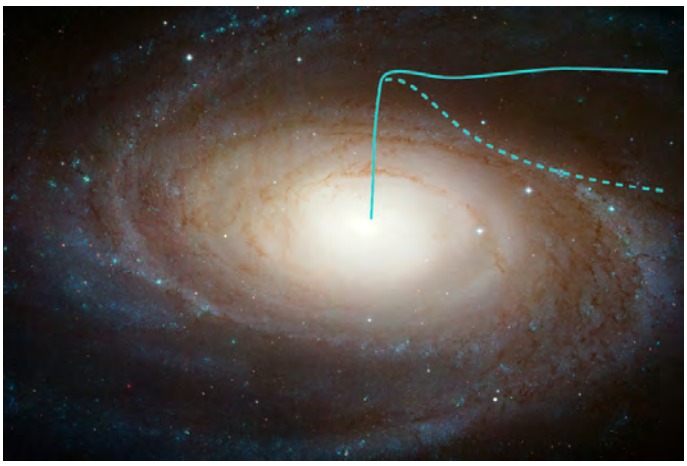

Figure 1.1: The spiral galaxy M81, from [3]. Differing from what one would expect according to the distribution of luminous matter and under the assumption that centrifugal forces are balanced by gravity, the orbital speed of stars and hydrogen clouds does not decrease with the distance to the center of the galaxy, but remains almost constant.

Wilkinson Microwave Anisotropy Probe (WMAP) satellite experiment [4, 5, 6] unprecedented precision data on the associated multipoles of the CMB angular power spectrum became available. Based on a ΛCDM model, i.e. a flat Universe filled with baryons, cold dark matter, neutrinos, and a cosmological constant, this has allowed to determine the dark matter density to an accuracy better than 10%.

Let us outline the framework of the so-called standard cosmological model, ΛCDM. It allows us to explain in a satisfactory way the thermal history, relic background radiation, abundance of elements, large scale structure and many other properties of the Universe. Given the observed isotropy and homogeneity of the Universe on large scales one seeks cosmological solutions from the Friedman equation

$$\left(\frac{\dot{a}}{a}\right)^2 + \frac{k}{a^2} = \frac{8\pi G_N}{3}\rho_{tot}, \tag{1.3}$$

where ρ_{tot} denotes the total energy density of the Universe, and k describes the spatial curvature which can take values $k = 0, 1, -1$. Equation 1.3 arises from the Einstein field equations of general relativity for the spherically symmetric Robertson-Walker line element (with c = 1)

$$ds^2 = dt^2 - a(t)^2\left(\frac{dr^2}{1-kr^2} + r^2 d\theta^2 + r^2 \sin^2\theta d\phi^2\right). \tag{1.4}$$

The coordinates (t, r, θ, ϕ) are referred to as comoving coordinates and $a(t)$ is

called the scale factor. It is common to introduce the Hubble parameter

$$H(t) \equiv \frac{\dot{a}(t)}{a(t)}. \tag{1.5}$$

The present value $H(t_0) = H_0$, i.e. the Hubble constant, is usually parameterized as $H_0 \simeq 100\, h\, \mathrm{km\, s^{-1} Mpc^{-1}}$ with $h \simeq 0.73(3)$.

From Equation 1.3 it follows that the Universe is flat ($k = 0$) when the energy density equals the critical density ρ_c:

$$\rho_c = \frac{3H^2}{8\pi G_N}. \tag{1.6}$$

The energy content ρ_i of a species i is usually expressed in terms of the density parameter $\Omega_i \equiv \rho_i/\rho_c$ so that with $\Omega \equiv \sum_i \Omega_i$ the Friedman equation (1.3) takes the form

$$\Omega - 1 = \frac{k}{H^2 a^2}. \tag{1.7}$$

Note that Ω tells the sign of k and that the Universe is spatially flat for $\Omega = 1$. Identifying the dominant contributions to Ω is paramount for our understanding of the thermal history (and future) of our Universe.

The WMAP data (together with the supernovae measurements) has shown that we live to high accuracy in a flat Universe with $k = 0$. The major contributions to $\Omega = 1$ are then given by the following pieces: The baryon density Ω_b, the cold dark matter density Ω_{dm}, and the contribution of a cosmological constant Ω_Λ.

By counting stars and galaxies and measuring their luminosity, one obtains an estimate for the density of the visible (baryonic) matter in the Universe. This yields, however, only about 1% of the critical energy content, $\Omega_b \ni \Omega_{vis} \simeq 0.01$ [7]. A better handle on the baryon content of the Universe is provided by considering the framework of Big Bang Nucleosynthesis (BBN) which makes predictions on the primordial light element abundances such as ^{2}H and ^{4}He. Comparison of the BBN predictions with the observationally inferred primordial abundances yields the estimate $\Omega_b \sim 0.05$. Note that Ω_b parameterizes the nucleon content at the onset of the primordial nucleosynthesis reactions when the Universe was only about 1 s old. Indeed, the CMB measurements pin the baryon density down to $\Omega_b h^2 = 0.02273 \pm 0.00062$ [8], i.e. to a bit more than 4% for Ω_b. This concordance between CMB and BBN provides an important consistency check of the Big Bang model.

Given the small contribution of baryons to the total energy content of the Universe we are facing the presence of dark components in form of non-baryonic matter and dark energy. Depending on their velocity one distinguishes two different kinds of dark matter particles. Those ones that were still relativistic at the time of matter-radiation equality are called hot dark matter (HDM). Candidates

with non-relativistic speeds are called cold dark matter (CDM). The observed density contrast in structure implies that the dominant part of dark matter is cold since HDM particles tend to stream out of overdense regions thereby erasing structure on small scales. The WMAP 5-year result on the CDM density parameter reads [8]

$$\Omega_{dm}h^2 = 0.1099 \pm 0.0062 \tag{1.8}$$

This tells us that, with 20 %, non-baryonic dark matter contributes the largest part to the total matter content of the Universe. Finally, for the Universe to be flat, the vacuum energy in form of a cosmological constant is conjectured to be $\Omega_\Lambda = 0.742 \pm 0.030$ [8]. This concludes the mini-review on the ΛCDM model and in the following section some prime candidates for dark matter particles are discussed.

1.2 Dark matter candidates

There is no shortage of dark matter candidates and even the Standard Model (SM) has to offer a candidate. On general grounds, if the temperature T of the early Universe was $T \gg m_\chi$, where m_χ denotes the mass of a massive particle species χ, then χ had once been in thermal equilibrium with the primordial plasma. As the Universe expands, reactions of the kind $\chi\overline{\chi} \leftrightarrow f\overline{f}$ (with f denoting a SM particle) cease and χ cannot track its equilibrium abundance any more. The species freezes out from the plasma and a first estimate on its abundance gives [9]

$$\Omega_\chi h^2 \equiv \frac{n_\chi m_\chi}{\rho_c} \sim \frac{3 \times 10^{-27}\ \mathrm{cm^3\,s^{-1}}}{\langle \sigma_A v \rangle}. \tag{1.9}$$

Here, $\langle \dots \rangle$ denotes a thermal average over the mutual χ annihilation cross section σ_A times the relative velocity v. Remarkably, if χ is a particle species whose interactions to the SM particles is of electroweak strength, then $\Omega_\chi \simeq \Omega_{dm}$ is possible. This has led to the popular notion of a WIMP, a weakly interacting massive particle species. In the following a cursory overview of some dark matter candidates including WIMPs will be given.

Neutrinos Historically, SM neutrinos have been considered a prime candidate due the their undisputed virtue of being known to exist [10]. Indeed the discovery of neutrino oscillations, i.e. the mixing between the three neutrino flavors ν_e, ν_μ, and ν_τ, can be understood if neutrinos are massive.

Tight laboratory constraints on the neutrino masses come from tritium β-decay experiments [11], giving an upper limit on the neutrino mass

$$m_\nu < 2.8\ eV\ (95\ \%\ CL). \tag{1.10}$$

Together with the mass differences from neutrino oscillations, this implies an upper bound on the total neutrino relic density of

$$\Omega_\nu h^2 < 0.0076, \tag{1.11}$$

which means that neutrinos are simply not heavy enough to be the dominant component of non-baryonic dark matter.

Axions Introduced in an attempt to solve the problem of conjugation parity violation in strong interactions, axions (light bosons) have also often been discussed as a dark matter candidate. Laboratory searches, stellar cooling and the dynamics of supernova 1987A constrain axions to be very light (< 0.01 eV). Furthermore, they are expected to be extremely weakly interacting with ordinary particles, which implies that they were not in thermal equilibrium in the early Universe. The calculation of the axions relic density is uncertain, and depends on the assumptions made regarding the production mechanism. Nevertheless, it is possible to find an acceptable range where axions satisfy all present day constraints and represent a possible dark matter candidate [12].

One of the extensions of the SM is supersymmetry (SUSY). It is a symmetry of space-time that has been discovered in the process of unifying the fundamental forces of nature (electroweak, strong, and gravitational), and relates bosons (interaction mediators) with fermions (the constituents of matter). Of importance for cosmology is the fact that SUSY requires the existence of a new particle for each particle in the SM but with a different mass (since SUSY must be broken). SUSY particles have the same quantum numbers as their SM partners apart from the spin (SUSY partners differ by half a unit of spin), and a new quantum number R, which distinguishes between ordinary matter and SUSY partners. It can be defined in terms of baryon B, lepton L and spin S quantum numbers as [13]:

$$R = (-1)^{3B+L+2S}. \tag{1.12}$$

It follows that R = 1 for ordinary particles and R=- 1 for SUSY particles. The latter come under the names of sleptons (partners of leptons), squarks (partners of the quarks), gauginos (partners of the gauge bosons) and higgsinos (partners of the Higgs bosons).

Weakly Interacting Massive Particles It was realized long ago by Goldberg [14] and Ellis [15] that the lightest superposition of the neutral gauginos and the neutral higgsinos (which having the same quantum numbers mix together) is an excellent dark matter candidate. It is often the lightest supersymmetric particle, it is stable under the requirement that superpartners are only

produced or destroyed in pairs (R-parity conservation), it is weakly interacting (even weaker than the standard weak interaction) as dictated by SUSY, and it is massive.

WIMPs are assumed to carry a conserved quantum number R, which suppresses or forbids the decay into lighter particles. Such particles should have been copiously produced in the early Universe. As the Universe expanded and cooled, the number density of the WIMPs successively became too low for the annihilation process to keep up with the Hubble expansion rate. A relic population of WIMPs should thus exist. The CRESST experiment aims to detect such particles.

Gravitinos The gravitino, being the superpartner of the graviton, is the gauge field of local supersymmetry transformations. Its mass is intrinsically connected with the underlying SUSY breaking mechanism and in some models (e.g. gauge mediated SUSY breaking) the gravitino can be the LSP. It is an extremely weakly interacting particle with its interactions to the (MS)SM fields suppressed by inverse powers of the Planck mass $M_P = 1.2 \times 10^{19}$ GeV [16]. Therefore, it is impossible to detect gravitinos in direct dark matter searches.

1.3 Direct detection of WIMPs

As already mentioned, one of the strongest observational evidence for the existence of dark matter comes from the dynamics of spiral galaxies with WIMPs supposed to be gravitationally bound to the galaxy, and forming a halo around its center. Direct searches for dark matter can therefore be performed in the Milky Way. The basic idea on which all direct experiments are based on relies on the fact that if our galaxy is filled with WIMPs, then many of them should pass through the Earth. Thus it may be possible to detect the interaction of dark matter particles with ordinary matter via their elastic scattering off nuclei in the target material of a suitable detector.

The key ingredients for the calculation of the signal in direct detection experiments are the local dark matter density ρ_χ, the WIMP velocity dispersion $\bar{v} = \sqrt{\langle v^2 \rangle}$ in the solar neighborhood, and the WIMP-nucleon scattering cross-section σ.

Theoretical and experimental results on direct detection are usually obtained under some simplifying assumptions on the dark matter profile. The most commonly used model for the halo is the spherical halo, whose density profile $\rho_\chi \propto r^{-2}$ is consistent with the observed flat rotation curves of spiral galaxies. General dynamical arguments suggest that WIMP velocities were thermalized by the fluctuations in the gravitational collapse. In this model WIMP particles are assumed to have a Maxwell-Boltzmann velocity distribution in the galactic

rest frame (the halo is assumed to be non-rotating). The canonical value for the velocity dispersion in our galaxy is $\bar{v} = 270$ km s^{-1}. A value commonly adopted for the local dark matter density ρ_χ at the position of the Sun and the Earth is $\rho_\chi = 0.3$ GeV cm^{-3} [9]. Yet, one has to take into account considerable uncertainties and model dependencies while using these values.

The flux of the dark matter particles Φ at the position of the Earth can be calculated as

$$\Phi = \frac{\rho_\chi \ \langle v_\chi \rangle}{m_\chi} = 10^7 \frac{GeV/c^2}{m_\chi} \ 1/cm^2 \, s, \tag{1.13}$$

where m_χ and $\langle v_\chi \rangle$ are the mass and the average WIMP velocity respectively.

1.3.1 Low recoil energy

Direct detection of dark matter particles is based on the scattering of WIMPs off target nuclei. With

$$m_r = \frac{m_\chi \, m_N}{m_\chi + m_N} \tag{1.14}$$

the reduced mass of the WIMP-nucleus system, where m_N is the mass of the nucleus and m_χ is a WIMP mass, the energy of the recoiling nucleus E_r is

$$E_r = \frac{m_r^2}{m_N} \, v^2 (1 - \cos\theta), \tag{1.15}$$

with θ being the scattering angle in the center of mass system and v is the velocity of an incoming WIMP. Nuclear physics and astrophysics imply the maximum recoil energies of O(10keV), thus requiring detectors with very low energy thresholds.

1.3.2 Event rates

The event rate in a target material is determined by the incoming WIMP flux Φ, the cross-section for WIMP-nucleus scattering σ, and the number of nuclei in the laboratory target as

$$R = n_0 \, \langle v_\chi \rangle \, \sigma \, \frac{M_{target}}{m_N}. \tag{1.16}$$

Here, $n_0 = \rho_\chi / m_\chi$ is the local number density of WIMPs, $\langle v_\chi \rangle$ is their average velocity, M_{target} is the target mass of a material with mass number A and nucleon mass m_N. From Equation 1.16 it is evident that the WIMP-nucleus cross-section is a very important property in determining the detection rate.

Present direct dark matter search experiments constrain the WIMP event rate to be less than 0.1 events per kilogram of the target and per day [17, 18, 19, 20]. At the same time the background rate is orders of magnitudes higher, even after placing detectors in a well-shielded facility. Therefore, together with low energies anticipated in WIMP-nucleon interactions, this sets the challenge for any direct dark matter detection experiment.

1.3.3 Interaction modes

WIMP scattering off nuclei is commonly discussed in the context of two classes of couplings, namely, **spin-dependent** (axial) and **spin-independent** (coherent). For the first class of interactions WIMPs may couple to the net spin of the target nucleus. For direct detection experiments this suggests to use light nuclei with odd number of protons and/or neutrons.

On the other hand, estimation of the de Broglie wavelength of a hypothetical WIMP shows that it is of the order of an atomic nucleus ($\lambda/2\pi \approx r_{nucleus}$). Therefore, a WIMP may be not able to resolve individual nucleons but instead interacts coherently with the nucleus as a whole. Thereby, for spin-independent interactions, the WIMP-nucleon cross-section is proportional to A^2 (where A is atomic mass, thus favoring heavy nuclei in the target).

The total elastic scattering cross-section σ is the sum of these two contributions. In the CRESST-II experiment $CaWO_4$ crystals are used as the main target material. Since the contribution of nuclei with the net spin is minor in this material, the experiment is not sensitive to spin-dependent interactions. Therefore, in the following, only the spin-independent mode of interaction will be considered.

1.3.4 Expected recoil spectrum

The elastic scattering cross-section is modified by the form factor $F(q)$ at high momentum transfer q. The latter reflects the spatial distribution of nucleons inside the nucleus. The form factor parameterizes the loss of coherence due to the finite size of the nucleus for the WIMP-nucleus interaction as the WIMP energy increases, and thus it reduces the effective cross-section for heavy WIMPs and heavy nuclei. For spin-independent scattering the form factor can be derived analytically, being defined at non-zero momentum transfer as the Fourier transform of the nuclear matter distribution. The effective cross section can then be written as

$$\sigma(q) = \sigma_0 F^2(q), \tag{1.17}$$

where σ_0 is the zero momentum transfer cross-section which contains all dependencies on the specific interaction and $F(q)$ depends only on the momentum transfer. More details on parameterization of the form factor describing elastic scattering of WIMPs can be found in [21].

The differential rate for the elastic WIMP-nucleus scattering is given by [9]:

$$\frac{dR}{dE_r} = N_T \frac{\rho_\chi \sigma_0}{2 m_\chi m_r^2} F^2(q) \int_{v_{min}}^{v_{esc}} \frac{f_{lab}(v)}{v} dv, \quad v_{min} = \sqrt{\frac{E_r m_N}{2 m_r^2}} \tag{1.18}$$

where N_T represents the number of target nuclei, $f_{lab}(v)$ is the velocity distribution of WIMPs in the laboratory frame, m_N is the mass of the nucleus, and m_r is the reduced mass. Assuming a simple Maxwellian WIMP halo and neglecting the

motion of the Earth and Sun, the integration over all detectable recoil energies between the energy threshold of the detector E_{thr} and maximum recoil energy $E_{max} = 2m_r^2 v^2/m_N$ gives the total event rate as

$$R = N_T \frac{\rho_\chi \sigma_0}{m_\chi m_N} \frac{2}{\sqrt{\pi}} v_0 \exp\left(-\frac{E_{thr} m_N}{2 m_r^2 v_0^2}\right), \tag{1.19}$$

with $v_0 = 220$ km s^{-1} being the rotational velocity of the Sun around the galactic center and the form factor $F(q) \sim 1$ for light WIMPs.

In order to obtain a more realistic WIMP event rate than the one described by Equation 1.19, one has to take into account the motion of the Earth around the Sun. This increases the total WIMP rate and yields a yearly modulation in the event rate which may serve for discriminating background from a dark matter signal. In June the Earth's rotation velocity adds to the Sun velocity through the halo, whereas in December the two velocities are in the opposite directions. An exact expression for the velocity can be found in [22]. These fluctuations produces a rate variation of about 7 % over the course of the year. Therefore direct detection experiments based on this signature need large statistics.

Figure 1.2 shows the integrated recoil spectra plotted as a function of the discrimination threshold energy expected for 100 GeV/c^2 WIMPs scattering on various scintillating targets with a spin-independent WIMP-nucleon scattering cross-section of 1 pb.

Direct detection experiments always only measure the product $\rho_\chi \sigma_0$, and the individual local WIMP density ρ_χ cannot be disentangled from the cross section σ_0. To assist the comparison between different direct detection experiments, the cross section is not quoted for the particular nucleus because different experiments use different targets. Instead, assuming a spin-independent interaction of WIMPs with the target nucleus, and following [24] the WIMP-nucleus cross section is rescaled as

$$\sigma_{coherent,nucleon} = \left(\frac{1 + m_\chi/m_N}{1 + m_\chi/m_p}\right)^2 \frac{\rho_\chi}{A^2} \tag{1.20}$$

where m_N and m_p are the mass of the target nucleus and of the proton respectively.

1.3.5 Signal Identification

As can be seen in Figure 1.2 the expected recoil spectra of WIMPs on different targets is rather featureless and rapidly decreases towards high energies. Since it is very reminiscent to the shape of typical background, the suppression of the latter caused by known particles which may mimic a WIMP signal is of crucial importance.

Furthermore, a special approach is needed in order to identify events as being caused by WIMPs. Since the expected WIMP spectrum and rate depend in a

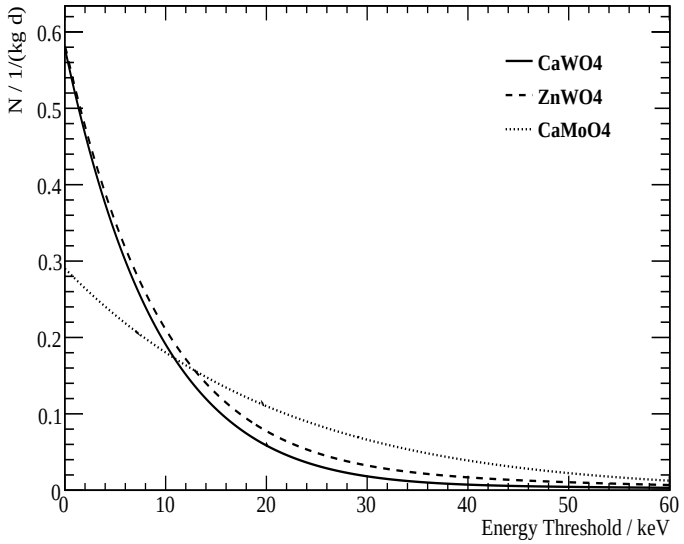

Figure 1.2: The integrated recoil spectra expected for 100 GeV/c^2 WIMPs scattered elastically on $CaWO_4$ (solid line), $ZnWO_4$ (dashed line), and $CaMoO_4$ (dotted line) targets. The coherent WIMP-nucleon scattering cross-section is 1 pb [23]. The count rate on a $CaMoO_4$ target above a discrimination threshold of ~14 keV is higher than that on a $CaWO_4$ target. In a $CaWO_4$ target most of the WIMP induced recoils are expected to appear below 40 keV, while in a $CaMoO_4$ target this value is shifted towards a higher energy of ~60 keV.

known way on the target nucleus, the comparison between the WIMP-nucleon interaction rate on different target materials would give us an unique possibility to verify a positive WIMP signal and to learn about WIMP properties. In CRESST-II, such multi-targets are intrinsic to $CaWO_4$ crystals (O, Ca, W). Moreover, extensive research on alternative target materials is ongoing. In particular, investigation of $CaMoO_4$ and $ZnWO_4$ as new target materials for the CRESST-II experiment is the topic of this work. On $CaMoO_4$ crystals WIMPs are expected to scatter mainly on molybdenum nuclei[1], whereas on $CaWO_4$ (or $ZnWO_4$) targets they would mainly scatter on tungsten nuclei. Once we see a signal with consistent behavior in various targets, this will be a very strong point for the dark matter discovery claim.

[1]This is due to the factor A^2 in the spin-independent scattering cross-section.

Chapter 2

The CRESST-II experiment

The aim of the CRESST experiment is to measure signals caused by WIMP dark matter particles via their elastic scattering off nuclei in a target [25, 26]. As discussed in Section 1.3.4, the maximum energy transfer to the target following a WIMP-nucleus interaction is expected to be in the order of a few tens of keV. To be able to detect such a small amount of energy the CRESST experiment employs very sensitive cryogenic calorimeters. Furthermore, due to the small WIMP-nucleus interaction cross-section, the event rate is expected to be less than 0.1 events per day per kg of the target mass. Therefore it is of crucial importance to quell background from various sources and/or to discriminate against it. Besides placing the experimental facility deep underground and shielding it, the CRESST-II experiment uses active background discrimination technique to further suppress the residual background.

This chapter presents the setup of the experiment and discusses the main aspects of the CRESST-II light-phonon measuring technique with cryogenic detectors.

2.1 Background and shielding

The sensitivity of rare event searches is limited by the presence of the unidentified radioactive background which can be caused not only by radioactivity inside or in the surroundings of the detectors, but also induced by cosmic radiation. It is therefore very important to consider various sources of background in the design of an experiment with low counting statistics. In the following sections, some possible background sources and the ways to suppress them will be discussed.

Element	flux in m^{-2} s^{-1}
muons	~400
photons	~300
electrons, positrons	~200
protons	~6

Table 2.1: Composition of the cosmic ray flux at sea level [27].

2.1.1 Muons

At sea level cosmic rays are subdivided into a soft (electrons/positrons, photons) and a penetrating muon component, see Table 2.1.1. Muons, with energies ranging from ~ 100 MeV to ~ 1 TeV, contribute to the detector background in different ways, e.g.

- by depositing energy while traversing the detector
- by interacting with materials surrounding the detector, and thus leading to X-rays, γ's or neutrons spallation
- by cosmogenic activation, i.e. neutrons produced by muons through the spallation processes can produce radionuclides.

The shielding of the experiment against cosmic radiation can be achieved by installing the setup in a deep underground site. The CRESST-II experiment is hosted by the Laboratori Nazionali del Gran Sasso (LNGS) [28], located in the Gran Sasso highway tunnel connecting L'Aquila to Teramo, in central Italy. The laboratory is operated by Instituto Nazionale di Fisica Nucleare (INFN). It is located on the vertical of Monte L'Aquila (2600 m high) and has an average rock coverage of 1400 meters; see Figure 2.1. The underground area includes three main halls called *A*, *B* and *C*; see sketch in Figure 2.2. The facility of the CRESST-II experiment is situated in the hall *A*. Such a deep underground location helps to reduce the muon flux by six orders of magnitude to about 2 m^{-2} h^{-1} [29].

To further reject prompt muon background the second phase of the CRESST experiment uses an anti-coincidence technique, namely, a muon veto counter. A system of 20 plastic scintillator panels, each read out by a photomultiplier, surrounds the experimental setup with a solid angle coverage of ~ 99 %. When a muon triggers a veto, events recorded in the detector are rejected. Moreover, cosmogenic activation of the materials used in the experiment can be prevented by storing them deep underground. Muon-induced secondary electrons, photons and protons can be suppressed by various passive shields.

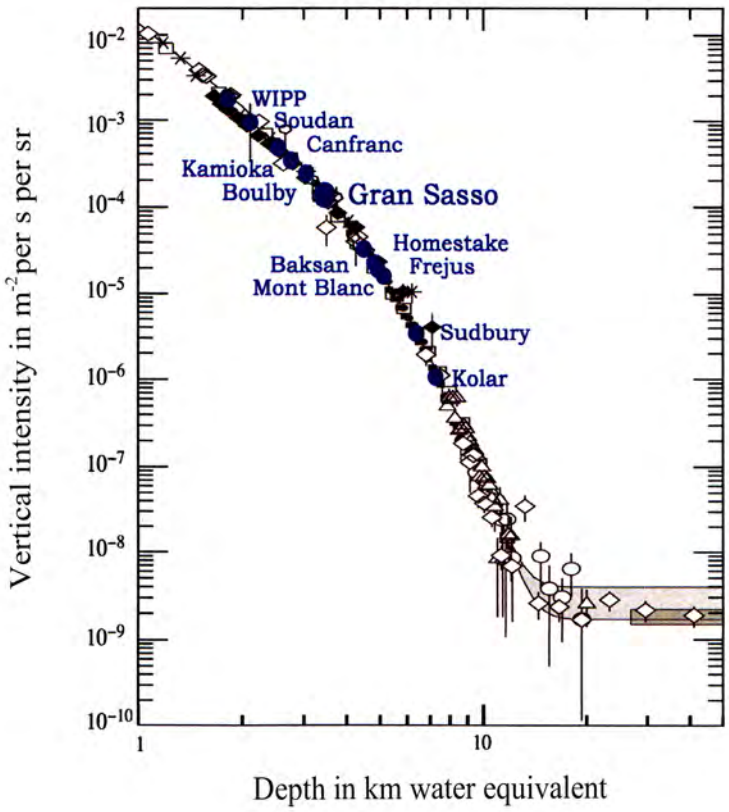

Figure 2.1: The muon flux versus depth. Superimposed are the minimum overburdens of a few underground laboratories. At depth greater than ~ 10 km water equivalent the muon flux levels off due to neutrino induced muons. The CRESST-II experiment is located at Gran Sasso laboratories. Figure taken from [27].

2.1.2 Radionuclides

Besides cosmogenically activated radionuclides, the main contribution to the environmental radioactivity comes from primordial radionuclides and from man-made radioactive isotopes (^{90}Sr, ^{137}Cs). Form the background point of view, the most abundant radionuclides are those belonging to the natural uranium and thorium decay chains as well as potassium originating in the target material itself. A thorough investigation on α-active contaminants present in some $ZnWO_4$ and $CaWO_4$ crystals will be presented in Section 8.2.2.

An important contribution to the total background activity at LNGS comes from the decay of radon and its daughters. The half-life of ^{222}Rn ($t_{1/2}$ = 3.8 days [30]) is long enough for this gas to diffuse through the rock to the air or to the ground water. Hence, the radon content in a low background facility strongly depends on the ventilation. For example, in the Gran Sasso

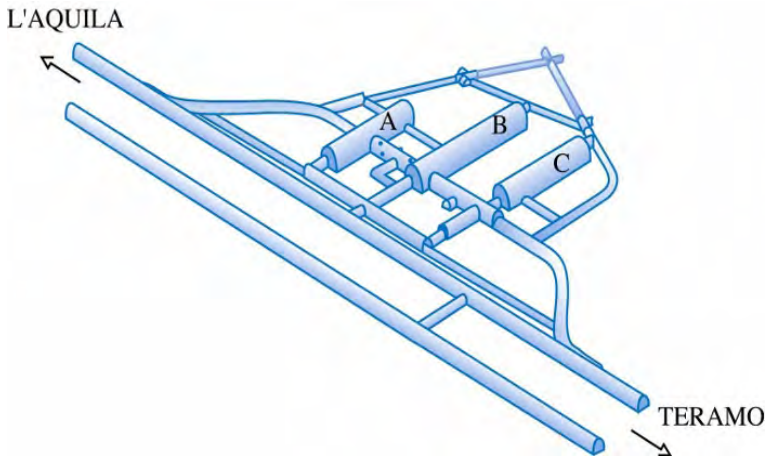

Figure 2.2: Sketch of the Gran Sasso underground laboratories.

laboratories the radon content is reduced with the help of the ventilation from about 300 Bq m^{-3} to 20 - 50 Bq m^{-3} [31, 32]. To prevent the radon from diffusing inside the shielding, the latter is enclosed in an air tight stainless steel container. This so-called radon box is constantly flushed with gas boiling off from liquid nitrogen and kept at a small overpressure.

Furthermore, in addition to radionuclides from natural decay series, also potassium may contribute to the total environmental radioactivity. In spite of its low isotopic abundance there is more potassium than uranium or thorium in the environment. Therefore, the background level from this isotope is comparable with that from the ^{238}U or ^{232}Th decay chains.

In the decays of the radionuclides a variety of α- and β-particles are produced. Alpha-particles, emitted in the surrounding of the detector due to environmental radioactivity, are monoenergetic with energies up to ~ 10 MeV. They can be easily stopped by less than one millimeter of a solid material since their penetration depth is of the order of μm. Beta-particles have continuous energy spectra with endpoints below a few MeV. They can also be stopped by a solid material of a few mm thickness. Depending on the energy[1], γ-particles can travel considerable distances without energy loss. The measured gamma activities from the ^{238}U and the ^{232}Th decay chains as well as ^{40}K, present in the Gran Sasso laboratories, are reported in Table 2.2. The integral gamma flux for all natural decay chains is measured to be about 1 cm^{-2} s^{-1} [34].

The interactions of α-, β- and γ-particles with the target material induce electron recoil events. In principle, these events can be identified with the help of the CRESST-II light-phonon measuring technique which will be explained in the subsequent sections. Nevertheless, a high count rate caused by electron recoil

[1]Energies of γ-particles produced in the ^{232}Th decay chain can reach up to 2.6 MeV.

sample	^{238}U	^{232}Th	^{40}K
Hall A rock	116	12	307
Hall B rock	7	0.3	7
Hall C rock	11	0.4	4

Table 2.2: Measured gamma activity in Bq/kg for various rock samples from the Gran Sasso laboratories. Errors are less then 1 %. The difference between various samples is due to the different local composition of the rock. Data taken from [33].

events may sufficiently increase the dead time of the experiment thus prolonging its measuring time. Therefore, it is important to passively shield the target detectors from this type of background as much as possible.

Special attention should be paid to the choice of shielding materials, since they may themselves be a source of background. For example, the isotope ^{210}Pb ($t_{1/2}$=22 years [30]), which occurs in natural lead, is unstable. ^{210}Pb and its daughters are the source of α-, β-, and γ-particles, which, in turn, may contribute to the low energy background of the experiment. One way to avoid this type of background is to use ancient (Roman) lead or Boliden lead. Alternatively, an additional copper layer within the lead shielding can be used to avoid residual radioactivity from ^{210}Pb and to shield the bremsstrahlung. The impurity content of some shielding materials measured within the framework of this thesis is presented in Appendix A.

In order to reduce the flux of γ's, detectors are enclosed by a high density, large atomic number, massive shield. In CRESST-II a 20 cm thick Boliden lead shield, followed by a 14 cm thick radiopure **copper shield** is used. Both of them surround the experimental volume and are mounted on movable wagons to allow access to the detectors.

Furthermore, most of the background remaining after shielding originates from intrinsic radioactive impurities in the target material. Due to the powerful active discrimination capabilities of the CRESST-II detectors this source of background can be suppressed with high efficiency. Nevertheless, in order to reach the highest possible sensitivity of the experiment, special precautions must be taken to obtain as radiopure targets as possible.

2.1.3 Neutrons

In direct dark matter searches neutrons are very dangerous background since they produce the same signature as expected from WIMPs. Neutrons can scatter elastically on target nuclei and induce nuclear recoil events. Even at deep

Energy range in MeV	Neutron flux in 10^{-6} cm^{-2} s^{-1}
below 5×10^{-8}	1.07 ± 0.05
5×10^{-8} to 10^{-3}	1.99 ± 0.05
10^{-3} to 2.5	0.53 ± 0.01
2.5 to 5	0.18 ± 0.04
5 to 10	0.04 ± 0.01
10 to 15	below 10^{-3}
15 to 20	below 10^{-5}

Table 2.3: Neutron flux measured in the Hall A of the Gran Sasso underground laboratory with the help of BF_3 counters. Data taken from [35].

underground sites the experiments have to cope with the problem of neutrons. There are several sources of low energy (few MeV) neutron production, namely,

- (α, n) reactions on light elements;
- fission of nuclei in the experimental setup and surrounding rock;
- muon-induced spallation reactions in the rock and shielding.

Due to the low content of uranium and thorium isotopes in the dolomite rocks of the mountain at Gran Sasso laboratory, the neutron flux is reduced by three orders of magnitude from the sea level flux [28]. The residual neutron flux in the Hall A is presented in Table 2.3.

To further suppress the flux of neutrons, the experimental volume should be surrounded by materials with a high hydrogen content. Such materials are ideal to moderate neutrons, since the energy transfer is maximized. Polyethylene or water are commonly used to slow down neutrons to thermal energies. The CRESST-II setup is surrounded by a 45 cm thick polyethylene neutron moderator.

Simulations of the expected neutron recoil spectra in a $CaWO_4$ target, induced by various neutron sources and with possible neutron shielding, have been performed in [36]. From Figure 2.3 it can be seen that with an installed neutron moderator the remaining neutron flux is dominated by muon-induced neutrons. This background can be suppressed with the help of the muon veto.

Finally, computing the interaction of a neutron of mass m_n = 939.6 MeV [16] and energy E_n and a WIMP of mass M_χ with a nucleus of mass M_N gives the

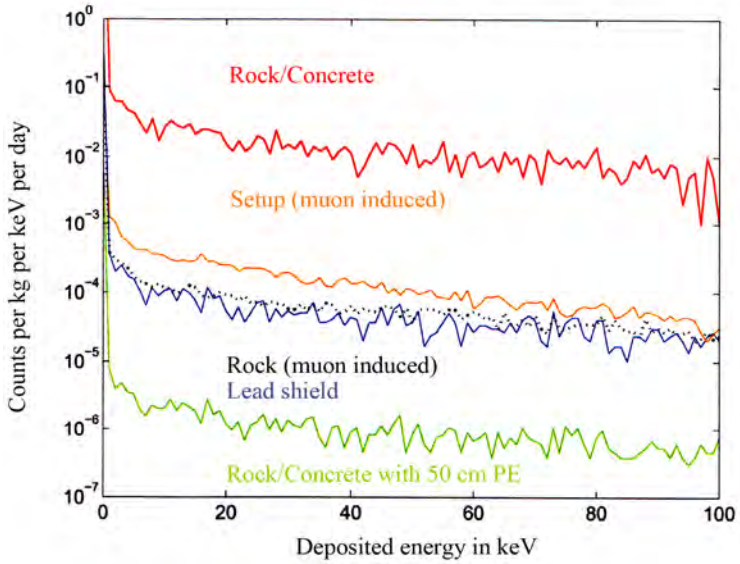

Figure 2.3: Simulated recoil spectra in a $CaWO_4$ crystal induced by various neutron sources in the CRESST-II setup. Shown in **red** is the spectrum caused by low energy neutrons from the rock or concrete and which can be moderated with a 50 cm thick PE shield (**green**). Other sources of background are neutrons induced by muon interactions in the rock (**black**) or in the setup (**orange**). The spectrum caused by low energy neutrons from fission reactions of 0.1 ppb ^{238}U in the lead shield is shown in **blue**. Figure taken from [37].

recoil energy E_{recoil} as

$$E_{recoil}(n) = \frac{2E_n M_N m_n}{(M_N + m_n)^2}\,(1 - \cos\theta)\,, \tag{2.1}$$

$$E_{recoil}(\chi) = \beta^2 \frac{M_\chi^2 M_N}{(M_\chi + M_N)^2}\,(1 - \cos\theta)\,, \tag{2.2}$$

where $\beta = v/c$ is the WIMP velocity in the units of c and θ is scattering angle in the center of mass frame. Assuming an average WIMP velocity at the position of the Earth of $v = 230$ km/s $\approx 8 \times 10^{-4}$c [38], and a head-on collision of 60 GeV/c^2 WIMPs or 1 MeV neutrons with the nucleus, the calculated maximum recoil energy for several nuclei is presented in Table 2.4. It can be seen that the recoil energies for various nuclei in case of neutron-induced events overlap with the ones from WIMP-induced events. Moreover, the heavier the nucleus is, the smaller the energy transfer from the scattered neutron is. Consequently, less energy is converted into the scintillation light. Hence for heavy nuclei it is more difficult to identify neutron-induced recoils and to distinguish them from possible WIMPs.

element	nucleus mass in GeV	neutron-induced	60 GeV/c^2 WIMP-induced
^{16}O	14.89	223	11
^{28}Si	26.06	134	15
^{40}Ca	37.21	96	17
^{64}Zn	59.54	61	18
^{98}Mo	91.18	40	17
^{112}Cd	104.21	35	16
^{184}W	171.31	22	14

Table 2.4: Maximum recoil energies of various nuclei in keV for 1 MeV neutron-induced and 60 GeV/c^2 WIMP-induced events.

2.2 Layout of the experiment

2.2.1 The cryostat

The CRESST detectors are operated as cryogenic calorimeters at temperatures of about 10 mK. In order to obtain such a low temperature, a ^{3}He/^{4}He dilution refrigerator[2] is used. This is the so-called cryostat which has a base temperature of $\sim$ 6 mK. A sketch of the CRESST-II experimental setup is presented in Figure 2.4.

To provide a low background environment, the detectors are housed in the custom made cold box constructed from a specially selected materials. It is kept away from the cryostat, while the cooling power of the mixing chamber is transfered to the shielded detector volume via a 1.3 m high purity copper cold finger. Moreover, to prevent any line of sight from the experimental volume to the cryostat, there is a Boliden lead shield installed directly below the mixing chamber and on the thermal shield at nitrogen temperature.

The cold box contains five thermal shields made of radiopure copper. These are at 80 mK, 600 mK, 4 K, 77 K and at room temperature; see the right panel of Figure 2.5. Each shield was electropolished in order to reduce surface contaminations. Since mechanical vibrations can limit the operation capability of the CRESST detectors, the cryostat rests on air dampers and does not touch the passive shields. The pumping lines of the cryostat are also decoupled from the setup. Under normal operation conditions, the main helium bath of the cryostat lasts for three days before refilling with cryogenic liquids.

[2]Principles of the operation of dilution refrigerators can be found in [39].

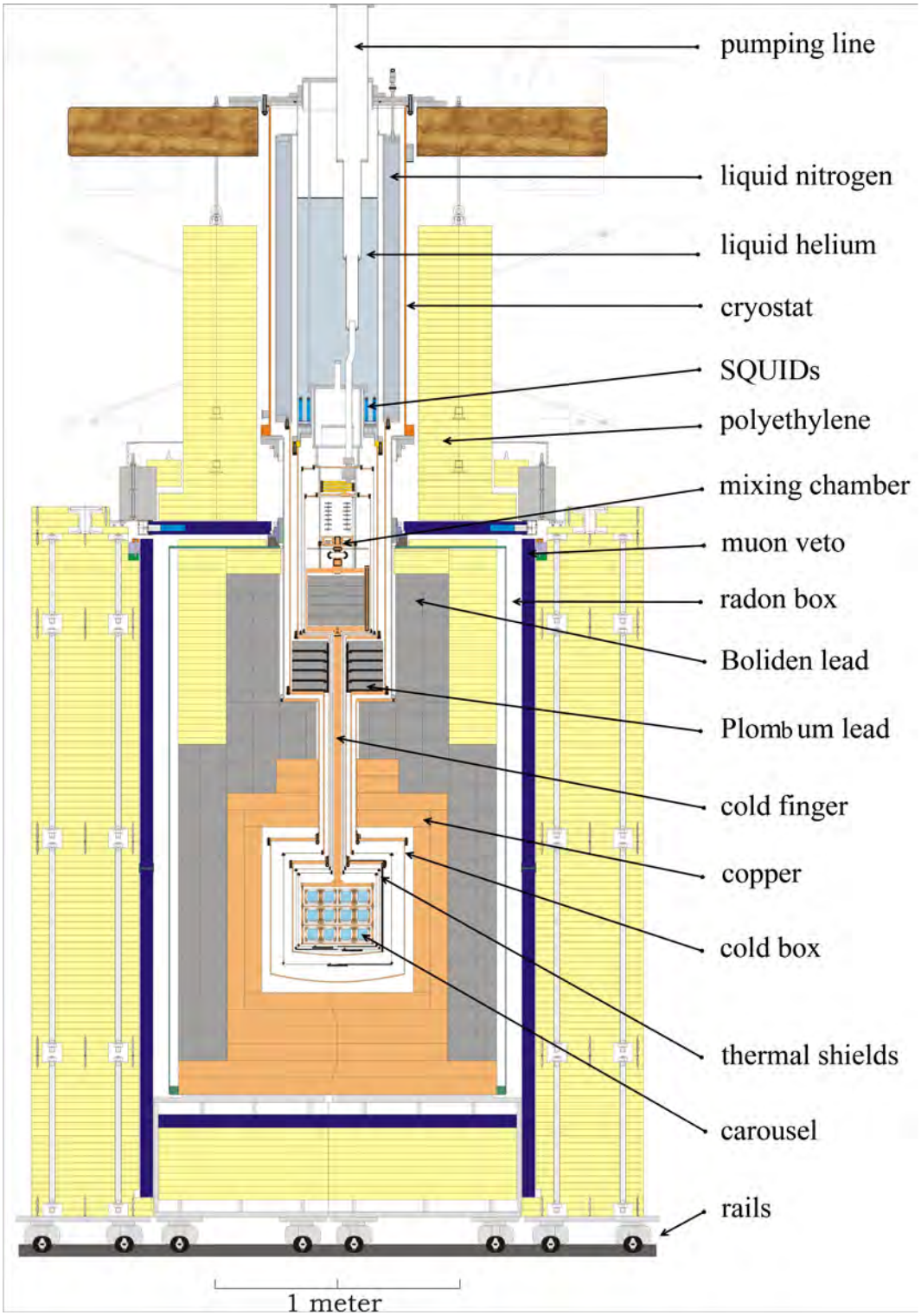

Figure 2.4: Illustration of the CRESST-II cryostat (Oxford Instruments S1000 dilution refrigerator), shields, and the cold box. See text for details.

2.2.2 Setup

To protect sensitive electronics from electromagnetic interferences, the cryostat and the surrounding shields are installed inside a two-storey Faraday cage. To reduce the contaminations with radioactive isotopes while detector mounting, the ground floor of the cage is equipped as a clean room. From the upper level of the cage the maintenance of the cryostat and electronics can be performed. Gas handling, pumping system and data acquisition electronics are located outside the Faraday cage. Finally, on the top level of the CRESST hut there is a small chemistry lab, a small clean room where detectors can be prepared for the installation in the cold box, and some workspaces.

2.2.3 Experimental volume

The current 80 mK thermal shield has a capacity to enclose 24 liters of the experimental volume. A support structure, the so-called **carousel**, is designed to hold up to 33 detector modules arranged in the 12 towers; see Figure 2.5. Equipping all 33 detector modules with $CaWO_4$ crystals allows for a target mass of $\sim$ 10 kg (with $ZnWO_4$ crystals for $\sim$ 13 kg). With this target mass and the present design, the experiment probes the spin-independent WIMP-nucleon cross-section at the level of 10^{-8} pb [40].

The carousel is decoupled from the mechanical vibrations of the cryostat (mainly caused by boiling cryogenic liquids) with custom made springs [41] and is only weakly coupled thermally to the cold finger of the cryostat, thus providing an efficient "filter" to fast temperature fluctuations of the mixing chamber.

A significant advantage of the CRESST-II detectors is their modularity. Individual handling and dismounting of the modules is possible. Once a design for an individual module has been successfully established, the same design can be replicated in many copies of the module. Another important feature of the modular structure is the possibility to host various target materials. Moreover, arranging the detectors in array allows for testing of a uniform WIMP event rate within various modules. This provides an additional dark matter signature by requiring a single interaction only for a dark matter candidate event and allows for identification of residual background caused by neutrons through coincident events.

2.3 The CRESST-II detectors

In order to detect a small recoil energy (typically of the order of some tens of keV), expected in elastic WIMP-nucleon scattering, CRESST employs cryogenic

Figure 2.5: *Left*: Drawing of the detector support structure. Detector modules are mounted on towers which can be handled as a whole. *Right*: Photograph of the carousel equipped with the detector modules for the Run 31. The top parts of the five thermal shield are visible.

calorimeters. The basic concept of a calorimeter is to measure the energy via a temperature rise ΔT. A calorimeter usually consists of:

- a target with heat capacity C in which a particle interaction takes place,
- a thermometer which is thermally coupled to the target,
- and a thermal link to a heat bath that returns the target to the equilibrium temperature T_b.

2.3.1 Active background discrimination

The main limitation in rare event searches is the residual radioactive background. Dramatic improvements in sensitivity are achieved by the powerful **active background discrimination technique**. It utilizes the fact that the light output from **nuclear recoil** events in the crystal caused by neutrons and expected from WIMPs, is reduced/quenched compared to the light output observed from **electron recoil** events, induced by α-, β-, or γ-particles.

For the simultaneous detection of scintillation light and phonons the experiment uses dedicated **detector modules**. A single module consists of two cryogenic calorimeters: a scintillating target crystal with a temperature sensor attached to its surface, referred to as the **phonon detector**, and the nearby but separated **light detector**, which is a wafer with a temperature sensor on its surface. To increase the collection efficiency of scintillation light, the module is encapsulated with the scintillating and reflecting foil VM2002 from 3M com-

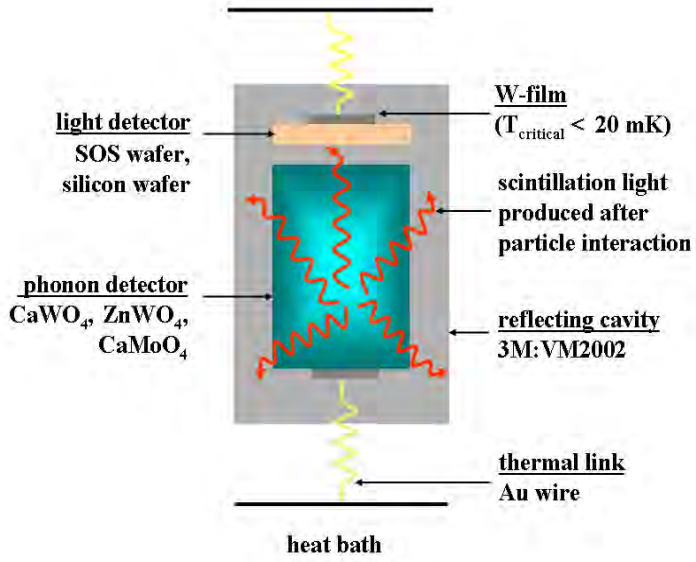

Figure 2.6: Schematic representation of a CRESST-II detector module for coincident phonon and light signal measurements. See main text for details.

pany. The arrangement of these two cryogenic detectors is shown schematically in Figure 2.6. Figure 2.7 is a picture of an open detector module.

The first active background discrimination proof-of-principle experiment was carried out with a phonon detector realized on a small $CaWO_4$ crystal and operated together with a light detector made of a small sapphire wafer with a silicon layer [42]. A more recent study proved that the discrimination technique also works nicely with a phonon detector based on a small $ZnWO_4$ crystal and operated together with a silicon light detector. The results of the later work are shown in Figure 2.8. Two bands in the scatter plot presented in the right panel of Figure 2.8 are clearly distinguishable down to ~15 keV energy in the phonon detector. The upper band is due to electron recoil events in the $ZnWO_4$ crystal caused by cosmic background as well as γ's from a ^{57}Co and a ^{137}Cs calibration source. The lower band is due to nuclear recoil events caused by neutrons from an americium/beryllium source.

2.3.2 Phonon detector

A standard phonon detector consists of a cylindrical scintillating crystal (40 mm in diameter and 40 mm in height) and a thermometer deposited directly onto its surface[3]. The active discrimination technique can work with various scintillating crystals. They, however, must satisfy several criteria:

[3]The thermometer layout will be described in Section 2.3.4.

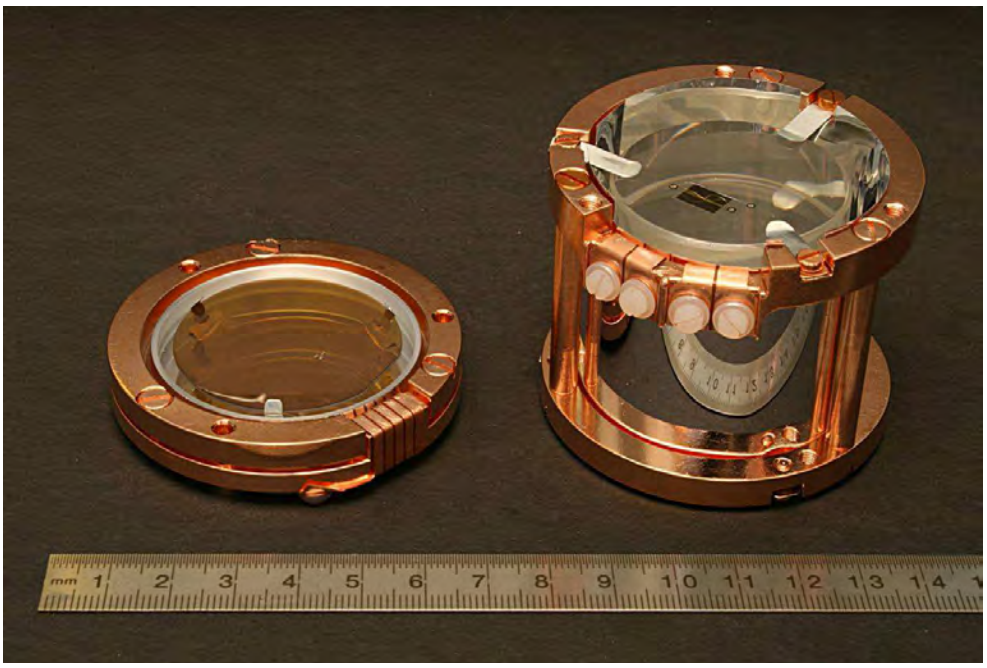

Figure 2.7: Picture of an open CRESST-II detector module. On the *left* is a light detector, on the *right* is a phonon detector. Each detector is mounted on a copper holder which is thermally coupled to the carousel. The setup is surrounded by a highly reflecting cavity in order to improve the light collection efficiency.

- no surface degradation of light yield;
- high scintillation efficiency at low energy threshold;
- minimal amount of radioactive impurities;
- heavy nuclei;
- diamagnetic;
- mechanically and chemically stable.

Given all those requirements the list of scintillating crystals suitable for the experiment becomes limited. Currently CRESST-II employs $CaWO_4$ crystals as the basic target material [40, 25, 17]. Among different scintillators it was selected because of its scintillation properties at low temperature. However, in order to further improve the capability of rejecting background caused by known particles, crystals with scintillation efficiency higher than that of $CaWO_4$ are

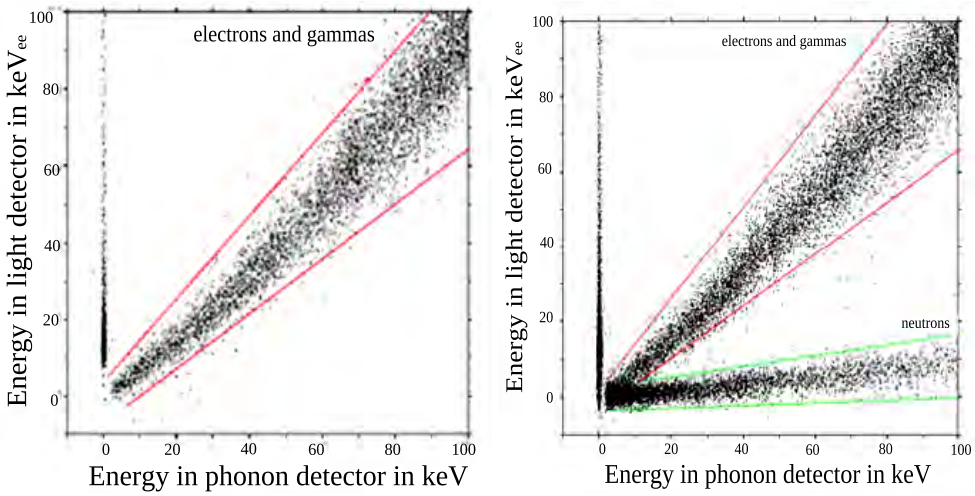

Figure 2.8: Scatter plots of the energy in the silicon light detector versus the energy in the phonon detector based on a $ZnWO_4$ crystal, on the **left** measured by irradiation of the crystal with a ^{57}Co and a ^{137}Cs γ-source, and on the **right** with an additional Am/Be neutron source. Electron recoils are clearly distinguishable from nuclear recoils. A well defined class of events with zero energy in the phonon detector originates from direct hits on the light detector. The straight lines depict the recoil bands.

constantly under investigation. Moreover, the comparison between the WIMP-nucleon interaction rate on various target crystals would give the experiment an unique possibility to verify a positive WIMP signal and to learn about WIMPs properties. In this regard, materials containing heavy nuclei different from tungsten are particularly interesting.

Alternative target materials

Among the ABO_4 ternary materials (with A = Ca, Zn, Pb, Cd, etc., and B = Mo or W) $CdWO_4$ crystals have the highest scintillation efficiency[4] [47]. However, in contrast to $CaWO_4$, this material similarly to the commonly used $PbWO_4$ crystals has an intrinsic long-lived radioactive isotope. Hence, $CdWO_4$ crystals are not favorable for the rare event searches unless enriched in ^{106}Cd or ^{116}Cd.

Resent studies carried out with $ZnWO_4$ [48, 49, 50, 43] and $CaMoO_4$ crystals [51, 52, 43] revealed their high potential to be employed as targets for rare event search experiments. In particular, the measurements with a small $(20 \times 10 \times 5)$ mm^3 $ZnWO_4$ crystal at mK temperatures have shown that its scintillation efficiency is comparable with that of $CaWO_4$. Moreover, due to the zinc

[4]The research on alternative scintillating materials for CRESST-II but different from ABO_4 crystals can be found in [43, 44, 45, 46].

based powders used for $ZnWO_4$ crystal growth versus the calcium based ones used for $CaWO_4$, $ZnWO_4$ crystals promise better radiopurity [53].

On the other hand, $CaMoO_4$ crystals have an advantage of having the heaviest nuclei different from tungsten. In these crystals WIMPs are expected to scatter mainly on molybdenum (Mo) nuclei whereas on a $CaWO_4$ or a $ZnWO_4$ target they would mainly scatter on tungsten (W) nuclei. Figure 1.2 shows simulations of integrated recoil spectra plotted as a function of the discrimination threshold energy expected for a 100 GeV/c^2 WIMP scattering on $CaWO_4$, $ZnWO_4$, and $CaMoO_4$ crystals with a spin-independent WIMP-nucleon scattering cross-section of 1 pb. The count rate on a $CaMoO_4$ target above a discrimination threshold of $\sim$ 14 keV is higher than that on a $CaWO_4$ target. In a $CaWO_4$ target most of the WIMP induced recoils are expected to appear below 40 keV, while in a $CaMoO_4$ target this value is shifted towards a higher energy of $\sim$ 60 keV. Thus, in case of a positive WIMP signal a scaling in the nuclear recoil spectrum should be observed.

Last but not least, $ZnWO_4$ and $CaMoO_4$ crystals are excellent candidates to search for rare double beta decay (2β) processes which are important for the determination of the absolute neutrino mass scale [50, 54, 51, 55]. With the help of the CRESST-II measuring technique a competitive upper limit on the half-lives of some 2β-processes can be obtained, e.g. with the ^{100}Mo isotope (natural abundance is 9.667% [56]) present in $CaMoO_4$ crystals or with the ^{64}Zn (natural abundance is 48.268 % [56]) present in $ZnWO_4$ crystals. Thus, integration of phonon detectors based on these materials would provide a possibility to perform multi-purpose experiment on one target simultaneously.

2.3.3 Light detector

A light detector consists of a light absorbing wafer and a thermometer. In order to absorb the scintillation light emitted by a crystal, silicon or silicon-on-sapphire (SOS) wafers of circular shape (ϕ 40 mm) are used. As shown in Figure 2.9, the absorption properties of these materials are wavelength dependent. Hence, special attention should be paid for finding an optimal light detector suitable for materials different from $CaWO_4$.

2.3.4 Thermometers

For measurements of the temperature rise after a particle interaction, both cryogenic calorimeters, namely, the phonon detector and the light detector, have **superconducting phase transition thermometers** made from tungsten (W-SPT, W-film). In this section we shall concentrate on the design of the thermometer layout, whereas information about the fabrication of W-films will be presented later on in Section 5.3.1.

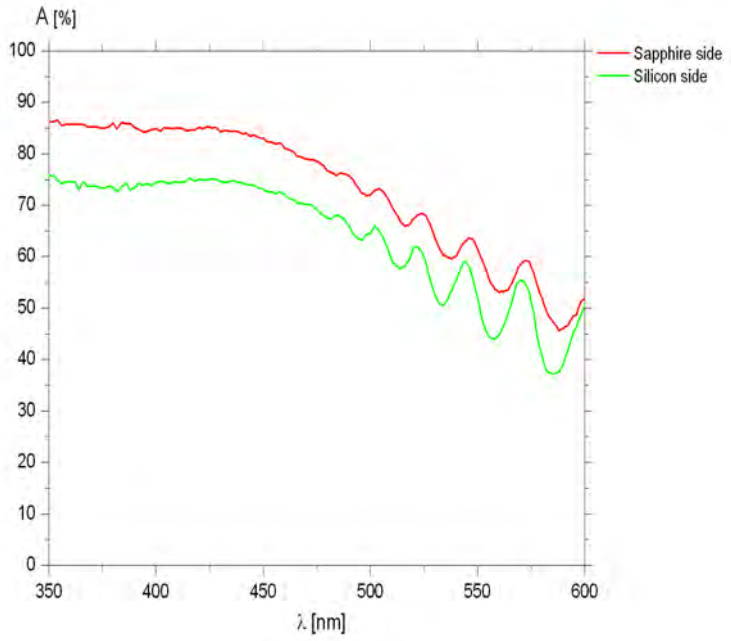

Figure 2.9: Absorption efficiency of the silicon on sapphire wafer between 350 nm and 600 nm. Shown in green and red are the different values obtained by measuring on the silicon and on the sapphire side, respectively. Clearly visible for wavelengths larger than 450 nm is an interference due to the reflection on the two surfaces of the thin silicon layer. Figure taken from [57].

Thermometer on phonon detectors

Tungsten-thermometer of a phonon detector consists of a $\sim$ 200 nm thick **tungsten layer** evaporated on the crystal surface. The area of the W-layer is (6×8) mm^2 small. A silicon dioxide buffer layer is evaporated between the W-film and the crystal for preventing interdiffusion between the two. The electrical and thermal connections of the thermometer are shown in Figure 2.10. A **gold contact pad** in the middle of the film is connected to the copper detector holder via a gold bond wire of 25 μm in diameter, providing both, an electrical ground and a thermal link to the heat bath. **Aluminium contact pads** are used to connect the W-SPT to the readout circuit. Electrical connections are provided via superconducting aluminum wires, ultrasonically bonded from the aluminum pads to the insulated Cu-Kapton-Cu pads on the detector holder. Temperature control is provided by an **electrical heater** in the form of a 25 μm in diameter gold wire bonded to the gold pad and two aluminum circular pads on both sides of the W-SPT. In order to avoid electrical cross talk with the readout circuit,

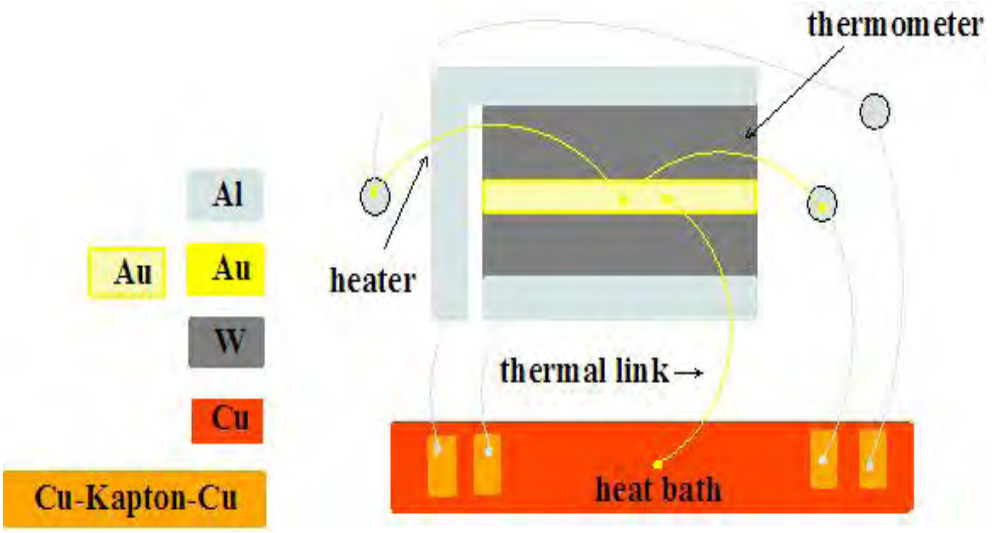

Figure 2.10: Schematic representation of a thermometer layout realized on a phonon detector.

the heater is only in point-like contact with the thermometer. Aluminium bond wires connect the heater structure pads to the temperature control circuit[5].

Phonon detectors with glued thermometers

It has been observed that the scintillation efficiency of a $CaWO_4$ crystal degrades due to evaporation of the W-film [58]. In order to prevent this, a new technique for producing phonon detectors was developed on the basis of research carried out in [59]. The thermometer is grown on a small $(20 \times 10 \times 1)$ mm^3 crystal wafer which is then glued to the target crystal.

Thermometer on light detectors

In order to achieve good sensitivity and a low energy threshold of the light detectors, a small heat capacity of the W-films is obligatory. The light detectors have a modified tungsten thermometer which includes phonon collectors made of an Al/W bilayer [60, 57]. It provides a collection area for phonons. The area of the W-layer is only (0.45×0.3) mm^2 small. Since phonon collectors get superconducting at much higher temperatures than the operating temperature of the detector, they do not contribute to the heat capacity of the thermometer.

The thermal link of the light detectors to the bath is weak enough to enable the thermometer to integrate over the scintillation light which is typically of the order of several hundred μs. The design of the thermometer layout on the light

[5]The readout and heater circuit will be presented in Section 2.4.1 and 2.4.3, respectively.

detectors was subject to several optimization studies, and more details can be found in the dedicated theses [57, 61, 62].

2.3.5 Pulse formation model

Different parts of the detector and the thermal couplings among them govern the signal formation. Let us consider the processes that take place in the detector following a particle interaction.

Creation of phonons

Ionizing radiation releases its energy mainly in the electron system of the target via inelastic scattering with its electrons. This creates highly excited electrons which relax back to the ground state via the transfer of their excitation to other electrons and/or by creating electron-hole pairs. In dielectrics, once the energy of the excited electrons is lower than twice the energy gap E_g, the relaxation occurs via the emission of optical phonons[6] which rapidly decay into acoustic phonons[7] of about half the Debye frequency ν_D[8]. As a result, an almost monoenergetic population of acoustic phonons is created. The energy released in the nuclear system of the target via elastic interactions with nuclei leads to a continuous spectrum of acoustic phonons up to ν_D. The fraction of energy released via this channel is negligible for γ's and electrons, but becomes important for α-particles, and is dominant for neutrons and WIMPs interactions. Thus, within a nanosecond, most of the energy deposited in the target is transferred to high frequency acoustic phonons. Both, ionizing and nuclear events, produce acoustic phonons but their initial phonon spectra are different.

For example, for dielectric crystals like $ZnWO_4$, $\nu_D/2 = 1.9$ THz (see Table 5.1), so that the associated phonons have energies of a few meV. Since at the temperature of interest ($\sim$ 15 mK) thermal energies are very small $E = k_B T \sim 1$ μeV, these THz phonons are called **non-thermal phonons**. Due to the anharmonicities of the crystal lattice these phonons rapidly decay with a rate $\Gamma \propto \nu^5$. Simulations show that starting with a phonon population at $\nu_D/2$, both initial phonon spectra decay to a distribution with a mean frequency of a few 100 GHz. Due to the strong frequency dependence of the decay rate, the non-thermal phonon generation remains almost constant for a few milliseconds. During this time, phonons spread ballistically throughout the target, and after a few surface reflections they uniformly fill the crystal.

[6] Optical phonons are called such because they are easily exited with the electric field of a light wave [63].

[7] Acoustic phonons correspond to sound waves in the lattice [63].

[8] In dielectric crystals the emission of scintillation photons (which is extremely important for the event discrimination) is highly suppressed by the small density of states for these excitations.

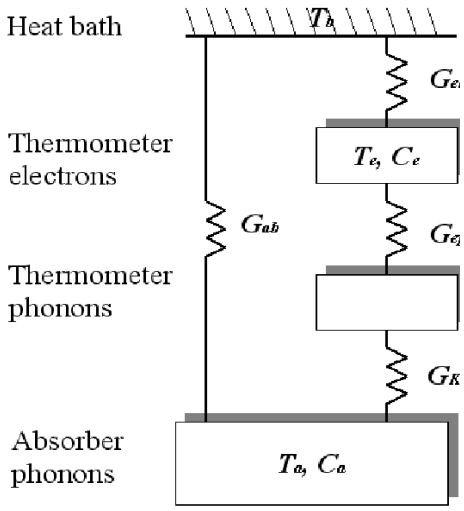

Figure 2.11: Thermal model of the calorimeter. T_b is the temperature of the heat bath. T_e and T_a represent the temperatures of the electron system of the thermometer and of the phonon system of the target, respectively. C_e and C_a are their respective heat capacities. $P_e(t)$ and $P_a(t)$ are power inputs into the electron system of the thermometer and the phonon system of the absorber crystal, respectively. The various G's are the thermal couplings between the systems.

Transmission of phonons

Such non-thermal phonons hitting the boundary between the crystal and the thermometer can be either reflected back or transmitted to the thermometer. When phonons enter the thermometer they are readily absorbed by free electrons of the tungsten film. This leads to a temperature rise in the thermometer. Since the lifetime of non-thermal phonons is relatively long (order of ms), their absorption in the thermometer competes with the thermalization in the target. Thereby, phonons in the target are considered to be composed of the two populations, namely, of non-thermal and thermal phonons. The latter determine the temperature of the target (T_a).

Calorimeter model

To describe the process of pulse formation quantitatively, the absorber crystal and the thermometer are modeled as shown schematically in Figure 2.11 [64]. The phonon system of the target as well as the phonon and the electron systems of the thermometer are represented as three independent parts. Each part is

described by the heat capacity C and temperature T.

After an energy deposition in the target (ΔE), the initial power input to the thermometer via non-thermal phonons can be defined as:

$$P_0 = \frac{\epsilon \Delta E}{\tau_n} \, , \tag{2.3}$$

where τ_n is the lifetime of the non-thermal phonons, and ϵ is the fraction of the non-thermal phonons, which are thermalized in the thermometer. The rest of the phonons (1 - ϵ) are thermalized in the target. The time dependent power input of the thermometer $P_e(t)$ and of the absorber $P_a(t)$ are given as

$$P_e(t) = \Theta(t)\, \epsilon\, \frac{\Delta E}{\tau_n}\, \exp^{-t/\tau_n} \, , \tag{2.4}$$

$$P_a(t) = \Theta(t)\, (1-\epsilon)\, \frac{\Delta E}{\tau_n}\, \exp^{-t/\tau_n} \, , \tag{2.5}$$

where the time between interactions in the target and the formation of a homogeneous distribution of non-thermal phonons is expressed by the step function $\Theta(t)$. The time constant τ_n is given as

$$\tau_n = \left(\frac{1}{\tau_e} + \frac{1}{\tau_a} \right)^{-1} \, , \tag{2.6}$$

where τ_e and τ_a are the time constants for thermalization in the thermometer and in the absorber, respectively.

The temperatures T_e and T_a can be described by two coupled differential equations

$$C_e \frac{dT_e}{dt} = P_e(t) - (T_e - T_a)G_{ea} - (T_e - T_b)G_{eb} \, , \tag{2.7}$$

$$C_a \frac{dT_a}{dt} = P_a(t) - (T_a - T_e)G_{ea} - (T_a - T_b)G_{ab} \, . \tag{2.8}$$

With the initial condition $T_a(t = 0) = T_e(t = 0) = T_b$ they obey the following solution for the thermometer signal $\Delta T_e(t) \equiv T_e - T_b$

$$\Delta T_e(t) \; = \; \Theta(t) \left[A_n (\exp^{-t/\tau_n} - \exp^{-t/\tau_{intr}}) + A_{th} (\exp^{-t/\tau_{th}} - \exp^{-t/\tau_n}) \right] \, . \tag{2.9}$$

Here τ_{intr} is the intrinsic thermal relaxation time constant of the thermometer, and τ_{th} is the thermal relaxation time of the target.

According to Equation 2.9, the solution which models the pulse shape consists of two components. One is the non-thermal component of the signal with amplitude A_n. It is connected to the direct absorption of the non-thermal phonons in the thermometer. The other amplitude A_{th} is connected to the temperature rise caused by the thermal phonons. Two different modes of thermometer operation are possible[9]:

[9]The different modes of thermometer operation refer to the processing of the incoming flux of non-thermal phonons. For the incoming particles, all CRESST-II detectors work as calorimeters measuring total energy depositions on an event by event basis.

- When $\tau_n \ll \tau_{intr}$, the duration of incoming flux of non-thermal phonons is shorter than the thermal relaxation time of the thermometer. Therefore, the thermometer integrates the flux of the incoming non-thermal phonons, $P_e(t)$. A_n then defines the integrated energy of non-thermal phonons absorbed in the thermometer. Thus, for a given ΔE, the heat capacity of the electron system of the thermometer C_e determines the amplitude $A_n \sim -\epsilon\Delta E/C_e$. This mode of thermometer operation is called **calorimetric mode**. The life time of non-thermal phonons (τ_n) defines the rise time of both, the non-thermal and the thermal signal component. The intrinsic thermal relaxation time constant of the thermometer (τ_{intr}) defines the decay time of the non-thermal signal component and the thermal relaxation time constant of the target (τ_{th}) determines the decay time of the thermal component. The thermometers of the CRESST-II light detectors are optimized to work in the calorimetric mode.

- When $\tau_n \gg \tau_{intr}$, the duration of the incoming flux of non-thermal phonons is larger than the relaxation time of the thermometer. Therefore, the thermometer measures the flux of the incoming non-thermal phonons. This mode of the thermometer operation is called **bolometric mode**; again $A_n \sim \Delta E$. The rise time of a non-thermal signal component is determined by τ_{intr}, whereas the decay time is given by τ_n. On the other hand, the rise time of the thermal component is defined by τ_n, and its decay time is defined by τ_{th}. The thermometers of the CRESST-II phonon detectors work in the bolometric mode.

2.4 Data taking

2.4.1 The thermometer readout

At the critical temperature (T_c) a superconducting material undergoes a phase transition from its normal conducting state to the superconducting state, i.e. the electrical resistance of the material drops to zero very sharply. The critical temperature of the bulk tungsten is around 15 mK. However, for thin tungsten films the transition temperature varies depending on the conditions of evaporation. In particular, the deposition temperature and stress inside the grown films can play an important role.

Figure 2.12 shows a sketch of a thermometer transition curve. The shape of the transition curve from the normal to the superconducting state of the W-film can vary for different thermometers and depend not only on the fabrication process but also on the type of the material onto which the W-film is evaporated. Typically, the resistance of the W-SPTs is in the range of 100 to 300 mΩ.

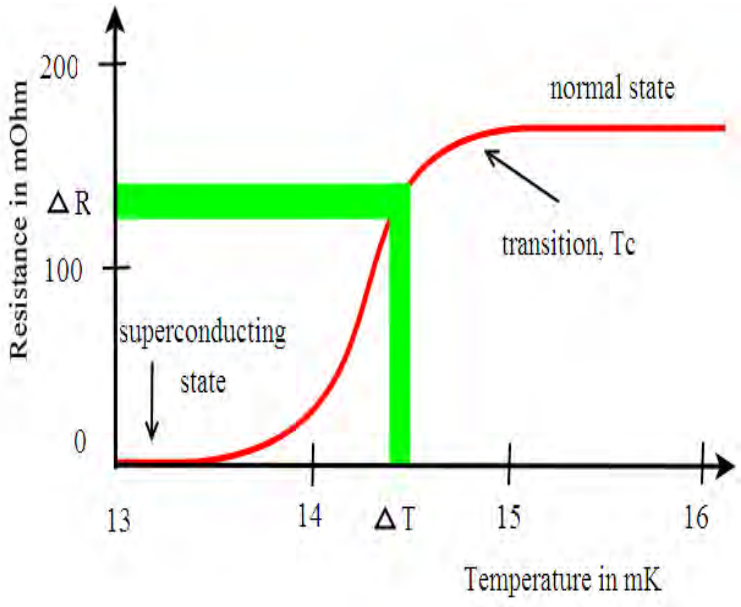

Figure 2.12: Principle of a superconducting phase transition thermometer (W-SPT). The detector can be stabilized at the operating point by means of the heater structure on the W-SPT. A small temperature rise of the detector ΔT causes a measurable rise ΔR of the resistance of the W-SPT.

Within the width of the phase transition a small rise of the thermometer temperature ΔT causes a rise of its resistance ΔR. For measuring this change we use **superconducting quantum interference devices** (SQUIDs) which transform the current change caused by the resistance change ΔR into a voltage output.

An electrical circuit for reading out the resistance of W-SPT is schematically shown in Figure 2.13. The resistance $R_f(T)$ of the thermometer is measured by passing a constant **bias current** I_0 through the readout circuit. In this circuit the thermometer is connected electrically in parallel with two shunt resistors and an input coil which matches the impedance of the low-ohmic tungsten thermometer. The bias current is provided by a floating current source and is typically a few μA. Depending on the ratio of the resistances in the readout circuit, the bias current splits into two branches. The current through the SQUID branch (input coil) is given by

$$I_{sq} = \frac{I_0 R_f(T)}{R_f(T) + R_s} . \tag{2.10}$$

If a change of the thermometer resistance is small, $\Delta R_f(T) \ll R_f(T)$, the current

through the SQUID changes as [27]

$$\begin{aligned}\Delta I_{sq} &= \frac{dI_{sq}}{dR_f}\,\Delta R_f(T) \approx \\ &\approx \frac{I_0 R_s}{(R_f(T)+R_s)^2}\,\Delta R_f(T) \approx \\ &\approx \frac{I_0 R_s}{(R_f(T)+R_s)^2}\,\frac{dR_f}{dT}\,\Delta T\ ,\end{aligned} \tag{2.11}$$

which is proportional to ΔT.

The amplified output voltage signal from the SQUID (V_{squid}) is given as

$$V_{squid} = \gamma(\Phi_{input} + n\Phi_0)\ , \tag{2.12}$$

where γ is the gain of the system, $\Phi_0 = \hbar/2e$ is the flux quantum, and n is an integer number. The ambiguity in the last term of Equation 2.12 is due to the periodicity of the SQUID's response (one period is equal to one flux quantum Φ_0). Consequently, the SQUIDs are operated in a flux-locked mode by means of a separate feedback loop. In this way the output signal of the SQUID is the current in the feedback loop and the relation between the input magnetic flux Φ_{input} and the output SQUID voltage is linear. In order for the feedback mechanism to function properly, the change of the input signal should not exceed the slew rate of the SQUID. Otherwise, the flux lock can be lost resulting in a change of n to a new value. This mechanism is called a **flux quantum loss**.

The SQUIDs employed at the main experimental facility at Gran Sasso are commercially available DC-SQUIDs from the Supracon company [65].

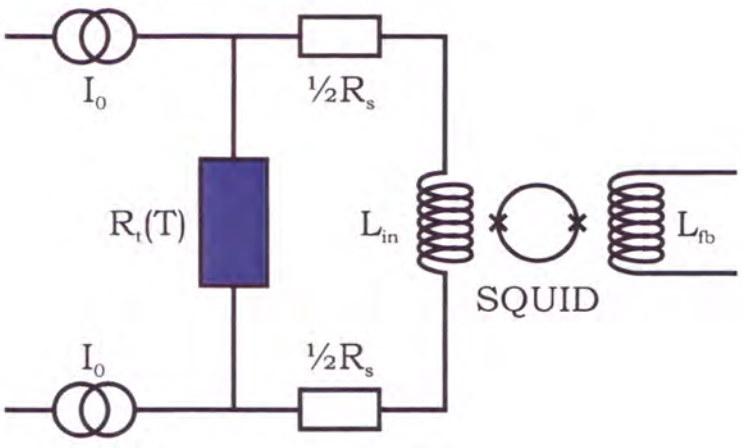

Figure 2.13: Schematic view of the readout circuit. Figure taken from [27].

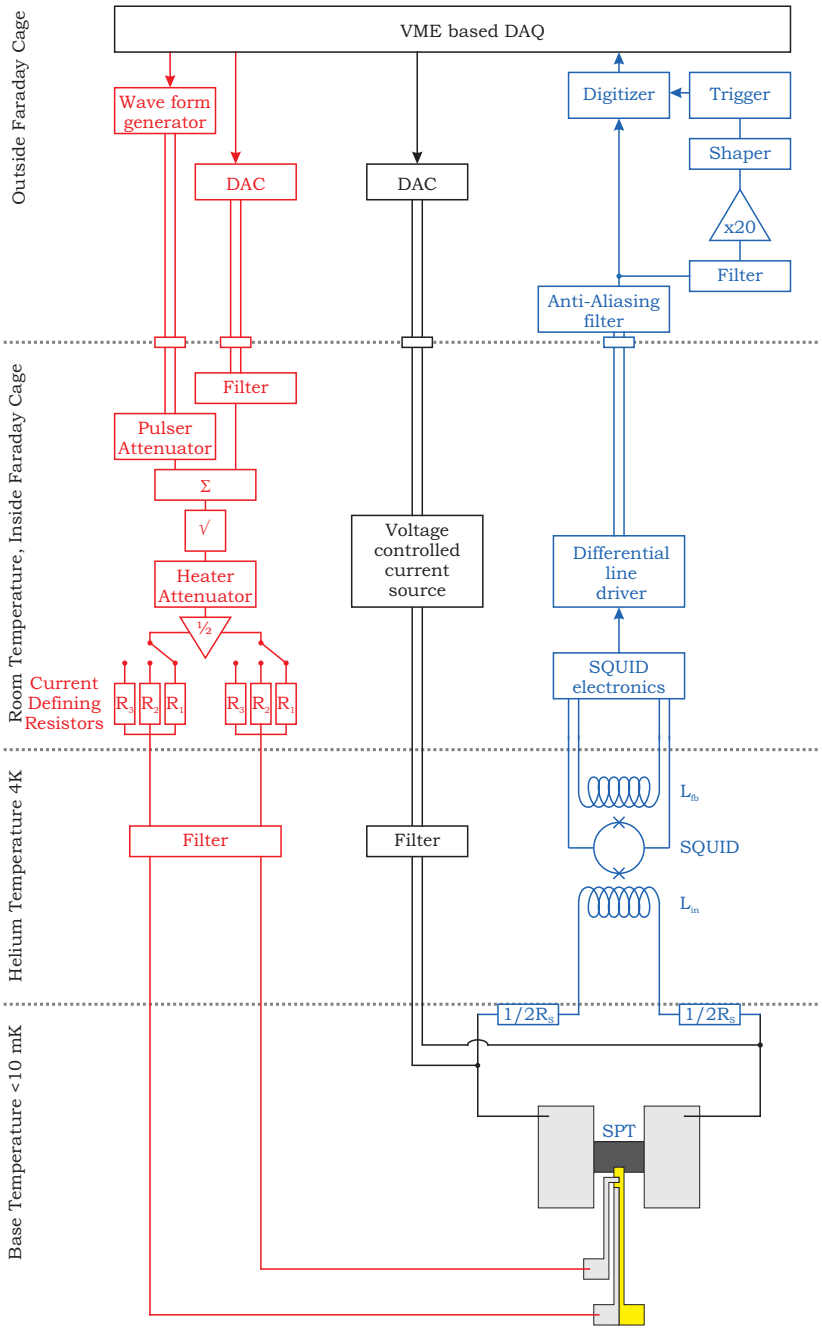

Figure 2.14: Block diagram of the upgraded data aquisition system at Gran Sasso. The *readout circuit* with SQUID and trigger is depicted in **blue**. Shown in **black** is the *bias circuit* and in **red** is the heater system for the *temperature control circuit*. Figure taken from [27].

2.4.2 Data acquisition

A block diagram of the data acquisition is shown in Figure 2.14. The detectors are connected to their holders via 25 μm aluminuim bond wires. The detector holders are connected to the SQUIDs with the help of woven twisted pair superconducting NbTi wires with CuNi matrix. In order to handle all 33 detector modules, a multichannel system which consists of 66 SQUID units is used [66]. These units are located at the bottom of the helium bath at the temperature of ~ 4 K; see Figure 2.4. In addition to the readout-line pair of wires for the SQUID, each thermometer has a control-line pair for temperature control and for injecting calibration pulses. The readout-line pair and control-line pair are spatially separated to avoid electrical cross talk. As the number of lines within the mK environment is relatively large, special attention was paid to the design and fabrication of flanges and feed-throughs [65]. Additionally, the thermal anchoring of the lines is provided on various places in the cryostat.

The bias current for the SQUID readout circuit is supplied by a voltage controlled floating current source. The shunt resistors are thermally linked to the mixing chamber in order to minimize Johnson noise. After a differential amplification, the SQUID signals are transferred through 50 kHz low-pass Faraday cage filters and 10 kHz 8-pole anti-aliasing filters. One branch of the signal is fed through an 8 Hz high pass filter, amplified $\times$ 20, low-pass shaped, and then AC-coupled to the trigger unit. In the other branch, the signal is DC-coupled to a 16-bit transient digitizer.

For every triggered event the transient digitizer data is written to the disk for the off-line analysis. The record length was chosen such that the full decay of a pulse is recorded and a sufficient number of samples is taken during the pulse rise. In the runs of interest, namely, Run 31 and Run 32, pulses were sampled with 25 kHz (40 μs time base) and the record length was selected to be 8192 samples (328 ms). The total record length of 8192 time samples includes a **pre-trigger region** of 2048 samples (to record the baseline before the event), and a **post-trigger region** of 6144 samples which contains the pulse itself. The phonon and the light detectors of each detector module are read out simultaneously whenever at least one of them triggers.

2.4.3 Temperature control

The heater structure of each thermometer, explained in Section 2.3.4, is used to individually stabilize each detector in its operating point and also to inject heater pulses. They help to monitor the temperature stability of the detector and provide its energy calibration[10].

[10]Details on the detector operation and data analysis is presented in Chapter 3.

Heater pulses are produced by two wave form generators (see Figure 2.14) and injected independently in different detectors. Since one of the generators produces pulses for the phonon detectors, while the other one for the light detectors, a pulse attenuator is used to adjust the amplitude of the pulses. The attenuated pulser signal is then added to the constant current needed for the stabilization of the operating point. This current is regulated by a computer controlled digital analog converter (DAC). In order to linearize the dependence of the applied heating power with respect to the input voltage, an analog square-rooter is used.

Heater structures on light and phonon detectors are significantly different and require heating powers of different strength. Therefore, an additional heater attenuator with a set of series heater reference resistors allowing for a fine adjustment of the heating power according to the dynamic range and heater resistance is provided.

2.4.4 Noise sources

The energy threshold and energy resolution of a cryogenic detector are determined by the noise. The main sources of noise are outline below. More information can be found in [61].

- **Thermal noise**
  There are always fluctuations present in the energy content of the cryogenic calorimeter. This is due to the random propagation of energy carriers through the thermal link to the heat bath of temperature T_b. The final limitation on the amplitude of these fluctuations is given by

  $$< \Delta E^2 > \ \propto \ k_B \, T_b^2 \, C_{oper} \, , \tag{2.13}$$

  where k_B is the Boltzmann constant and C_{oper} is the heat capacity of the thermometer at its operating point. For example, a cryogenic detector with C_{oper} = 1 pJ/K at the operating temperature of $\sim$ 10 mK has $<\Delta E^2>$ of $\sim$ 1 eV [61].

  The thermal noise represents a constant background in the detector and thus determines the ultimate limit of the achievable energy resolution. The thermal noise is more significant for the light detectors because they have a smaller heat capacity.

- **Johnson noise**
  For both types of CRESST-II detectors the thermal noise is exceeded by Johnson and SQUID noise. For the readout circuit the Johnson noise, caused by the thermal motion of charge carriers in the shunt resistor and

tungsten thermometer, gives a current noise of

$$< \Delta I^2 > \ \propto \ \frac{4\, k_B\, T}{R_f + R_s}\,. \tag{2.14}$$

This noise has a white frequency spectrum and at typical operating temperatures of around 10 mK $<\Delta I^2>$ $\propto$ 1-3 pA/$\sqrt{Hz}$ [67].

- **SQUID noise**
  The Josephson junctions of DC-SQUIDs require shunt resistors in parallel to prevent hysteresis effects. Their Johnson noise produce a white noise spectrum which has $<\Delta I^2>$ of $\sim$ 1.2 pA/$\sqrt{Hz}$ [66].

Additionally, thermal fluctuations of the heat bath and electrical interferences in the surrounding of the detector may lead to additional sources of the detector noise.

2.5 Recent results

As already mentioned, the CRESST experiment has been upgraded to CRESST-II by several changes and improvements. This includes a new detector support structure (carousel), the associated 66-SQUID channels, a neutron shield, and the installation of the muon veto. In 2007, CRESST-II successfully completed a commissioning run and recently published an upper limit on the spin-independent WIMP-nucleon scattering cross-section [17] presented in Figure 2.15. For the dark matter analysis[11] the data obtained between March and July with the help of two detector modules based on $CaWO_4$ crystals have been used. The cumulative exposure was $\sim$ 48 kg days. Three candidate events of uncertain origin are present in the acceptance region for tungsten recoils yielding a rate of 0.063 per kg day. A limit on coherent WIMP-nucleon scattering is obtained, which at its lowest value, for $M_{WIMP} \approx 50$ GeV, is 4.8×10^{-7} pb [17]. This corresponds to a factor of 3 improvement in the performance with respect to the previously published limit [25].

[11] Details on the dark matter analysis of data obtained in commissioning run can be found in [17] or in dedicated theses [27, 68, 67].

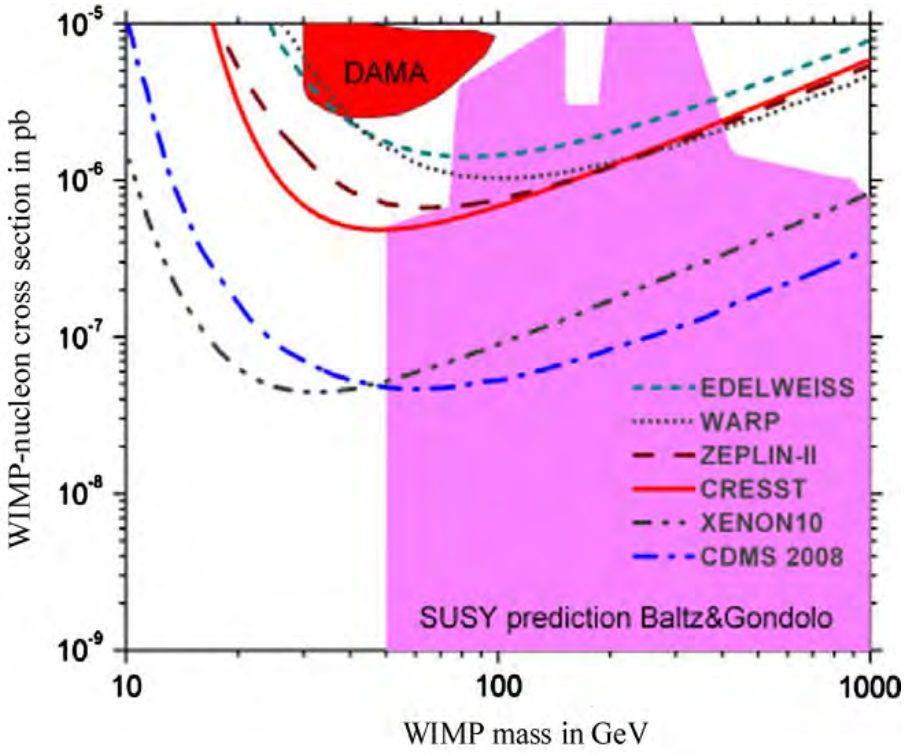

Figure 2.15: Upper limit on the spin-independent scattering cross-section obtained with the CRESST-II experiment with the help of data recorded in the commissioning Run 29-30. For comparison, the limits from other experiments and the range predicted by some SUSY models are also shown. Figure taken from [17].

Chapter 3

Detector operation and data analysis

This chapter discusses the principles of CRESST-II detector operation and data analysis. In Section 3.1 the measuring techniques for a thermometer transition curve from its normal to the superconducting state are described. Then, criteria for the selection of a suitable operating point at which the detector is stabilized during the measurement and its stability control are presented. In Section 3.2 a detailed description on how to obtain the spectra for low and high energy γ- as well as α-particles is given.

3.1 Detector operation

3.1.1 Transition curve

The performance of a detector mainly depends on its thermometer transition curve from the normal to the superconducting phase. The lower the transition temperature, the smaller is the heat capacity of the thermometer and the larger is the signal for a given interaction. The width of the phase transition in temperature defines the dynamical range of the detector, i.e. the maximum particle energy measurable with the detector without saturation. The slope of the transition curve affects the sensitivity of the detector. The steeper the transition curve, the more sensitive is the detector to small energy depositions.

One way to measure the transition curve is to slowly sweep the temperature of the carousel or the mixing chamber of the cryostat. Figure 3.1 shows an example of a transition curve obtained this way. Another way, closer to the actual operating requirements, is to sweep the heating power through the thermometer heater structure and record the thermometer resistance while fixing the temperature of

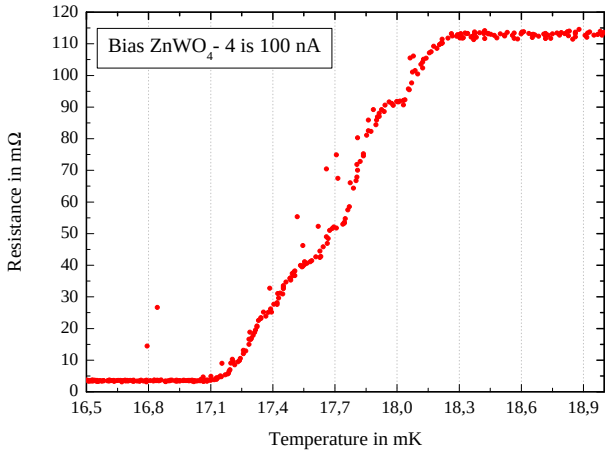

Figure 3.1: Transition curve of detector $ZnWO_4$-4, measured with a bias current of 100 nA by slowly varying the temperature of the mixing chamber of the cryostat.

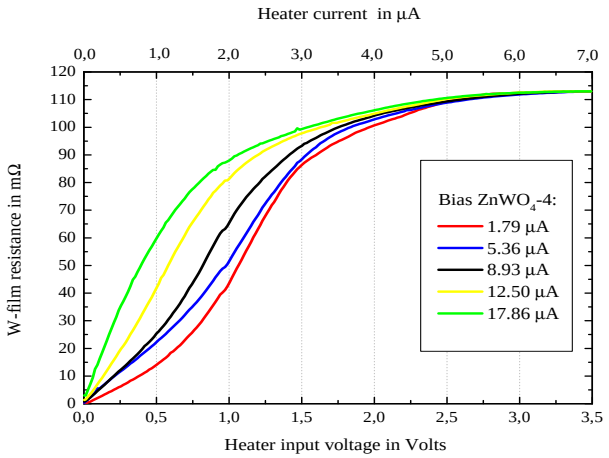

Figure 3.2: Transition curves of $ZnWO_4$-4 recorded by varying the heating power through the thermometer heater structure with fixed mixing chamber temperature. The shape of the transition curve depends on the bias current.

the mixing chamber. For example, the transition curves presented in Figure 3.2 are obtained with the help of this method. Since the bias current needed for readout also heats the thermometer, the shape of the transition curve depends on the current.

Criteria for the optimum transition curve are its critical temperature, steepness, and linearity. The last criterion affects the linearity of the detector response which may result in distortions of the measured pulse height spectrum.

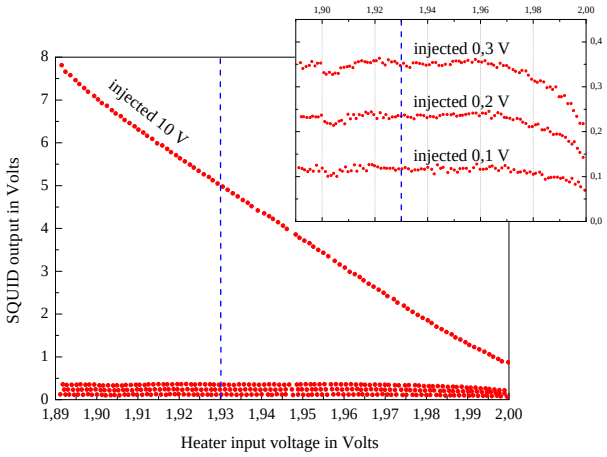

Figure 3.3: Optimization curve recorded with $ZnWO_4$-4 with a constant bias current while sweeping through the transition curve with the help of the thermometer heater structure and injecting heater pulses of various amplitudes. The dashed line shows the selected operating point of the detector.

3.1.2 Operating point

The operating point is usually selected close to the top of the transition. This choice typically gives a smaller noise level [61] and thus the best signal to noise ratio in the energy region of interest. At the top of the transition the noise is often independent of the operation point. Therefore, in practice, the response is maximized.

For a fixed bias current, heater pulses of varying amplitudes can be injected, thus probing the response of the detector to various energies. Figure 3.3 shows the response of the $ZnWO_4$ phonon detector for a given bias current while sweeping through the transition curve with the help of the thermometer heater structure. One chooses an operating point where the response to the injected energy is mostly linear with increasing injected heater pulse energy and shows little variation with respect to the fluctuations from the operating point for the energies of interest.

3.1.3 Stability control

The width of a phase transition is around a few mK, whereas a typical measured temperature rise following an energy deposition of few tens of keV is of the order of tens of μK. Hence, it is necessary to stabilize the temperature of thermometer at least to this precision.

Once the operating point has been chosen, each detector is stabilized independently via its heater structure by periodically injecting **control pulses**. They drive the thermometer out of its transition (or saturate the detector). Their pulse

height is evaluated online by software and serves as an input parameter for a PI (proportional integral) control of the heater circuit. The operating point can be adjusted via applying a steady voltage across the heater. The rate of the injected control pulses is chosen to be frequent enough to sample temperature variations and at the same time not to introduce too much dead time.

The external heater circuit sums the voltages for controlling the temperature (U_T) and the voltage injected by a heater pulse (U_P), and subsequently computes the square root of the sum so that the heater pulses always deliver a known heating power proportional to U_P[1].

Additionally, the heater pulses of amplitudes other than that of the control pulses are injected periodically. These **test pulses** serve for energy calibration down to the lowest energies. Moreover, test pulses are used to monitor the long-term stability of the detector. As an example, the achieved stability of the $ZnWO_4$ phonon detector in Run 31 is shown in Figure 3.4.

3.2 Data analysis

3.2.1 Pulse height evaluation

The data analysis for the CRESST detectors is performed off-line. The raw data set consists of records of the pulses for each channel with some parameters attributed to them. As a first step, several main parameters are being calculated for each of the recorded pulses. These include baseline[2], onset time (the shift with respect to the trigger time), pulse height, peak position, rise and decay times, and some other parameters. Both, pulse height and peak position are calculated using a moving average filter with an adjustable width.

The recorded data sample under analysis have to be cleaned from spurious pulses originating from temperature fluctuations, vibrations, and other noise sources. For this, a stability cut is performed. In this cut, time intervals in which the pulse height of the control pulses deviate more than 2σ from their mean value are omitted.

The next step is to determine the linear range of the detector response, i.e the regime in which the pulse amplitude is proportional to the deposited energy, and to reconstruct the amplitude spectrum of the detector. This is usually done with the help of a standard event (template) fit procedure.

[1]Since the heating power depends on the square of the input current ($P = R\,I^2$), the square rooter removes this dependence and thus linearizes the relation.

[2]The SQUID outputs a constant value that is substracted from the pulse. Due to flux quantum losses, a SQUID can reset. Therefore, the SQUID offset (baseline) can vary.

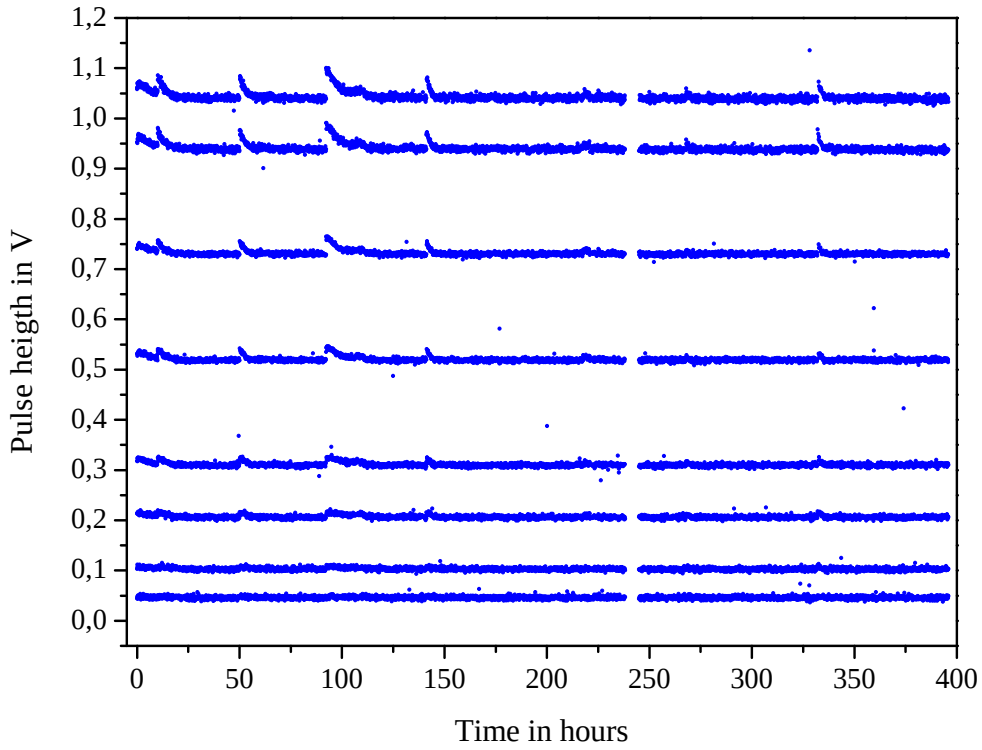

Figure 3.4: Pulse heights of the heater test pulses versus time for the prototype $ZnWO_4$ phonon detector during half a month of data taking in Run 31. The detector response can be seen to be stable within the resolution. The small time gaps and slight variations in the test pulse height are due to interruptions of the measurement in order to refill the cryostat (warm-up). The variations can be corrected with a spline fitted through all test pulses of a given amplitude.

Linearization of the spectrum using standard events

Standard events are built from averaging many pulses of a given type, i.e. from particle pulses or heater pulses selected in a certain energy interval. The only constraints on the event selection criteria are that the chosen energy interval must be entirely in the linear region of the detector response and that there have to be enough events in the chosen region in order to allow for a high statistics template (to average out noise).

The created template is then fitted to the individual pulses with baseline, onset time, and amplitude of the pulse set as free parameters. The root mean square value (RMS or the χ^2) defines the quality of the fit and is used for making further cuts. The left panel of Figure 3.5 shows the scatter plot of the RMS of the standard event versus the amplitude reconstructed with the help of the template fit described above. The region in which the RMS value is constant is called the linear region of the detector response. The maximum linear amplitude can be

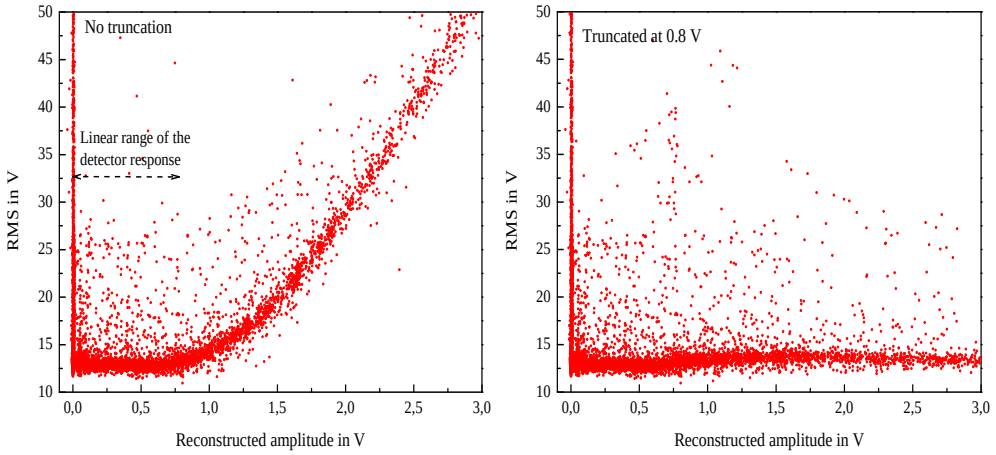

Figure 3.5: *Left:* The RMS of the standard event versus amplitude scatter plot reconstructed from a standard event fit with detector $ZnWO_4$-4. The template is produced from 122 keV pulses from a ^{57}Co calibration source. Above an amplitude of ~ 0.8 V the fit quality decreases due to non-linearities of the thermometer transition curve. *Right:* The same data set reconstructed with the help of the standard event fit with the same template but truncated at 0.8 V. The detector response is now linearized up to the highest amplitudes (1 V corresponds to ~ 193 keV).

obtained from the kink position in the RMS.

This standard event fit works as long as the pulse amplitude is in the linear regime of the detector response. Since at the top of the transition curve the resistivity bands over to its normal conductivity (see Figure3.1), the detector response starts to be non-linear above a certain energy deposition. This results in an increasing RMS value of the fit with increasing amplitude. For signals that approach the top of the transition, the pulse height is extracted by excluding from the fit the part of the pulse where the response becomes non-linear (i.e. only the data points in the linear region are included in the fit); see Figure 3.6. After applying the truncated fit procedure the detector response is linearized up to energies of a few hundreds of keV; see the right panel in Figure 3.5. However, a necessary condition for the applicability of the truncated fit procedure is the absolute stability of the detector at its operating point.

3.2.2 Calibration

After linearization of the detector response, the energy scale of the detector has to be established. This is done with the help of a ^{57}Co source inserted inside the shielding. The source emits 122 keV and 136 keV photons; the decay level diagram of this isotope is shown in Figure 8.2. The calibration at 122 keV is

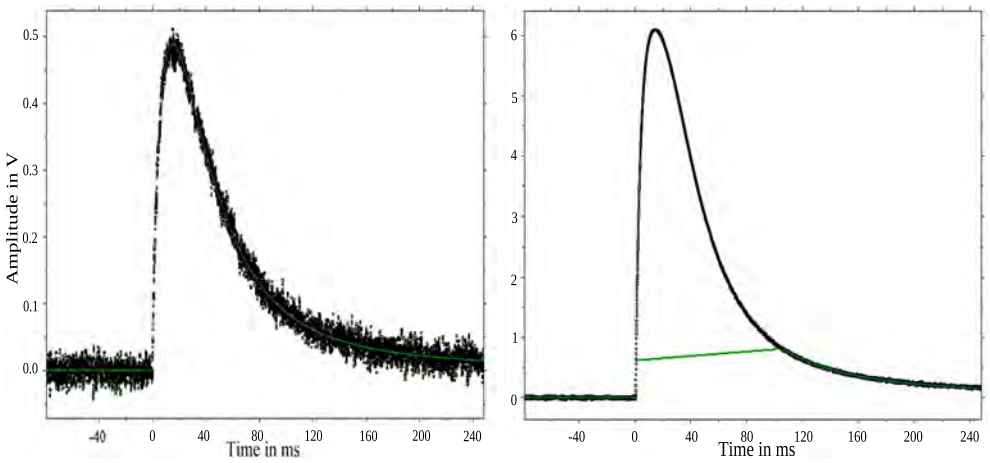

Figure 3.6: Pulses (black points) recorded with $ZnWO_4$-4 in Run 31. Shown in green are fits. When pulse heigh is below the truncation limit of 0.8 V the fit procedure is standard (left panel), otherwise only the data points in the linear region of the detector are included in the fit (right panel).

transferred to low energies with the help of heater **test pulses**. They are injected at regular time intervals with a set of fixed voltages. Similarly to particle pulses, the amplitude spectrum of the heater test pulses is reconstructed with the help of the truncated fit procedure as has been described in Section 3.2.1. The amplitude scale factor (proportional to energy) yields the pulse height. Comparing the amplitude of pulses from the 122 keV peak with the test pulses of a similar amplitude, the injected voltage can be translated into a γ-equivalent energy; see Figure 3.7.

Time variations

As already mentioned in the previous section, the pulse height probes the transition curve of the thermometer. Depending on the shape of the transition curve, pulses of a particular energy range can suffer more from slight variations from the operating point than others; see Figure 3.4. In most of the cases, these variations happen after refilling of the cryostat with cryogenic liquids or after earthquakes. Using the test pulses, such variations can be corrected by fitting a spline through all heater pulses of a given amplitude; see Figure 3.8. The values of the splines, obtained at the time of the pulse, then give the detector response to the discrete set of injected energies. Following this procedure, an excellent energy resolution for the phonon detectors over the full energy range of interest can be obtained; see Figure 8.2.

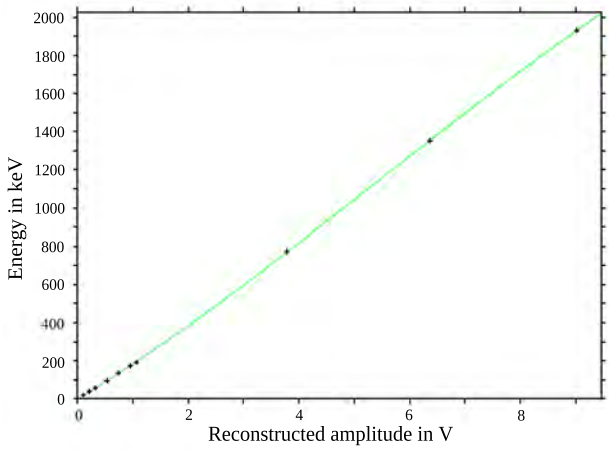

Figure 3.7: Response function of detector $ZnWO_4$-4 recorded in Run 31. Shown in black are the amplitudes for the heater test pulses. They are reconstructed with the help of the truncated fit procedure using an appropriate template. The polynomial function is then used to calibrate the amplitudes of test pulses down to the lowest energies. The scale factor between the injected heater voltage and γ-equivalent energy is obtained comparing the amplitude of ^{57}Co pulses with heater test pulses of similar amplitude.

3.2.3 Parametric fit

In Section 2.3.5 a thermal model for the signal formation in the CRESST detectors has been described. According to this model the pulse shape can be described following Equation 2.9. However, (2.9) describes correctly only the pulses with amplitudes in the linear range of the detector response. A detector response in the MeV energy range which is of interest for the α-background analysis is highly non-linear and pulses are almost saturated. This means that the pulse shape changes dramatically with energy and the same template cannot be used over the full energy range for reconstructing the amplitude spectrum of the detector without truncation.

To model the non-linearities of the detector response, a fitting procedure based on a polynomial expansion of Equation 2.9 has been formulated. The function which describes the pulse shape of saturated pulses is approximated by

$$\Delta T_e(t - t_0) = U(t - t_0) = \sum_{i=0}^{n} b_i \, U_0(t - t_{0i})^i \,, \tag{3.1}$$

where b_0 is the baseline, $b_1 = 1$ and $b_i < 1$ are expansion parameters and U_0 is the detector response in the linear region. These parameters together with ones describing the pulse shape (τ_{intr}, τ_n, τ_{th}, A_n, and A_{th}) can then be determined by a simultaneous fit of several pulse templates which are produced from various

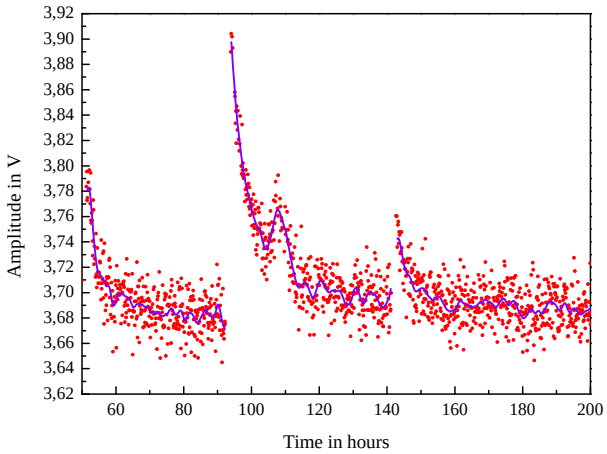

Figure 3.8: A set of heater test pulses of the $ZnWO_4$ phonon detector recorded in Run 31. Slight variations in the operating point can cause variations for pulses with a given amplitude. A spline, shown as solid violet line, is fitted to correct for such variations.

amplitude regions. An example of such a set of templates superimposed with fits according to Equation 3.1 is shown in Figure 3.9.

The parametric fit method described above allows for the reconstruction of amplitude spectra of the phonon detectors up to energies of more than 8 MeV with a resolution high enough to separate various α-lines from radionuclides. The method was applied for the α-background analysis of some phonon detectors of interest. Their spectra will be presented later on in Section 8.2.2.

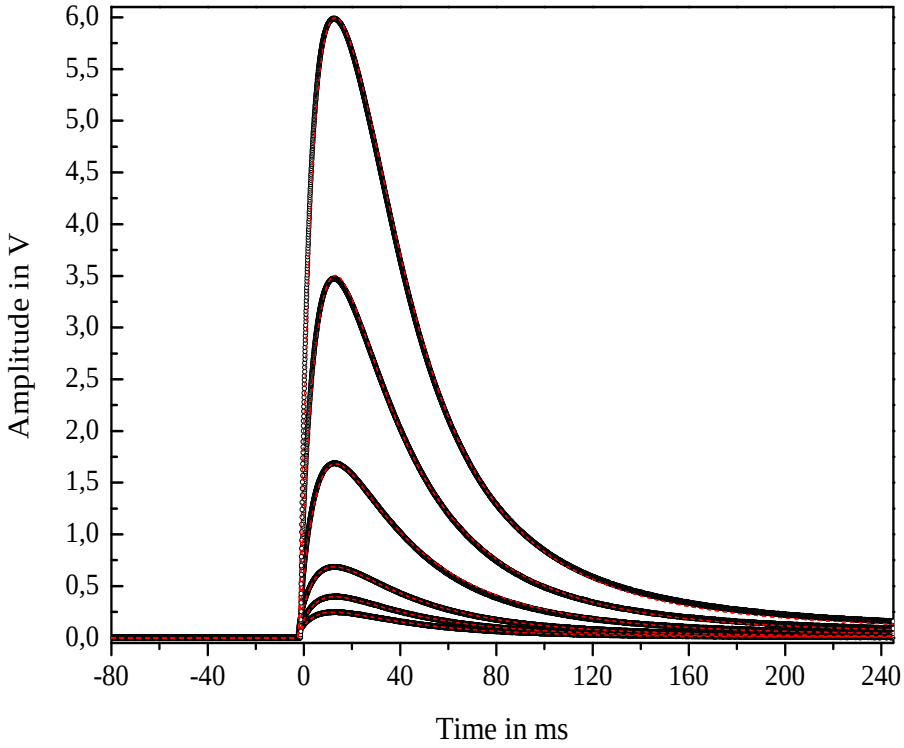

Figure 3.9: A set of the templates produced from both, linear and non-linear, amplitude regions of $ZnWO_4$-4. Shown in gray are data points and dashed red lines are fits according to Equation 3.1.

Chapter 4

Scintillation mechanisms in crystals

The interpretation of the measurements performed with $CaMoO_4$ and $ZnWO_4$ crystals and which presented in the subsequent chapters requires an understanding of their scintillation mechanism. Therefore, in this chapter, an introduction to the scintillation mechanisms in inorganic crystals with an emphasis on self-activated scintillating crystals is given. Special attention is payed to quenching mechanisms and temperature dependent effects which influence on the scintillation efficiency and are particularly relevant for the rare event search with CRESST.

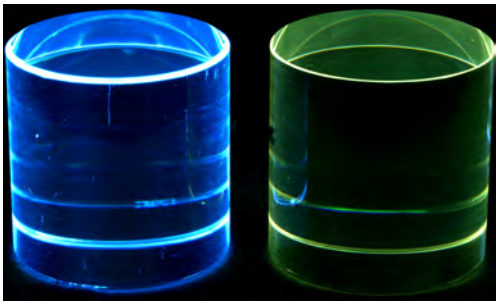

Figure 4.1: Photograph of a scintillating $CaWO_4$ (left) and a $CaMoO_4$ (right) crystal under excitation with UV-light.

4.1 Introduction to the scintillation process

Figure 4.1 shows the phenomenon of scintillation, widely observed in nature, in $CaWO_4$ and $CaMoO_4$ crystals. A scintillator can be viewed as a wavelength shifter. The energy of an incident particle (UV-light, X-ray, γ-ray, etc.) which is deposited in the crystal is converted into photons in the visible or near visible range of the electromagnetic spectrum. For the understanding of the scintillation process a simple band structure model can be used.

4.1.1 Band structure

The band structure of a scintillating crystal is represented schematically in Figure 4.2. Within a solid crystal electrons occupy extended energy bands. The outermost electrons of the atoms occupy levels in the valence band. This band is separated from the conduction band, which is not populated in an insulator, by the forbidden band which is several eV wide.

The lattice of solid crystals is not ideal and usually contains point defects. The simplest type of point defects are ions missing from their regular lattice sites, known as Schottky defects. Another type of point defects are atoms occupying interstitial positions in the crystal lattice, known as Frenkel defects. The point defects may be thermal in origin, be present by impurities or created if there exists a stoichiometric excess of one type of ion in the lattice, be created directly by incident nuclear radiation, or even be excited by electronic excitations (e.g. electron-hole (e-h) pairs, excitons). By capturing either electrons or holes, defects can form a localized electronic energy level within the energy band gap called the exciton level. The regions of the lattice where the exciton band is present are called emission centers (luminescent centers, color centers). Additionally, various impurities and defects form energy levels within the band gap which may act as electron traps.

At temperatures of ~ 300 K the width of the forbidden band is too large for an electron to be thermally excited across it ($k_B T \simeq 26$ meV). To pass from the valence band to the conduction band, an electron must gain energy equivalent to the energy of the band gap of the crystal, E_g. After a particle interaction within the crystal, primary or secondary electrons in the keV range excite electrons from the occupied electronic states (valence or deeper bound states) to different levels in the conduction band. This results in a hole with an effective positive charge in the valence band; an electron-hole pair is created. Typically, it takes two to seven times the band gap energy in order to create an (e-h) pair [69]. The number of created (e-h) pairs (N_{eh}) is usually expressed via the average energy required for the creation of the thermalized (e-h) pair ($E_{eh} = \beta E_g$). If the deposited energy by

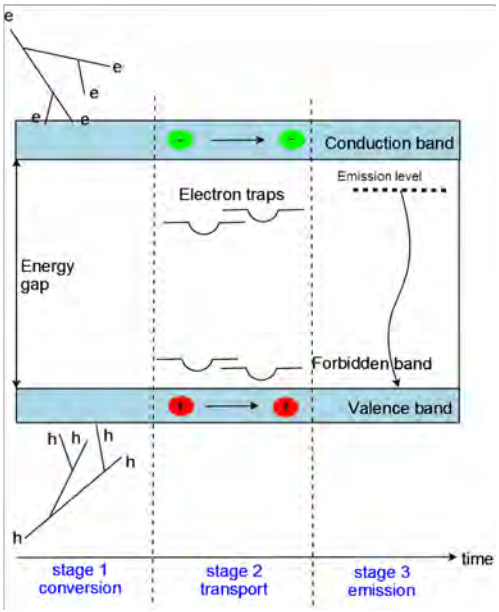

Figure 4.2: Schematic representation of the band structure in scintillating crystals. A sketch of the energy conversion mechanism in self-activated scintillators is superimposed. The entire process is divided into three stages: conversion, transport, and emission. See main text for discussion.

an incoming particle into the crystal is E_{abs}, then

$$N_{eh} = \frac{E_{abs}}{E_{eh}} = \frac{E_{abs}}{\beta\, E_g}\,, \tag{4.1}$$

where β is a constant. The larger E_g is, the lower is N_{eh}. If the energy of an electron in the (e-h) pair is high enough to reach the ionization threshold, it can be considered as a free carrier.

Electrons and holes can also be bound by the Coulomb potential and form an **exciton** whose energy is slightly smaller than the energy of the band gap. The energy level of an electron (E_e) in the exciton is given by

$$E_e = E_g - E_b\,, \tag{4.2}$$

where E_b is the exciton binding energy.

4.1.2 Stages of the scintillation process

A consistent phenomenological description of the energy conversion into scintillation light was developed in the seventies [70] and further refined later [71]. Scintillation, which occurs as the result of a relatively complicated chain of processes, can be divided into three stages, schematically presented in Figure 4.2. They are called **energy conversion**, **energy transport**, and **scintillation emission** stage.

Energy conversion and thermalization

The formation of thermalized (e-h) pairs occurs within 10^{-18} s to 10^{-9} s after an initial energy deposition in the crystal [47]. When electron energies become smaller than the ionization threshold, (e-h) pairs can thermalize by intra-band transitions (inelastic scattering) and relax via electron-phonon interactions until holes reach the top of the valence band and electrons reach the bottom of the conduction band. The time range of this process is rather fast being 10^{-16} s to 10^{-12} s [47].

Energy transport to luminescent centers

Free or quasi-free electron-hole pairs and excitons can migrate and thus transport their energy through the crystal lattice. During migration, (e-h) pairs may sufficiently ionize the lattice and create a potential well in which they become trapped. This phenomenon is called **self-trapping**. In the process of thermalization after reaching the top of the valence band, a hole can bind to a certain molecular group of a crystal. This state is called a **self-trapped exciton** (STE).

During the energy migration process a considerable amount of electronic excitations can repeatedly be trapped and released in the forbidden band. Since the number of point defects, flaws inside a crystal, and the quality of crystal surfaces differ among species of a crystal, the number of energy trapping sublevels introduced into the forbidden band is also different. Therefore, migration of electronic excitations can be affected in many different ways before interacting with luminescence centers. This makes the stage of the energy transport very unpredictable.

During the energy transport stage, electronic excitations transfer their energy to luminescent centers which also become excited. The formation of excitonic states and groups of excited luminescent centers happens between 10^{-12} s to 10^{-8} s [47].

Emission of scintillation light

The excited luminescent centers relax to the ground state by non-radiative processes or by emitting a scintillation photon (radiative process). The emission mechanism depends on the electronic structure of both, the luminescent ions and the crystal lattice in which they are embedded as well as on their mutual interactions. The radiative process can be as short as 10^{-9} s for (e-h) pair recombination and free exciton or STE emission. Time constants (τ_{scint}) which characterize the scintillation emission are determined by the wave-functions which describe characteristics of the different levels participating in radiative transitions.

The precise mechanism of scintillation emission varies among different materials. In general, the physics of various mechanisms is well studied. The reader is referred to [70, 72, 73] for more details.

Summary

It has been pointed out that the lattice structure of the crystal determines not only its band structure but also has a major influence on the scintillation properties of the crystal. For a crystal to be a scintillator it should contain luminescent centers. Depending on the type of the emission center one distinguishes between extrinsic (or **activated**) and intrinsic (or **self-activated**) scintillators. The first class of crystals is generally doped with ions, while in the second class molecular systems of the crystal lattice (or defects incorporated into it) possess a radiative transition between an excited and ground state of the luminescent center. The luminescence may involve (e-h) pair recombination, free, self-trapped, and defect-trapped exciton luminescence as well as charge transfer transitions within a molecular complex.

The crystals studied in this work, namely, $CaWO_4$, $ZnWO_4$, and $CaMoO_4$, belong to the class of the self-activated dielectric inorganic scintillators with a wide energy band gap ($\sim$ 4 eV). In the next chapter their lattice structure and individual scintillation mechanisms will be discussed in more detail.

4.1.3 Light yield

The absolute light yield (LY) of a crystal, also known as scintillation efficiency, is the constant that links the generated energy of scintillation photons to the amount of energy dissipated in the crystal. At temperature T it can be defined as the ratio of the total energy of produced scintillation photons E_{total} to the energy deposited in the crystal E_{abs},

$$LY(T) = \frac{E_{total}}{E_{abs}} , \tag{4.3}$$

where

$$E_{total} = \sum_{i=1}^{N_{produced}} E_i , \tag{4.4}$$

with E_i being the energy of a single scintillation photon. In reality, the amount of light emitted by a scintillating crystal is not strictly proportional to the energy deposited by an ionizing particle.

In the literature the absolute scintillation efficiency of a crystal is usually expressed as the number of photons produced ($N_{produced}$) by a 1 MeV energy deposition by a photon. Taking into account all stages of the scintillation process,

the scintillation efficiency can be expressed as a product of three factors [47]

$$LY(T) = \frac{N_{produced}}{E_{abs}} \approx N_{eh}\, S(T)\, Q(T)\,. \tag{4.5}$$

Here, N_{eh} is the conversion efficiency of E_{abs} into energy of electronic excitations expressed as a number of (e-h) pairs and excitons (see Equation 4.1). $S(T)$ is the quantum efficiency of the transfer of energy of the termalized electronic excitations to the excited states of the luminescence centers and $Q(T)$ is the quantum efficiency of luminescence, i.e. the efficiency of the luminescent center for emitting photons[1]. It should be noted that in crystals with complicated electronic structure not all created (e-h) pairs (N_{eh}) are translated into electronic excitations leading to the emission of scintillation light. Therefore, the absolute light yield expressed by Equation 4.5 is usually much higher than the experimentally observed light yield.

4.2 Quenching mechanisms

From Equation 4.5 it follows that only a fraction of energy deposited in a scintillator by incident particles is eventually converted into scintillation light. There are many mechanisms occurring during the various stages of the scintillation process which may finally limit the scintillation efficiency of a crystal. For example, the trapped excitations lead either to the emission of scintillation light or to the radiationless recombination of electronic excitations. The process of the non-radiative energy transfer in scintillators is known as **quenching**. Various types of quenching phenomena exist. Most of them are well known and detailed information can be found in [70, 47, 72, 73]. Here, only the most important ones are mentioned.

4.2.1 Impurity quenching and reabsorption

The path which the scintillation light travels before escaping the crystal usually extends over many lattice constants and depends on the material, size, and shape. An important requirement for a crystal to emit scintillation light is that energy levels involved in the radiative transition must be smaller than the energy gap of the crystal (to avoid self-absorption). This phenomenon is described by Stokes law and the difference in wavelength between emitted and absorbed scintillation light is called Stokes shift; see Fig 4.3. If emission and absorption occur at the same wavelength most emitted photons will be reabsorbed within a short distance.

[1] A theoretical description of the dependency of the energy transfer and the luminescence quantum efficiency on temperature can be found in [44].

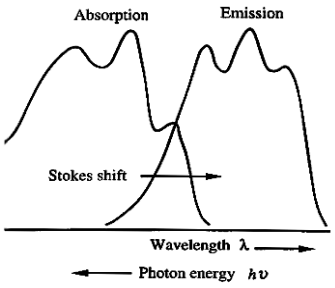

Figure 4.3: Schematic representation of the absorption and emission spectra.

Many types of light absorbing centers may be present in a crystal (e.g. point defects, lattice flaws, color centers). Therefore, the emitted scintillation light, while travelling through the crystal, may be reabsorbed. Overall, the reduction of the number of defects and improvement of crystal transparency in the wavelength region of the scintillation emission increase the scintillation efficiency of the material.

4.2.2 Thermal quenching

Thermal quenching of scintillation light is related to the interactions of the ions in the host lattice with vibrations, i.e. electron-phonon interactions, which usually result in radiationless processes.

Configurational model

The development of a radiationless process may be explained by the potential energy diagram which represents the Franck-Condon principle; see Figure 4.4. Each curve represents an electronic energy state of a molecule. The potential energy is plotted against the interatomic distance X, which is taken to be the average change in the normal radial distance between an ion and one of its nearest neighbors. When a molecule is thermally excited, the distance changes. The curve aAa$'$ represents the ground state of a luminescence center, while the curve bBb$'$ represents one of its electromagnetically excited states. In both states the luminescent center vibrates around its equilibrium positions A and B, which are sufficiently separated (in the X-coordinate) in order to yield the adequate Stokes shift. The horizontal lines represent the vibrational levels of the emission center. For small vibrational amplitudes the curves aAa$'$ and bBb$'$ are approximately parabolic. The occupation number of each energy level is determined by the temperature of the crystal.

The transition $A \rightarrow C$ represents the excitation of the luminescent center due to the capture of an electronic excitation (e.g. photon absorption). Since

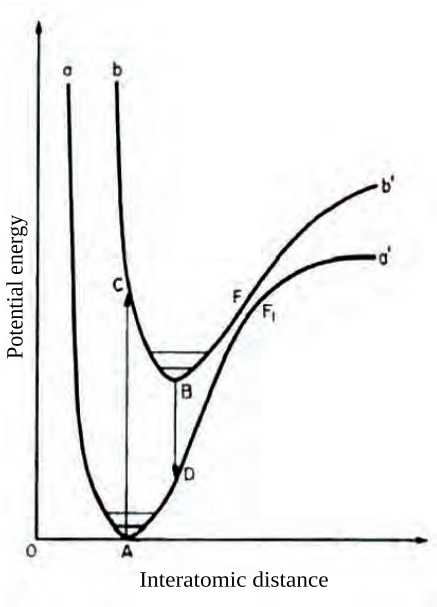

Figure 4.4: Potential energy diagram illustrating the Franck-Condon principle. The curve aAa′ represents the ground state of a molecule, curve bBb′ represents an excited electronic energy state and horizontal lines represent various vibrational levels. Absorption and emission processes are indicated by vertical lines. Figure taken from [70]. See text for details.

electronic transitions proceed much more rapidly than the rearrangement of the nuclei or the lattice in the crystal (Franck-Condon principle [74, 75]) they are represented by vertical lines in the configurational space. The position C is not in thermal equilibrium with the surrounding and the system relaxes back to the equilibrium position $C \rightarrow B$ with the creation of phonons. Now the system can relax to its ground state $B \rightarrow D$ with the emission of photons which are observed as scintillation light.

Since positions of A and B are not the same, the potential energy curves can approach each other at large vibrational levels, such as in the position F. If the vibrational amplitude of the excited state is large enough, the transition $F \rightarrow F_1$ is possible. The system relaxes from F_1 back to the thermal equilibrium position A with the emission of phonons. This process is known as **thermal quenching**. This non-radiative process competes with the scintillation process and therefore can significantly reduce the scintillation efficiency. In some crystals the proximity region $F \rightarrow F_1$ is very close to the minimum of the excited state. These crystals are heavily quenched.

Temperature dependence of the scintillation efficiency

The emission and absorption spectra are schematically presented in Figure 4.3. The emission spectrum is shifted to longer wavelengths relative to the absorption spectrum. At temperatures of ~300 K the absorption and emission bands are broadened. This increases the overlap between their respective bands which results in the loss of scintillation photons due to reabsorption. Decreasing the temperature narrows the overlap and thus decreases the probability for non-radiative transitions. Therefore, at low temperatures, crystals reveal higher scintillation efficiency than at room temperatures.

The gradual decrease of the scintillation efficiency with increasing temperature is caused by thermal quenching [72]. The temperature dependence of the quantum efficiency of luminescence $Q(T)$ is usually described by the Mott equation [72]

$$Q(T) = \frac{1}{1 \; + \; C \; \exp\left(-\frac{E_q}{k_B T}\right)} \, , \tag{4.6}$$

where C is a quenching constant, E_q is the quenching energy, and k_B is the Boltzmann constant. At low temperatures ($k_B T \ll E_q$), the radiative decay mode is dominant and variation of $Q(T)$ in this temperature range is small. When the temperature increases, the non-radiative decay mode starts to compete with the radiative decay mode and the luminescence becomes quenched.

For various crystals the dependence of scintillation efficiency on temperature is different. Since in CRESST-II detectors are operated at a few mK, the scintillation efficiency of a crystal at low temperatures is of major importance.

4.2.3 Ionization quenching

For weakly ionizing particles (for example, fast electrons) the spacing between successive ionization or excitation sites is relatively large (several molecular distances) and interactions between these sites are negligible. Under these conditions the scintillation response of a crystal (L) is proportional to the particle energy (E) deposited in it [70]

$$L = A \, E \tag{4.7}$$

with A being the absolute scintillation efficiency of a crystal in terms of number of photons per unit energy. Differentiation of (4.7) yields

$$\frac{dL}{dx} = A \, \frac{dE}{dx} \, , \tag{4.8}$$

with x being the residual track length of a particle in the scintillator.

Ionization and excitation densities are high for large energy deposition per unit length dE/dx. This is the case for highly ionizing particles (for example, slow electrons, protons, or α-particles). A high ionization density leads to overlapping

excitations and the energy migration can occur via radiationless energy transfers which decrease the scintillation efficiency of a crystal. Losses in emission due to high ionization or excitation density are called **ionization quenching**.

For a phenomenological parameterization of the described energy deposition per unit length as a function of ionization density the semi-empirical **Birks' formula** [70] can be applied

$$\frac{dL}{dx} = \frac{A\, dE/dx}{1 + kB\, dE/dx} . \tag{4.9}$$

Here, dL/dx is the differential light yield in terms of number of photons emitted per unit length, k is a quenching parameter, and B is Birks' constant. The parameters A and kB relate the amount of emitted scintillation light to energy deposition per unit length dE/dx. These values are specific for every scintillating material and have to be obtained experimentally. At large ionization densities the differential light yield (dL/dx) becomes constant

$$\frac{dL}{dx} = \frac{A}{kB} = const . \tag{4.10}$$

This model thus predicts that for heavily ionizing particles the scintillation light yield varies linearly with the track length.

4.3 Quenching factor measurements and interpretation

Nuclear recoils, caused by neutrons and expected from WIMPs, produce much less scintillation light than electron recoils, caused by α-, β-, or γ-particles. The difference in the light output, which depends on the ionization density of an incident particle, is the basis for the CRESST-II active background discrimination; see Section 2.3.1. As already mentioned in Section 2.1.3, neutrons are the most dangerous background for direct dark matter searches because they may mimic a WIMP signal. The cross section for coherent scattering of both WIMPs and neutrons is proportional to A^2. However, due to the interaction kinematics, neutrons transfer more energy to the light elements (like oxygen). In contrast, WIMPs are expected to transfer more energy to heavy nuclei (like tungsten or molybdenum).

To compare the light output of different events we define the **quenching factor**[2] (QF) as the ratio of the light output from an electron recoil of energy E to the light output from a nuclear recoil of the same energy:

$$\text{QF} = \frac{\text{light output from electron recoil of energy } E}{\text{light output from nuclear recoil of energy } E} . \tag{4.11}$$

[2]Note that in the literature the effect of the ionization density on the scintillation efficiency of a crystal is often expressed in terms of the ratio α/β. It is defined as the ratio of the light output per unit energy loss for ^{210}Po (5.3 MeV) α-particles and ^{137}Cs (624 keV) internal conversion electrons [72].

Energy range in keV	QF
40 - 60	10.4 ± 0.1
60 - 80	10.7 ± 0.1
80 - 100	10.1 ± 0.1
100 - 150	11.3 ± 0.1

Table 4.1: Quenching factors for oxygen recoils measured with the ($20 \times 10 \times 5$) mm^3 $ZnWO_4$ crystal and an americium-beryllium neutron source at ~20 mK. Statistical error of 1σ on the fitted peak position are given.

As the tungsten recoil is relevant for a WIMP search with $CaWO_4$ or $ZnWO_4$ targets, the knowledge of the light quenching factor for W recoils is very important. Knowing the QF for oxygen, it would allow for discrimination between neutron background and possible WIMP events, thus providing additional sensitivity for the experiment.

The CRESST collaboration developed several techniques to measure the quenching factors of various recoiling nuclei in the crystal. One possibility to measure the quenching factor is to study the scintillation response of a crystal to nuclear recoils via neutron scattering. Measurements with an americium-beryllium neutron source using the active background discrimination technique were carried out with $CaWO_4$ in [76] and with $ZnWO_4$. However, the observed nuclear recoils are induced mainly by neutrons scattered off oxygen nuclei and to a lesser degree on calcium or zinc nuclei. Tungsten recoils, which become dominant only at energies well below a few keV , were not distinguishable from the background. Table 4.1 shows the QF for oxygen recoils measured in the energy interval between 40 keV and 150 keV with a $ZnWO_4$ crystal. The quenching factor for oxygen recoils in the $ZnWO_4$ crystal was found to be ~ 10.

Another study based on neutron scattering involves irradiation of a scintillator by a 11 MeV neutron beam [77, 78]. The scintillation light emitted from the crystal is detected by two PMTs facing the crystal on the opposite sides. Scattered neutrons are detected by arrays of neutron detectors whose angles are fixed with respect to the beam axis. With such an arrangement the kinematics of the scattering process is completely fixed. Therefore, for each event, the energy release and the scattering partner are known so that the quenching factors can be calculated. This technique was applied to study the quenching factors of $CaWO_4$ nuclei at room temperature. However, most of the tungsten recoils are hidden in the background or lie below the threshold of the experiment. Thus, only an upper limit for heavy nuclei has been obtained. A low temperature neutron scattering experiment is ongoing [79, 80].

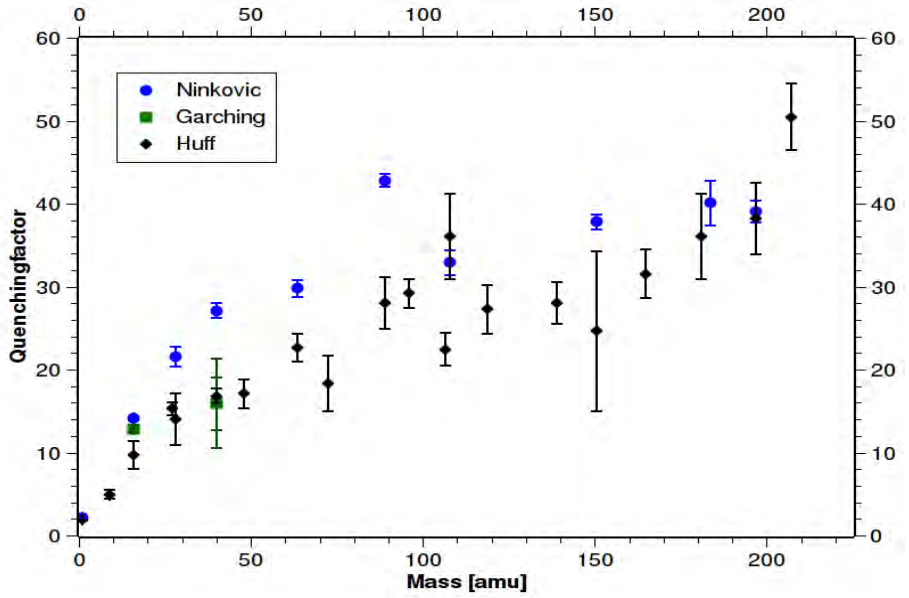

Figure 4.5: Results of various measurements of the quenching factor for different nuclei in $CaWO_4$ crystals. In **blue** measurement results using the time-of-flight mass spectrometer technique at room temperature are shown (errors are statistical) [58]. The **black** points show refined measurements obtained with the same technique (errors are statistical and systematic) [62]. Shown in **green** are measurements using the neutron scattering technique at room temperature [76]. Figure taken from [83].

Finally, a third technique, the time-of-flight mass spectrometer (TOF-MS), simulates nuclear recoils by bombarding a scintillating crystal with different ions of fixed energy. The method uses a mass spectrometer to accelerate an ion and measures the number of photons produced when an ion is impinging on the crystal [81, 58, 62]. This technique was applied to study the quenching factor of many different nuclei in $CaWO_4$ crystals at room temperature. Measurements with a $ZnWO_4$ sample are in preparation [82].

Figure 4.5 shows the results of various measurements of the quenching factor for different nuclei in $CaWO_4$. The quenching factor smoothly increases with the atomic mass of the ion. It should be noted that the quenching factors are approximately energy independent, since various measuring techniques involve ions of different energies. A rough consistency between various measurements performed at room temperature is observed. A more detailed interpretation of the light-quenching factor measurements can be found in [83].

The quenching factor for tungsten recoils in $CaWO_4$ was found to be ~ 40 [81]. For tungsten recoils in $ZnWO_4$ crystals the quenching factor is expected to be approximately the same. It should be noted that such a large quenching results

in a very small amount of scintillation light (only few photons per tungsten recoil) which is eventually seen in the light detector. From this point of view, a material with a smaller quenching factor for the heaviest nuclei in the compound than that for tungsten in $CaWO_4$ (A_W = 184) would be desirable, whereas, at low temperatures, a scintillation efficiency similar to it would be favorable. As the quenching factor for molybdenum recoils in $CaMoO_4$ crystals (A_{Mo} = 96) is expected to be well below 40, this material is very interesting in this respect.

Chapter 5

Crystals properties at room temperature

For the CRESST-II dark matter search good crystal quality means high transparency of a large single crystal, high purity, and excellent scintillation efficiency. An initial assessment of the potential of the new scintillating materials can be obtained by comparing their properties with that of $CaWO_4$ crystals which is the standard material for the experiment[1]. Since large $CaMoO_4$ and $ZnWO_4$ crystals with the dimensions of (ϕ 40 $\times$ 40) mm^2 became available only recently, detailed studies on various characteristics of these materials have been performed in this work. Moreover, to obtain crystals of the desired quality, a strong feedback to the producers is required in order to optimize the crystal growth process.

Since the crystal lattice defines the fundamental properties of a material, this chapter starts with a presentation of lattice structures for the crystals of interest. Afterwards, the conditions of crystal growth and after-growth processing are described. Studies on optical properties of $CaMoO_4$ and $ZnWO_4$ crystals are presented in Section 5.4. Then, luminescence properties of these crystals are discussed in Section 5.5. Finally, in Section 5.6 the results of the room temperature studies on the scintillation efficiency of the crystals are presented.

5.1 Lattice structure

$CaMoO_4$ and $ZnWO_4$ are naturally occurring minerals which can also be produced synthetically. The mineral names associated with these materials are powellite and sanmartinite [96, 97], respectively. $CaMoO_4$, similarly to $CaWO_4$,

[1] Characteristics of $CaWO_4$, $CaMoO_4$, and $ZnWO_4$ crystals that are useful in the following discussions are summarized in Table 5.1

	$CaWO_4$	$ZnWO_4$	$CaMoO_4$
Atomic mass in g/mol	~ 288	~ 313	~ 200
Lattice structure	scheelite	wolframite	scheelite
Cleavage (plain)	weak (1 0 1)	marked (0 1 0)	weak (0 0 1)
Melting point (°C)	~ 1650 [51]	~ 1200 [84]	~ 1430 [51]
Density in g/cm^3	~ 6.1 [49]	~ 7.8 [85]	~ 4.5 [86]
Index of refraction	1.93 at 475 nm [87]	2.32 at 490 nm [88]	1.96 at ~ 600 nm [87]
Critical angle, θ_c crystal→air interface	31.3°	25.5°	30.3°
Energy gap, E_g in eV	~6.0 [89]	~4.6 [89]	~3.4 [90]
λ_{max} in nm at 300 K	420	480	520
Light yield at 300 K in photons per MeV	~16200 [91]	21500 [88]	2072 [92]
τ_{scint} in μs (at 300 K)	6 [47]	20 [88]	20 [92]
Debye frequency in THz	~4.7	~3.8	~8.2
Hydroscopicity	no	no	no

Table 5.1: Physical properties of $CaWO_4$, $ZnWO_4$, and $CaMoO_4$ scintillating crystals [84, 47, 72]. Debye frequencies are calculated from Debye temperatures, taken from [93, 94, 95]. In the case of $CaWO_4$ and $CaMoO_4$ ordinary index of refraction is given.

crystallizes in a scheelite structure, whereas $ZnWO_4$ crystallizes in a wolframite structure. The parameters of the primitive unit cells for the crystals are listed in Table 5.2.

The scheelite structure (or tetragonal structure) has a $I4_1/a$ or C_{4h}^6 space group (listed as No. 88 in the International Tables [100]). In this structure, the primitive unit cell has two ABO_4 units (for example, with A =Ca and B = Mo or W). The A and B sites possess an S_4 point symmetry and the crystal has an inversion center. The O sites only have a trivial point symmetry and are approximately arranged in a tetrahedral coordination about each B site.

wolframite (monoclinic) $a \neq b \neq c$ $\alpha = \gamma = 90° \neq \beta$					scheelite (tetragonal) $a = b \neq c$ $\alpha = \gamma = \beta = 90°$		
	a (Å)	b (Å)	c (Å)	β		a (Å)	c (Å)
$ZnWO_4$[98]	4.7	5.7	4.9	90°6′	$CaMoO_4$[99]	5.2	11.4

Table 5.2: Unit cell dimensions for some ABO_4 (with A=Zn or Ca and B=W or Mo) crystals at room temperature.

The wolframite structure (or monoclinic structure) has a $P\ 2/c$ or C_{2h}^4 space group (listed as No. 13 in the International Tables [100]). In this structure, the primitive unit cell also has two ABO_4 units (for example, with A = Zn and B = W). Each W site is surrounded by six O atoms in approximately octahedral coordination. The O sites have two distinct positions. The O_1 forms one short length bond to the W site and two longer bonds to the Zn sites. The O_2 connects to two different W sites with longer bond lengths and to one Zn site.

The wolframite structure is generally more closely packed, naturally forming in materials with small A^{2+} ions, whereas the scheelite structure naturally forms in materials with larger A^{2+} ions [98]. For example, $ZnMoO_4$ and $ZnWO_4$ with a radius of Zn^{2+} of 0.74 Å have wolframite structure, while $CaMoO_4$ and $CaWO_4$ with a radius of Ca^{2+}=0.99 Å have the scheelite structure [87].

Because of their crystallographic structure $CaMoO_4$ and $ZnWO_4$ are anisotropic. Therefore, the speed of light propagation varies with the crystallographic direction. Anisotropic crystals are subdivided into the isodametric class, which embrace crystals with the tetragonal structure and the anisometric class, which embrace crystals with the monoclinic structure. Isodametric crystals are uniaxial. This means that the speed of light is constant in all directions perpendicular (or equally inclined) to a fixed optical axis, and there is no double refraction in this direction. Anisometric crystals exhibit two directions analogous in character to the single optical axis of isodametric crystals and are called biaxial.

Due to the split of incident light into two polarization components which travel at different speed optically anisotropic crystals are known to be multiple refractive or birefringent. The latter refers to the difference between ordinary and extraordinary refractive indices, $\Delta n = n_o - n_e$. For example, $CaMoO_4$ crystals have n_o=1.959 for light propagating perpendicular to the c-axis of a crystal, and n_e=1.967 for light propagating parallel to it (at λ = 667 nm [87]). For light propagating through the crystal in directions between parallel and

Figure 5.1: Illustration of the birefringence of a $CaMoO_4$ crystal. A single line by viewing through the crystal looks doubled.

perpendicular to the c-axis, the refractive index is intermediate between those values. Birefringence can be illustrated, for example, by viewing lines through a crystal with anisotropic structure, see Figure 5.1.

Propagation of scintillation light

The propagation of scintillation light through a crystal is accompanied by multiple reflections from the crystal surfaces. The critical angle (θ_c) of a crystal determines whether light will be totally internally reflected back into a crystal or refracted at the surface. It is calculated by Snell's law [101]

$$\theta_c \;=\; \arcsin\left(\frac{n_{air}}{n_{crystal}}\right) . \tag{5.1}$$

The critical angles for the crystals of interest are presented in Table 5.1.

Let us consider light traveling in a cylindrical crystal ($\phi\, 40 \times 40$) mm^2 with the roughened[2] flat surface facing a separate light detector; see Figure 2.6. A photon propagates though the crystal under the angle θ with respect to the crystal axis. According to Equation 5.1, photons can escape the crystal and, hence, reach the light detector only when moving at angles $\theta \leqslant \theta_c$, i.e. inside the cone defined by the solid angle [84]

$$\Omega \;=\; 2\pi\,(1 - \cos\theta_c) . \tag{5.2}$$

The smaller the critical angle θ_c the more likely a photon will be reflected at the crystal surfaces. The corresponding exit angle aperture ω is defined as the ratio of the doubled solid angle Ω inside the cone to the full solid angle of 4π [84]

$$\omega \;=\; 1 - \cos\theta_c . \tag{5.3}$$

However, the solid angle Ω is only a small fraction of the total solid angle, within which scintillation photons are emitted. Therefore, the amount of photons which can escape from the crystal directly to the light detector is also small. The

[2] A roughened surface is a large set of smooth microareas, each oriented randomly with respect to the normal surface. It is often assumed that each elementary area reflects specularly.

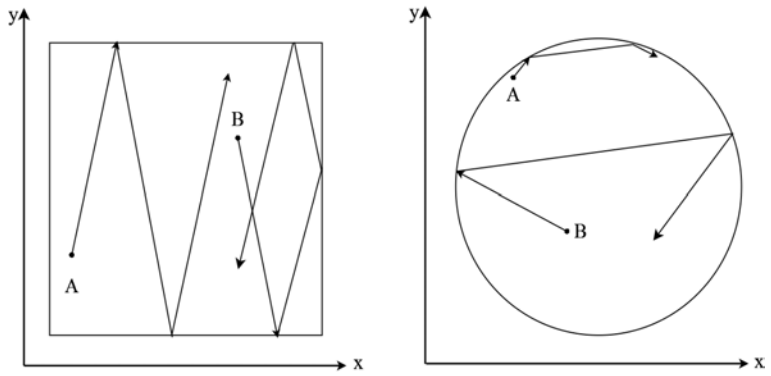

Figure 5.2: Schematic views of the light trajectory in the transverse plane of a rectangular crystal (left) and cylindrical crystal (right).

remaining photons (emitted outside Ω) can escape from the crystal only after changing the propagation direction by scattering off the roughened surface.

The efficiency of the scintillation light collection by the light detector is largely determined by the angular distribution of photons reflected at the crystal surface. Moreover, the collection efficiency is dictated by the path length of a photon in the crystal. When the path length of a photon trajectory before escaping the crystal is larger than the effective absorption length of the crystal, the probability for the photon reabsorption is high. Thereby, the factor that limits the collection efficiency is the reabsorption of the scintillation light in the bulk.

There is an essential difference in the light collection efficiency of scintillation photons produced in cylindrical and in prism-shaped crystals. Let us consider the light collection efficiency as a function of the transverse coordinates (x, y) of the scintillation points in cylindrical and rectangular crystals, see Figure 5.2. In the case of a cylindrical crystal the probability to reach the exit surface for a photon emitted at the point beyond the exit angular aperture (ω) depends on the transverse coordinates (x, y). This entails an essential transverse nonuniformity of light collection in cylindrical crystals. In the case of rectangular-prism crystals this transverse nonuniformity is always negligibly small [84]. If longitudinal and transverse dimensions of a crystal are approximately the same, then longitudinal nonuniformity in a prism and in the cylindrical crystal are almost the same. Simulations have shown that the optimum geometrical shape for crystals with high index of refraction is a truncated prism [60, 84].

5.2 Crystal growth

All calcium molybdate crystals considered in this work were grown from purified raw materials by the conventional Czochralsky technique [47] at the Bogoroditsk Plant of Technochemical Products (BTCP, Bogoroditsk, Tula region, Russia). The

zinc tungstate crystals were produced by the unique low temperature gradient Czochralsky (LTG) technique [102] at the Nikolaev Institute of Inorganic Chemistry (NIIC, Novosibirsk, Russia). They have been grown from zinc oxide (ZnO) powder of 99,995 % purity (Umicore company, Belgium) and tungsten oxide (WO_3) powder produced at NIIC.

In the Czochralsky technique the melt of the polycrystalline material is held in a vertically positioned crucible. The top surface of the melt is just barely above the melting temperature. A seed crystal is then lowered into the melt and slowly withdrawn. As the heat from the melt flows up to the seed, the melt surface cools and the crystal begins to grow. The conventional Czochralsky technique uses high temperature gradients between the melt and the crystal during the process of solidification in order to suppress the face formation and to archive the fully rounded front of the crystal.

In contrast, the LTG Czochralsky technique uses very low temperature gradients ($\sim$ 0.05-1 °/cm), so that the solidification front becomes fully faceted. Details on the growth process of $ZnWO_4$ single crystals with the help of the LTG can be found in [103]. With the LTG Czochralsky technique the ingot crystal stays inside the crucible during the entire growth process. This prevents temperature fluctuations in the melt which are usually causing crystal inhomogeneity. Also, residual thermoelastic stress within the crystal then remains small. Additionally, the shape of the crucible precludes the melt from the hits of unintended impurities from the heating system of the LTG puller, which further improves the crystal quality. The LTG technique keeps the ratio of the diameters of the ingot crystal to that of the crucible almost at unity which points towards an efficient usage of raw materials.

The growth of large, optically clean $ZnWO_4$ crystals is a very challenging task since the material tends to easily cleave along the (0 1 0) plane. Moreover, the crystals are very sensitive to mechanical treatments; see Figure 5.5. Given those difficulties NIIC is currently one of the worldwide few producers growing large volume $ZnWO_4$ crystals. An example of a $ZnWO_4$ sample pulled in air atmosphere from a platinum crucible of 70 mm in diameter and 150 mm in height with help of the LTG Cz technique at NIIC is shown in Figure 5.3.

One of the main problems associated with the growth of $ZnWO_4$ crystals is the undesirable high segregation of ions from the iron group [104]. This makes the utilization of the residual $ZnWO_4$ parts left after cutting the crystal and the re-crystallization of the raw materials unprofitable. On the other hand, for $CaMoO_4$ crystals two or three re-crystallizations of the raw materials typically improve the optical quality of the crystal. The question of finding an optimum between the number of $CaMoO_4$ re-crystallizations and acceptable number of crystallizations from one crucible is still under investigation [86].

The quality of a crystal depends on many parameters and is very sensitive

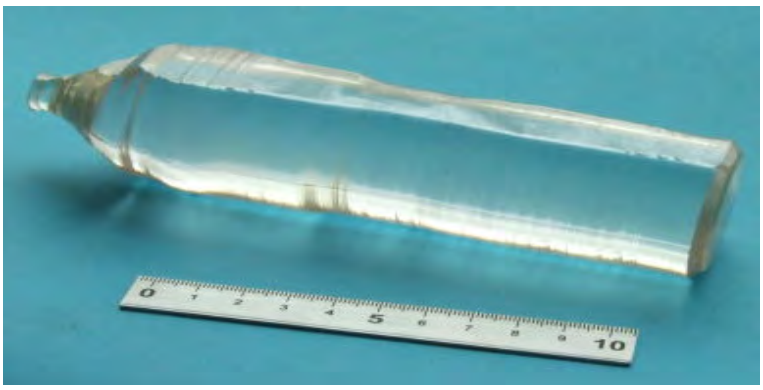

Figure 5.3: Ingot of a large zinc tungstate crystal grown with LTG Cz technique.

to the conditions of the growth process. For example, it is crucial that the producer maintains the purity of the exchange gas in the system, of the oven and surrounding environment, of the raw materials, and of the crucible. It is evident that for the mass production of high quality crystals with identical properties, which is an important issue for the CRESST-II or the future large scale project EURECA [105], special attention should be paid to the mentioned growth conditions.

5.2.1 Orientation

According to simulations [43], the orientation of the principal optical axis of a cylindrical crystal may influence the scintillation light extraction efficiency from the crystal, and hence the light collection efficiency of the CRESST-II detector module. For example, in the case of $CaWO_4$, the orientation of the optical axis produces little difference on the light collection efficiency, whereas in the case of $ZnWO_4$ inclining the optical axis by 45 ° or more relative to the cylinder axis leads to an increase in detected light by $\sim$ 5 %. Moreover, information about the crystal orientation is important for the implementation of the novel gluing technique discussed in detail in Section 7.2.

The orientation of cylindrical $CaMoO_4$ and $ZnWO_4$ crystals from the first delivery was checked by the X-ray diffraction technique; see Figure 5.4. The measurements have shown that the $ZnWO_4$ crystals have one of their optical axis aligned in parallel with the cylinder axis, while the $CaMoO_4$ crystals exhibit a $\sim$ 6 °disorientation. Since the growth direction of zinc tungstates was specified by the producer to be perpendicular to the cleavage plane (0 1 0), the flat surface of the crystal is the (0 1 0) plane, the other two axis are aligned arbitrarily.

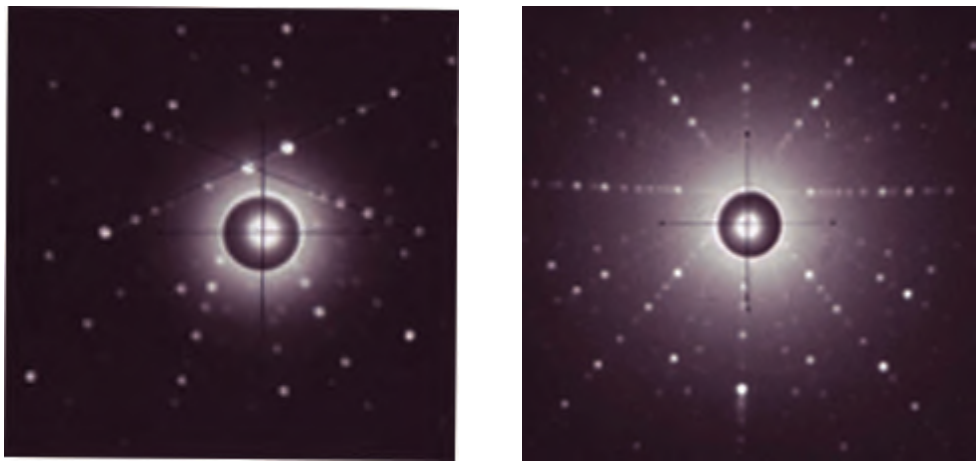

Figure 5.4: Representative images of the Laue diffraction pattern of a $CaMoO_4$ crystal (left) and a $ZnWO_4$ crystal (right). See main text for details.

5.2.2 Purity

As discussed in Chapter 1, the event rate from WIMPs in a typical direct dark matter detection experiment is expected to be less than 0.1 event per kg of target mass per day [17, 18, 19, 20] whereas the background rate is orders of magnitudes higher, even after placing the detector in a well-shielded facility. The CRESST simultaneous light-phonon measuring technique demonstrates the very good capability to reject events caused by interactions of γ-, β-, and α-particles with the scintillating crystal. Nevertheless, the count rate due to intrinsic radioactivity of a crystal may noticeably affect the sensitivity of the experiment to the detection of rare processes. Therefore, it is mandatory to inspect intrinsic contaminations of scintillating crystals. Moreover, the light output of a scintillator may be reduced due to the presence of impurities, see Section 4.2. Thus understanding of the impurity content of a crystal may provide a hint for the potential optimization of its optical properties.

Non-radioactive impurities of the $CaMoO_4$ and the $ZnWO_4$ samples were studied with the help of inductively coupled plasma mass spectrometry (ICP-MS). The results of the measurements are summarized in Table A.1 and A.2, respectively. Significant amounts of rare earth elements were present in the $CaMoO_4$ crystal (Y $\sim$ 0.7 ppm; La $\sim$ 3 ppm; Lu $\sim$ 0.23 ppm; Ce, Nd, Eu, Gd, Er, Yb, all < 93 ppb) while the $ZnWO_4$ sample was almost clean from them (all rare earth elements < 34 ppb). A samarium contamination was found in both samples (in the $CaMoO_4$ < 10 ppb; in the $ZnWO_4$ < 5 ppb). High concentration of oxygen group elements was present in both samples (Te, Se; $\sim$ 6 ppm in the $CaMoO_4$; $\sim$ 1.5 ppm in the $ZnWO_4$). A significant amount of iron ($\sim$ 5 ppm)

and sodium (~ 5 ppm) was detected in the $ZnWO_4$ sample. Contamination with lead was relatively low in both samples (in the $CaMoO_4$ < 33 ppb; in the $ZnWO_4$ < 58 ppb). Overall, the $ZnWO_4$ sample appeared to be much cleaner than the $CaMoO_4$ sample.

Finally, the operation of the prototype $ZnWO_4$ phonon detector in the CRESST-II low background facility provides an opportunity to examine radioactive contaminations of this crystal with an extremely high sensitivity (better than a few μBq/kg). Details and results of the analysis will be presented in Chapter 8.

5.3 After-growth crystal processing

The quality of a crystal may be greatly modified by the after-growth crystal processing. Various conditions of thermal (annealing, tungsten film deposition) and/or mechanical (surface roughening) treatment were applied to the $CaMoO_4$ and $ZnWO_4$ crystals in order to test how they influence their light yield. In the following sections, the description of these treatments is given and mechanisms via which they may influence the quality of crystals are discussed.

5.3.1 Thermal treatment

Annealing

Intrinsic defects, such as vacancies and interstitial ions or impurities arising inside the crystals during their growth are responsible for a number of point like defects. During **annealing** those defects may be substantially modified. Moreover, new color centers can be formed. Thereby, crystal annealing at different temperatures and in various atmospheres is an efficient tool for influencing the crystal defect system. As a result, annealing under certain conditions may help to improve its scintillation efficiency.

The emission of the scintillation light in $CaMoO_4$ and $ZnWO_4$ crystals is associated with the molecular anion groups $(MoO_4)^{2-}$ and $(WO_6)^{6-}$, respectively. The details of scintillation light emission in these crystals will be discussed in Section 5.5. Defects such as oxygen vacancies, may influence the energy structure of these regular complexes. Measurements performed in [106] have shown that high temperature annealing in vacuum increases the oxygen vacancy concentration. This reduces the scintillation efficiency of tungstate crystals. However, the deficit of the oxygen content may be compensated by the annealing in air or in oxygen flow. Indeed, the studies performed with $CaWO_4$ revealed up to 50 % improvement of the scintillation response after annealing in oxygen at 1150 °C [58].

Before annealing, the crystal under test is preliminary cleaned in an ultrasonic bath in acetone, isopropanol, and deionized water (for 5 minutes each) and then

dried with nitrogen gas. This is done in order to remove accumulated dirt from the crystal surface. All these operations are performed in a clean room. Afterwards, the crystal is placed inside a high quality quartz glass tube HSQ 300 [107], which is thermally stable up to 1160 °C. The oven with the crystal inside is slowly heated up to the desired temperature with a ramp of 1-2 °C per minute where it can be kept stable up to several days. Usually, we anneal crystals in a flow of high purity oxygen at 800 °C for 48 hours. The influence of annealing on optical and luminescence properties of $ZnWO_4$ is presented in Section 5.4 and 5.5 and Section 5.6.3 and 5.6.4 discuss the effect of annealing on the scintillation properties of the crystals under study.

Thermometer production

The production of a tungsten superconducting-phase-transition thermometer on a scintillating crystal involves several steps. These are tungsten layer deposition, aluminum layer evaporation, gold layer sputtering, and structuring of each detector layer. The description of the thermometer layout is presented in Section 2.3.4. As already explained in the previous section, oxide crystals are very sensitive to thermal treatments. The conditions of tungsten layer deposition are such that this process may be thought of as a high temperature annealing of a crystal in vacuum and which is harmful for its scintillation efficiency. This effect may be partially explained by the increase of the oxygen vacancy concentration.

Clearly, there is a need for a technology which allows the production of a phonon detector without affecting the crystal quality. Therefore, research on the development of phonon detectors with a separate thermometer carrier has been started [108, 109, 110]; see Section 2.3.4. Results of the first glued $ZnWO_4$ phonon detectors will be presented in Section 7.2. An alternative solution involves a different method for W-film production, namely, tungsten chemical vapor deposition. The research in this direction has begun only recently [85].

Prior to the deposition of the tungsten film the crystals are cleaned in a special procedure (ultrasonic cleaning in acetone, isopropanol and deionized water, each for 5 min; drying with clean nitrogen gas). This is necessary in order to obtain reproducible transition temperatures of the films. Already small amounts of ferromagnetic contaminations (ppm range) on the surface can lower the transition temperature by 1-10 mK [60].

The tungsten films are grown by electron-beam evaporation in a dedicated ultra high vacuum system. For the W-film deposition a crystal is mounted in a tantalum holder. The holder surrounds the crystal from all sides and is supported by a shadow mask with an opening of (6×8) mm^2. This shadow mask is used for large crystals (ϕ 40 $\times$ 40 mm^2). In this way the deposition is realized only on the area above the hole in the mask. When evaporating a tungsten layer on small $(20 \times 10 \times 1)$ mm^3 crystal wafers almost the complete (20×10) mm^2

surface is covered with tungsten. The deposition system is slowly heated up to the desired temperature via radiative heating. The temperature at which the deposition of the SiO_2 buffer layer and the tungsten layer take place depends on the material and is normally higher than 450 °C. The design of the deposition system allows to maintain small temperature gradients and high temperature uniformity. The environmental conditions during the deposition of the tungsten layers on $CaMoO_4$ and $ZnWO_4$ crystals are presented in Section 7.2 and 7.1, respectively.

After tungsten layer deposition the films are structured with photolithography and wet chemical etching. For tungsten etching, a dilute mixture of NaH_2PO_4, NaOH, and $Na_3Fe(CN)_6$ is used instead of conventional potassium based etchants in order to avoid contamination of the surface with radioactive ^{40}K. Then, aluminum and gold contact layers are produced and structured. During their production the temperature of the crystal is kept below 100 °C. A very detailed description of all structuring steps is presented in [60].

5.3.2 Mechanical treatment

The CRESST-II crystal housing is designed to hold cylindrical crystals, see Section 2.3. As a drawback of such a shape, scintillation photons may be trapped inside cylindrical crystals with high index of refraction. This is due to the total internal reflections at the crystal-vacuum(air) surface; see Section 5.1. Studies with $CaWO_4$ have shown that surface roughening minimizes the effect of light trapping and, moreover, helps to make the light collection more uniform [111]. Therefore, surface roughening was also performed on $CaMoO_4$ and $ZnWO_4$ crystals.

Usually, a 800 μm grain size boron carbide (BC_4) powder [112] is used. The carbon component is extracted from a fossil oil. Therefore, radioactive impurities should not be an issue. The $ZnWO_4$ crystals have been roughened at NIIC with silicon carbide (SiC) powder [113]. The influence of $ZnWO_4$ and $CaMoO_4$ surface roughening on the light collection efficiency is discussed later on in Section 5.6.3 and Section 5.6.4.

A tight holding of a crystal is usually employed in cryogenic work in order to avoid problems with microphonic noise. The CRESST-II crystals are tightly held by six pairs of metal clamps inside the detector module. However, the holding may be so tight that it induces cracks inside a crystal. Since cracking may cause an enormous count rate, which definitely would spoil the measurement of rare events [114], the holding of crystals is an important issue. In order to reduce stresses inside crystals they are usually annealed at high temperatures. Also bevelling of the crystal edges helps to decrease mechanical stresses. Therefore, CRESST-II crystals normally have small $\sim$ 0.5 mm bevels on each side.

The marked cleavage of $ZnWO_4$ crystals makes them extremely sensitive to

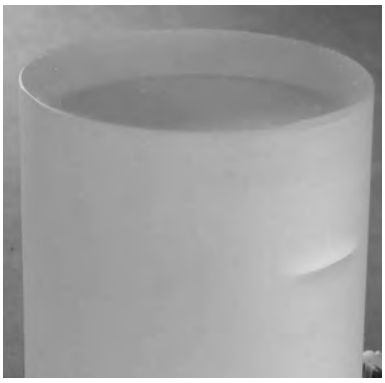

Figure 5.5: Photograph of a $ZnWO_4$ crystal with a crack along its cleavage plane.

mechanical treatments. Cutting of a cylindrical crystal from an ingot as well as surface polishing are very challenging and require special technologies. Figure 5.5 shows the cracking of a cylindrically shaped $ZnWO_4$ crystal along its cleavage plane after careless surface treatment. The operation of a phonon detector based on a cylindrical $ZnWO_4$ crystal as cryogenic calorimeter has shown a reasonably low count rate; see Chapter 8. Moreover, a careful inspection of the crystal surface after dismounting it from the holder has shown that the surface remained unchanged. Hence, the $ZnWO_4$ crystal has proved to be mechanically stable under conditions of tight holding inside a CRESST-II detector module at low temperature.

The crystal surface is usually polished by a method called wet polishing. A silk cloth with diamond paste of some μm grain size is used to achieve optical quality with an accuracy which is better than the wavelength of scintillation light. Usually all the mechanical processing is performed at the Kristall-Labor of the Technische Universität München.

5.4 Optical properties

Besides the geometrical shape of a single crystal, its transparency at the emission wavelengths is one of the key characteristics which determines the efficiency of the scintillation light extraction and, hence, the efficiency of the light collection; see Section 2.3. Typically, only $\sim 1\%$ of the energy deposited by a γ-particle in a $CaWO_4$ crystal is detected in form of scintillation light by the corresponding light detector. Thereby, finding a way to improve the crystals' transparency holds the potential to increase the total amount of light collected from the scintillator per particle event. In this section we discuss the results of the optical transmission and absorption studies on $CaMoO_4$ and $ZnWO_4$ crystals performed at room

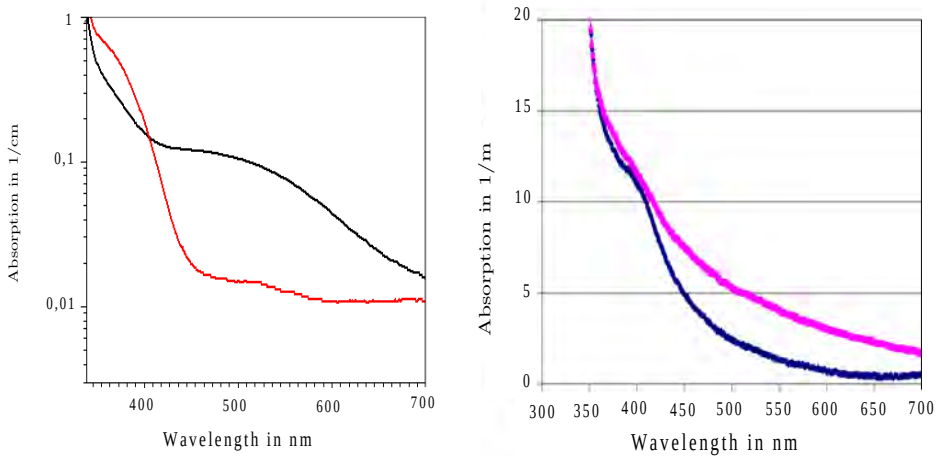

Figure 5.6: *Left*: Absorption curve of a $ZnWO_4$ crystal from NIIC before (black) and after (red) annealing at 900 °C in oxygen flow, measured by [115]. *Right*: Absorption spectra of two different $CaMoO_4$ crystals from BTCP, measured by [116].

temperature[3].

5.4.1 Absorption

In general, optical absorption is related to the crystal color. The presence of undesired impurities may lead to crystal coloration and thus to an optical absorption in the emission range of a crystal. Therefore, extraction of scintillation light from a highly transparent crystal is more efficient. Moreover, simulations performed in [60] have shown that scintillation photons produced in crystals with cylindrical geometry have to travel a relatively long path before escaping the crystal. Thereby, they are more likely to be reabsorbed by a colored crystal.

The $ZnWO_4$ crystals delivered from NIIC have a weak pink coloration. Previous studies attributed the pink coloration of $ZnWO_4$ crystals to the presence of iron impurities [117, 118, 104, 119]. Indeed, from the ICP-MS measurements we find that the concentration of Fe in the $ZnWO_4$ tested sample is approximately 5 ppm, see Table A.2. Other possible sources of the pink coloration of $ZnWO_4$ crystals suggested in literature are chromium impurities [120], trace presence of platinum[4] [121], or a stoichiometric excess of Zn ions [44].

The influence of the high temperature annealing in oxygen atmosphere on the absorption properties of a $ZnWO_4$ sample from NIIC is illustrated in the left panel of Figure 5.6. After annealing of the sample the absorption band around 500 nm decreases, while for the band around 360 nm it increases. Since $ZnWO_4$ crystals from NIIC contain traces of Fe impurities, the enhancement of the Fe^{3+}

[3]Optical properties of $CaWO_4$ crystals were studied in [58]

[4]The crucible used during growth of the zinc tungstate crystals is fabricated from platinum.

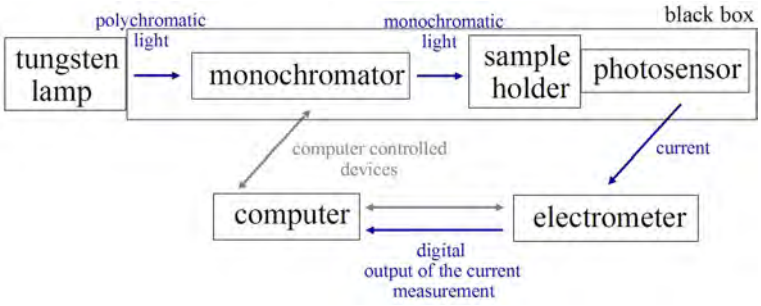

Figure 5.7: Diagram of the setup for the transmission measurements at room temperature, see text for details.

concentration by converting Fe^{2+} to Fe^{3+} due to the oxidation[5] may explain the change of the spectral shape of the absorption curve after annealing [119, 122, 117]. Impurities like Fe and Cr can be removed from the raw materials by chemical purification [122]. Therefore, further studies on the purification of raw materials at the producers' side could help to improve the optical quality of $ZnWO_4$ crystals.

The absorption spectra of $CaMoO_4$ samples produced at BTCP are presented in the right panel of Figure 5.6. Both samples have a pronounced absorption band around 420 nm. It may be attributed to the yellow coloration of the samples, which is also observed in large $CaMoO_4$ crystals delivered from BTCP. A yellow coloration may be caused by oxide based impurities present in $CaMoO_4$ crystals. Upon annealing of the large $CaMoO_4$ crystal performed at 800 °C in oxygen flow for 48 hours the yellow coloration became even more intense. This points to further oxidation of the impurities. Moreover, after being stored at room temperature in air for one year the transparency of this $CaMoO_4$ crystal further degraded.

5.4.2 Transmission

The transparency is an intrinsic property of a crystal and is partially determined by purity and stoichiometry of the raw materials. In this work a study on transmission properties of $CaMoO_4$ and $ZnWO_4$ crystals from the first delivery has been carried out. For this purpose, a setup for comparative transmission measurements was assembled.

Experimental setup

Figure 5.7 shows a schematic diagram of the experimental setup for the transmission measurements at room temperature. It consists of:

[5]The Fe^{3+} ions have an absorption band around 350 nm, while the Fe^{2+} band is around 460 nm.

- AS222 tungsten lamp from the CVI Laser Corporation: The output spectrum of the light source is related to a black body temperature of 3100 K. The light output of the lamp is stable after a warming-up period of ~ 1 hour;

- Monochromator DIGIKROM CM110 from the CVI Laser Corporation: The width of the output slit is 0.6 mm. The monochromator can be controlled from a PC via a serial port. The optical filter BG-18 from Schott is coupled to the exit of the monochromator. The output window of the filter is 5 mm in diameter;

- Cylindrical holder for crystals: The side wall of the holder (diameter=40 mm, height=40 mm) is covered with a highly reflecting polymeric foil VM2002. One flat surface of the portable cylindrical holder is open and is facing the output window of the light source. The opposite surface has a (20×20) mm^2 hole which is matching the size of the photosensor;

- The photosensor is a silicon photodiode S6337-01 from Hamamatsu Photonics: In order to collect the transmitted light, the (18×18) mm^2 photodiode is placed in parallel to a flat crystal surface at ~ 1 mm distance from it. There is no optical coupling between the crystal and the diode. Since the photodiode generates current due to the photovoltaic effect there is no need for the external biasing. In order to create an ideal dark environment, the monochromator, the holder, and the photosensor are housed in a metallic black box;

- A Keithley 6517A electrometer is used to measure the current produced in the photodiode. The electrometer is read out via a digital interface. The obtained data are stored on a PC for off-line analysis.

Most of the components were kindly provided by the MAGIC collaboration.

Discussion

The transmission spectra have been taken in the visible range of the electromagnetic spectrum from 400 nm to 600 nm in 2 nm steps with a screening speed of 2 nm per second. The transmission curve is obtained by normalizing the average transmission at a certain wavelength recorded with a crystal mounted in the holder to the average value recorded with the empty holder. The average dark current of the photodiode, obtained in the beginning and in the end of each measurement, is subtracted from the data.

The transmittivity of the $ZnWO_4$ crystals from NIIC is checked with the help of $ZnWO_4$-5 and $ZnWO_4$-6 crystals. Each of them is measured along the cylindrical axis. The left panel in Figure 5.8 shows their transmission curves which are almost identical in the wavelength region between 400 nm and 600 nm. As

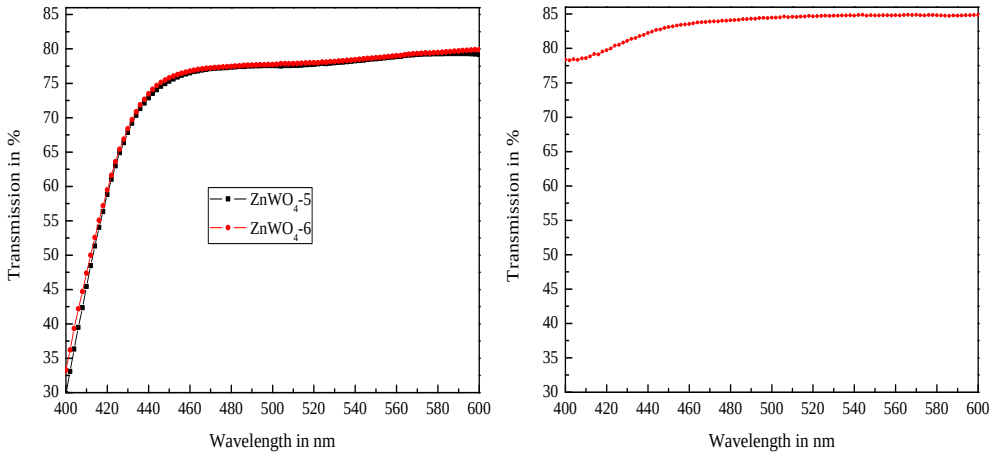

Figure 5.8: *Left*: Comparison of optical transmission spectra of the $ZnWO_4$-5 and the $ZnWO_4$-6 crystals measured as delivered. *Right*: Optical transmission spectrum of the $CaMoO_4$-2 crystal. All crystals are measured along their cylindrical axis.

crystal ingots were produced in different growth runs, the obtained results point towards good reproducibility of the $ZnWO_4$ crystal quality. Both crystals have shown a good transmissivity, which was measured to be higher than 75 % above 450 nm. The transmission decreases towards lower wavelengths due to intrinsic absorption. No peculiar absorption regions are observed in the shape of the transmission spectra of these $ZnWO_4$ samples.

The right panel in Figure 5.8 shows the transmission curve recorded with the $CaMoO_4$-2 crystal measured as delivered. This sample shows a good transmittivity which was measured to be higher than 80 % above 430 nm. No peculiarities in the spectral shape were observed. Since some parts of the experimental setup were available only temporarily, comparative studies between the $CaMoO_4$ crystals were not possible.

It should be noted that the data presented in Figure 5.8 is systematically high by a few percent. This is due to multiple Fresnel reflections appearing on the crystal-air and air-silicon surfaces between the crystal and the photodiode, respectively. Thereby, the light which is initially reflected by the silicon surface bounces back from the crystal and may eventually be absorbed by the photodiode (the initial reflection drops out in the measurement without a crystal in the holder used for the normalization). This leads to a systematic enhancement of the transmission measurement by a factor of $1/\kappa \simeq 1/(1 - R_c R_{Si})$ which arises from a geometrical series with R_i denoting the respective reflectivities.

It is, however, not possible to correct for this effect since there seem to be no measurements of the crystal refractive indices n_c of $ZnWO_4$ and $CaMoO_4$ over

the whole optical range. Nevertheless, using

$$R_{c/Si} = \left(\frac{1 - n_{c/Si}}{1 + n_{c/Si}}\right)^2, \tag{5.4}$$

for perpendicular light incidence relative to the reflecting surface, κ can be estimated at a fixed wavelength for which n_c is available. For $ZnWO_4$, at λ = 490 nm, one finds $\kappa \simeq 0.95$ with $n_c = 2.32$ [88] and $n_{Si} = 4.35$ [123]. For $CaMoO_4$, at λ = 600 nm, $\kappa \simeq 0.96$ with $n_c = 1.96$ [87] and $n_{Si} = 3.94$ [123]. Thereby, the effect on the transmission is of the order of ~ 5 %. Moreover, by noting that the maximum transmission (without absorption) is given by

$$T_{max} = 1 - R_{tot} = \frac{1 - R_c}{1 + R_c} \tag{5.5}$$

one may calculate the attenuation length of the crystals at these wavelengths. For λ = 490 nm ($ZnWO_4$) and λ = 600 nm ($CaMoO_4$) one finds T_{max} = 73 % and 83 %, respectively. However, after correcting by κ at the measured data points, the associated transmittivities read T = 73 % and 82 % so that the losses inside the crystal due to absorption and scattering in the bulk are not resolved by the measurements (the expected attenuation is ~ 1% per cm, see Figure 5.6).

5.5 Luminescence properties

As discussed in Section 2.3.3, the sensitivity of silicon and silicon-on-sapphire light detectors to the absorption of scintillation light is wavelength dependent. Hence, it is important to know the emission characteristics of a scintillating crystal in order to maximize the light collection efficiency of the CRESST-II detector module by selecting the appropriate light absorber. Thereby, emission spectra of the large $ZnWO_4$ and $CaMoO_4$ crystals have been examined. Additionally, the influence of thermal treatments on the emission characteristics of a $ZnWO_4$ crystal has been investigated.

Experimental setup

The measurements were carried out at the spectroscopy laboratory of the E12 group at the Technische Universität München. Figure 5.9 shows the schematic diagram of the experimental setup. The scintillation was induced by illuminating a crystal with UV-light emitted by a deuterium lamp. The lamp is a low-pressure gas-discharge light source. The optical output window of the lamp is made of magnesium fluoride in order to prevent absorption of UV-light. The emission spectrum of the deuterium lamp is presented in the left panel of Figure 5.10. The UV-light was focused onto a sample with the help of a quartz lens. The latter was positioned such that the image of the light source was sharp. The

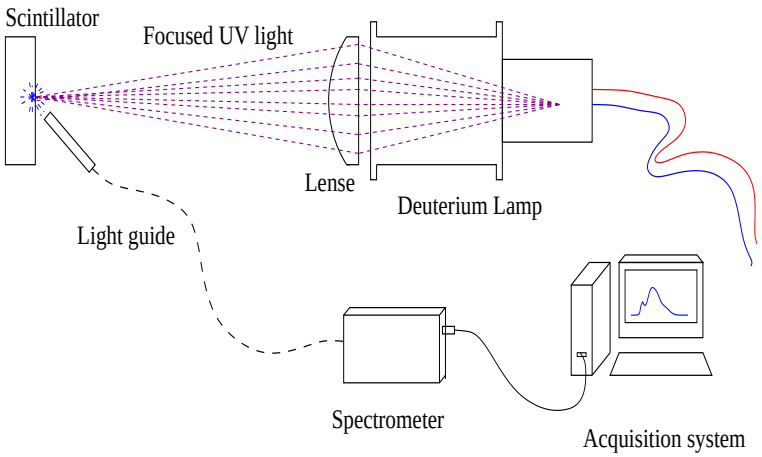

Figure 5.9: Diagram of the setup for measurements of emission spectra at room temperature. Components discussed in main text.

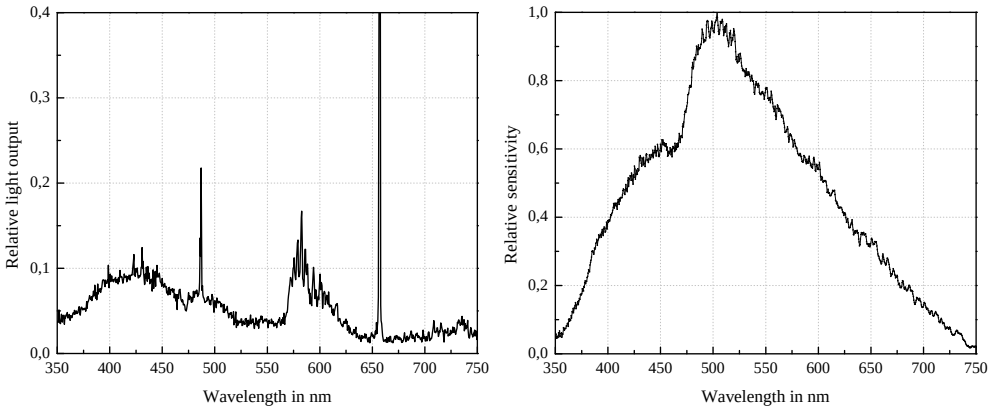

Figure 5.10: *Left*: Emission spectrum of the deuterium lamp. The contribution in the UV-region originates from the molecular continium of the deuterium molecule D_2. Molecular transitions of D_2 are responsible for the Fulcher-α band between 560 nm and 640 nm. The lines at 486 nm and 656 nm are the characteristic hydrogen Balmer lines. *Right*: Spectral response of the Ocean Optics spectrometer. The substructures on the curve are due to the presence of filters in front of the CCD array.

emitted scintillation light was detected by a medium-resolution miniature Ocean Optics HR2000CG-UV-NIR spectrometer via a quartz-guide (length = 210 cm, ϕ = 600 μm) [124]. The guide was placed under the angle of 45 ° relative to the crystal surface. Inside the spectrometer the light transmitted via the guide was focused on a blaze grating and then on a detection plane, where it was absorbed by a linear ILX511 CCD array from Sony. The data were read out by the Ocean Optics software for off-line analysis. All recorded spectra are corrected

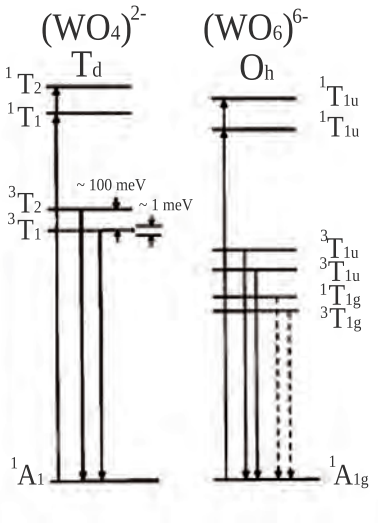

Figure 5.11: Schematic diagram of the energy levels in scheelite (left) and wolframite (right) crystals. The full arrows indicate allowed absorption and emission transitions. The dotted arrows denote forbidden transitions. $^1A_1$ represents the ground state, while triplet T denotes for various excited energy states. Figure taken from [127].

for the spectral response of the spectrometer, which is shown in the right panel of Figure 5.10 [125].

Discussion

In order to explain the shapes of the measured $CaMoO_4$ and $ZnWO_4$ emission curves the band structure of their luminescence centers should be introduced first. A schematic representation of energy levels responsible for the radiative transitions in generic tungstates with scheelite and wolframite lattice structure are shown in Figure 5.11. These diagrams are obtained from molecular orbital calculations in the $(WO_4)^{-2}$ complex in T_d point symmetry [90] and in the $(WO_6)^{-6}$ complex in O_h point symmetry [126]. The emission characteristics of $CaMoO_4$ crystals are almost the same as for $CaWO_4$ crystals because of the similarities in their electronic configurations [90].

It is generally accepted that the intrinsic luminescence component in $CaMoO_4$ crystals is due to electronic transitions $^3T_2 \rightarrow {}^1A_1$ and $^3T_1 \rightarrow {}^1A_1$ in the tetrahedral oxyanion $(MoO_4)^{-2}$ complexes [128, 129, 130]. As shown in the left panel of Figure 5.11 the emission in crystals with scheelite structure is composed of a superposition of bands separated only by $\sim$ 100 meV [90]. The allowed transitions $^1A_1 \rightarrow {}^1T_2$, $^1T_1$ account for the fundamental absorption edge.

The intrinsic luminescence component in $ZnWO_4$ crystals is due to electronic

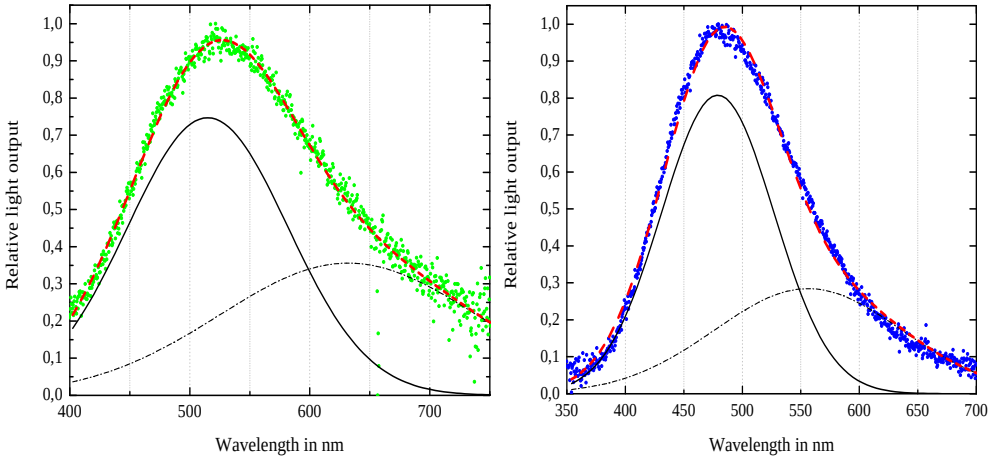

Figure 5.12: *Left*: Emission spectrum of the $CaMoO_4$ sample. *Right*: Emission spectrum of the $ZnWO_4$ sample. Both spectra were recorded under excitation with the UV-light source at room temperature. Gaussian fits are superimposed.

transition ${}^3T_{1u} \rightarrow {}^1A_1$ between O^{2-} and W^{6+} ions within the octahedral $(WO_6)^{6-}$ molecular complexes [131, 132, 127]. Absorption by the $(WO_6)^{6-}$ complex is assigned to the ${}^1A_{g1} \rightarrow {}^1T_{1u}$ transitions.

The left panel of Figure 5.12 shows the emission spectrum of the $CaMoO_4$ crystal obtained under excitation with the UV-light source at room temperature. The luminescence spectrum of the $CaMoO_4$ crystal spans from $\sim$ 380 nm (3.26 eV) to $\sim$ 750 nm (1.65 eV) and has its maximum intensity around 515 nm (2.40 eV). The emission curve can be decomposed into two Gaussian curves, corresponding to the *green emission band* peaking around 515 nm (solid line) and *orange emission band* peaking around 630 nm (1.97 eV) (dashed dotted line). The shorter wavelength emission band is attributed to the intrinsic emission in $CaMoO_4$ crystals; see discussion above. The longer wavelength band is ascribed to a similar transition in a molybdate group lacking an oxygen ion, i.e. the MoO_3 center [128].

The right panel in Figure 5.12 shows the emission spectrum of the $ZnWO_4$ crystal. The luminescence spectrum of the $ZnWO_4$ crystal spans from $\sim$ 350 nm (3.54 eV) to $\sim$ 650 nm (1.90 eV) and has its intensity maximum around 480 nm (2.58eV). The spectrum can be decomposed into two broad Gaussians, corresponding to the *blue-green emission band* peaking at $\sim$ 480 nm (2.58eV) (solid line) and *green emission band* peaking at $\sim$ 556 nm (2.23 eV) (dashed dotted line). The blue-green emission is intrinsic to $ZnWO_4$ crystals. The green emission is often ascribed to the presence of impurities and different structural defects. However, the origin of these defects is still under discussion [133, 106].

To check the role of oxygen vacancies (WO_3 centers) in the process of the

green luminescence emission in $ZnWO_4$ crystals the emission spectrum of the $ZnWO_4$ sample was measured before and after annealing in oxygen flow (see Section 5.3.1). Since annealing in oxygen flow leads to the reduction of oxygen vacancies, one expects a decrease in the green emission intensity with respect to the blue-green emission. However, the experiment revealed that the ratio of the blue-green maximal intensity to the green one remains constant at ~ 2.9. The annealing in oxygen flow did not reduce the green luminescence with respect to the blue-green. The observed effect may be explained by the fact that oxygen vacancies are not involved in the formation of luminescence centers responsible for the green emission. Indeed, the authors in [106] suggest that radiative relaxation of excited W^{6+}-O^{2-} bonds could be an origin of the green luminescence in $ZnWO_4$ crystals.

5.6 Scintillation properties

The amount of absorbed ionizing radiation which is converted into scintillation light is one of the most important characteristics of a crystal. This quantity, the so-called light yield, differs for the various scintillators[6]. As already mentioned in Section 2.3.1, the scintillation efficiency is one of the key parameters that defines the discrimination threshold between nuclear and electron recoils. Thus, a measurement of scintillation light yield at room temperature can be considered as the first step in the selection process of crystals for the production of a phonon detector.

This section discusses the technique for measuring the light yield of a scintillating crystal and presents the results of the comparative light yield measurements of the $CaMoO_4$ and the $ZnWO_4$ crystals.

Experimental setup

The experimental setup used for the comparative light yield measurements is depicted in Figure 5.13. The photomultiplier tube (PMT) is Photonis, type number XP3461B, with a bialkali photocathode sensitive to the green part of the electromagnetic spectrum; see Figure 5.15. The base of the PMT is modified to integrate the scintillation light over ~ 500 μs. Pulses from the PMT's anode are then fed to a differential amplifier. An Ortec 450 research amplifier with individually selectable integration and differentiation time constants is used for pulse shaping and further amplification of the signal. Histograms of the pulses are obtained by using an Ortec 926 multichannel buffer which is read out by the Ortec MAESTRO software installed on a PC. The position of the photopeak in the histogram is a measure of the scintillation efficiency of the crystal.

[6]The generally accepted room temperature values of the absolute light yield for crystals considered in this work are presented in Table 5.1.

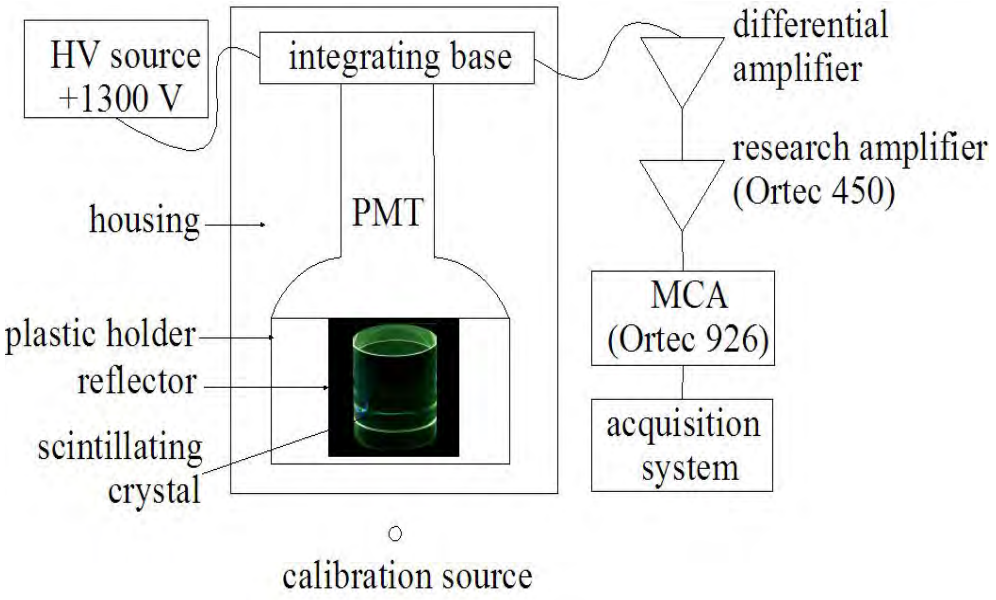

Figure 5.13: Schematic view of the experimental setup for measuring the relative light yield of scintillating crystals at room temperature.

The crystal is mounted in a cylindrical plastic holder whose walls are covered with a highly reflecting 3M polymeric foil VM2002. The crystal holder with a crystal inside and the PMT's entrance window form the optical system, which is mounted in a light-tight black box. Since there is no optical coupling between phonon and light detectors, an optical coupling between the crystal and the PMT is not used. To induce scintillation in a crystal as well as for calibration, a ^{137}Cs source is used. Figure 5.14 depicts the decay scheme of this isotope.

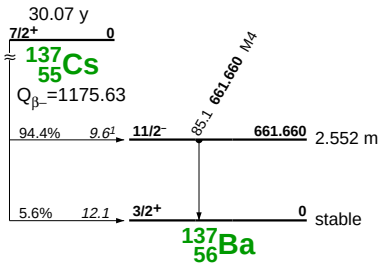

Figure 5.14: ^{137}Cs decay scheme. In 94.4 % of the cases ^{137}Cs β-decays into the metastable ^{137}Ba isotope which, upon emission of a 661.66 keV γ-ray, becomes stable. Figure taken from [30].

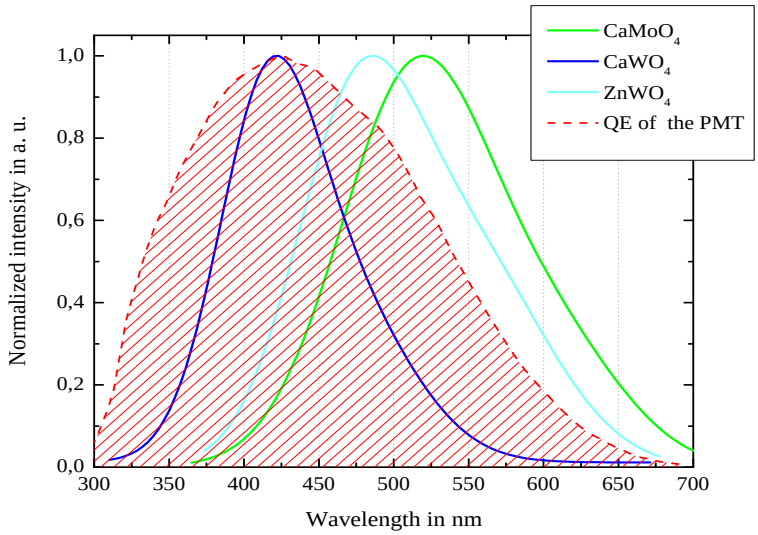

Figure 5.15: The quantum efficiency curve of the XP3461B PMT (dashed line) [134], together with the luminescence spectra of a $CaWO_4$ (blue line), a $ZnWO_4$ (light-blue line) and a $CaMoO_4$ crystal (light-green line). All spectra are normalized to unity for convenience.

5.6.1 Spectral corrections

The light yield of the measured crystals is evaluated relative to the reference $CaWO_4$ crystal BORIS[7], e.g. for each test sample the measured position of the photopeak is normalized to the one recorded with BORIS. However, it should be noted that photon detection and photoelectric conversion of the optical system[8] are wavelength dependent. Therefore, if the emission spectrum of a crystal under test is different from the reference crystal, the result of light yield measurement can be strongly affected.

From Figure 5.15 it can be seen that the quantum efficiency of the PMT in the energy range of the $CaWO_4$ scintillation emission is higher than that for $ZnWO_4$ or $CaMoO_4$. In order to correct for this effect, spectral corrections have to be taken into account.

The spectral relationship between the optical system and the response of the PMT, in terms of number of photoelectrons liberated from the photocathode (N_{pe}), can be expressed quantitatively by the following relation [135]:

$$N_{pe} = E_{abs} \int_0^{\infty} \epsilon(\lambda)\, \tau(\lambda)\, \eta_{cathode}(\lambda)\; d\lambda. \tag{5.6}$$

Here, E_{abs} is the energy which a particle dissipates in the crystal, $\epsilon(\lambda)$ is the

[7]Properties of the reference crystal BORIS are discussed in [58]

[8]The optical system consists of the crystal under test, reflector of the crystal holder, and the PMT's entrance window.

number of scintillation photons generated per unit wavelength interval and per unit absorbed energy, $\tau(\lambda)$ is the fraction of photons which actually arrive at the PMT's photocathode, and $\eta_{cathode}(\lambda)$ is the quantum efficiency. In order to account for the spectral corrections, the quantities in the integral of Equation 5.6 are usually separated into two factors, one giving the magnitude and the other one the spectral shape factor,

$$\epsilon(\lambda) \longrightarrow LY\, s(\lambda)\,, \tag{5.7}$$

$$\tau(\lambda) \longrightarrow T\, t(\lambda)\,, \tag{5.8}$$

$$\eta_{cathode}(\lambda) \longrightarrow P\, p(\lambda)\,, \tag{5.9}$$

with $LY=\int_0^\infty \epsilon(\lambda)\, d\lambda$ and $\int_0^\infty s(\lambda)\, d\lambda=1$. Now, P is simply the maximum of the quantum efficiency $\eta_{cathode}(\lambda)$ while $p(\lambda)$ is normalized to unity at the peak position [135]. Equation 5.6 then becomes

$$N_{pe} \;=\; E\, LY\, T\, P\, m\,, \tag{5.10}$$

where

$$m \;=\; \int_0^\infty s(\lambda)\, t(\lambda)\, p(\lambda)\, d\lambda\,. \tag{5.11}$$

The parameter m contains all the spectral relationships between the crystal under test and the PMT[9]. It is a dimensionless quantity ranging from 0 to 1 and may be thought of as a spectral matching factor. It is apparent from Equation 5.10 that the light yield of a crystal "1" relative to a crystal "2" is simply

$$\frac{LY_1}{LY_2} \;=\; \frac{PP_1\, m_2}{PP_2\, m_1}\,, \tag{5.12}$$

with the position of the photopeak in the histogram (PP_n) being proportional to the number of liberated photoelectrons (N_{pe}).

Our measurements are concerned with the determination of the light yield of $ZnWO_4$ and $CaMoO_4$ crystals relative to BORIS. By numerical integration of the curves shown in Figure 5.15 (in accordance with Equation 5.11) the spectral matching factor for $CaWO_4$, $ZnWO_4$, and $CaMoO_4$ are calculated to be 0.87, 0.66, and 0.54, respectively. Thus, the ratios of the spectral matching factors for $CaMoO_4$ and $ZnWO_4$ crystals relative to $CaWO_4$ are

$$\frac{m_{CaWO_4}}{m_{CaMoO_4}} \;=\; 1.58\,, \qquad \frac{m_{CaWO_4}}{m_{ZnWO_4}} \;=\; 1.31\,.$$

[9]Since in all tests we use the same type of the reflector whose reflectivity remains almost constant above ~390 *nm*, we assume here that $\int_0^\infty \tau(\lambda)\, d\lambda = constant$.

5.6.2 Energy resolution

The energy resolution can be estimated as the ratio of the full width at half maximum (FWHM) of the photopeak to the position of its maximum:

$$Resolution \equiv \frac{FWHM}{peak\ position} = k\frac{\sqrt{E}}{E}\ ; \tag{5.13}$$

k is a constant of proportionality. Statistical broadening of the photopeak is the dominant source for the loss of energy resolution.

5.6.3 Studies with $ZnWO_4$ crystals

Cesium absorption spectrum

Calibration photons of 662 keV entering a crystal can undergo a photoelectric effect or Compton scattering. In the latter process, a photon can escape the crystal depositing only a part of its energy. Based on the reaction kinematics, the ratio of the scattered photon energy ($E_\gamma^{'}$) to the incident photon energy (E_γ) is given by [136]

$$\frac{E_\gamma^{'}}{E_\gamma} = \frac{1}{1+\epsilon(1-\cos\theta_\gamma)}\ , \tag{5.14}$$

where $\epsilon = E_\gamma/m_e c^2$ is the reduced photon energy (m_e is mass of an electron at rest), and θ_γ is the scattering angle of the photon. The energy transferred by a Compton-scattered photon to the crystal is

$$E_T = E_\gamma - E_\gamma^{'}\ . \tag{5.15}$$

The amount of transferred energy varies with θ_γ. For $\theta_\gamma \to 0$ no energy is transferred to the crystal whereas for $\theta_\gamma \to \pi$ the maximum amount of energy is transferred. Thus, the maximum energy transfer of a Compton scattered photon is

$$E_{Compton\ edge} = \frac{2E_\gamma^2}{m_e c^2 + 2E_\gamma} \tag{5.16}$$

with the cutoff energy of $E_{Compton\ edge}$ called the Compton edge.

Photons emitted by the calibration source in a direction other than directly into the crystal may be scattered by the local environment and eventually be absorbed by the crystal after one or more collisions with the surrounding. In each scattering the photon loses energy. Therefore, once detected, it will appear in the spectrum at a lower energy than the photopeak energy. This is where the backscatter region of the spectrum originates from. The backscatter edge is due to photons emitted directly away from the crystal ($\theta_\gamma = \pi$) and then scattered back, i.e.

$$E_{backscatter\ edge} = E_\gamma - E_{Compton\ edge}\ . \tag{5.17}$$

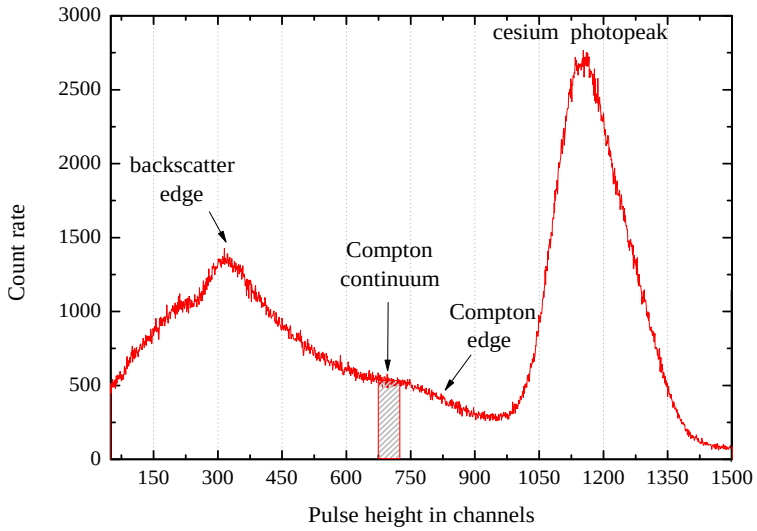

Figure 5.16: Spectrum measured with $ZnWO_4$-4 crystal (annealed) at room temperature under irradiation with a ^{137}Cs source. See main text for details.

Figure 5.16 shows a typical spectrum measured with the $ZnWO_4$ crystal under irradiation with a ^{137}Cs source. Both edges mentioned above, i.e. the Compton edge and the backscatter edge, can be found in the spectrum on top of the background. The sharpness of the Compton edge is smeared by the resolution of the crystal and by secondary photon interactions.

Structure of the photopeak

From Figure 5.17 it is evident that the decomposition of the photopeak into two Gaussians gives a much better fit to the measurement than the fit of a single Gaussian. Independently on their dimensions, the cesium spectra measured with $ZnWO_4$ crystals show a double structure of the photopeak. The effect is more pronounced for the crystals with all surfaces polished to optical quality; see Table 5.3. As already mentioned in Section 5.1, the amount of scintillation light trapped inside crystals with large index of refraction and cylindrical geometry is high. From simulations of cylindrical crystals [60] one expects that the number of scintillation photons escaping the crystal after γ-absorption at high radial position to be lower than that for γ's absorbed at small radial position. Therefore, the differences in amount and energy distribution of photons escaping the crystals through the cylindrical and the flat surfaces may result in the observed broadening of the photopeak. In order to demonstrate this effect the $ZnWO_4$-1 crystal was measured as delivered, after annealing, and after subsequent surface roughening while keeping the experimental setup unchanged. Figure 5.18 presents the results of these measurements. Though annealing improved the

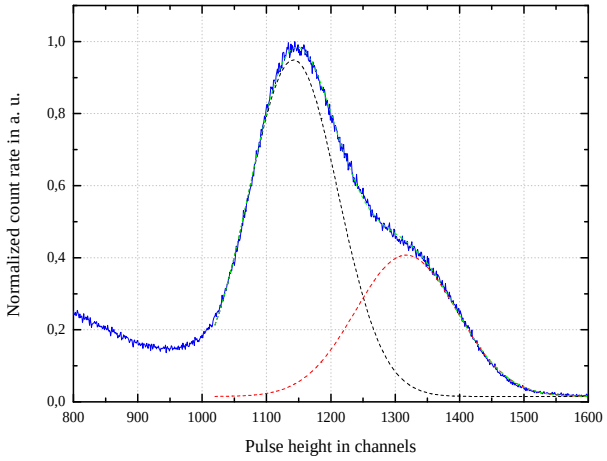

Figure 5.17: Structure of the photopeak measured at room temperature with $ZnWO_4$-1 crystal (as delivered) under irradiation with a ^{137}Cs source. Gaussian fits are superimposed. See main text for details.

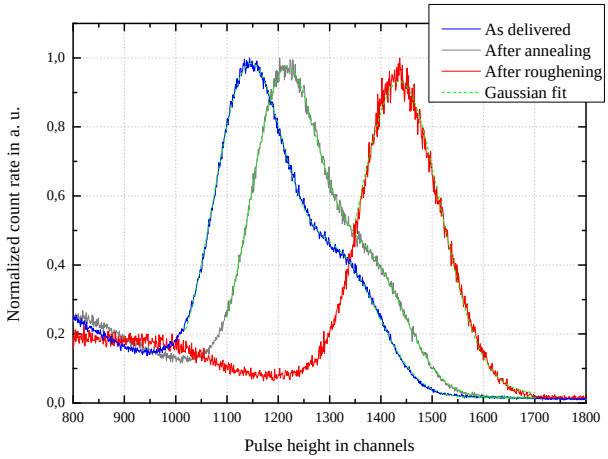

Figure 5.18: Spectra measured with $ZnWO_4$-1 crystal as delivered, after annealing, and after subsequent surface roughening under irradiation with a ^{137}Cs source. Gaussian fits are superimposed. See main text for details.

relative light yield [10] of the crystal from ~ 117 % to ~ 124 %, the broad structure of the photopeak was still present. However, after roughening of one of the flat surfaces of the crystal (facing the PMT) the double structure disappeared. The RLY further improved from ~ 124 % to ~ 138 %. A good energy resolution of 13 % from the fit of the photopeak with a single Gaussian was obtained. Thus, the effect of light trapping was minimized and scintillation light collection became more uniform.

[10] The relative light yield (RLY) is calculated according to Equation 5.12.

Name	Diameter in mm	Height in mm	Mass in grams	Surface
$ZnWO_4$-1	40	10	93	polished
$ZnWO_4$-2	40	10	93	polished
$ZnWO_4$-3	40	16	163	roughened
$ZnWO_4$-4	40	40	404	roughened
$ZnWO_4$-5	40	40	399	polished
$ZnWO_4$-6	40	40	401	polished
BORIS	40	40	300	polished

	As delivered		After annealing	
	RLY (%)	Res (%) at 662 keV	RLY (%)	Res (%) at 662 keV
$ZnWO_4$-1	109.2 (125.7)	14.1 (15.2)	116.1 (131.7)	13.1 (12.7)
$ZnWO_4$-2	109.7 (128.2)	15.3 (15.2)		
$ZnWO_4$-3	132.5 (142.1)	10.8 (12.1)		
$ZnWO_4$-4	83.4 (97.0)	16.5 (15.5)	98.0 (108.3)	12.8 (12.3)
$ZnWO_4$-5	51.8 (67.6)	27.4 (23.1)	54.5 (65.6)	25.8 (18.5)
$ZnWO_4$-6	57.5 (68.5)	24.5 (22.0)		
BORIS	100.0	14.0		

Table 5.3: The relative light yield of the $ZnWO_4$ crystals measured at room temperature with the PMT. The light yield of each $ZnWO_4$ crystal with applied spectral correction is normalized to the light yield of BORIS. When a double structure of the photopeak is present, the position of the second peak is given in parenthesis. Statistical errors for the RLY and the energy resolution are significantly below 0.1 %. See main text for details.

Relative light yield of $ZnWO_4$ crystals

Table 5.3 presents dimensions of the $ZnWO_4$ crystals considered in this work and summarizes the results of their relative light yield (RLY) measurements at room temperature in the experimental setup described in Section 5.6. In general, the RLY of the $ZnWO_4$ crystals is comparable with that of the reference crystal. All measured $ZnWO_4$ crystals, independently on their dimensions, exhibit the broad structure of the cesium photopeak. As discussed in the previous section, this effect is caused by geometrical trapping of scintillation light. Roughening of the flat surface of the $ZnWO_4$ crystal substantially reduces the trapping of

scintillation light and thereby improves the RLY and energy resolution of the $ZnWO_4$ crystals; see Figure 5.18.

Additionally, we observe an increase of the RLY of 10-30 % after annealing of the $ZnWO_4$ crystals at 800 °C for 48 hours in oxygen flow. The energy resolution is typically improved by ~ 4%. Further studies on the influence of annealing temperature and atmosphere on the scintillation properties of $ZnWO_4$ crystals are in progress.

Thin $ZnWO_4$ crystals ($ZnWO_4$-1, $ZnWO_4$-2, $ZnWO_4$-3) exhibit better scintillation efficiencies than large crystals with the standard dimensions because less scintillation photons are reabsorbed before escaping. The large crystals from the first delivery ($ZnWO_4$-4 with RLY ≈ 90 %) and from the second delivery ($ZnWO_4$-5 with RLY ≈ 60 % and $ZnWO_4$-6 with RLY ≈ 63 %) have shown comparable scintillation efficiency. Since the $ZnWO_4$-4 crystal was delivered with one flat surface roughened its RLY is higher. An increase of the RLY by ~ 15 % for the crystals from the second delivery is expected after roughening of the flat surface. Taking into account that each large $ZnWO_4$ crystal was chopped from a different ingot, the results of the comparative light yield measurements point to a good reproducibility of the crystal quality.

Photopeak to Compton ratio

The photopeak to Compton ratio is an indicator for the ability of a crystal to distinguish low-energy peaks in the presence of high-energy sources. The peak to Compton ratio is obtained by dividing the height of the photopeak at the position of its maximum by the average height of the Compton continuum associated with the peak. For the Compton continuum associated with the cesium peak the average is defined between ~ 358 keV and ~ 382 keV[11]. Due to the high atomic number of tungsten ($Z = 74$) and its high density, $ZnWO_4$ is a very efficient γ-ray absorber. Because of its high effective atomic number, Z_{eff} [12] the photofraction for γ-ray absorption is high (see Appendix B.1). This should result in a good photopeak to Compton ratio. In our experimental configuration, in which there is no optical coupling between a crystal and the PMT, the typical value of the photopeak to Compton ratio was found to be ~ 4.6 and ~ 5.1 for the $ZnWO_4$ crystals and the reference $CaWO_4$ crystal, respectively.

Linearity

Figure 5.19 shows the dependence of the scintillation response on the absorbed energy for the crystal $ZnWO_4$-4. The measurements were performed before and

[11] The region is officially defined by the ANSI/IEEE standards.

[12] Scintillating crystals usually contain several compounds. In this case, it is necessary to use mean parameters for the interaction cross-section calculations. The precise definition of the effective atomic number Z_{eff} of the $A_xB_yC_z$ compound can be found in [72].

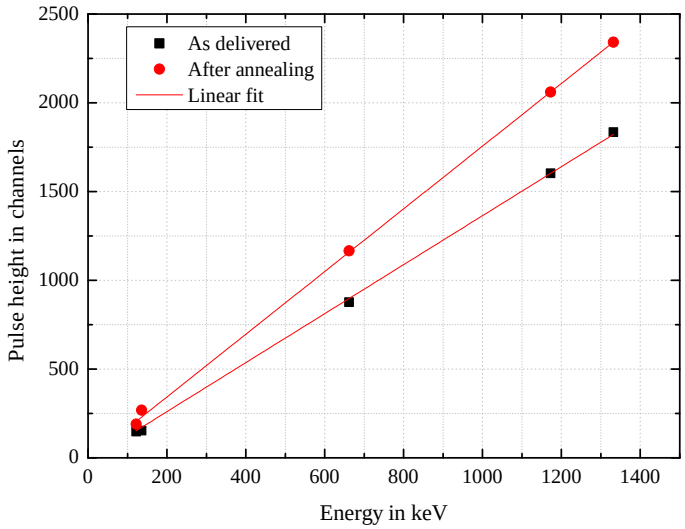

Figure 5.19: Linearity of the scintillation response of the $ZnWO_4$-4 before and after thermal treatment. Measurements were taken with the PMT at room temperature via irradiation of the crystal with γ's from a ^{57}Co, a ^{137}Cs and a ^{60}Co source. During the measurements the roughened surface of the crystal was facing the PMT. See main text for details.

after thermal treatment via irradiation with 122 keV and 136 keV γ's from a ^{57}Co , 662 keV γ's from a ^{137}Cs, and 1.17 MeV and 1.33 MeV γ's from a ^{60}Co source. The geometry of the setup was kept unchanged. No deviations from the linear behavior of the scintillation response of this $ZnWO_4$ crystal between 122 keV and 1330 keV can be observed.

5.6.4 Studies with $CaMoO_4$ crystals

Table 5.4 gives the dimensions of the $CaMoO_4$ crystals considered in this work and summarizes the results of their relative light yield measurements at room temperature. The RLY of the $CaMoO_4$ crystals measured after delivery is only $\sim$ 20 % of that for BORIS. It was found that annealing at 800 °C for 48 hours in oxygen flow, improves the scintillation efficiency of a small (20 $\times$ 10 $\times$ 5) mm^3 $CaMoO_4$ sample by $\sim$ 15 %, see the left panel of Figure 5.20. Therefore, the large $CaMoO_4$-1 crystal was annealed under the same conditions. However, the optical properties of this crystal have changed after thermal treatment. The slight yellow coloration of the crystal became more pronounced and its RLY and the energy resolution degraded. Figure 5.21 illustrates this effect. The fact that the producer annealed the crystal at $\sim$ 1300 °C in oxygen flow before delivery may explain why annealing at 800 °C (which probably modified the defect system of the crystal) degraded the crystal properties. Unfortunately, information about the annealing history of the crystal became available only after the thermal

Name	Diameter in mm	Height in mm	Mass in grams	Surface
$CaMoO_4$-1	40	40	217	polished
$CaMoO_4$-2	40	40	216	polished
BORIS	40	40	300	polished

	As delivered		After annealing		After W-film deposition, roughening	
	RLY (%)	Res (%)	RLY (%)	Res (%)	RLY (%)	Res (%)
$CaMoO_4$-1	17.0	36.2	15.5	37.6	20.4	30.2
$CaMoO_4$-2	20.3	37.8			22.0	23.7
BORIS	100.0	14.0				

Table 5.4: The relative light yield of the $CaMoO_4$ crystals measured at room temperature with the PMT. The light yield of each $CaMoO_4$ with applied spectral correction is normalized to the light yield of the reference crystal BORIS. The energy resolution is estimated as FWHM at 662 keV. Statistical errors for the RLY and the energy resolution are significantly below 0.1 %. See main text for details.

treatment had been performed.

The position of the cesium photopeak after W-film deposition onto the $CaMoO_4$ crystals at 450 °C in vacuum was not distinguishable from the background. Therefore, the RLY after deposition is not given. It should be noted that for $CaWO_4$ crystals, which also have scheelite lattice structure, a decrease of the RLY up to 40 % after W-film deposition under the same conditions was observed [58].

Roughening of the flat surfaces of the $CaMoO_4$ crystals, which followed tungsten deposition, increased the RLY and improved the energy resolution of the crystals; see Figure 5.21. This behavior was expected since a smaller number of scintillation photons is trapped inside a roughened crystal due to total internal reflections.

The relative light yields of both large $CaMoO_4$ crystals were found to be ~ 5 times worse than that of the reference crystal. Though we measure the RLY of a particular experimental configuration, which is different from the absolute light yield of a crystal, it is interesting to compare the measured scintillation efficiencies of the $CaMoO_4$ crystals with the results of previous studies. Since the absolute light yield of $CaWO_4$ at room temperature is ~16200 photons per MeV [91],

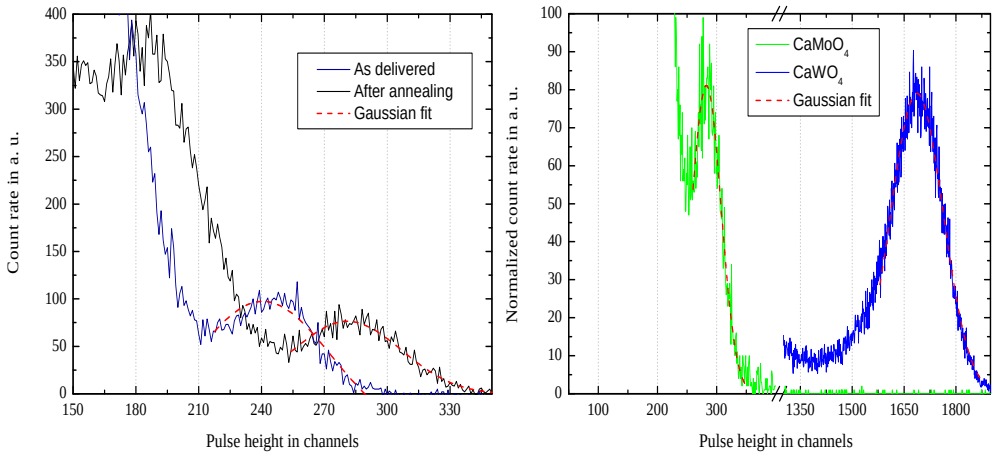

Figure 5.20: *Left*: Spectra measured in the PMT setup at room temperature with the small ($20 \times 10 \times 5$) mm^3 $CaMoO_4$ crystal as delivered (blue line), and after annealing at 800 °C in oxygen flow for 48 hours (black line). *Right*: Comparison of spectra of the small $CaMoO_4$ crystal (green line) and the $CaWO_4$ crystal of the same dimensions (blue line). All measurements have been performed in a ($20 \times 10 \times 5$) mm^3 plastic holder with walls covered by the reflector and under irradiation of the crystal under test with a ^{137}Cs source. Gaussian fits are superimposed. See main text for details.

the observed RLY of 20 % for the $CaMoO_4$ crystal equals ~ 3560 photons per MeV. Scintillation efficiencies of ~ 2070 photons per MeV and ~ 8900 photons per MeV were measured in [92] and [52], respectively. The obtained result lies between these two values.

Reproducibility of good crystal quality is essential for large scale experiments like CRESST-II or EURECA. Relative light yield measurements have shown that a strong R&D is needed in order to further improve quality of the $CaMoO_4$ crystals from BTCP.

Due to the difference in dependency of the scintillation efficiency on temperature between $CaWO_4$ and $CaMoO_4$ crystals (see Section 4.2.2), at low temperature, the latter may exhibit similar or a higher scintillation efficiency relative to $CaWO_4$. Therefore, despite the relatively low light yield of the $CaMoO_4$ crystals at room temperature, this material was also tested at mK temperatures. The results of the low temperature measurements are presented in Chapter 6.

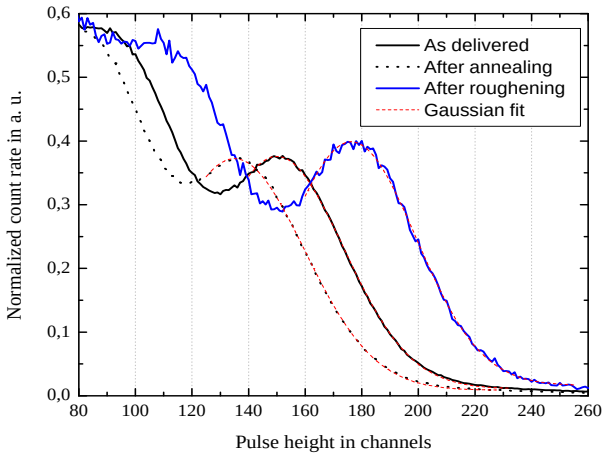

Figure 5.21: Spectra measured at room temperature in the PMT setup with $CaMoO_4$-1 crystal as delivered (black line), after annealing (dashed line), and after W-film deposition with the subsequent surface roughening (blue line) under irradiation with a ^{137}Cs source. During the measurement, the roughened surface of the crystal was facing the PMT. Gaussian fits are superimposed. See main text for details.

Chapter 6

Crystals properties at low temperature

Due to the small energies in the range of a few keV to several tens of keV expected to be transferred by a WIMP particle to the recoiling nucleus after elastic scattering off $CaMoO_4$ and $ZnWO_4$ targets, the amount of detectable scintillation light is a crucial quantity for the event discrimination. Following an electron recoil event after a particle interaction with a $CaWO_4$ crystal, typically only about 1 % of the deposited energy is detected in form of scintillation light. In order to explore the potential for the discrimination between nuclear and electron recoils, the scintillation efficiency of $CaMoO_4$ and $ZnWO_4$ crystals have to be investigated.

This chapter reports on scintillation efficiency studies of $CaMoO_4$ crystals (produced at BTCP) and $ZnWO_4$ crystals (produced at NIIC), performed at mK temperatures. In particular, the light yield and scintillation decay time constants of these crystals were measured for the first time. The obtained characteristics are compared with those of $CaWO_4$ crystals.

6.1 Detected light yield

The energy deposition by a photon in a target crystal can be divided into three channels:

$$E_{dep} = E_{phonon} + E_{scint} + E_{lost} . \tag{6.1}$$

Here, E_{phonon} is the energy transferred to phonons and E_{scint} is the total energy of all scintillation photons detected by a corresponding light detector. E_{lost} is the energy lost in form of scintillation photons escaping the reflector system of a detector module (or absorbed in it). E_{phonon} and E_{lost} constitute the dominant

part of E_{dep}. Finally, the scintillation light yield of the crystal is defined as the fraction of the total energy deposited in the scintillator eventually seen in the light detector (ε)

$$\varepsilon = \frac{E_{scint}}{E_{dep}} \,. \tag{6.2}$$

This ratio reflects not only the efficiency of the scintillation light production in the crystal, but also the efficiency of the light detector for absorption of the emitted light (see Section 2.3.3) and the light collection efficiency of the detector module, which is mainly given by the properties of the reflector system.

Absorption of scintillation light

It is important to note that the maximum of the emission intensity in $ZnWO_4$ crystals shifts significantly from ~ 480 nm to ~ 510 nm as temperature decreases from room temperature to below 8 K [49]. Such a shift is a characteristic feature of a crystal with the wolframite lattice structure [87]. The position of the emission maximum of $CaMoO_4$ crystals remains the same as at room temperature and peaks around 520 nm; see Section 5.5. The silicon layer of silicon-on-sapphire light detectors absorbs about 60 % of the emission intensity at the maximum of both, $CaMoO_4$ and $ZnWO_4$, crystals. It increases to about 70 % when measured through the sapphire layer; see Figure 2.9. In normal operating conditions both sides of the light detector absorb the scintillation light with the side facing the crystal being the dominant one [60]. Hence, the total absorption of silicon-on-sapphire light detectors is an average of the two and, at ~ 515 nm, it is ~ 65 %. The absorption efficiency of silicon light detectors around 515 nm is approximately the same [61]. Though above 500 nm the absorption efficiency of both detector types is almost the same, studies performed in [57] have shown that from the scintillation detection point of view the silicon light detectors are superior for the measurements with $ZnWO_4$ crystals. In the mean time the silicon light detectors are in favor for measurements with $CaMoO_4$ or $ZnWO_4$ crystals.

6.2 Experimental setup

The tests were carried out in a cryostat at the Max-Planck-Institute for Physics in Munich. In order to obtain temperatures below 30 mK a small self-made He^3/He^4 dilution refrigerator was used. Information about thermometer readout is given in Section 2.4.1; details on detector operation, stabilization, and data analysis have been presented in Chapter 3.

The measurements were performed in an assembly similar to the standard detector module; see Figure 2.6. It consists of a scintillating crystal sample and a nearby but separated light detector. The crystal and the light detector are mounted on copper holders which are thermally coupled to the mixing chamber

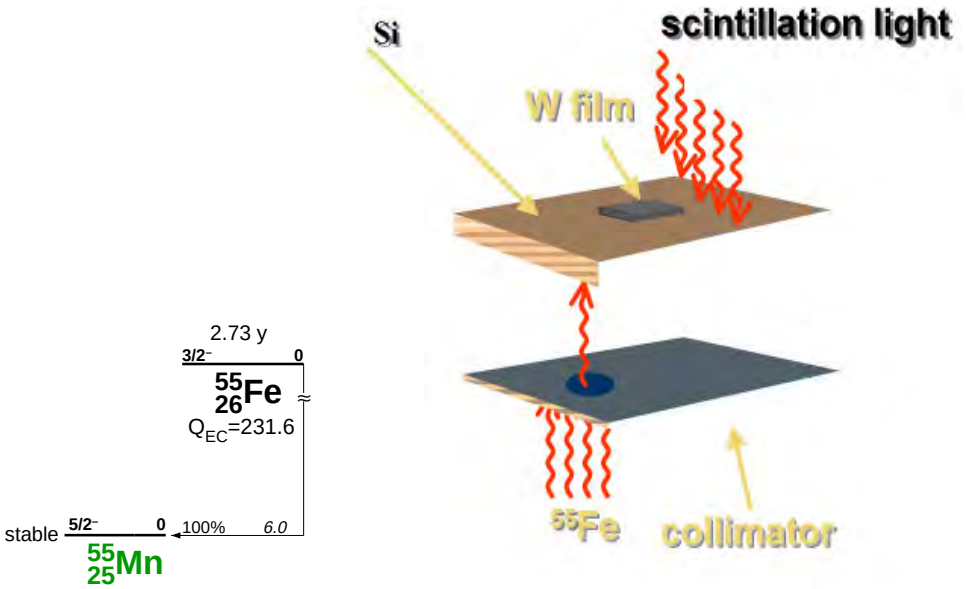

Figure 6.1: *Left*: ^{55}Fe decay scheme. This isotope has a half-life of 2.73 years and decays via electron capture into stable ^{55}Mn, emitting manganese K_α and K_β X-rays of energy 5.9 keV and 6.5 keV, respectively. Figure taken from [30]. *Right*: Sketch of the irradiation scheme of a light detector during the light yield measurements.

of the dilution refrigerator with a copper wire. In order to maximize the amount of the detected scintillation light the setup is surrounded by a highly reflecting cavity of VM2002 foil.

For the absolute energy calibration of the light detector an ^{55}Fe X-ray source with an activity of $\sim$ 10 kBq is installed inside of the cryostat. It illuminates the light detector in one single spot (ϕ0.5 mm) using a collimator positioned close to the light detector at a distance of $\sim$ 15 mm; see sketch in Figure 6.1. In order to induce scintillation, the crystal under test is irradiated with 59.5 keV photons from an external ^{241}Am source. The absolute amount of the scintillation light detected by the light detector for each 59.5 keV photon is used to calculate the scintillation light yield of the crystal.

Since measurements are performed in an unshielded cryostat at ground level, the rate of cosmic-ray particles per unit area is rather high. Due to the high count rate, it is very challenging to stabilize and to operate the sensitive light detectors together with big scintillating crystals of the standard CRESST-II dimensions. Therefore, only $(20 \times 10 \times 5)$ mm^3 or smaller crystal samples have been tested in the Munich setup.

Figure 6.2: *Left*: (20 × 10 × 5) mm^3 $CaMoO_4$ sample mounted in a holder. The crystal is held by two pairs of copper clamps covered with an aluminum tape. *Middle*: Silicon light detector BE11 mounted in a copper holder which is surrounded by a teflon ring. The detector is held by four thin teflon pegs. *Right*: Silicon–on–sapphire light detector HANS mounted in a copper holder which is also surrounded by a teflon ring. The detector is held by three copper clamps covered with a layer of sputtered aluminum. The bond wires for the electrical contact are visible.

Detector module with the $CaMoO_4$ crystal

The left panel of Figure 6.2 shows a picture of the (20 × 10 × 5) mm^3 $CaMoO_4$ sample mounted on the holder used in the measurement. The light yield of this crystal at room temperature was measured to be 3.8 times lower than that of the reference $CaWO_4$ crystal of the same dimensions; see the right panel of Figure 5.20. The comparative measurements were performed with the PMT setup in a (20 × 10 × 5) mm^3 plastic crystal holder whose walls were covered by the reflector (see Section 5.6.4 for more details). In order to improve the scintillation output of the crystal it was annealed at 800 °C in oxygen flow for 48 hours before the low temperature test. The influence of this thermal treatment on the scintillation efficiency of the $CaMoO_4$ sample is presented in Figure 5.20 (left). Additionally, the (20 × 10) mm^2 surface of the crystal was roughened with boron carbide powder. The roughened surface was facing the light detector during the measurement.

For the detection of the $CaMoO_4$ scintillation light we used the silicon light detector BE11; see middle panel in Figure 6.2. It is based on a (30 × 30 × 0.45) mm^3 silicon wafer with a 20 nm SiO_2 layer on both surfaces. The transition from normal to superconducting state of the W-SPT deposited on the wafer occurs around 20 mK. The detector was stabilized at a few tens of a μK below the top of its transition via the heater structure of the thermometer while applying a constant bias current of 3.5 μA.

Detector module with the $ZnWO_4$ crystal

A $(20 \times 10 \times 1)$ mm^3 $ZnWO_4$ crystal with all surfaces polished to optical quality was tested. The light yield of this sample at room temperature was measured to be 107 % relative to the $CaWO_4$ sample of the same dimensions.

During the test, silicon light detectors were not available. Therefore, the silicon-on-sapphire light detector HANS, shown in the right panel of Figure 6.2, was used. This detector is based on a 40 mm in diameter and ~0.46 mm thick sapphire substrate with a ~1 μm layer of silicon. The transition of the W-SPT occurs around 25 mK. The detector was stabilized several tens of a μK below the top of its transitions via the heater structure of the thermometer while applying a constant bias current of 6 μA.

6.3 Results

Besides being exposed to background radiation, the light detectors are irradiated with manganese X-rays and scintillation light coming from the test crystal. Whereas the energy input into the light detector in form of X-rays and background radiation is instantaneous, the scintillation light arrives over a certain time interval, reflecting the time response of the crystal. This results in different pulse shapes for different event classes. Figure 6.3 shows an energy versus rise time scatter plot for the events recorded with BE11 under irradiation with manganese X-rays and scintillation light from the $CaMoO_4$ sample. Two classes of events clustered in bands are clearly distinguishable. The upper band corresponds to the absorption of the $CaMoO_4$ scintillation light in the light detector. The lower band corresponds to the absorption of background radiation and X-rays (these events are called direct hits).

For each class of events a template is made by averaging many measured pulses of the given type. They are selected in the linear region of the detector response. In order to illustrate the time response of light detectors BE11 and HANS, Figure 6.4 shows templates obtained for direct hit events (solid lines) and templates for events caused by the scintillation light (dashed lines). In both cases a longer rise time is observed for pulses caused by the collection of scintillation light.

Comparison of the pulse heights of the 5.9 keV X-rays with heater pulses of similar energy provides an absolute calibration for the voltage of the heater pulses in terms of energy. The calibration is transfered to lower energies by using the heater test pulses.

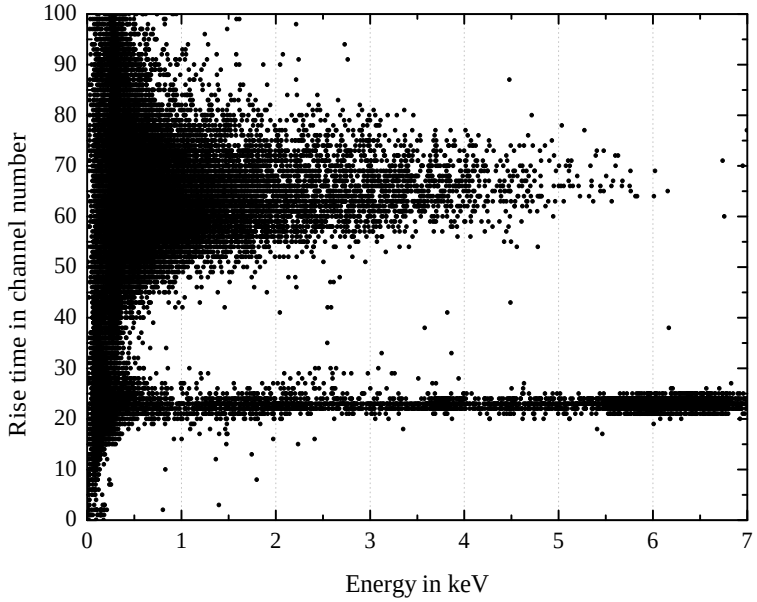

Figure 6.3: Energy versus rise time scatter plot recorded with the silicon light detector BE11 under irradiation with manganese X-rays and scintillation light coming from the ($20 \times 10 \times 5$) mm^3 $CaMoO_4$ crystal. The rise time is measured from the pulse onset to its maximum. The crystal is excited by 59.5 keV photons from an external ^{241}Am source. The upper band in the peak position corresponds to the absorption of the $CaMoO_4$ scintillation light in BE11. The lower band corresponds to the absorption of X-rays and direct background hits in the light detector.

6.3.1 Light yield of $CaMoO_4$

Figure 6.5 shows the energy spectrum measured by the silicon light detector BE11 facing the $CaMoO_4$ sample. Characteristic manganese K_α and K_β lines together with the sharp photopeak at (0.286 ± 0.001) keV caused by the absorption of the $CaMoO_4$ scintillation light (induced by 59.5 keV photons) are visible on the top of the background. The energy resolution of the silicon light detector BE11, estimated as the FWHM of the 5.9 keV line, is ~ 5 %. The energy resolution of the ^{241}Am photopeak is ~ 63 eV.

Only about 0.48 % of the energy deposited in the $CaMoO_4$ crystal by 59.5 keV photons is observed in form of scintillation light in the light detector at ~ 20 mK. Taking into account that the maximum intensity of the emission spectrum of $CaMoO_4$ crystals is at ~ 520 nm (~ 2.38 eV), this translates the obtained scintillation peak position of 0.286 keV into ~ 120 photons per 59.5 keV. Assuming that towards higher energies the relation between energy input into the crystal by γ's and its scintillation light output is linear, about 2000 scintillation photons can be detected at 1 MeV.

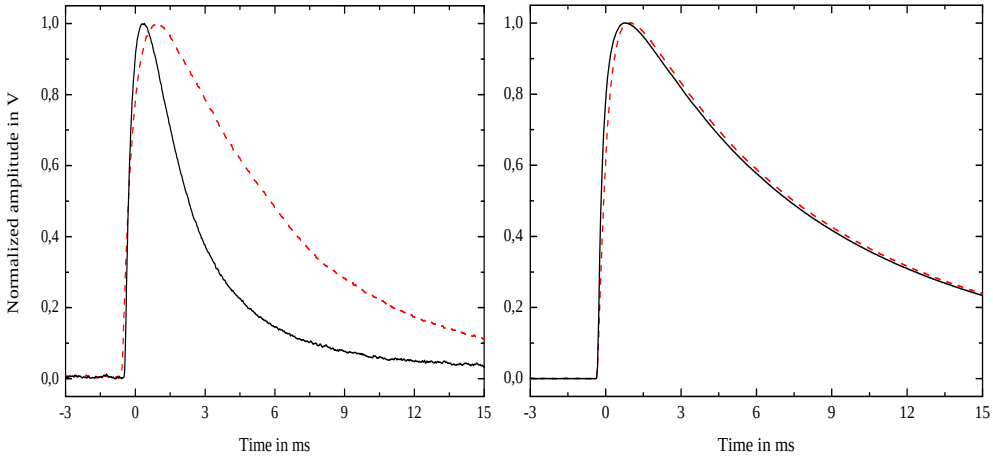

Figure 6.4: *Left*: Pulse templates for direct hit events (solid line) and $CaMoO_4$ scintillation light events (dashed line) recorded with detector BE11. *Right*: Pulse templates for direct hit events (solid line) and $ZnWO_4$ scintillation light events (dashed line) recorded with detector HANS.

6.3.2 Light yield of $ZnWO_4$

The top panel of Figure 6.6 shows the background energy spectrum measured by detector HANS facing the $ZnWO_4$ sample. A very good energy resolution of ~ 2 % at 5.9 keV was measured with this silicon-on-sapphire light detector. It is almost 2.5 times better than that measured with detector BE11 at the same energy. The fact that the transition of the W-SPT on the detector HANS is very broad in temperature explains the good sensitivity of this detector to large energy depositions of ~ 6 keV. The structure below 5.5 keV is caused by direct absorption of background radiation and by $ZnWO_4$ scintillation light induced by absorption of background radiation in the detector HANS. When the external ^{241}Am source is present, a broad peak at (1.257 ± 0.007) keV appears on the top of the background; see the bottom panel of Figure 6.6. It is caused by the absorption of the $ZnWO_4$ scintillation light induced by 59.5 keV γ's. The energy resolution of the scintillation peak is ~ 295 eV.

With the $ZnWO_4$ crystal ~ 2.1 % of the energy after absorption of 59.9 keV γ's were detected. Taking into account that the maximum intensity of the emission spectrum of $ZnWO_4$ crystals at low temperatures is at ~ 510 nm (~ 2.43 eV) [49], this translates the $ZnWO_4$ scintillation peak position of 1.257 keV into ~ 517 scintillation photons per 59.5 keV. Therefore, at least ~ 8690 photons per 1 MeV can be detected if we assume that the dependence of the $ZnWO_4$ scintillation response to the absorbed energy is linear. As this is about 4 times higher than for the BE11/$CaMoO_4$ pair, one would expect the energy resolution of the Am photopeak recorded with the detector HANS to be much better than the observed

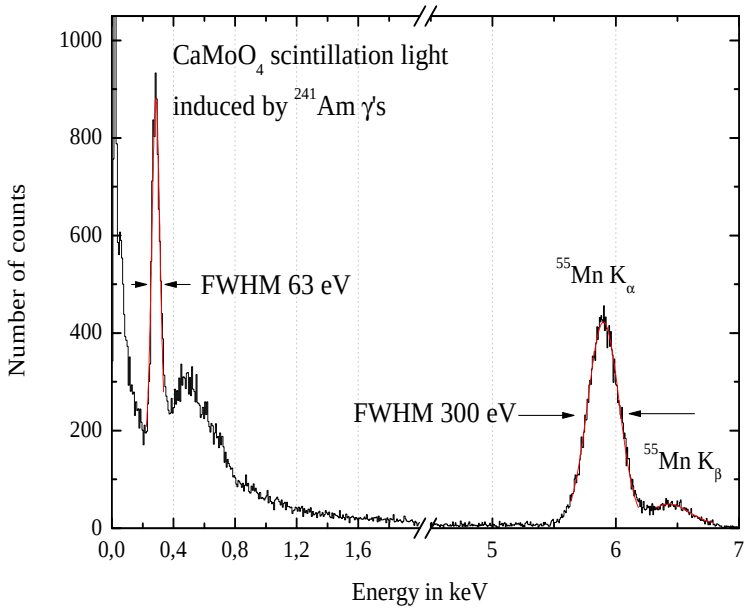

Figure 6.5: Energy spectrum measured at ~ 20 mK by detector BE11 facing the $CaMoO_4$ sample. A sharp peak at (0.286 ± 0.001) keV on the top of the background is caused by the absorption of the $CaMoO_4$ scintillation light induced by 59.9 keV photons from an ^{241}Am source. Characteristic manganese X-ray lines at (5.900 ± 0.001) keV and (6.43 ± 0.01) keV are visible. Gaussian fits are superimposed. See text for details.

one.

Non-uniform light collection in the detector module with the non-roughened $ZnWO_4$ sample may be a source for broadening of the photopeak structure. A measurement to check the influence of the $ZnWO_4$ surface roughening on the light collection uniformity within the same detector module has still to be carried out.

6.3.3 Scintillation decay time constants

Another important property of a crystal is the duration of its scintillation emission (τ_{scint}) after excitation. As already mentioned in Chapter 4, τ_{scint} is governed by the kinetics of the scintillation process. It is related to the time variation of the number of luminescence centers. For crystals which have more than one type of luminescent center, the time variation of the scintillation emission intensity $I(t)$ is often described by a series of exponentials with different decay time constants,

$$I(t) = \sum_i \frac{(N_{ph})_i}{\tau_i} \exp\left(-\frac{t}{\tau_i}\right), \tag{6.3}$$

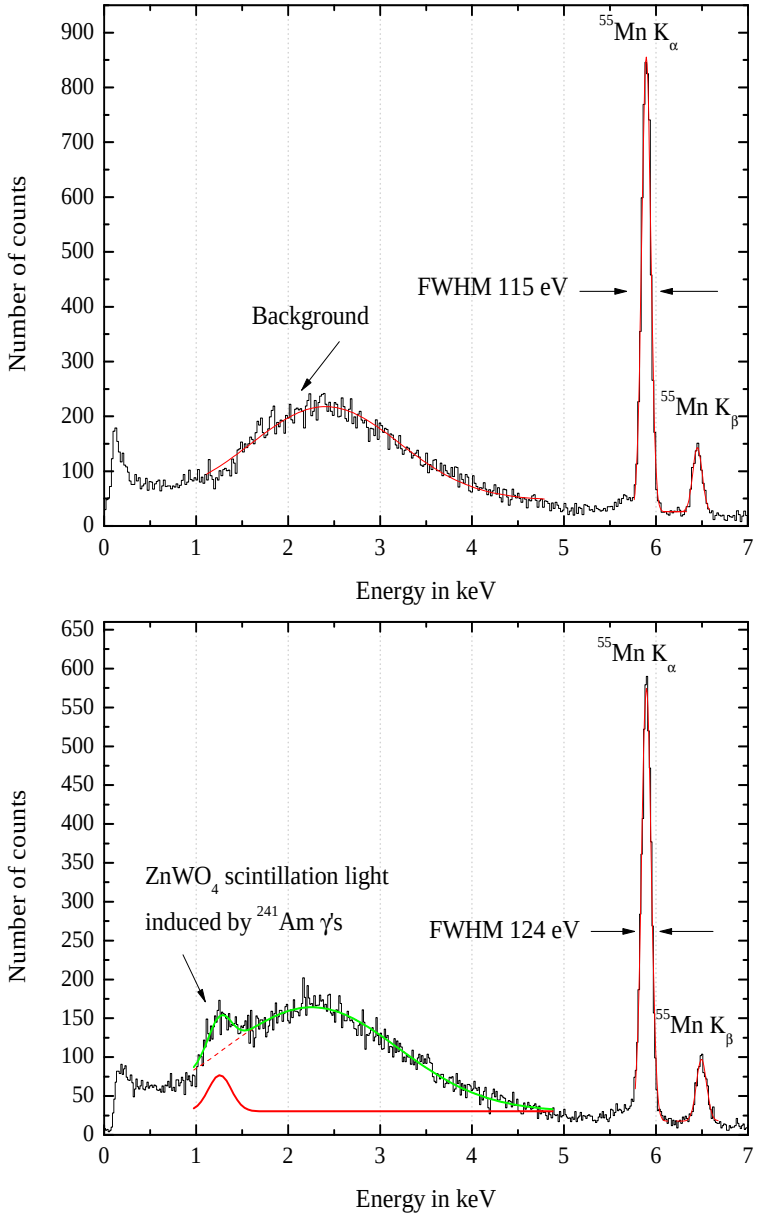

Figure 6.6: *Top*: Background energy spectrum measured at ~ 25 mK by detector HANS facing the $ZnWO_4$ sample. Characteristic manganese K_α and K_β lines at (5.895 ± 0.008) keV and (6.494 ± 0.006) keV are visible. The structure below 5.5 keV is caused by the absorption of background radiation. *Bottom*: Energy spectrum measured at ~ 25 mK by detector HANS facing the $ZnWO_4$ sample. The peak at (1.257 ± 0.007) keV visible on the top of the background is caused by the absorption of the $ZnWO_4$ scintillation light induced by γ's from an ^{241}Am source placed outside the cryostat. Gaussian fits are superimposed.

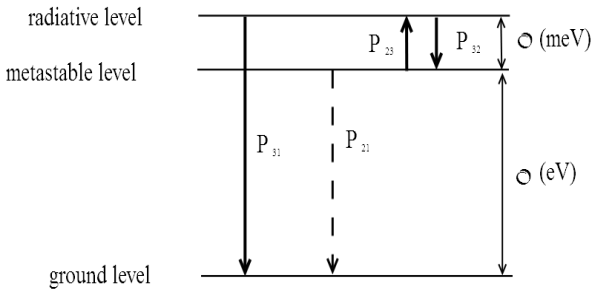

Figure 6.7: Three level scheme of ABO_4 trinity crystals used to explain an increase in the scintillation decay time constant at low temperatures. The energy gap between the radiative level and the metastable level is a few meV. The various P's are the probabilities of the transitions between the levels.

where $(N_{ph})_i$ is the number of photons emitted within the decay time component τ_i of the i-th type of the luminescent center [72].

The scintillation decay time constants for the main intrinsic emission of $CaWO_4$, $CaMoO_4$, and $ZnWO_4$ crystals have been measured at 300 K by various authors; see Table 5.1. The decay time constant of $CaWO_4$ crystals at mK temperatures is reported to be ~ 400 μs [137, 138]. The integration time of the CRESST-II light detectors is adjusted for the detection of $CaWO_4$ scintillation light. For $CaMoO_4$ and $ZnWO_4$ the temperature dependence of τ_{scint} from room temperature to temperatures of $\sim$ 4 K was recently studied in [128, 133, 52, 139, 140]. However, no data on the time constants of $CaMoO_4$ and $ZnWO_4$ crystals at temperatures below 30 mK were found. Therefore, a dedicated analysis in order to determine the time characteristics of the mentioned crystals was performed. The results of the analysis are summarized in Table 6.1.

Temperature dependence

Decreasing the temperature of a crystal leads to a prolongation of its scintillation decay time constants. It is thought that spin-orbit splitting[1] of the radiative $^3T_1$ level in scheelites and the $^3T_{1u}$ levels in wolframites is responsible for the prolongation of the emission time τ_{scint} at low temperatures [141]; see Figure 5.11. To understand this, let us consider the diagram in Figure 6.7. The energy structure of a luminescent center may contain the metastable energy level just a few meV below the radiative energy level. Transitions from the metastable to the ground state are thought to be forbidden. At temperatures higher than 50 K, the energy gap of a few meV is small compared to the kinetic energy of electrons. Both

[1]Spin-orbit splitting can be due to the perturbations caused by the inter-ionic bonding [43].

levels are equally populated, so that excited electrons can go to the ground state via the radiative transition from the radiative to the ground level.

At low temperatures the probability of excitation from the metastable to the radiative level P_{23} is suppressed because the kinetic energy of the electrons is small compared to the energy gap. Hence, the radiative level is de-populated, and relaxation to the ground state is significantly suppressed. This slows down the entire scintillation emission process. Therefore, scintillation decay time constants of crystals at mK temperatures may be much larger than at room temperature.

Discussion

Due to the different time characteristics seen in the light detector between two classes of events, namely, the class of faster direct light detector hits and the class of slower events caused by scintillation light coming from the crystal, the light emission curve of $CaMoO_4$ and $ZnWO_4$ crystals can be deduced. Assuming that the shape of pulses in the linear region of the light detector response is energy independent, a scintillation photon (similar to a direct hit event) would be instantaneously absorbed in the light detector but be scaled down in energy. Thus, the scintillation light pulse can be thought of as a convolution of the direct hit pulse and the light emission curve of the crystal. The latter can then be obtained via deconvolution of the pulse templates for scintillation light and direct hits using fast Fourier-transformation. In order to prepare a data sequence for the analysis in Fourier space the onset of each template (found with the help of the fitting Equation 2.9) was moved to time zero, the pre-trigger region was omitted, and templates of equal length were selected. Additionally, data sets were padded with zeros in order to obtain periodic data samples.

The convolution theorem states that a convolution in the time domain corresponds to multiplication in the frequency domain. Thus, dividing the Fourier spectrum of the scintillation template by the one of the direct hit template results in the Fourier spectrum of the light emission curve. Accordingly, the amplitude of its inverse Fourier transform then gives the time evolution of the light emission curve of the crystal. The emission curves of the $ZnWO_4$ and the $CaMoO_4$ samples obtained with the procedure described above are presented in Figure 6.8.

The best fit of the $CaMoO_4$ crystal scintillation decay curve is achieved by using a sum of a single exponential function (according to Equation 6.3) and a constant offset y_0. At a temperature around 20 mK the rather slow decay time constant of this material is measured to be ~ 340 μs.

The scintillation decay spectrum of the $ZnWO_4$ crystal is fitted by a function which is a sum of two exponentials plus a constant offset y_0. The values of the decay time constants of this sample are given in Table 6.1. Around 25 mK the largest decay time constant of the $ZnWO_4$ crystal is almost two times smaller

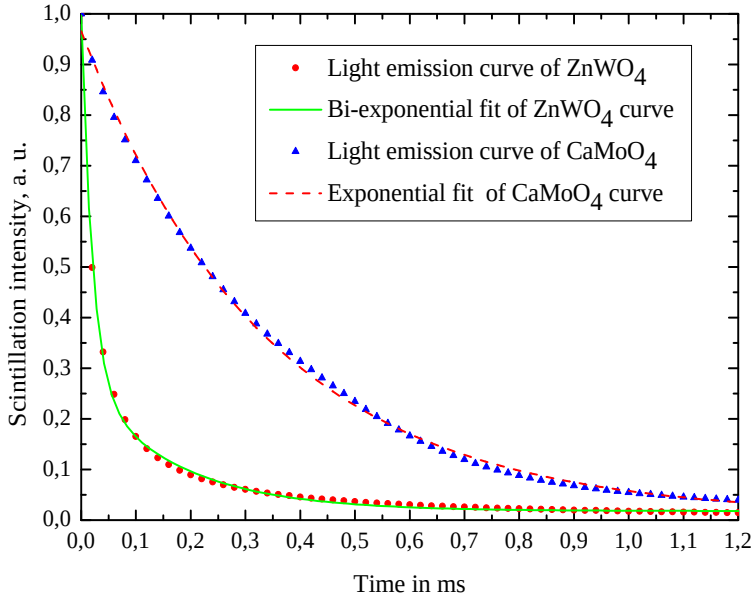

Figure 6.8: Light emission curve of the $ZnWO_4$ crystal (circles) and the $CaMoO_4$ crystal (triangles) obtained via numerical deconvolution of the templates for direct hits and scintillation pulses. The $ZnWO_4$ and $CaMoO_4$ data points are fitted with bi-exponential and single exponential functions, respectively. See main text for details.

Crystal	Temperature in K	A_1 in %	τ_1 in μs	A_2 in %	τ_2 in μs
$CaMoO_4$	0.02	100	338 ± 4	-	-
$ZnWO_4$	0.025	25 ± 1	20.3 ± 0.5	75 ± 1	170 ± 6

Table 6.1: Scintillation decay time constants of $CaMoO_4$ and $ZnWO_4$ crystals obtained below 25 mK.

than that of $CaWO_4$, being only ~ 170 μs.

6.3.4 Energy dependence of the $ZnWO_4$ scintillation response

A constant scintillation efficiency implies that a scintillator is "proportional", meaning that the amount of scintillation light is proportional to the energy deposited in the crystal. The deviation from a constant scintillation efficiency is referred to as **non-proportionality**.

Figure 6.9 shows measurements of the scintillation efficiency versus electron energy for different scintillators [142]. The general shape of the electron response curves is very similar in almost all crystals. The scintillation efficiency is rising with increasing energy and then leveling off or decreasing slightly. In the case of

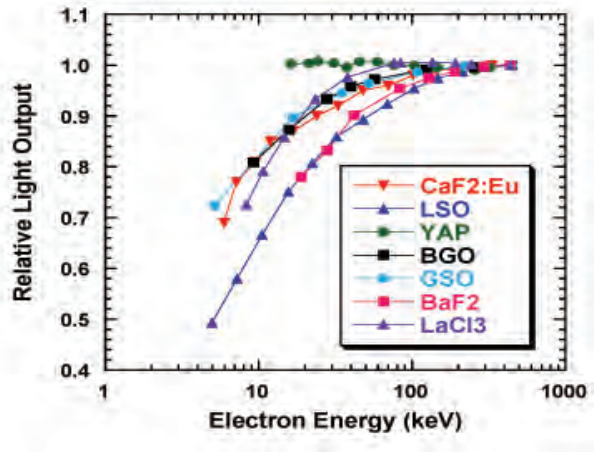

Figure 6.9: Electron energy response (relative light output is normalized to the value at 662 keV) for various scintillators. The response of the ideal scintillator would be independent of the electron energy. Figure taken from [142].

$ZnWO_4$ crystals no deviations from a linear behavior was observed at energies above 150 keV; see Figure 5.19. However, the analysis of the data recorded with a small $ZnWO_4$ phonon detector[2] shows that below 150 keV the scintillation efficiency of the $ZnWO_4$ crystal is not constant; see Figure 6.10. A similar behavior has recently been reported for $CaWO_4$ crystals [27].

At energies below $\sim$ 100 keV the shape of the measured scintillation response curve can potentially be explained with the help of Birk's equation. However, due to the difficulty to disentangle a possible non-proportionality of the response caused by electrons from the response caused by photons (the crystal was simultaneously irradiated by β/γ-particles) and due to the probable position dependency of the light output,[3] no attempt to apply Birk's equation combined with the ionisation density in order to explain the shape of the obtained curve has been performed. Most probably, the shape of the $ZnWO_4$ light curve is the combination of these three effects.

In summary, scintillator non-proportionality has been studied both experimentally and theoretically for more than 50 years [144, 145, 146, 147, 142]. Nevertheless, the origins of the non-proportionality are yet not well understood and even their implications are not completely clear [148]. The present consensus is that the origin of the non-proportionality lies in the scintillation efficiency of a crystal which itself depends on the energy of the particle that excites it.

[2]Data were obtained in [143].

[3]Due to the conditions of the W-SPT deposition on the $ZnWO_4$ crystal surface layers with lower light yield could have been formed.

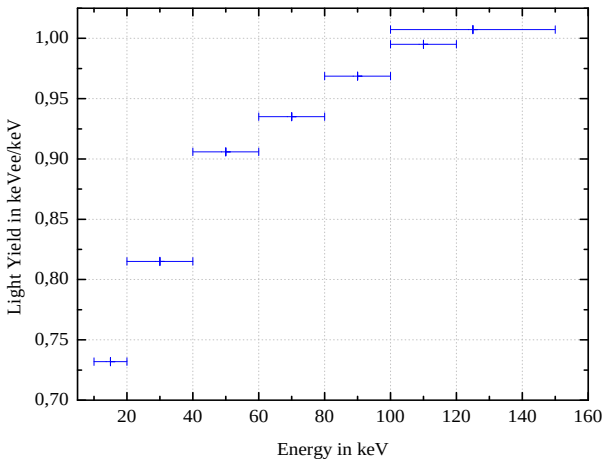

Figure 6.10: Response to electron recoils caused by absorption of β/γ-particles in the ($20 \times 10 \times 5$) mm^3 $ZnWO_4$ crystal measured at $\sim$ 20 mK with the help of a silicon light detector. The y-axis measures the scintillation efficiency in keV$_{ee}$ per keV normalized to the one at 122 keV as a function of energy. Several tens of events are taken together as one energy bin. The mean values of Gaussian fits (applied to each energy interval) are shown. A non-proportionality of the scintillation efficiency below $\sim$ 150 keV is clearly visible.

6.4 Conclusions

The scintillators measured so far in a CRESST-II like setup at mK temperatures are $Bi_4Ge_3O_{12}$ (BGO), Ba_2F, Al_2O_3(Ti), $PbWO_4$, $CaWO_4$, $ZnWO_4$, and $CaMoO_4$ [42, 45, 137]. In Table 6.2 the absolute amounts of energy detected by the light detectors after interaction of γ-particles of a certain energy with some of these crystals are shown. The given numbers are detected energies and they are not corrected for light detector efficiency and light collection efficiency which vary for different scintillators because of their different refraction indices and emission spectra. Taking into account the parameters of the various setups listed in Table 6.2, in average 1.2 % of the deposited energy in $CaWO_4$ can be observed in form of scintillation light.

Though the choice of a silicon-on-sapphire light detector was not optimal for the measurement with the $ZnWO_4$ sample, almost two times more scintillation light was detected from this sample compared to the amount from $CaWO_4$. Indeed, this is the largest amount of scintillation light detected among the various scintillating crystals tested up to now. The number of detected scintillation photons is expected to be even larger when using a silicon light detector, and roughening of the $ZnWO_4$ surface facing the light detector should further increase the amount of detected scintillation light and make the light collection more uniform.

Due to multiple problems with the cryostats, the attempts to operate detectors were not successful for a long time. In the course of this work this represented an important limitation on the number of tests performed for the investigation of the sensitivity of different light detectors to the detection of scintillation light from $ZnWO_4$ and $CaMoO_4$ crystals at mK temperatures. Therefore, further studies are needed in this respect.

Overall, the measurement with the $ZnWO_4$ crystal from NIIC revealed its high scintillation potential at mK temperatures. On the other hand, measurements with the $CaMoO_4$ sample have shown that its light yield at low temperature is approximately 2.5 times worse than that of $CaWO_4$. Additional R&D should be carried on the producers side in order to further improve scintillation properties of this material.

Light detector	Crystal	Detected light, ε in %
silicon, W-SPT (30 × 30) mm^2	$CaMoO_4$ (20×10×5) mm^3	0.48
silicon, W-SPT (30 × 30) mm^2	$ZnWO_4$ (20×10×5) mm^3	1.4
SOS, W-SPT ϕ 40 mm	$ZnWO_4$ (20×10×1) mm^3	2.1
silicon, W-SPT (30 × 30) mm^3	$CaWO_4$ ϕ 40 mm × 40 mm	1.3 [137]
silicon, Ir/Au-SPT (20 × 20) mm^2	$CaWO_4$ ϕ 20 mm × 20 mm	1.7 [149]
silicon, Ir/Au-SPT (20 × 20) mm^2	$CaWO_4$ ϕ 20 mm × 5 mm	1.9 [149]
silicon, W-SPT (20 × 20) mm^3	$CaWO_4$ (20×10×5) mm^3	0.55 [60]
SOS, W-SPT ϕ 40 mm	$CaWO_4$-VERENA ϕ 40 mm × 40 mm	1.1
SOS, W-SPT (20 × 20) mm^3	$CaWO_4$ (20×10×5) mm^3	0.5 [60]
SOS, W-SPT (20 × 10) mm^2	$CaWO_4$ (20×10×5) mm^3	0.33 [42]
SOS, W-SPT (20 × 10) mm^2	BGO (20×10×5) mm^3	0.35 [42]
silicon, W-SPT (30 × 30) mm^2	Al_2O_3 (Ti) (20×10×5) mm^3	1.3 [45]

Table 6.2: Measurements of the absolute amount of energy deposited in the light detector following a particle interaction in the scintillating crystal performed at mK temperatures.

Chapter 7

Fabrication of phonon detectors

In order to have the possibility to integrate new target materials into the modular structure of the experiment, one first has to perform R&D on the production of phonon detectors on their basis. This includes finding the parameters for the production of tungsten superconducting phase transition thermometers (W-SPT) with the desired characteristics. As discussed in Section 3.1, the shape and the steepness of the thermometer transition curves determine the sensitivity, the dynamical range, and the linearity of the detector response. Steep and narrow transition curves with critical temperatures below 20 mK are needed. The CRESST-II collaboration developed a reliable technique to grow W-films on $CaWO_4$ crystals [40, 25, 17]. Due to the structural differences between $CaWO_4$ and the crystals under study, this technique has to be tuned in order to grow W-films on $CaMoO_4$ and $ZnWO_4$.

This chapter reports on the fabrication of the first phonon detectors based on $CaMoO_4$ and $ZnWO_4$ crystals. In particular, the gluing technique for the production of $ZnWO_4$ phonon detectors with a separate thermometer carrier is investigated. Results of the first low temperature tests are presented.

7.1 $CaMoO_4$ detector

For preventing an inter-diffusion between the tungsten film and the $CaMoO_4$ crystal surface, a 2 kÅ layer of SiO_2 is deposited first. In order to achieve good adhesion between the SiO_2 layer and the crystal surface, the area below the thermometer is roughened on an atomic level with an ion-gun prior to the SiO_2 deposition which takes place at 450 °C. The crystal is heated up to this temperature with a small gradient (the ramping speed is 75 °C per hour). Then, a 2 kÅ layer of tungsten is evaporated onto the crystal at the same temperature with a rate of 2 Å/s. The structuring of the deposited film follows the procedure

Figure 7.1: Photograph of detector $CaMoO_4$-1 mounted in the holder for the transition measurements. The bond wires for the electrical contacts to the readout circuit are visible.

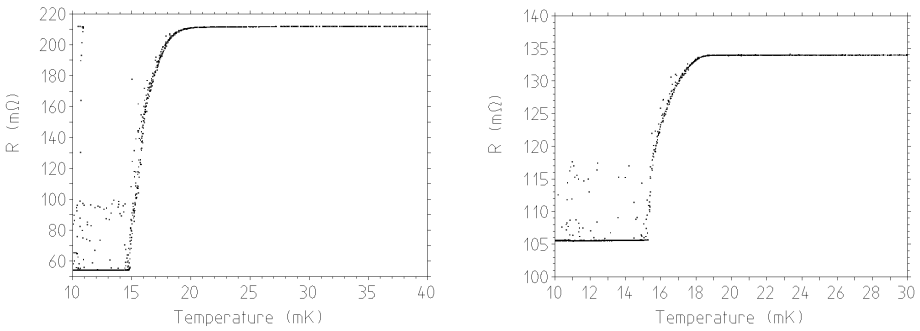

Figure 7.2: Transition curve of the tungsten-film measured with detector $CaMoO_4$-1 (left) and detector $CaMoO_4$-2 (right). Both transition curves are recorded with a 1 μA bias current applied through the readout circuit while cooling the cryostat to its base temperature.

described in Section 5.3.1. Figure 7.1 shows the $CaMoO_4$-1 crystal with the structured thermometer deposited on its surface.

Transition curves obtained with the tungsten-films produced on the two different $CaMoO_4$ crystals are presented in Figure 7.2. Both curves have a steep and narrow shape with a critical temperature around 18 mK and a width of a few mK. Normal-conductivity resistances of ~ 210 mΩ and ~ 130 mΩ have been measured while applying 1 μA bias current. The nonzero (residual) resistance of the films in the superconducting regions is caused by imperfect contacts to the readout circuit. The obtained characteristics satisfy the quality requirements of the films for the phonon detectors.

Figure 7.3: Photograph of the $(20 \times 10 \times 1)$ mm^3 $ZnWO_4$ wafer mounted into a tantalum holder for the tungsten-film deposition.

The thermal response of detector $CaMoO_4$-1 (stabilized in the normal-to-superconducting state) has shown promising results. However, due to the high count rate on ground level no calibration spectrum could be recorded.

7.2 $ZnWO_4$ detector with glued thermometer

The research performed in [143] has shown that high deposition temperatures (T_D > 700 °C) are needed in order to obtain transition temperatures of W-films grown on small $ZnWO_4$ samples below 20 mK. Heating up $ZnWO_4$ crystals to such high temperatures in vacuum degrades their scintillation property. Therefore, the direct evaporation of W-films on large $ZnWO_4$ crystals should be avoided. For that, the detector design with the separate thermometer carrier has been investigated[1].

Thermometer production

In order to grow a tungsten-film on a small $ZnWO_4$ wafer the latter is mounted in the deposition system (see Figure 7.3) where it is slowly heated up to 600 °C and kept at this temperature during the whole deposition process. A 2 kÅ layer of SiO_2 is deposited first. Then, a 2 kÅ layer of tungsten is evaporated. $ZnWO_4$ crystals are very brittle due to their marked cleavage and are prone to crack formation when large temperature gradients occur. Therefore, putting a $ZnWO_4$ crystal onto hot/cold surfaces or into cold liquids during the thermometer struc-

[1]The concept of the glued phonon detectors is introduced in Section 2.3.4

turing process has to be avoided. An oven, instead of a hot plate, should be used when needed.

An example of the transition curve of the tungsten thermometer deposited on a $ZnWO_4$ wafer as described above is shown in Figure 3.1. Transition curves deposited on $ZnWO_4$ crystals often show substructures (kinks). They may be explained by inhomogeneities of critical temperature across the film. When cooling down to mK temperatures some locally confined islands of the film become superconducting first. Then, these islands eventually connect to provide a superconducting path between the electrical contacts. Each time an island gets superconducting, the total resistance drops by a certain amount. This leads to the observed structures in the transition curve.

Tungsten-films which were recently grown on different $ZnWO_4$ wafers have shown similar properties: transition below 20 mK, width of ~ 1 mK, and presence of substructures. The substructures may degrade the linearity of the detector response. Nevertheless, since it was possible to measure reasonable spectra while stabilizing the $ZnWO_4$ phonon detectors close to the top of their transition curves (see Chapter 8), it can be concluded that the characteristics of the W-films satisfy the quality requirements for the phonon detectors.

Thermometer gluing

The second step in the production of a $ZnWO_4$ phonon detector is gluing of the thermometer carrier to the main target crystal. Since $ZnWO_4$ crystals tend to easily cleave along the (0 1 0) crystallographic plane, the influence of the glue layer on the surface properties of this material has been investigated first. For that, two different glues, namely, Araldite 2011 and Epo-Tek 301-2[2], and two different thermometer carrier crystals, namely $CaWO_4$ and $ZnWO_4$, were tested. In each test, a $CaWO_4$ or $ZnWO_4$ wafer was glued with a certain glue type onto a large $ZnWO_4$ crystal (ϕ 40$\times$ 10 mm^2). This composite structure was then cooled down to mK temperatures; see Figure 7.4.

Only with Epo-Tek 301-2[3] the quality of the crystal surfaces remained unchanged, whereas cracks were observed in the case of gluing with Araldite 2011; see Table 7.1. Though both wafers ($ZnWO_4$ and $CaWO_4$) glued onto the $ZnWO_4$ crystal with Epo-Tek 301-2 have shown reasonable surface quality after the tests at mK temperatures, it was decided to use the $ZnWO_4$ wafers as thermometer carriers for the $ZnWO_4$ phonon detectors. This is because $ZnWO_4$ wafers and large $ZnWO_4$ crystals have the same crystal structure and the same crystallographic orientation. Thus, the amount of stress which may originate from

[2] Araldite 2011 is a registered trademark of Huntsman Corporation. Epo-Tek 301-2 is a registered trademark of Epoxy Technology.

[3] Epo-Tek 301-2 is a two components epoxy mixed in the ratio of 100 parts of resin to 35 parts of catalytic hardener. It has a density of 0.95 g/cm^3, an index of refraction of about 1.53 at 589 nm, and is suitable for cryogenic applications [150].

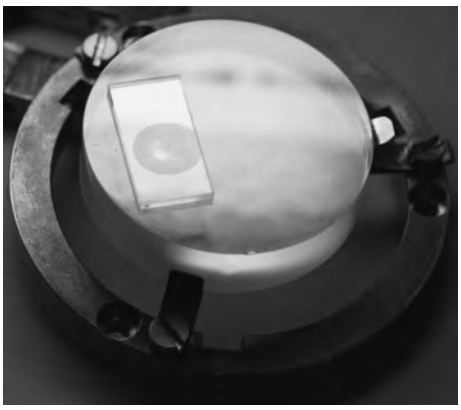

Figure 7.4: Photograph of the $ZnWO_4$-1 crystal with a $ZnWO_4$ wafer glued onto its surface with help of Araldite 2011 glue after the low temperature test.

	$CaWO_4$ wafer $(20 \times 10 \times 1)$ mm^3	$ZnWO_4$ wafer $(20 \times 10 \times 1)$ mm^3
Epo-Tek 301-2	+	+
Araldite 2011	-	-

Table 7.1: Gluing of different thermometer carriers onto a $ZnWO_4$ crystal. After cooling to mK temperatures, the surface quality of some crystals remained unchanged (+), whereas a degradation was observed for others (-).

the thermo-mechanical mismatch between two different materials or their thermal expansion incompatibility in different crystallographic directions during the temperature change is expected to be small.

Figure 7.5 shows the photograph of the prototype $ZnWO_4$ phonon detector. The $(20 \times 10 \times 1)$ mm^3 $ZnWO_4$ thermometer carrier with (0 1 0) plane parallel to the (20×10) mm^2 surface is glued with Epo-Tek 301-2 on the (ϕ 40 $\times$ 40) mm^2 $ZnWO_4$ crystal with (0 1 0) plane parallel to its flat surface. The area of the glue is ~ 40 % of the thermometer area and its mass is (0.06 ± 0.01) mg. This translates to an average thickness of ~ 3 μm. For the possible optimization of detector design, a detailed understanding of the signal evolution is needed. General conclusions in this respect will be drawn in the following chapter.

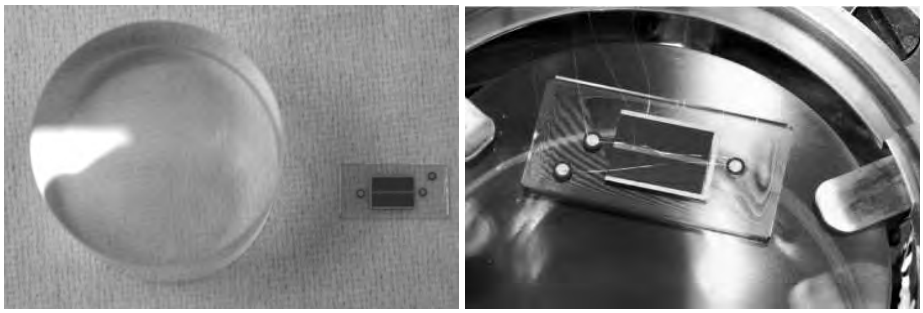

Figure 7.5: *Left*: Photograph of the cylindrical $ZnWO_4$-4 crystal and the $ZnWO_4$ wafer with the W-SPT deposited onto its surface before gluing. *Right*: Photograph of the prototype $ZnWO_4$ phonon detector with the glued thermometer mounted in the copper holder for Run 31. The crystal is held by six pairs of bronze clamps coated with an Al layer and with an Araldite 2011 scintillating layer. The whole structure is surrounded by a highly reflecting foil VM2002. The bond wires for the electrical contacts are visible.

Chapter 8

Measurements with $ZnWO_4$ detectors at Gran Sasso

In spring 2008 the first detector module with a phonon detector based on a $ZnWO_4$ crystal was integrated into the main CRESST-II experimental setup at Gran Sasso. During the cool down Run 31 the developed $ZnWO_4$ detector was operated for the first time. Besides allowing for investigation of the novel detector design, the data taken with this detector made a detailed study of radioactive contaminations present in the $ZnWO_4$ crystal possible. The obtained results reveal a high radiopurity of the phonon detector under study. This has motivated the installation of a second $ZnWO_4$ phonon detector in the setup.

This chapter starts with a brief overview of the experimental environment during Run 31 and Run 32. Afterwards, the investigation of calibration and background spectra obtained with one of the $ZnWO_4$ phonon detectors is presented. In particular, the level of identified radioactive contaminants present in the crystal has been compared with those in $CaWO_4$. Finally, results on the performance of $ZnWO_4$ detectors with glued thermometers are presented with a focus on the pulse shape analysis.

8.1 Experimental environment

The data acquisition system used in Run 31 and Run 32 has been described in Section 2.4. In both runs the operating point of detectors is kept stable via monitoring the pulse heights of the control pulses as it has been described in Section 3.1.3. For details on the data analysis, the reader is referred to Chapter 3.

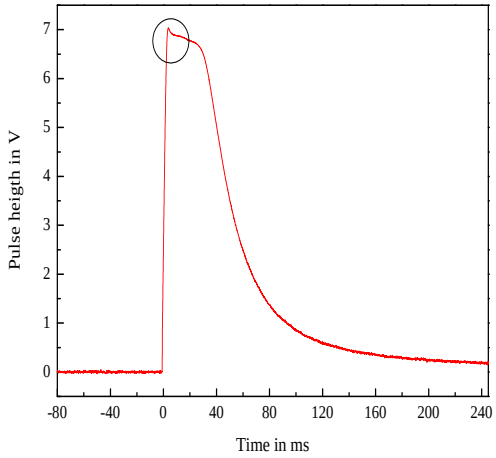

Figure 8.1: Example of a heater test pulse of the highest injected voltage amplitude recorded with $ZnWO_4$-4 during Run 31. A small king on the top of the saturated pulse is caused by an electrical cross talk between the heater current and the readout current. This due to the problem of the open heater line which was present during the operation of the detector.

8.1.1 Run 31

Run 31 took place between April and December 2008 after commissioning of the upgraded CRESST-II experimental setup; see Section 2.2. Nine detector modules have been able to be operated reliably during this run. Unfortunately, the light detector partner of $ZnWO_4$-4 was not operational throughout the run. Additionally, one of the thermometer's electrical contacts to the heater circuit (see Fig 2.10) was open when the cryostat reached its base temperature. This was most probably due to the screwed contacts at the detector holder, where the superconducting wires of the heater circuit are screwed to an electrically insulated Cu-Kapton-Cu pad. With one heater line open, the heating current injected via the other line flows via the Au stripe to the Au wire, serving as thermal coupling. This current flowing perpendicular to the readout current produces an electrical cross talk to the readout circuit via critical current effects. As the amount of cross-talk changes with heater demand, the open heater line affected the stability control of $ZnWO_4$-4. Nevertheless, is was possible to obtain data of reasonable quality which will be presented later on in this chapter.

8.1.2 Run 32

The currently ongoing Run 32 has started in June 2009. In total, eighteen detector modules were mounted in the setup. Five of them are phonon detectors with glued thermometers and two of these are based on $ZnWO_4$ crystals. $ZnWO_4$-4

was faced by the silicon light detector (ULRICH) and $ZnWO_4$-6 by the silicon-on-sapphire light detector (WERNER), each equipped with a weak ^{55}Fe source for the absolute energy calibration.

Due to the problem of the dark (no light) events in the WIMP acceptance region observed with the operational detector modules in Run 31 [151], the crystal holding clamps have been exchanged. In Run 32 crystals are held by thinner and therefore less stiffer bronze clamps coated with a reflecting silver layer. Moreover, all screwed electrical contacts were replaced by soldered ones. In order to avoid contamination of the detectors with lead[1] (often present in soldering alloys) a radiopure lead free tin (Sn) was used instead. The soldering was done using ammonium chloride as flux [152]. Currently, nine detector modules are fully operational and one of them is the $ZnWO_4$-4/ULRICH pair. $ZnWO_4$-6 is also working, while its light detector partner WERNER may still become operational.

8.2 Spectral analysis and background studies

As already mentioned in Section 5.2.2 measuring and classifying radioactive background intrinsic to the detectors is crucial for the development of new target crystals. In general, background rates are so small that they are undetectable by most of the standard techniques, for example, Ge-spectroscopy. Therefore, the crystal providers usually rely on analyses from CRESST detectors in order to optimize their production methods and supply-chains of raw materials. A background study of $ZnWO_4$ from NIIC was performed with the help of detector $ZnWO_4$-4.

The background rate in different energy intervals obtained with $ZnWO_4$-4 is compared with those in $CaWO_4$-VK33. The latter one is the standard phonon detectors. In Table 8.1 parameters relevant for the background analysis of both detectors are summarized.

8.2.1 ^{57}Co calibration

The detectors have been calibrated with 122 keV and 136 keV γ's emitted by a ^{57}Co source; see decay scheme in Figure 8.2. The source is mounted outside of the cold box and can be inserted without opening the shielding. Since there is some material (copper) in between the source and the detectors, emitted γ's can undergo Compton scattering before reaching the detector. This results in Compton shoulders below the 122 keV and 136 keV peaks. This is indeed the case, as can be seen in the calibration spectrum presented in Figure 8.3.

[1] The presence of lead in the vicinity of detectors may potentially introduce radioactive contaminants.

Detector	Measuring time in days	Dead time in days	Stability cut (2σ) in grams in days	Mass	Total exposure in kg days
$ZnWO_4$-4	15.929	2.566	0.369	404.4	5.249
$CaWO_4$-VK33	18.744	2.655	0.865	309.8	4.404

Table 8.1: Measuring time and exposure of $ZnWO_4$-4 and $CaWO_4$-VK33 during Run 31.

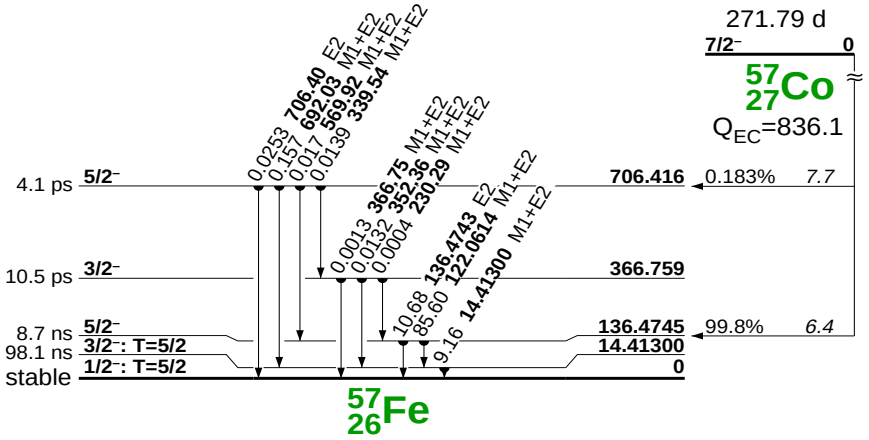

Figure 8.2: ^{57}Co decay scheme. Taken from [30].

In Table 8.2 the energy resolution measured at the 1σ width of the 122 keV peak in various phonon detectors is presented. It is important to note that, independently on their type (with glued or standard detector design), all phonon detectors show excellent energy resolution better than 1 keV (1σ) at 122 keV.

Escape peaks

At the recoil energies relevant for dark matter searches, i.e. below 100 keV, the photoelectric effect is the dominant interaction mode for photons. When interacting with matter photons mostly eject electrons from atomic shells. The produced voids will in turn quickly be filled with electrons from the higher atomic shells and, therefore, characteristic X-rays will be emitted. If an original γ-interaction happens close to the crystal surface, the produced X-ray may escape from it. Hence, in the calibration data we can expect to see some escape lines at energies E_γ - E_{esc}, as well as lines at E_{esc} due to interactions in the neighboring crystals.

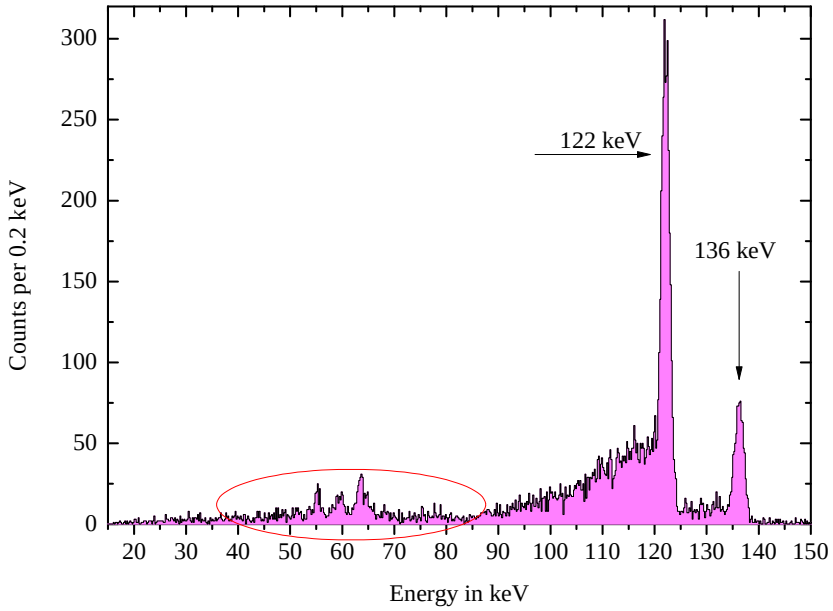

Figure 8.3: Energy spectrum obtained during Run 31 via irradiation of $ZnWO_4$-4 with 122 keV and 136 keV γ's from a ^{57}Co calibration source. The spectrum is reconstructed with the help of the truncated fit procedure (truncation at 0.8 V). Marked in red is the energy region zoomed in Figure 8.4.

Detector	Description	Resolution (1σ) at 122 keV in keV
$ZnWO_4$-4	glued W-SPT	0.77 ± 0.02
$ZnWO_4$-6	glued W-SPT	1.10 ± 0.02
$CaWO_4$-MAJA	glued W-SPT	0.84 ± 0.01
$CaWO_4$-VK33	conventional	0.75 ± 0.01

Table 8.2: Energy resolution (1σ) at 122 keV in various phonon detectors obtained during the ^{57}Co calibration in Run 31. In case of $ZnWO_4$-6 the resolution is obtained from data collected in Run 32.

The X-ray energies E_{esc} for some relevant materials are presented in Table 8.3. Indeed, almost all expected escape lines can be identified; see Figure 8.4.

Element	Transition	Energy in keV	Intensity
Cu	K_α	8.0	39
W	$K_{\alpha 1}$	59.3	47
W	$K_{\alpha 2}$	58.0	27
W	$K_{\beta 1}$	67.2	10
W	$K_{\beta 2}$	69.1	4

Table 8.3: X-ray energies and the corresponding intensities (per 100 K-shell vacancies) for some materials. Data taken from [30].

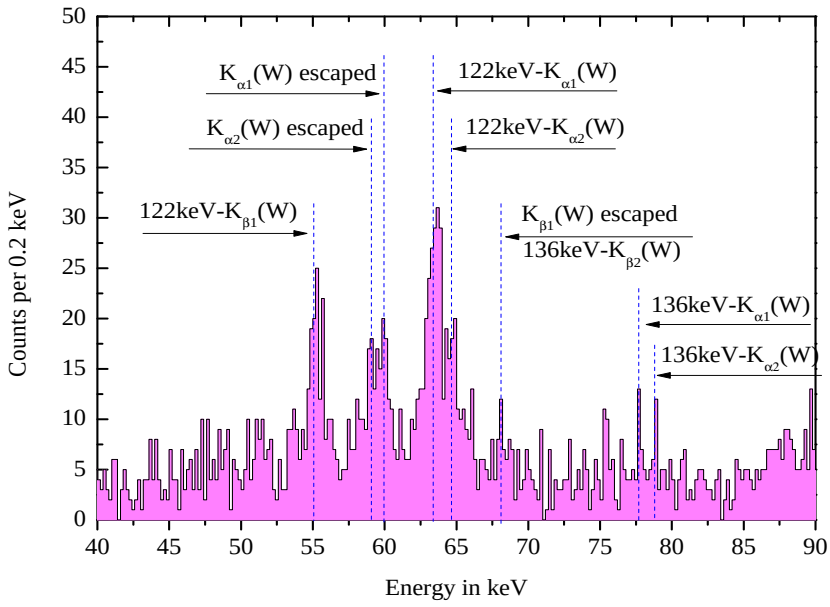

Figure 8.4: Cobalt calibration spectrum obtained with $ZnWO_4$-4 during Run 31 in the energy interval between 40 keV and 90 keV. The peaks are labeled according to their origin.

8.2.2 α-background

The results of the ICP-MS measurements (see also Appendix A) indicate that the $ZnWO_4$ crystals are contaminated with various α-unstable rare earth elements at the ppb level. Therefore, measurable α-activity from long-lived natural actinide isotopes and corresponding chains of daughters (^{238}U, ^{232}Th, and ^{235}U decay chains), along with some lanthanide isotopes may be reasonably anticipated.

Most of the total kinetic energy available from an α-decay (Q-value) is carried away by the emitted α-particle. The remaining energy goes to the recoiling nucleus. If the decay takes place in the bulk of a crystal, the α-particle as well as the recoiling nucleus will be stopped within the crystal. In this case, the Q-value of the decay will be seen in the phonon detector. On the other hand, α-decays from external surfaces will deposit only a fraction of their energy in the volume of the detector, depending on the registered fragment of the decay. Events in which α-particle escapes the detection and the recoiling nucleus hits the crystal are the most "dangerous" ones because they may mimic a WIMP signal. Therefore, these events have to be vetoed carefully [151]. To this end, radioactive contaminations (including α-unstable ones) that are present in the crystals and their surrounding have to be understood.

Calibration

The pulse amplitude spectrum of the data used in the α-background analysis was reconstructed following the parametric fitting procedure described in Section 3.2.3. Having produced a linear amplitude spectrum, the energy calibration is simply a matter of scaling this quantity by an appropriate factor. In principle, one may derive this factor using the ^{57}Co calibration data. However, the source emits 122 keV and 136 keV γ's. These energies are well below the typical energies involved in α- and β-decays of isotopes from the natural decay chains, O(MeV). Extrapolation over an energy interval of ~ 7 MeV is not accurate due to the non-linear detector response. Therefore, for the α-analysis the response of $ZnWO_4$-4 was calibrated using the most prominent α-line, identified as from the natural ^{226}Ra decay (^{238}U decay series; see Appendix D). The Q-value of the ^{226}Ra decay is 4871 keV [153]. The final refinement of the pulse amplitude to the α-energy conversion is made by fitting a straight line passing through $(0, 0)$.

The calibration of $CaWO_4$-VK33 was done using α-lines identified as from natural ^{226}Ra (4871 keV), ^{222}Rn (5590 keV), ^{224}Ra (5789 keV), and ^{220}Rn (6404 keV) decays; see Appendix D. The resulting calibration curve for this detector is presented in Figure 8.5.

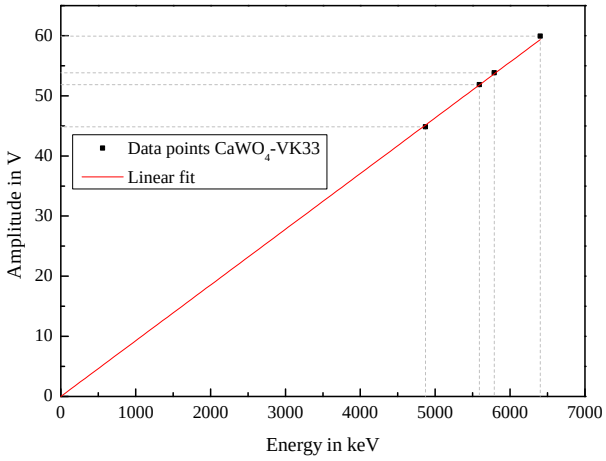

Figure 8.5: Energy calibration for the α-background analysis of $CaWO_4$-VK33. The energy scale is fixed by the Q-values of ^{226}Ra (4871 keV), ^{222}Rn (5590 keV), ^{224}Ra (5789 keV), and ^{220}Rn (6404 keV) α-emitters. The amplitude positions of these peaks are obtained with Gaussian fits. The statistical error on each of the fitted peaks is less than 0.1 %. The fitted straight line is passing through the point $(0, 0)$.

Identification

In principle, the CRESST-II light-phonon measuring technique (see Section 2.3.1) allows for discrimination between α- and γ/β-particles. However, since the corresponding light detectors of both phonon detectors under study ($ZnWO_4$-4 and $CaWO_4$-VK33) were not operational during the measurement, α- and β/γ-bands cannot be separated. Therefore, discrimination cuts were not applied. Figures 8.6 and 8.7 show the reconstructed energy spectra obtained with detectors $ZnWO_4$-4 and $CaWO_4$-VK33, respectively. The α-peaks are marked by the names of their (potential) parent nuclei.

The mean energies of most of the peaks observed in the spectra were determined via Gaussian fits over a flat background. For the (^{210}Po + ^{228}Th + ^{222}Rn) and (^{218}Po + ^{212}Bi) peaks in the spectrum of $ZnWO_4$-4 (see Figure 8.6), and (^{218}Po + ^{227}Th + ^{212}Bi) peak in $CaWO_4$-VK33 (see Figure 8.7) fits of two or more superimposed Gaussians were used. The mean and integral for each peak, along with the difference between measured and expected energies, is given in Table 8.4 for $ZnWO_4$-4 and in Table 8.5 for $CaWO_4$-VK33. Since energy calibration towards lower energies was performed by linear extrapolation from the calibration points (selected in the region of interest, i.e. above 4 MeV), its accuracy between 4 MeV and 7 MeV is much better than between 2 MeV and 4 MeV.

In the spectra of both detectors a few peaks were observed between 2 MeV and 4 MeV, i.e. outside the energy region occupied by the natural decay chains. It should be remarked that there are not so many α-unstable candidates with a

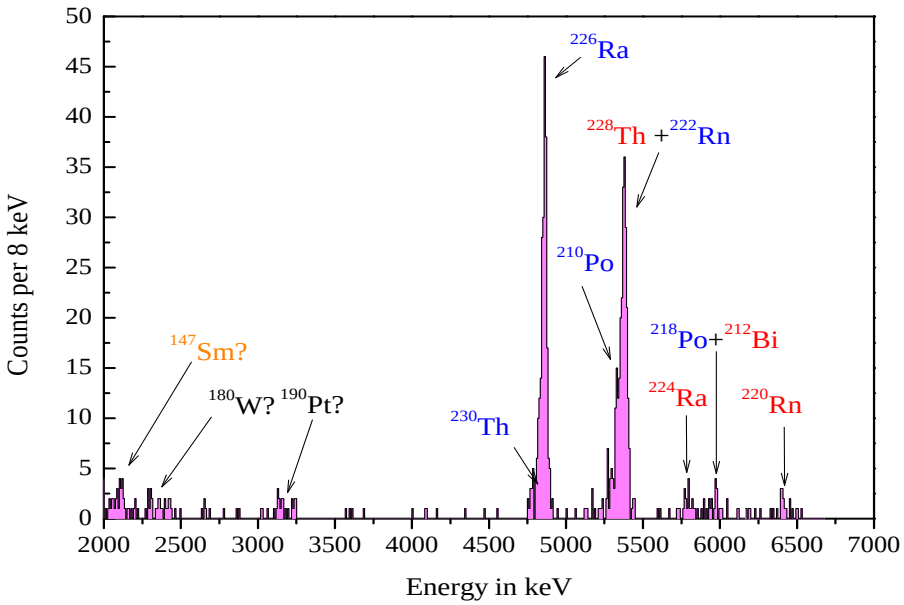

Figure 8.6: α-background spectrum of $ZnWO_4$-4 recorded in Run 31 with an exposure of ~5.19 kg days. The spectrum is reconstructed with the help of the parametric fit. Isotopes marked in blue are belonging to the ^{238}U natural decay chain, in red to ^{232}Th, and in orange are α-unstable rare-earth isotopes. Other α-active isotopes are marked in black.

Q-value at this energy range. The list of these candidates is given in Table 8.6. It is worth noting that the α-decay of naturally occurring ^{180}W was unambiguously identified for the first time with the help of sensitive CRESST detectors [155].

Tungsten: ^{180}W is an α-emitter with a half-life of 1.5×10^{18} years [155] and decays into the stable ground state ^{176}Hf. The Q-value is 2516 keV. This decay may be the cause of the peak around (2350 ± 12) keV seen in the spectrum of $ZnWO_4$-4 and of the peak around (2362 ± 6) keV in $CaWO_4$-VK33. Though the energy calibration for both detectors in this energy region is not as accurate as at higher energies (mismatch between the expected Q-value and the reconstructed energy is ~ 6 %) the correctness of the assumption can be checked by comparing the half-life of ^{180}W in each detector with its tabulated value. The isotopic abundance of ^{180}W translates into 9.3×10^{20} nuclei in the $ZnWO_4$ crystal and to 7.7×10^{20} in the $CaWO_4$ crystal. From the count rate observed in detector $ZnWO_4$-4 (given an exposure of 5.19 kg days) a half-life of $(1.5 \pm 0.7) \times 10^{18}$ years can be calculated. In detector $CaWO_4$-VK33 (given an exposure of 4.37 kg days) a half-life of $(1.3 \pm 0.5) \times 10^{18}$ years can be calculated. Within the error bars, both of the obtained half-lives are in agreement with the tabulated value.

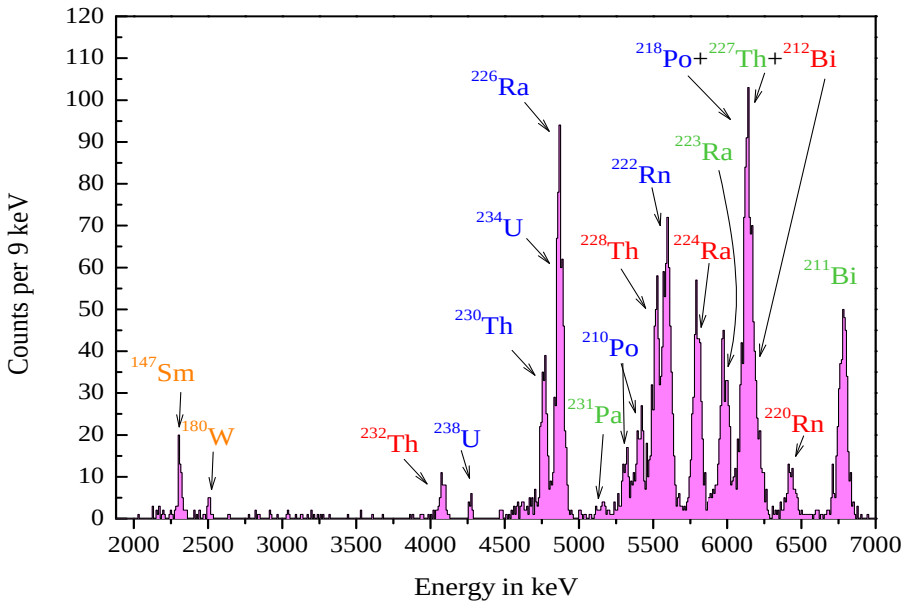

Figure 8.7: α-background spectrum of $CaWO_4$-VK33 recorded in Run 31 with an exposure of 4.37 kg days. The spectrum is reconstructed with the help of the parametric fit. The color coding is the same as in the previous figure. Isotopes belonging to the ^{235}U chain are shown in green.

Samarium: Contaminations with rare-earth samarium have been found in the ICP-MS measurements of both representative samples, $ZnWO_4$ and $CaWO_4$ [58], at the level of $\sim$ 5 ppb and $\sim$ 5.8 ppb, respectively. This element has an α-active isotope, ^{147}Sm. It is a pure α-emitter with a half-life of 1.1×10^{11} years [30] and a 100 % branching fraction for the decay into the stable ground state ^{143}Nd. The Q-value of this decay is 2311 keV [153]. The structure at (2101 $\pm$ 4) keV, observed with $ZnWO_4$-4, and the one at (2158 $\pm$ 1) keV, observed with $CaWO_4$-VK33, have been identified as being due to decay of ^{147}Sm.

Platinum: A broad peak at (3140 $\pm$ 12) keV observed with detector $ZnWO_4$-4 (see Figure 8.6) may be attributed to the internal contamination of the crystal with platinum. This element has an α-unstable ^{190}Pt isotope with a half-life of (6.5×10^{11}) years [30] and a 100 % [154] branching fraction for the decay to the stable ground state of ^{186}Os. The Q-value of this decay is 3250 keV. The observed count rate of (8.6 $\pm$ 5.1) events per 12.84 days represents a contamination of the crystal with ^{190}Pt at the level of (3.4 $\pm$ 2.0) ppb. Taking into account that during the growth process (see Section 5.2) a $ZnWO_4$ ingot crystal is completely surrounded by a platinum crucible, a contamination with ^{190}Pt seems plausible.

Reconstructed mean energy in keV	Candidate	Q-value in keV	Mismatch in %	Peak integral
2101 ± 4	^{147}Sm	2311	9.0	24.9 ± 7.7
2350 ± 12	^{180}W	2516	6.5	17.5 ± 8.9
3140 ± 12	^{190}Pt	3250	3.4	8.6 ± 5.1
4825 ± 4	^{230}Th	4770	-1.2	25.7 ± 8.9
4848 ± 4	^{234}U	4856	0.2	51.9 ± 20.0
4867 ± 23	^{226}Ra	4871	0.1	109.6 ± 25.0
5285 ± 10	$^{210}_{int}$Po	5407	2.3	12.5 ± 5.3
5337 ± 4	^{228}Th	5520	3.3	54.3 ± 11.0
5379 ± 2	^{222}Rn	5590	3.7	168.1 ± 16.0
5793 ± 4	^{224}Ra	5789	-0.1	6.2 ± 3.1
6403 ± 8	^{220}Rn	6404	0.02	5.9 ± 3.6

Table 8.4: Reconstructed energies with decay parent candidates and deviations from tabulated Q-values measured with $ZnWO_4$-4 during Run 31 with an exposure of 5.19 kg days. Q-values are taken from [153]. $^{210}_{int}$Po stands for the internal crystal contamination. The relatively high errors on the peak integrals result form the background estimation.

Natural decay chains: In both Figure 8.6 and 8.7, a cluster of α-events with energies between 4 MeV and 7 MeV can be seen. Most of these are consistent with decays from natural decay chains (^{232}Th, ^{238}U, and ^{235}U one). Their decay schemes are presented in Appendix D.

At energies higher than ~ 4 MeV each line of the obtained spectra fits well to the Q-value of the α-active candidate. However, in the spectrum of $CaWO_4$-VK33 (see Figure 8.7) a peak around 5300 keV is observed. There is no Q-value that fits this energy. However, during contact with the air of the Gran Sasso laboratory, ^{222}Rn nuclei may have been implanted into the crystal surface or the surface surrounding the detector. This isotope belongs to the ^{238}U decay chain and is a pure α-emitter with a half-life of 3.825 days [30] and a 99.92 % branching fraction for the decay into ^{218}Po which is unstable. The chain ends with the α-decay of ^{210}Po into the stable ground state ^{206}Pb. The Q-value of this decay is 5407 keV [153], which splits into the α-particle kinetic energy of 5304 keV [30] and into the recoil energy of 103 keV of the ^{206}Pb nuclei. In decay of ^{210}Po at the crystal surface some of the ^{206}Pb-nuclei may escape detection, meaning that only the kinetic energy of the α-particle is deposited into the phonon detector. Then the total energy seen in the detector is ~ 5304 keV. Therefore, the line around

Reconstructed mean energy in keV	Candidate	Q-value in keV	Mismatch in %	Peak integral
2158 ± 1	^{147}Sm	2311	6.6	47.3 ± 7.3
2362 ± 6	^{180}W	2516	6.1	14.4 ± 4.1
4010 ± 3	^{232}Th	4083	1.7	37.9 ± 6.6
4207 ± 4	^{238}U	4270	1.5	13.1 ± 4.7
4727 ± 2	^{230}Th	4770	0.9	206.1 ± 22.0
4837 ± 1	^{226}Ra	4871	0.7	478.6 ± 24.2
5142 ± 14	^{231}Pa	5150	0.2	11.6 ± 5.6
5302 ± 4	$^{210}_{ext}$Po	5304	0.1	66.4 ± 9.5
5403 ± 3	$^{210}_{int}$Po	5407	0.1	145.6 ± 13.2
5516 ± 2	^{228}Th	5520	0.1	314.6 ± 20.9
5594 ± 2	^{222}Rn	5590	-0.1	432.1 ± 23.8
5805 ± 2	^{224}Ra	5789	-0.3	306.7 ± 24.0
5983 ± 2	^{223}Ra	5979	-0.1	101.0 ± 19.1
6121 ± 5	^{218}Po	6115	-0.1	88.7 ± 24.0
6161 ± 3	^{227}Th	6146	-0.2	369.0 ± 37.9
6464 ± 5	^{220}Rn	6404	-0.9	44.2 ± 10.7
6833 ± 2	^{211}Bi	6751	-1.2	305.8 ± 21.1

Table 8.5: Reconstructed energies with decay parent candidates and deviations from tabulated Q-values measured with $CaWO_4$-VK33 during Run 31 with an exposure of 4.37 kg days. Q-values are taken from [153]. $^{210}_{int}$Po stands for the crystal-internal contamination, whereas $^{210}_{ext}$Po for the external one. The relatively high errors on the peak integrals are due to the background estimation.

Isotope	Name	Isotopic abundance in %	Half-life in years	Q-value in keV
^{144}Nd	Neodymium	23.8	2.29×10^{15}	1905
^{148}Sm	Samarium	15.0	1.06×10^{11}	1986
^{152}Gd	Gadolinium	0.2	1.1×10^{14}	2205
^{147}Sm	Samarium	11.3	7×10^{15}	2311
^{174}Hf	Hafnium	0.162	2.0×10^{15}	2495
^{180}W	Tungsten	0.1198	1.8×10^{18}	2516
^{186}Os	Osmium	1.58	2.0×10^{15}	2822
^{190}Pt	Platinum	0.01	6.5×10^{11}	3250

Table 8.6: Parent candidates for α-contaminations in the energy range between 1.9 and 3.5 MeV. Data taken from [30]. Isotopic abundance and half-life of ^{180}W are taken from [154] and [155], respectively.

Contaminant	Activity in mBq/kg
^{147}Sm	~ 0.05
^{180}W	~ 0.04
^{190}Pt	~ 0.01
all natural decay chains	~ 1.1

Table 8.7: Principal α-contaminants present in the representative $ZnWO_4$ crystal from NIIC. Activities are calculated from values given in Table 8.4.

5300 keV may be attributed to the crystal surface contamination with ^{210}Po. Also in the spectrum of $ZnWO_4$-4 (see Figure 8.6) the structure on the left side of the ^{226}Ra peak may be assigned to the surface contamination with ^{210}Po.

Quantitative analysis

As explained in Section 8.1, the stability control of $ZnWO_4$-4 during operation was affected by an open heater line. Therefore, the resolution of the reconstructed amplitude spectrum of this detector is not as good as in the case of $CaWO_4$-VK33. Since various α-lines present in the spectrum of the $ZnWO_4$ crystal cannot be clearly separated, only the total α-activity due to contaminations with various isotopes, including radionuclides from natural decay chains, is given;

see Table 8.7.

In crystal $CaWO_4$-VK33 a much higher amount of α-active isotopes from the ^{238}U, ^{232}Th, and ^{235}U chains has been observed. The estimated activity for the identified isotopes is given in Table 8.8. It should be stressed that any secular

Contaminant	Activity in mBq/kg
^{147}Sm	$\sim$ 0.13
^{180}W	$\sim$ 0.04
^{238}U chain	$\sim$ 5.9
^{235}U chain	$\sim$ 1.2
^{232}Th chain	$\sim$ 1.9
all natural decay chains	$\sim$ 11.4

Table 8.8: Principal α-contaminants present in $CaWO_4$-VK33. Activities are calculated from values presented in Table 8.5. The total activity from natural decay chains does not take into account pile-up α-events.

equilibrium of ^{238}U, ^{232}Th, and ^{235}U chains in inorganic crystals is usually broken (see Appendix D). Therefore, any observed inconsistency in the number of decays within these chains is not unexpected.

In the spectrum of the $CaWO_4$ crystal, a significant amount of isotopes belonging to the ^{235}U chain have been identified, suggesting its contamination with ^{227}Ac. Signatures of this isotope were also observed in the spectra of different $CaWO_4$ crystals from the same producer [27, 156, 157].

In general, high energy α-events render the detector saturated for some period of the time ($\sim$ 60 ms for a glued phonon detector and $\sim$ 20 ms for a conventional one). If a second event occurs during this time it will be seen as a pile-up. They are usually fitted incorrectly due to a distorted pulse shape. Therefore, some of the expected α-lines, e.g. $^{219}\text{Rn} \xrightarrow{4\ s} {}^{215}\text{Po}$ followed by $^{215}\text{Po} \xrightarrow{1.8\ ms} {}^{211}\text{Pb}$ or $^{220}\text{Rn} \xrightarrow{56\ s} {}^{216}\text{Po}$ followed by $^{216}\text{Po} \xrightarrow{0.15\ ms} {}^{212}\text{Pb}$, appear in the spectrum of $CaWO_4$ crystal as a broad peak above $\sim$ 7 MeV. In this analysis pile-up events were not taken into account, meaning that the actual total α-activity from natural decay chains is higher than the estimated value.

Furthermore, there are still some other contaminants observed in both detectors which unveil themselves via α-radiation, namely, from ^{147}Sm and ^{180}W. In case of the $ZnWO_4$ crystal also a marginal contamination of $\sim 10\mu$Bq/kg with ^{190}Pt has been observed.

In summary, the total amount of internal α-active impurities measured with the $ZnWO_4$ crystal from NIIC turned out to be much lower ($\sim$ 1.2 mBq/kg) in

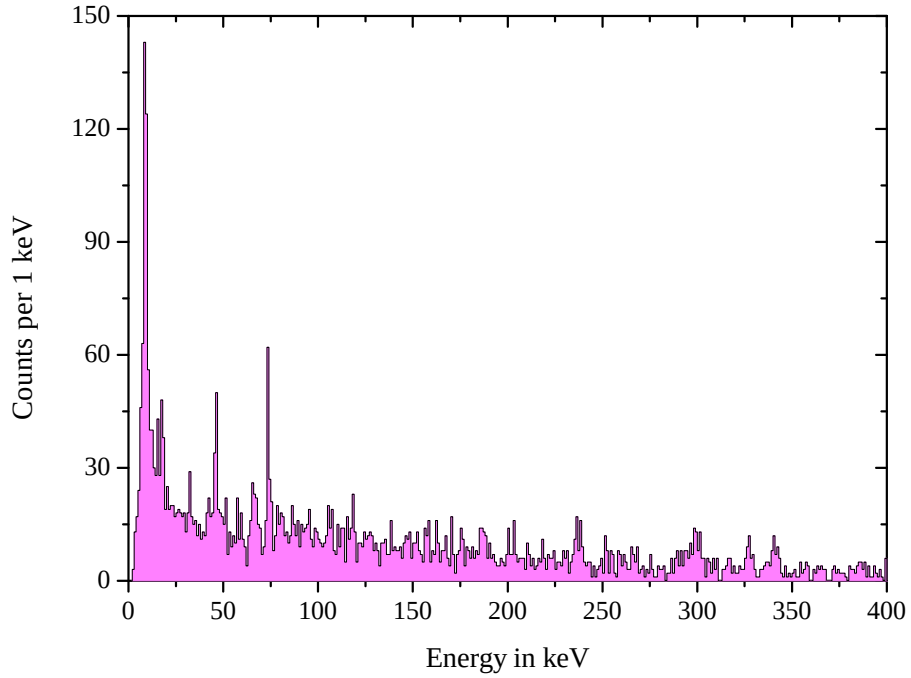

Figure 8.8: Background spectrum recorded with $ZnWO_4$-4 in Run 31 during an exposure of ~5.2 kg days. The energy is reconstructed with the help of the truncated fit procedure and the standard event template from 122 keV (^{57}Co). To clean the data sample from spurious pulses some basic pulse quality cuts have been applied.

comparison with the $CaWO_4$ crystal (~ 11 mBq/kg)[2]. The main sources of internal α-radioactivity in $ZnWO_4$ have been identified as being due to the daughters of the ^{238}U/^{232}Th decay chains. No traces of elements from the ^{235}U series as well as other peculiarities from rare-earth isotopes like neodymium or gadolinium, often present in $CaWO_4$ crystals, were observed in $ZnWO_4$. This points to a high radiopurity level of the $ZnWO_4$ target material.

8.2.3 γ- and β-background

In the preceding section the main sources of radioactive α-background from naturally occurring radionuclides have been discussed. Radioactive decay happens not only via emission of energetic α's, but also via emission of β-particles. The latter gives a rise to the low energy part of the $ZnWO_4$-4 background spectrum ($\lesssim 1$ MeV). Moreover, some radionuclides may be significant γ emitters[3]. The

[2]It is generally accepted that higher radioactive contamination in $CaWO_4$ crystals is mainly coming from $CaCO_3$ powder, which is one of the raw compounds for the growth of these crystals.

[3]Gamma radiation is not a mode of radiative decay, but rather a mechanism by which excess energy is emitted from certain radionuclides. Typical electromagnetic transition times are of the

Origin (Energy)	Reconstructed energy	Resolution (1σ) in keV	Activity in μBq/kg
^{210}Pb (46.5 keV)	46.2 ± 0.1	0.28 ± 0.04	58 ± 18
^{212}Pb (238 keV)	236.3 ± 0.4	1.03 ± 0.46	68 ± 17
^{214}Pb (295 keV)	297.8 ± 1.1	3.78 ± 0.89	75 ± 35
^{228}Ac (338 keV)	327.0 ± 0.6	2.20 ± 0.39	57 ± 16
^{214}Pb (352 keV)	340.7 ± 0.5	2.20 ± 0.39	94 ± 19
^{208}Tl (583 keV)	536.2 ± 1.1	3.35 ± 1.21	37 ± 15

Table 8.9: Activity of various γ-peaks measured with $ZnWO_4$-4 in Run 31 during exposure of 5.2 kg days. Gammas are emitted in the de-excitation process of impurities present in the neighboring crystals and in the vicinity of the detector. See text for discussion.

associated energies of some major decay modes in the natural decay chains along with the end points for β-decays are presented in Table D.1, D.2, and D.3.

Figure 8.8 shows the energy spectrum recorded by the detector $ZnWO_4$-4 during Run 31. In general, the spectrum is rather featureless above $\sim$ 100 keV. The origin of several observed peaks will be discussed in detail below.

Escaped photons

If an α-decay happens in the bulk of a crystal then the total Q-value of the decay should be seen in the corresponding phonon detector. However, γ-particles of sufficient energy, emitted in the process of a nucleus de-excitation, may escape the crystal. Since the CRESST-II detectors are assembled in a modular structure (see Figure 2.5), the probability for the escaped photon to hit the neighboring detectors is high. Therefore, in the spectrum of the $ZnWO_4$ crystal several peaks at energies of the characteristic γ's are expected. Indeed, in the spectrum presented in Figure 8.8 peaks at (46.2 ± 0.1) keV, (236.3 ± 0.4) keV, (297.8 ± 1.1) keV, (327.0 ± 0.6) keV, and (340.7 ± 0.5) keV are visible on top of the background. Each of them is attributed to the absorption of photons emitted by ^{210}Pb, ^{212}Pb, ^{214}Pb, and ^{228}Ac isotopes present in the neighboring crystals and in the vicinity of $ZnWO_4$-4, respectively. The corresponding activities in the identified peaks are listed in Table 8.9.

Furthermore, an escaped γ-particle can hit copper, which is abundant in the vicinity of the detector. In this case, characteristic copper X-rays with an energy of 8.04 keV can be emitted. Inspecting the low energy part of the $ZnWO_4$-4 spectrum

order of 1 ps.

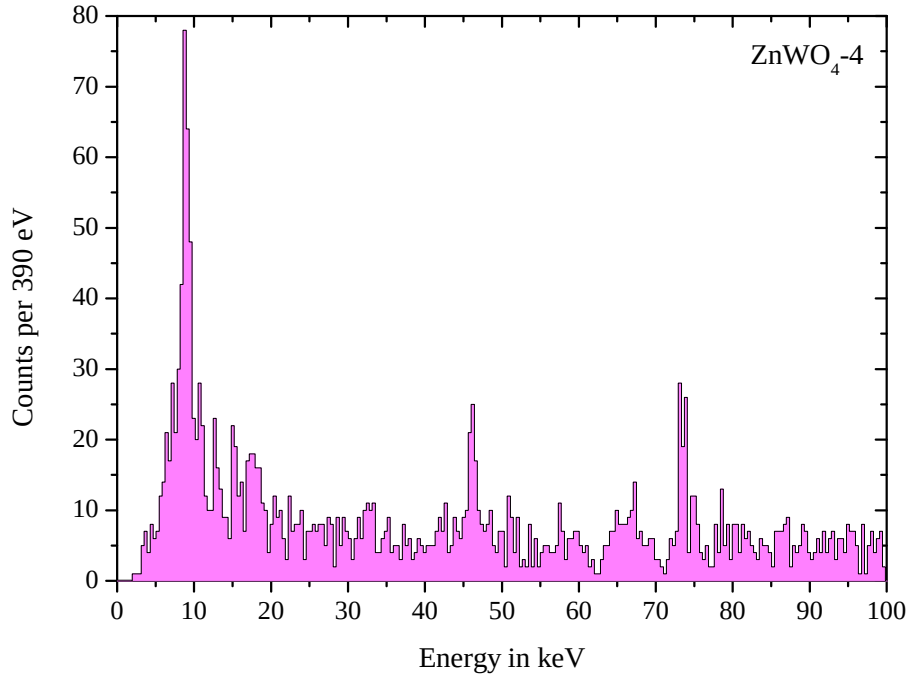

Figure 8.9: Low energy part of the background spectrum recorded with $ZnWO_4$-4 in Run 31 during an exposure of ~ 5.2 kg days. Peaks at (8.93 ± 0.04) keV, (46.2 ± 0.1) keV, (65.15 ± 0.1) keV, and (73.76 ± 0.15) keV are attributed to the decay of ^{65}Zn, ^{210}Pb, ^{179}Ta, and ^{181}W in the bulk of the crystal, respectively.

presented in Figure 8.9 one finds a prominent peak at (8.93 ± 0.04) keV. The unexpectedly high activity observed in this line is (377 ± 36) μBq/kg. This value is approximately three times larger than the activity measured with the crystal $CaWO_4$-VK33. However, the module with $ZnWO_4$-4 is mounted on the inner carousel tower and is completely surrounded by neighboring modules, whereas $CaWO_4$-VK33 is placed in the outer tower[4]. Thereby the line of sight between $ZnWO_4$-4 and the copper thermal shield is much smaller than that for $CaWO_4$-VK33. Therefore, the number of Cu X-rays detected with $CaWO_4$-VK33 must be the same or slightly higher than in $ZnWO_4$-4. Since this is in contradiction with the observed activity, there must be another source contributing to the peak at ~ 8.93 keV. Indeed, there is a process which may explain the measured activity. It will be discussed in the following section.

Cosmogenic activation

An exposure of crystals to cosmic rays may result in their activation. In this process, some relatively long-lived isotopes can be formed. They may contribute

[4] All copper detector holders are identical.

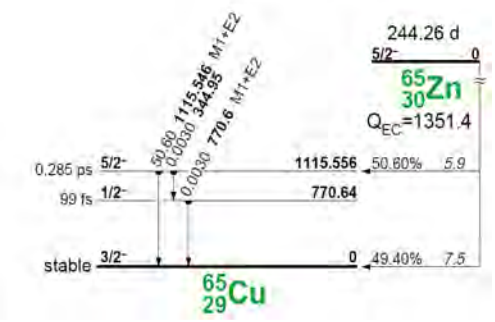

Figure 8.10: Level scheme of the ^{65}Zn electron capture process. Data taken from [30].

to the background of the experiment when decaying during the measurement. The $ZnWO_4$ crystals used for the detector fabrication were transported by plane at an altitude of ~ 10 km, where the hadronic contribution from air showers is ~ 1000 times stronger than at ground level. Therefore, decay signatures of cosmogenicaly activated crystal compounds, namely, zinc or tungsten, are expected[5].

Cosmogenic activation of zinc: Capture of thermal neutrons from cosmic rays can activate the ^{64}Zn isotope (48.6 % isotopic abundance) present in $ZnWO_4$ crystals. This results in the production of the ^{65}Zn isotope, which decays via electron capture into the stable ^{65}Cu isotope [30]. Since the half-life of this process is approximately 8 months, radiation from ^{65}Zn may contribute to the background of detector $ZnWO_4$-4. Furthermore, ^{65}Zn can be produced in the reaction ^{67}Zn (p, t) ^{65}Zn (isotopic abundance of ^{67}Zn is 4.1 %).

The decay scheme of the ^{65}Zn isotope is shown in Figure 8.10. In 51 % of the cases the electron capture in ^{65}Zn is accompanied by emission of 1115 keV γ-particles [30]. Therefore, the energy which will be seen in $ZnWO_4$-4, following a K-shell electron capture process in ^{65}Zn, is that of the K-shell binding energy of Cu (8.97 keV [30]) plus that of the emitted γ, namely, 1124 keV. In fact, there is a peak at (1103.3 ± 4.1) keV in the spectrum. The activity in the peak is (47.95 ± 16.45) μBq/kg and it can be attributed to the decay of activated ^{65}Zn. In the remaining 49 % of the cases, only the K-shell binding energy of Cu will be dissipated within the detector. This gives rise to an additional peak at ~ 8.93 keV.

Another possible activation channel of Zn which may result in the emission of low energy radiation (< 100 keV) comes from to the reactions ^{64}Zn (p, t) ^{62}Zn, ^{64}Zn (p, α) ^{61}Cu, and ^{67}Zn (p, α) ^{64}Cu. However, ^{62}Zn, ^{61}Cu, and ^{64}Cu have

[5] A spectral analysis of activated isotopes in $CaWO_4$ crystals can be found in [27].

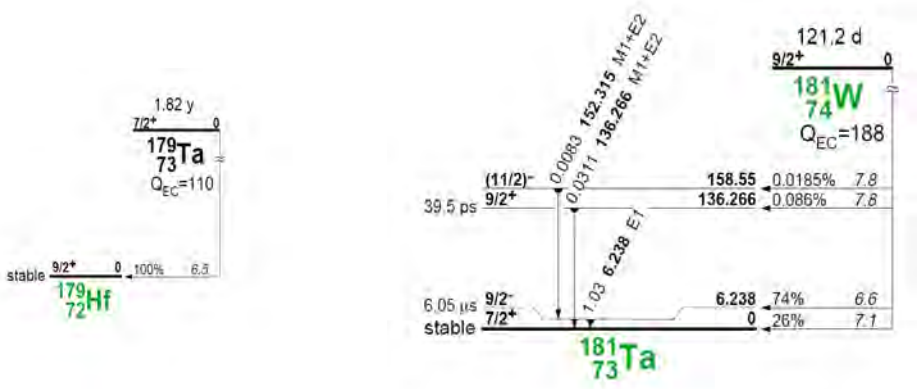

Figure 8.11: *Left:* Level scheme of the ^{179}Ta electron capture process. *Right:* Level scheme of the ^{181}W electron capture process. Data taken from [30].

half-lives of ~ 9 h, ~ 10 min, and ~ 13 h, respectively. Therefore, these isotopes are not expected to be present in the crystal at the moment of the measurement.

Cosmogenic activation of tungsten: There are two tungsten activation reactions which lead to radiation below 100 keV. The first one is the (p, α) reaction on ^{182}W (isotopic abundance is 26.3 %) which results in ^{179}Ta. ^{179}Ta has a half-life of ~ 2 years and decays via electron capture into the stable isotope ^{179}Hf [30]. The decay scheme of this process is presented in the left panel of Figure 8.11. Since no photons accompany the decay, the energy which will be seen in the detector following a K-shell electron capture process is that of the K-shell binding energy of hafnium (65.35 keV [30]). In the spectrum of $ZnWO_4$-4 presented in Figure 8.9 the peak-like structure at (65.15 ± 0.1) keV may be attributed to this process. The measured activity of this peak is ~ 21 μBq/kg.

The second proton reaction is ^{183}W (p, t) ^{181}W. Hence, ^{181}W is expected to be present in the $ZnWO_4$ crystal. This isotope has a half-life of ~ 4 months and decays via electron capture into the stable isotope ^{181}Ta [30]; see right panel in Figure 8.11. In most of the cases, the decay is accompanied by 6.2 keV photon-emission. Thus, a line at 73.6 keV is expected in the spectrum, being the sum of the tantalum binding energy of 67.4 keV and the 6.2 keV photon energy. Inspecting the spectrum presented in Figure 8.9 one finds the peak at (73.76 ± 0.15) keV. It may be attributed to the decay of ^{181}W. The activity in the peak is ~ 148 μBq/kg.

Additionally to the external and internal contaminations discussed above, a minor contamination with ^{40}K has been identified in the spectrum of the $ZnWO_4$ crystal. It is attributed to the peak at (1400 ± 1) keV. The measured activity is (15.6 ± 7) μBq/kg.

Moreover, there is a line at (32.79 ± 0.17) keV. A search was performed for ra-

Energy range in keV	Background rate in counts/keV/kg/day	
	$ZnWO_4$-4	$CaWO_4$-VK33
2 - 100	~ 4.1	~ 7.8
100 - 400	~ 0.6	~ 6.1
400 - 1000	~ 0.3	~ 12.1

Table 8.10: Background rate caused by γ- and β-particles at different energy intervals measured with $ZnWO_4$-4 in Run 31 during exposure of 5.20 kg days and with $CaWO_4$-VK33 in the same run during exposure of 4.37 kg days.

dionuclides from natural decay chains but with negative outcome. The observed activity in this peak is (48 ± 19.3) μBq/kg.

Level of contamination

Since it is the first time when $ZnWO_4$ is operated at the low background facility, it is interesting to compare the background rate of this material with that of $CaWO_4$; see Table 8.10. Below 100 keV the spectrum of the $CaWO_4$ crystal is dominated by radiation from ^{227}Ac and ^{210}Pb contaminants. Above 300 keV, the signatures of ^{176}Lu and anthropogenic ^{137}Cs have been observed. On the other hand, no traces of these isotopes as well as other peculiarities (like strontium) have been identified in the spectrum of the $ZnWO_4$ crystal. The total background rate below 1000 keV measured with the $ZnWO_4$ crystal corresponds to ~ 5 counts/keV/kg/day. This is a factor of ~ 5 lower than that of the $CaWO_4$ crystal. To conclude, the measured radiopurity content of $ZnWO_4$ fulfills the requirements on a new target material for the CRESST-II experiment.

8.3 Performance studies

8.3.1 Pulse shape analysis

For detectors with glued thermometers one expects to see two classes of events with distinct pulse shapes. The first class originates from interactions of particles in the thermometer carrier (wafer), whereas the second is due to interactions in the cylindrical absorber. Wafer pulses are expected to be much faster than absorber pulses since for the latter phonons have to travel through the absorber, the glue spot and the wafer boundaries before thermalizing in the W-film. Figure 8.12 shows the scatter plot obtained with detector $ZnWO_4$-4 during Run 31. In this plot, the pulses in the upper band of the rise time plane correspond to interactions in the cylindrical $ZnWO_4$ absorber, whereas the ones in the lower

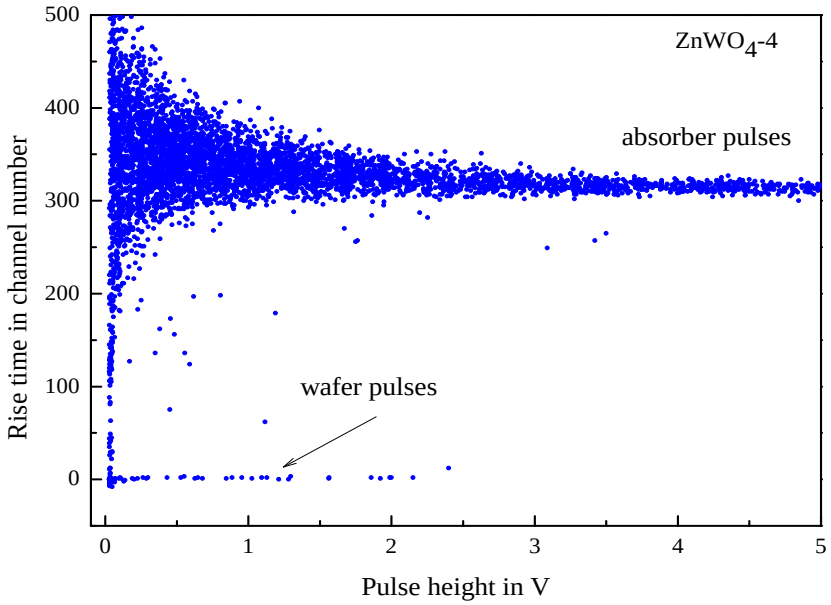

Figure 8.12: Pulse height versus rise time scatter plot obtained with $ZnWO_4$-4 during Run 31. The rise time is measured from the pulse onset to its maximum. The upper band in the rise time corresponds to signals caused by particle interactions in the cylindrical $ZnWO_4$ absorber, whereas the lower one is due to particle interactions in the $(20 \times 10 \times 5)$ mm^3 $ZnWO_4$ wafer.

band are due to interactions in the $ZnWO_4$ wafer. Moreover, from the data obtained during Run 32 in which $ZnWO_4$-4/ULRICH module is operational, it is evident that wafer pulses are not dark, i.e. the scintillation light associated with the event is visible in the light detector. A typical wafer pulse with the corresponding light signal recorded with this module is shown in Figure 8.13.

Figure 8.14, 8.15, and 8.16 show the template pulses of detectors $ZnWO_4$-4, $ZnWO_4$-6, and, for comparison, of $CaWO_4$-MAJA. The latter is a glued $CaWO_4$ phonon detector[6]. The pulses for each template were selected in the linear response region of the corresponding detector. It should be noted that in the case of $ZnWO_4$-4 no template for a wafer event was generated because most of the wafer pulses possess a composite structure; see Figure 8.13. This will be discussed below. Only a few pulses with a single component shape were found in the whole data set; see Figure 8.14. The reason may be a very fast rise time of the wafer pulses that exceeds the slew rate of the corresponding SQUID. This, in turn, causes flux quantum losses and results in pulses with characteristic shapes. An example of such a pulse is shown in the left panel of Figure 8.17.

The theoretical model for the pulse shape formation in a detector with separate thermometer is still under development since more experimental data is needed

[6]Some characteristics of detector $CaWO_4$-MAJA are discussed in [158].

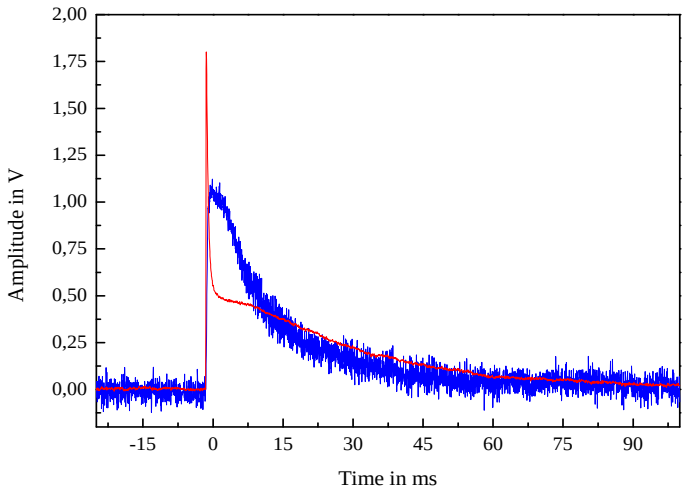

Figure 8.13: Coincident signals in the detector module $ZnWO_4$-4/ULRICH recorded during Run 32. The red line is the measured signal in the thermometer carrier of the phonon detector. The blue line is the measured signal in the corresponding light detector.

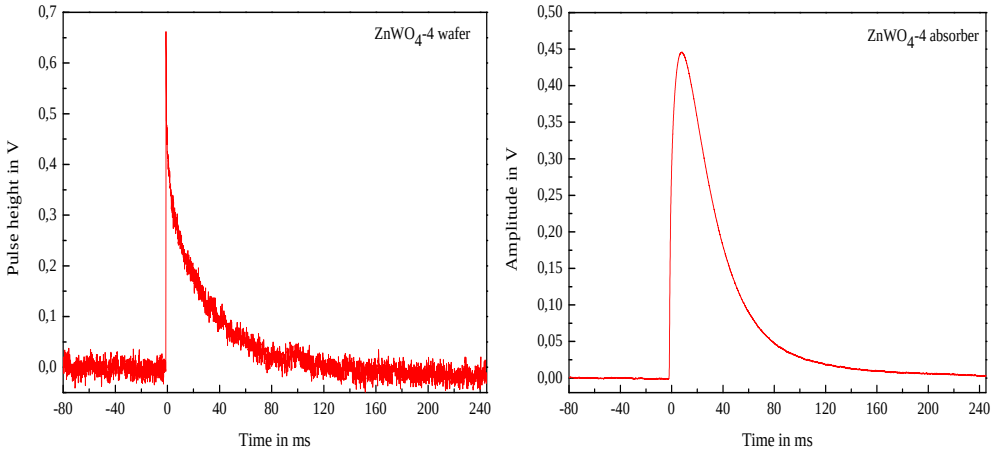

Figure 8.14: *Left*: A single wafer pulse obtained in the linear response region of detector $ZnWO_4$-4 during Run 31. *Right*: The absorber pulse template obtained with the same detector for a 122 keV energy deposition.

in order to judge between different approaches [110, 108] which are based on the extension of the thermal model discussed in Section 2.3.5. In this work the standard pulse formation model was applied in order to characterize specific pulse shapes.

Since the thermometers of the phonon detectors are operating in bolometric

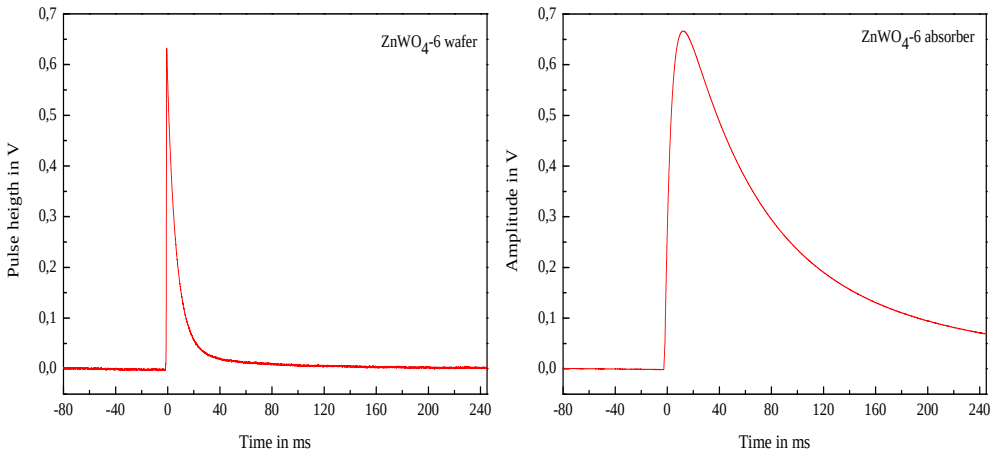

Figure 8.15: *Left*: The wafer pulse template obtained in the linear response region of $ZnWO_4$-6 during Run 32. *Right*: The absorber pulse template obtained with the same detector corresponding to a 122 keV energy deposition.

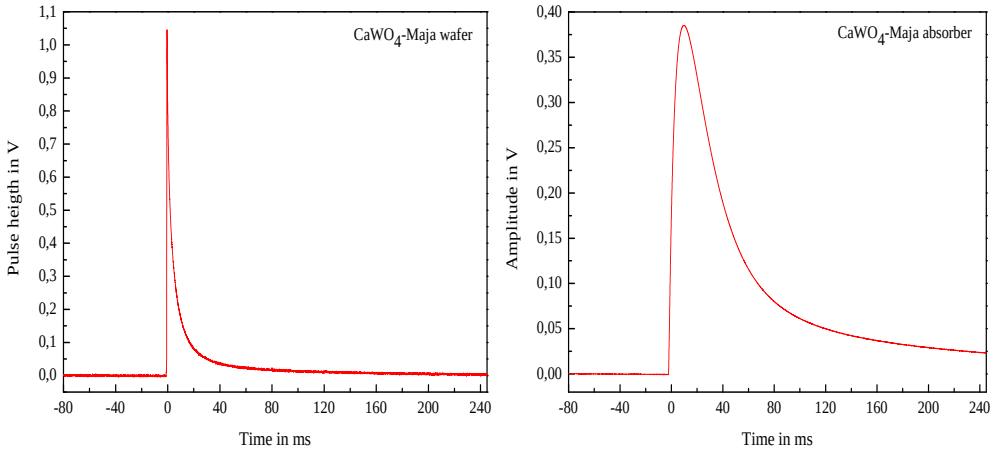

Figure 8.16: *Left*: The wafer pulse template obtained in the linear response region of $CaWO_4$-MAJA detector response during Run 32. *Right*: The absorber pulse template obtained with the same detector corresponding to a 122 keV energy deposition.

mode, the pulse shape can be described starting from Equation 2.9 as

$$f(t) = b + A_{tot}\,[\underbrace{A_n\,(\exp^{-(t-t_0)/\tau_n} - \exp^{-(t-t_0)/\tau_{intr}})}_{non-thermal\ component} + \underbrace{(1-A_{th})\,(\exp^{-(t-t_0)/\tau_{th}} - \exp^{-(t-t_0)/\tau_n})}_{thermal\ component}], \tag{8.1}$$

where t_0 is the onset time of the pulse, A_{tot}, A_n, A_{th}, and b represent the amplitudes of the total as well as two signal components, and the baseline, respectively. In

Detector	**$ZnWO_4$-4**	**$ZnWO_4$-6**	**$CaWO_4$-MAJA**	**$CaWO_4$-VK31**
Type	glued	glued	glued	conventional
Glue area	~ 20 mm^2	~ 5 mm^2	~ 10 mm^2	
Thermometer carrier pulses				
rise time, τ_n	< 0.04	0.084 ± 0.001	0.019 ± 0.002	-
fast decay, τ_{intr}	1.97 ± 0.07	6.85 ± 0.01	2.40 ± 0.08	-
slow decay, τ_{th}	35.21 ± 21	52.51 ± 0.24	18.63 ± 0.51	-
$\frac{A_n}{A_n+A_{th}}$ in %	61.97 ± 0.16	94.32 ± 0.02	76.75 ± 0.46	-
Absorber pulses				
rise time, τ_{intr}	4.46 ± 0.002	5.16 ± 0.002	5.81 ± 0.01	2.60 ± 0.01
fast decay, τ_n	28.89 ± 0.01	53.59 ± 0.01	25.65 ± 0.01	12.40 ± 0.01
slow decay, τ_{th}	546.85 ± 24.00	190.36 ± 0.06	207.13 ± 0.07	98.77 ± 9.5
$\frac{A_n}{A_n+A_{th}}$ in %	98.95 ± 0.01	78.94 ± 0.01	89.80 ± 0.01	93.14 ± 0.01

Table 8.11: Relevant parameters produced by fitting of various templates according to Equation 2.9. All time constants are given in ms. Parameters of $CaWO_4$-MAJA and conventional $CaWO_4$-VK31 are given for comparison. Given errors are statistical.

this operating mode pulses are characterized by different decay times for each signal component and by different exponential rises. The rise time of the non-thermal signal component (A_n) is determined by the intrinsic thermal relaxation time of the thermometer (τ_{intr}), whereas the decay time is given by the lifetime of non-thermal phonons (τ_n). On the other hand, the rise time of the thermal component (A_{th}) is defined by the lifetime of non-thermal phonons (τ_n) and the decay time is given by the thermal relaxation time of the absorber (τ_{th}). Absorber pulses presented in Figure 8.14, 8.15, and 8.16 are fitted according to Equation 8.1 with all parameters set as free variables. It is important to note that for wafer events the thermometer operates in the calorimetric mode[7]. Relevant characteristics obtained with the fits are given in Table 8.11.

From Table 8.11 it can be seen that the amplitude of the thermal component (A_{th}) gives only a marginal contribution to the signal amplitude, i.e. A_{th} is usually < 5 % of the total amplitude. Moreover, the slow decay time of the absorber pulses can exceed the time window in which the pulse is recorded. In

[7]In the calorimetric operating regime pulses are characterized by one common rise time (τ_n) and by two exponential decays, namely fast decay (τ_{intr}) and slow decay (τ_{th}).

these cases, τ_{th} cannot be determined accurately.

In general, the rise time and the decay time of the wafer pulses in all glued detectors are much faster than those of the absorber pulses. Since in glued phonon detectors the shape of the wafer pulses is significantly different from that of the normal absorber pulses, they can be rejected in the dark matter analysis. Therefore, thermometer carrier pulses do not affect the sensitivity in a dark matter search.

Event rate

It is also interesting to check the ratio of the count rates caused by events in the thermometer carrier and by events in the absorber. Taking into account that both of them are made from the same material and assuming purely intrinsic radioactive contaminations, this ratio should be approximately the same as the ratio of volumes of the wafer and the absorber.

From the data shown in Figure 8.12 a ratio of ~ 0.02 is extracted. This value is by 0.02 smaller than expected (0.04). The smaller ratio of the observed wafer events may be explained by SQUID flux quantum losses. Since wafer pulses are very fast, their rise time often exceed the slew rate of the corresponding SQUID, causing it to reset. This results in pulses with characteristic shapes (see left panel in Figure 8.17) which are removed by basic pulse shape cuts.

Stress-relaxation

Additionally to wafer and absorber pulses, another class of pulses with different shape was observed with detector $ZnWO_4$-4 during Run 31. These pulses are characterized by very long rise and decay times. Such a pulse is shown in the right panel of Figure 8.17. Both, the rise and the decay times, are five times longer than those of the normal absorber pulses.

We believe that these pulses originate from stress-relaxation which may occur at the contact area between a crystal and its holding clamps due to a rather tight clamping. In particular, the relaxation may occur in the scintillating plastic layer covering the surface of the clamp. In this case, one would expect pulses of different shape due to the slow propagation of created phonons in plastic. For this reason, the crystal holding has been exchanged to a less tighter one in Run 32. Moreover, there is no scintillating plastic layer covering a clamp any more.

Glue area

Independently on the energy content, more than 90 % of the wafer pulses obtained with detector $ZnWO_4$-4 have a composite structure. Let us consider a representative wafer pulse presented in Figure 8.18. Its structure can be de-

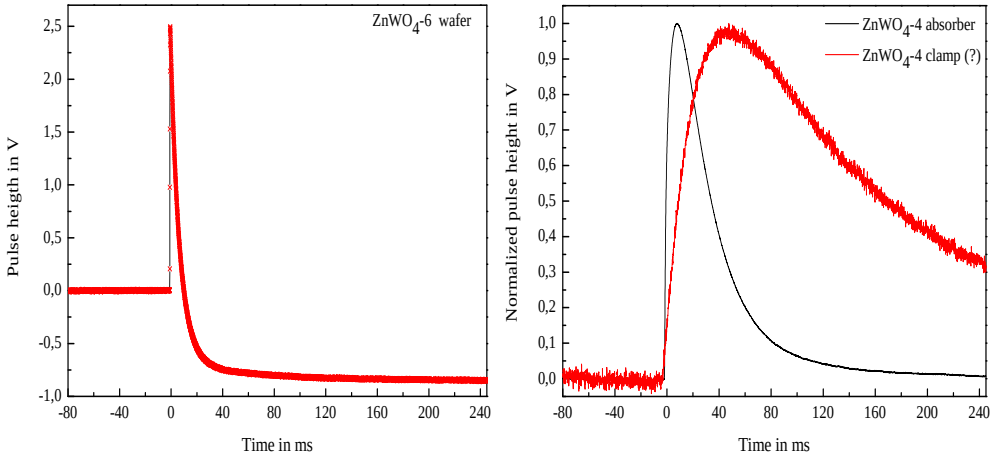

Figure 8.17: *Left*: Example of a wafer pulse with flux quantum loss following a high-energy particle interaction that exceeds the slew rate of the corresponding SQUID. The pulse is obtained with $ZnWO_4$-4 during Run 31. *Right*: Shown in red is an example of a potential stress-relaxation event recorded with the detector $ZnWO_4$-4 during Run 31. The rise time is τ_{intr} = (22.13 ± 0.04) ms and the decay time is τ_n = (148.54 ± 0.19) ms. For comparison, the 122 keV template obtained with the same detector is shown by the black line.

scribed by two components with distinct pulse shapes and amplitudes. The first component looks like a spike and has a very fast rise time, whereas the second one looks more like a normal absorber pulse. In general, the amplitude ratio of wafer-like and absorber-like components is arbitrary.

The composite pulse structure can be described by a superposition of two functions, each of them describing the specific component shape according to Equation 2.9, together with a common onset parameter t_0.

Taking the obtained characteristics for the normal $ZnWO_4$-4 absorber and the wafer pulse from Table 8.11 as input parameters, the result of an amplitude fit is shown in Figure 8.18. It can be seen that the fitting curve agrees reasonably well with the data points. This provides the origin of the wafer-like and the absorber-like signal components.

There can be several sources giving rise to a composite structure:

1 **Radioactivity in the glue**
The kinetic energy of an α-particle, emitted from an α-active contaminant in the glue, may be deposited in the wafer, whereas a γ-particle, emitted in the de-excitation of the daughter nucleus, can be absorbed in the cylindrical crystal. An energy deposition in both parts of the glued detector would result in a pulse with a composite structure.

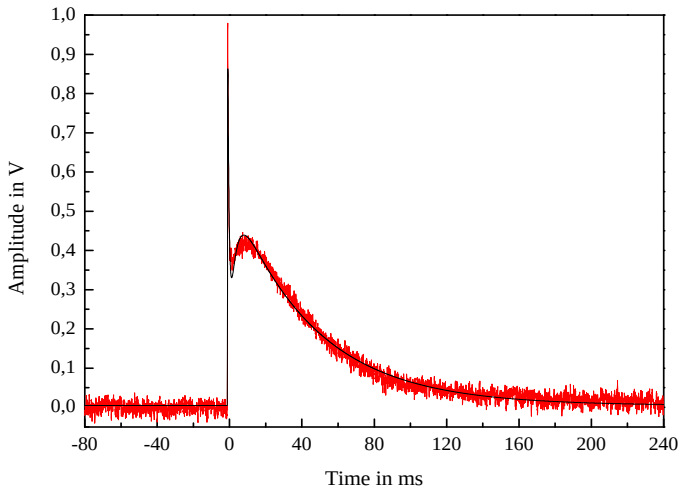

Figure 8.18: Shown in red is a typical thermometer carrier pulse obtained with $ZnWO_4$-4 during Run 31. A composite structure of the pulse is visible. The black line superimposed on the pulse is the result of a fit.

2 **Energetic particle traversing detector**
An energetic γ-particle can be stopped by Compton scattering either in the wafer or in the absorber, resulting in the composite structure.

3 **Transmission through the glue**
When the size of the glue area matches the size of the W-film (48 mm^2) the probability for thermalization of non-thermal phonons in the W-film is approximately the same as for their transmission into the absorber. Thus, $\sim$ 50 % of the non-thermal phonons created after a particle interaction in the wafer can be transmitted into the absorber. Some part of transmitted phonons can, in turn, flow back into the wafer, giving rise to an absorber-like component of the wafer pulse with time constants typical for a normal absorber pulse. The fraction of energy going directly into the thermometer or the absorber depends on the position of the energy deposition in the wafer, explaining the variable fraction of the components.

In the first case, all glued detectors within a certain energy interval should deliver approximately the same rate of wafer pulses with composite pulse structure because the type of glue is the same for all of them. However, most of the wafer pulses observed with $ZnWO_4$-6 and also with $CaWO_4$-MAJA have a single component shape; see Figure 8.15 and 8.16. Hence, the first process cannot be a source for the two-component wafer pulses observed with $ZnWO_4$-4.

Due to the approximate homogeneity of the external radioactive background, also in the second case different glued detectors made from the same material

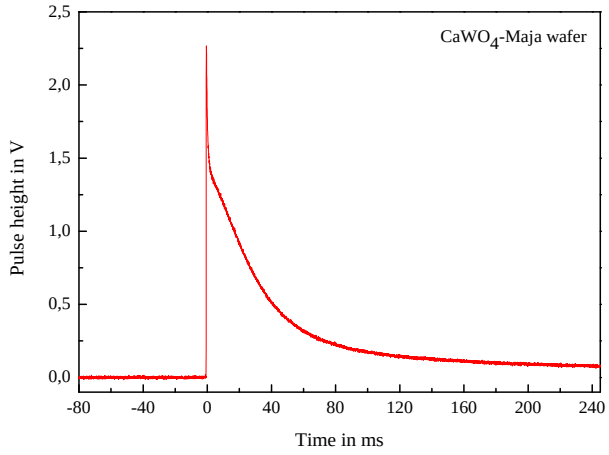

Figure 8.19: A thermometer carrier pulse obtained with $CaWO_4$-MAJA during Run 32. A composite structure of the pulse is visible.

should show roughly the same amount of composite pulses. Accordingly, also this process cannot fully explain the observed effect.

To check the third case let us compare the size of the glue area of $ZnWO_4$-4 and $ZnWO_4$-6. The latter has a glue area approximately four times smaller than that of $ZnWO_4$-4 (~ 40 % of W-SPT). Therefore, the amount of non-thermal phonons which can be transmitted into the absorber of $ZnWO_4$-6 is reduced compared to $ZnWO_4$-4. Thus, it can be conjectured that there are fewer phonons that contribute sufficiently to the rise of the absorber-like component in $ZnWO_4$-6. When the energy depositions are high, a composite structure of wafer pulses is also observed in the detectors $ZnWO_4$-6 and $CaWO_4$-MAJA (though it is less pronounced than in $ZnWO_4$-4); see Figure 8.19. Overall, the third process is the most consistent one with the observed data. Therefore, the composite structure of wafer pulses may be attributed to the transmission of phonons from a wafer to the corresponding absorber through the glue area.

Though the size of the glue area in different phonon detectors tested at Gran Sasso ranges between ~ 10 % to ~ 40 % of the W-film area, all of them can be operated in a stable manner and show excellent energy resolution in the energy region relevant for a WIMP search. Nevertheless, optimization and better control of the glue area size is the topic of ongoing investigations [159, 160]. In general, the smaller a glue area is the longer an absorber pulse lasts. It is important to note that the duration of pulses in the linear response region of a detector is important for the amplitude reconstruction with the help of the truncated fit procedure. For this reason, glue areas bigger than one fifth of the W-film size are currently favored.

Energy in keV	Origin	Detector	Resolution (1σ) in keV
8.0	Cu	$ZnWO_4$-4	0.40 ± 0.05
46.5	^{210}Pb	$ZnWO_4$-4	0.37 ± 0.06
54.8	122 keV-$K_{\beta 1}$	$ZnWO_4$-4	0.32 ± 0.09
62.7	122 keV-K_{α}	$ZnWO_4$-4	0.36 ± 0.07
		$CaWO_4$-VK33	0.47 ± 0.05
65.4	^{179}Ta	$ZnWO_4$-4	0.42 ± 0.18
73.6	^{181}W	$ZnWO_4$-4	0.56 ± 0.12
122.0	^{57}Co	$ZnWO_4$-4	0.77 ± 0.02
		$CaWO_4$-VK33	0.75 ± 0.01
136.5	^{57}Co	$ZnWO_4$-4	0.77 ± 0.04
		$CaWO_4$-VK33	0.73 ± 0.04

Table 8.12: Resolution (1σ) of $ZnWO_4$-4 and conventional $CaWO_4$-VK33 from Gaussian fits to suitable peaks. Data obtained during Run 31.

8.3.2 Energy resolution

In principle, for the dark matter analysis the expected WIMP recoil spectrum has to be convolved with the energy resolution of the phonon detector. Since a WIMP spectrum is expected to be rather featureless, the phonon detector resolution is of little relevance as long as it is significantly better than the discrimination threshold. For $ZnWO_4$-4 the resolution can be inferred from the observed peaks in the calibration and in the background data. Table 8.12 gives the measured resolutions for various energies.

8.3.3 Summary

In Section 8.3.1 it has been shown that events originating from the various parts of the glued $ZnWO_4$ detectors (wafer or absorber) can be clearly separated. An excellent energy resolution better than 1 keV (1σ) at 122 keV can be obtained with the developed detectors. This is comparable with the resolution of the conventional CRESST-II phonon detectors. To conclude, the overall performance of glued $ZnWO_4$ phonon detectors competes with the one for the conventional $CaWO_4$ phonon detectors.

Furthermore, the analysis of the data[8] obtained in Run 32 with the help of the $ZnWO_4$-4/ULRICH detector module showed a fraction of $\sim$ 2.6 % of the

[8]The analysis followed the procedure presented in Section 6.3

deposited energy detected in form of scintillation light[9]. This is an extraordinary high value compared to ~ 1% detected from the conventional $CaWO_4$ phonon detectors; see Table 6.2.

[9]With the glued $CaWO_4$ phonon detector RITA a fraction of ~ 2.2 % of the deposited energy is detected in form of scintillation light in the silicon-on-sapphire light detector [158].

Chapter 9

Conclusions

The main goal of this work has been to investigate the potential of large $CaMoO_4$ and $ZnWO_4$ scintillating crystals as new target materials for the CRESST-II dark matter search experiment and to develop phonon detectors on their basis. For this purpose, scintillation properties and radiopurity of various $ZnWO_4$ samples from NIIC and $CaMoO_4$ samples from BTCP have been studied at room temperature as well as at cryogenic temperatures.

Luminescence, optical and scintillation properties as well as the influence of the mechanical (polishing, roughening) and thermal treatment (annealing, tungsten-film deposition) on the scintillation efficiency have been investigated. This has helped to improve both, the light yield and the resolution of the crystals. Moreover, the studies have allowed to give feedback to the crystal-producers which may help to further optimize the conditions of crystal growth as well as after-growth processing.

A number of short cool down runs have been performed at MPI in order to investigate the scintillation properties of the crystals at mK temperatures. In particular, the light output and scintillation decay time constants of $CaMoO_4$ and $ZnWO_4$ crystals have been measured for the first time. With the small $ZnWO_4$ sample almost two times more scintillation light has been detected when compared to the reference $CaWO_4$ crystal. Indeed, this is the largest amount of scintillation light detected among the various scintillating crystals tested up to now. On the other hand, measurements with the $CaMoO_4$ sample have shown that its light yield is a factor of 2.5 worse than that of $CaWO_4$.

Subsequently, first phonon detectors with 200 g $CaMoO_4$ and 400 g $ZnWO_4$ absorbers were built. For $ZnWO_4$ detectors this has been achieved with a new detector design in which the thermometer carrier is decoupled from the absorber. This concept allows for a production of phonon detectors without affecting the scintillation properties of the absorber crystal due to tungsten-film deposition.

Furthermore, this design is particularly interesting for large-scale detector production as needed for experiments like EURECA [105]. First results on the development of $CaMoO_4$ and glued $ZnWO_4$ phonon detectors have been published in [109].

The thermal response of the $CaMoO_4$ phonon detectors has been tested at mK temperatures at MPI and has shown promising results. However, because of the relatively poor scintillation light output of the crystals, the developed detectors were not installed in the low background facility of the experiment. Optimization-studies of growth conditions and of raw materials in order to potentially improve the light yield of $CaMoO_4$ crystals are ongoing [161, 86]. It should be stressed that $CaMoO_4$ detectors are particularly interesting for the multiple target approach because the heaviest nucleus in the compound is different from tungsten. This is important for establishing a true WIMP signal by testing for an A^2 scaling of the elastic WIMP-nucleon scattering cross section.

The prototype $ZnWO_4$ detector has been integrated into the setup at Gran Sasso for Run 31 where it has been operated for the first time. In the course of this work, extensive studies have been carried out in order to characterize the detector performance. The obtained energy resolution of ~ 0.4 keV (1σ) at 46.5 keV achieved for the glued $ZnWO_4$ detectors is perfectly adequate for a dark matter search experiment and is comparable with that of standard $CaWO_4$ phonon detectors. It has also been shown that pulses originating in the thermometer carrier can be distinguished clearly from absorber pulses and, therefore, represent no danger for the dark matter analysis.

Furthermore, background from natural radioactive decay chains and other α-unstable isotopes, as well as background caused by γ/β-particles has been identified in $ZnWO_4$ with a sensitivity of a few μBq/kg and described quantitatively. The total amount of internal α-active impurities measured in the detector $ZnWO_4$-4 is $\sim$ 1.2 mBq/kg. This is one order of magnitude lower in comparison to the representative $CaWO_4$ crystal. The total background rate in the energy region relevant for a dark matter search, i.e. below 100 keV, is only 4 counts/kg/keV/day. This is a factor of two lower than the typical rate observed with $CaWO_4$ detectors.

The results discussed in this thesis have proven a high potential of $ZnWO_4$ crystals as target material for dark matter searches. Because of the excellent characteristics obtained with the developed 400 g $ZnWO_4$ phonon detectors, this material will be used as an additional target unit for the CRESST-II experiment.

At the time of writing, 18 detector modules are installed in the cold box of the CRESST cryostat at Gran Sasso, including two detector modules with $ZnWO_4$ crystals. Data taking in Run 32 is currently ongoing. However, due to technical reasons, no dark matter data has yet been obtained from the $ZnWO_4$ detectors. In the intermediate future it is planned to fill half of the experimental volume with

$ZnWO_4$ detectors. This would not only provide an increase of the experimental sensitivity due to higher scintillation efficiency and exceptional radiopurity of the $ZnWO_4$ crystals but would also offer a multiple target choice.

Bibliography

[1] F. Zwicky, *Die Rotverschiebung von extragalaktischen nebeln*, *Helv. Phys. Acta* **6** (1933) 110–127. [cited at p. 1]

[2] G. G. Raffelt, *Dark matter: Motivation, candidates and searches*, hep-ph/9712538. [cited at p. 2]

[3] *National Aeronautics and Space Administration*. Homepage at http://www.nasa.gov/, 2009. [cited at p. 3]

[4] Spergel, D. N. and others, *First Year Wilkinson Microwave Anisotropy Probe (WMAP) Observations: Determination of Cosmological Parameters*, *Astrophys. J. Suppl.* **148** (2003) 175–194. [cited at p. 3]

[5] Spergel, D. N. and others, *Three-year Wilkinson Microwave Anisotropy Probe (WMAP) observations: polarization analysis*, *Astrophys. J. Suppl.* **1**70 (2007) 335–376. [cited at p. 3]

[6] Komatsu, E. and others, *Five-Year Wilkinson Microwave Anisotropy Probe (WMAP) Observations: Cosmological Interpretation*, *Astrophys. J. Suppl.* **180** (2009) 330–376. [cited at p. 3]

[7] C. J. Copi and D. N. Schramm, *The nuclear impact on cosmology: The H(0)-Omega diagram*, *Comm. Nucl. Part. Phys.* **2**2 (1996) 1–18 [astro-ph/9504026]. [cited at p. 4]

[8] Dunkley, J. and others, *Five-Year Wilkinson Microwave Anisotropy Probe Observations: Cosmological Interpretation*, *Astrophys. J. Suppl.* **1**80 (2009) 330–379. [cited at p. 4, 5]

[9] G. Jungman *et. al.*, *Supersymmetric dark matter*, *Phys. Rept.* **2**67 (1996) 195–373 [hep-ph/9506380]. [cited at p. 5, 8, 9]

[10] Bergstrom, L., *Non-baryonic dark matter: observational evidence and detection methods*, *Reports on Progress in Physics* **63** (2000) 793. [cited at p. 5]

[11] **A**MANDA Collaboration, J. Ahrens *et. al.*, *Results from the AMANDA telescope*, *Nucl. Phys.* **A**721 (2003) 545–548. [cited at p. 5]

[12] L. J. Rosenberg and K. A. van Bibber, *Searches for invisible axions*, *Phys. Rept.* **3**25 (2000) 1–39. [cited at p. 6]

[13] K. A. Olive, *Primordial nucleosynthesis and dark matter*, astro-ph/9707212. [cited at p. 6]

[14] H. Goldberg, *Constraint on the photino mass from cosmology*, *Phys. Rev. Lett.* **5**0 (1983) 1419. [cited at p. 6]

[15] J. R. Ellis, J. S. Hagelin, D. V. Nanopoulos, K. A. Olive and M. Srednicki, *Supersymmetric relics from the big bang*, *Nucl. Phys.* **B**238 (1984) 453–476. [cited at p. 6]

[16] C. Amsler *et. al.*, *Particle data group*, *Phys. Lett.* **B**667 (2008) 1–1340. [cited at p. 7, 18]

[17] G. Angloher *et. al.*, *Commissioning Run of the CRESST-II Dark Matter Search*, *Astroparticle Physics* **3**1 (2009) 270–276 [**0**809.1829]. [cited at p. 8, 25, 39, 40, 72, 115]

[18] A. Benoit *et. al.*, *Improved exclusion limits from the EDELWEISS WIMP search*, *Phys. Lett.* **B**545 (2002) 43–49. [cited at p. 8, 72]

[19] D. S. Akerib *et. al.*, *First results from the cryogenic dark matter search in the Soudan Underground Lab*, *Phys. Rev. Lett.* **9**3 (2004) 211301 [astro-ph/0405033]. [cited at p. 8, 72]

[20] J. Angle *et. al.*, *First Results from the XENON10 Dark Matter Experiment at the Gran Sasso National Laboratory*, *Phys. Rev. Lett.* **1**00 (2008) 021303 [**0**706.0039]. [cited at p. 8, 72]

[21] J. Engel, *Nuclear form factors for the scattering of neutralinos*, *Nucl. Phys. Proc. Suppl.* **2**8A (1992) 310–313. [cited at p. 9]

[22] K. Freese *et. al.*, *Signal Modulation in Cold Dark Matter Detection*, *Phys. Rev.* **D**37 (1988) 3388. [cited at p. 10]

[23] R. Lang, *private communication*, 2008. [cited at p. 11]

[24] Donato, F. and others, *Effects of galactic dark halo rotation on WIMP direct detection*, *Astroparticle Physics* **9** (1998) 247–260. [cited at p. 10]

[25] G. Angloher *et. al.*, *Limits on WIMP dark matter using scintillating CaWO4 cryogenic detectors with active background suppression*, *Astropart. Phys.* **2**3 (2005) 325–339 [astro-ph/0408006]. [cited at p. 13, 25, 39, 115]

[26] *Cryogenic Rare Event Search with Superconducting Thermometers*, 2009. Homepage of the experiment at http://www.cresst.de/. [cited at p. 13]

[27] R. F. Lang, *Search for dark matter with the CRESST experiment*. PhD thesis, Technische Universität München, 2008. [cited at p. 14, 15, 35, 36, 39, 111, 134, 138]

[28] *LNGS-Gran Sasso National Laboratory*. Homepage of the laboratory at http://www.lngs.infn.it/, 2009. [cited at p. 14, 18]

[29] M. Aglietta *et. al.*, *Muon "depth–intensity" relation measured by the LVD underground experiment and cosmic–ray muon spectrum at sea level*, *Phys. Rev. D* **5**8 (1998) 092005. [cited at p. 14]

[30] R. B. Firestone *et. al.*, *Table of Isotopes (CD ROM Edition)*. John Wiley and Sons, New York, 1st ed., 1996. [cited at p. 15, 17, 86, 101, 124, 126, 130, 131, 133, 138, 139, 179, 181, 183]

[31] A. Bassignani *et. al.*, *Review of long term radon studies at the Gran Sasso underground laboratory*, *Rad. Meas.* **2**5 (1995), no. 1-4 557–560. [cited at p. 16]

[32] A. Bassignani *et. al.*, *Measurements of radon concentration and gamma ray activity in hall B of the Gran Sasso laboratory*, *Rad. Meas.* **2**8 (1997), no. 1-6 609–612. [cited at p. 16]

[33] Arpesella, C. and others, *Background measurements at Gran Sasso laboratory*, *Applied radiation and isotopes* **4**7 (1996), no. 9-10 991–996. [cited at p. 17]

[34] Arpesella, C. and others, *Background measurements at Gran Sasso laboratory*, *Nucl. Phys. B (Proc. Suppl.)* **2**8A (1992) 420–424. [cited at p. 16]

[35] C. Bellotti *et. al.*, *New measurement of rock contaminations and neutron activity in the Gran Sasso tunel*, *INFN/TC-85/19* (1985). [cited at p. 18]

[36] H. Wulandari, *Study on neutron-induced background in the dark matter experiment CRESST*. PhD thesis, Technische Universität München, 2003. [cited at p. 18]

[37] H. Wulandari *et. al.*, *Neutron background studies for the CRESST dark matter experiment*, *Arxiv preprint hep-ex/0401032* (2004). [cited at p. 19]

[38] F. J. Kerr *et. al.*, *Review of galactic constants*, *Monthly Notices of Royal Astronomical Society* **2**21 (1986) 1023–1038. [cited at p. 19]

[39] F. Probell, *Matter and methods at low temperature*. Springer Berlin, first ed., 1992. [cited at p. 20]

[40] G. Angloher *et. al.*, *CRESST-II: dark matter search with scintillating absorbers*, *Nucl. Instrum. Meth. A* **5**20 (2004) 108–111. [cited at p. 22, 25, 115]

[41] B. Majorovits *et. al.*, *Production of low background CuSn6-bronze for the CRESST dark matter search experiment*, *Applied Radiation and Isotopes* (2008). accepted. [cited at p. 22]

[42] P. Meunier *et. al.*, *Discrimination between nuclear recoils and electron recoils by simultaneous detection of phonons and scintillation light*, physics/9906017. [cited at p. 24, 112, 114]

[43] D. Wahl, *Optimization of light collection in inorganic scintillators for rare event searches*. PhD thesis, University of Oxford, 2005. [cited at p. 26, 71, 108]

[44] R. O. Keeling, *Studies of scintillators for the CRESST dark matter search*. PhD thesis, University of Oxford, 2002. [cited at p. 26, 56, 77]

[45] A. Askin, *Light Yield Investigation of Titanium Doped Al2O3 Crystals for CRESST DM Search*, Master's thesis, Universität Siegen, 2006. [cited at p. 26, 112, 114]

[46] P. C. F. Stefano *et. al.*, *The SciCryo project and cryogenic scintillation of Al2O3 for dark matter*, *J. Low Temp. Phys.* **1**51 (2008) 902. [cited at p. 26]

[47] P. Lecoq *et. al.*, *Inorganic scintillators for detector systems: Physical principles and crystal engineering*. Springer–Verlag Berlin Heidelberg, 2006. [cited at p. 26, 54, 56, 66, 69]

[48] I. Bavykina *et. al.*, *Investigation of ZnWO4 crystals as scintillating absorbers for direct dark matter search experiments*, *IEEE Trans. Nucl. Sci.* **5**5 (2008) 1449–1452. [cited at p. 26]

[49] H. Kraus *et. al.*, *Feasibility of a ZnWO4 scintillator for exploiting materials signature in cryogenic WIMP dark matter searches*, *Phys. Lett.* **B**610 (2005) 37–44. [cited at p. 26, 66, 100, 105]

[50] F. A. Danevich *et. al.*, *ZnWO4 crystals as detectors for 2-beta decay and dark matter experiments*, *Nucl. Instrum. Meth.* **A**544 (2005) 553–564. [cited at p. 26, 27]

[51] A. N. Annenkov *et. al.*, *Development of CaMoO4 crystal scintillators for double beta decay experiment with Mo-100*, *Nucl. Instrum. Meth.* **A**584 (2008) 334–345 [**0**707.1428]. [cited at p. 26, 27, 66]

[52] V. B. Mikhailik *et. al.*, *Temperature dependence of CaMoO4 scintillation properties*, *Nucl. Instrum. Meth.* **A**583 (2007) 350–355. [cited at p. 26, 96, 108]

[53] F. A. Danevich, *Radioactive contamination of crystal scintillators*, in *Proceedings of RPScint'2008*, pp. 28–36, Institute for Nuclear Research, Kyiv, Ukraine, 2008. nucl-ex/0903.1539. [cited at p. 27]

[54] S. Pirro *et. al.*, *Scintillating double beta decay bolometers*, *Phys. Atom. Nucl.* **6**9 (2006) 2109–2116 [nucl-ex/0510074]. [cited at p. 27]

[55] P. Belli *et. al.*, *Search for 2-beta processes in Zn64 with the help of ZnWO4 crystal scintillator*, *Phys. Lett.* **B**658 (2008) 193–197. [cited at p. 27]

[56] J. K. Bohlke *et. al.*, *Isotopic compositions of the elements, 2001*, *Journal of Physical and Chemical Reference Data* **3**4 (2005), no. 1 57–68. [cited at p. 27]

[57] F. Petricca, *Dark matter search with cryogenic phonon-light detectors*. PhD thesis, Ludwig-Maximilians-Universität München, 2005. [cited at p. 28, 29, 30, 100]

[58] J. Ninkovic, *Investigation of CaWO4 crystals for simultaneous phonon-light detection in the CRESST dark matter search*. PhD thesis, Technische Universität München, 2005. [cited at p. 29, 62, 73, 77, 87, 95, 130]

[59] J. C. Lanfranchi *et. al.*, *Development of a cryogenic detection concept for GNO*, *Nucl. Instrum. Meth.* **A**520 (2004) 135–137. [cited at p. 29]

[60] T. Frank, *Development of scintillating calorimeters for the discrimination of nuclear recoils and fully ionizing events*. PhD thesis, Technische Universität München, 2002. [cited at p. 29, 69, 74, 75, 77, 90, 100, 114]

[61] E. Pantic, *Performance of cryogenic light detectors in the CRESST-II dark matter search*. PhD thesis, Technische Universität München, 2008. [cited at p. 30, 38, 43, 100]

[62] P. Huff, *Sensitivity of light detectors in the CRESST–II experiment*. PhD thesis, Technische Universität München, in preparation. [cited at p. 30, 62]

[63] C. Kittel and P. McEuen, *Introduction to solid state physics*. Wiley New York, 1986. [cited at p. 30, 176]

[64] F. Pröbst *et. al.*, *Model for cryogenic particle detectors with superconducting phase transition thermometers*, *J. Low Temp. Phys.* **1**00 (1995) 69. [cited at p. 31]

[65] B. Majorovits *et. al.*, *Development of superconducting contacts for the CRESST-II 66-channel superconducting quantum interference device readout system*, *Rev. Sci. Instrum.* **7**8 (2007) 073301. [cited at p. 35, 37]

[66] S. Henry *et. al.*, *The 66-channel SQUID readout for CRESST II*, *J. of Instrum.* **2** (2007) 11003. [cited at p. 37, 39]

[67] R. McGowan, *Data Analysis and results of the upgraded CRESST dark matter search*. PhD thesis, University of Oxford, 2008. [cited at p. 39]

[68] B. Tolhurst, *OxRop: Data Analysis Software for CRESST-II*. PhD thesis, University of Oxford, 2007. [cited at p. 39]

[69] S. E. Derenzo *et. al.*, *The quest for the ideal inorganic scintillator*, *Nuclear Inst. and Methods in Physics Research, A* **5**05 (2003), no. 1-2 111–117. [cited at p. 52]

[70] J. B. Birks, *Theory and practice of scintillation counting*. Pergamon, 1967. [cited at p. 53, 55, 56, 58, 59, 60]

[71] Lempicki, A. and Wojtowicz, AJ and Berman, E., *Fundamental limits of scintillator performance*, *Nucl. Instrum. Methods Phys. Res. A* **333** (1993) 304–311. [cited at p. 53]

[72] P. A. Rodnyi, *Physical processes in inorganic scintillators*. CRC Press LLC, 1997. [cited at p. 55, 56, 59, 60, 66, 93, 108]

[73] G. Blasse and B. C. Grabmaier, *Luminescent materials*. Springer-Verlag Berlin, 1994. [cited at p. 55, 56]

[74] P. J. Franck and E. G. Dymond, *Elementary processes of photochemical reactions*, *Transactions of the Faraday Society* **2**1 (1926) 536–542. [cited at p. 58]

[75] E. Condon, *A theory of intensity distribution in band systems*, *Physical Review* **2**8 (1926), no. 6 1182–1201. [cited at p. 58]

[76] C. Coppi *et. al.*, *Quenching factor measurement for CaWO4 by neutron scattering*, *Nucl. Instrum. Meth.* **A**559 (2006) 396–398. [cited at p. 61, 62]

[77] T. Jagemann *et. al.*, *Neutron scattering facility for the measurement of nuclear recoil quenching factors*, *Nucl. Instrum. Meth.* **A**551 (2005) 245–260. [cited at p. 61]

[78] T. Jagemann *et. al.*, *Measurement of nuclear recoil quenching factors in CaWO4*, *Astropart. Phys.* **2**6 (2006) 269–281. [cited at p. 61]

[79] C. Coppi. PhD thesis, Technische Universität München, in preparation. [cited at p. 61]

[80] C. Ciemniak. PhD thesis, Technische Universität München, in preparation. [cited at p. 61]

[81] J. Ninkovic *et. al.*, *New Technique for the Measurement of the Scintillation Efficiency of Nuclear Recoils*, *Nucl. Instrum. Meth.* **A**564 (2006) 567–578 [astro-ph/0604094]. [cited at p. 62]

[82] Q. Kronseder Master's thesis, Ludwig-Maximilians-Universität München, in preparation. [cited at p. 62]

[83] I. Bavykina *et. al.*, *Interpretation of Light-Quenching Factor Measurements*, *Astropart. Phys.* **2**8 (2007) 489–493 [**0**707.0766]. [cited at p. 62]

[84] M. Globus *et. al.*, *Inorganic scintillators for modern and traditional applications*. Institute for single crystals Ukraine-Kharkiv, 2005. [cited at p. 66, 68, 69]

[85] Y. V. Vasiliev, *private communication*, 2008. [cited at p. 66, 74]

[86] M. Korzhik, *private communication*, 2007. [cited at p. 66, 70, 152]

[87] M. V. Pashkovskiy, *Influence of structural defects on the physical properties of wolframites*. Visha Shkola Lviv, 1978. in Russian. [cited at p. 66, 67, 81, 100]

[88] C. Ronda, *Luminescence: from Theory to Applications*. Wiley-VLH, 2008. [cited at p. 66, 81]

[89] V. N. Kolobanov *et. al.*, *Optical and luminescent properties of anisotropic tungstate crystals*, *Nuclear Inst. and Methods in Physics Research, A* **4**86 (2002), no. 1-2 496–503. [cited at p. 66]

[90] Y. Zhang *et. al.*, *Electronic band structures of the scheelite materials CaMoO4, CaWO4, PbMoO4 and PbWO4*, *Physical review. B, Condensed matter* **5**7 (1998), no. 20 12738–12750. [cited at p. 66, 83]

[91] M. Moszynski *et. al.*, *Characterization of cawo4 scintillator at room and liquid nitrogen temperatures*, *Nucl. Instrum. Meth.* **A**553 (2005) 578–591. [cited at p. 66, 95]

[92] M. V. Korzhik *et. al.*, *Large volume CaMoO4 scintillation crystals*, *IEEE Trans. Nucl. Sci.* **5**5 (2008) 1473–1475. [cited at p. 66, 96]

[93] M. Gluyas *et. al.*, *The elastic constants of calcium tungstate, 42-300 K*, *J. Phys. D: Appl. Phys.* **6** (1973) 2025–2037. [cited at p. 66]

[94] H. Wang *et. al.*, *The line shape and zero-phonon line of the luminescence spectrum from zinc tungstate single crystals*, *J. Phys.: Condens. Matter* **6** (1994), no. 28 5373. [cited at p. 66]

[95] A. Senyshyn *et. al.*, *Thermal properties of CaMoO4: Lattice dynamics and synchrotron powder diffraction studies*, *Phys. Rev. B* **7**3 (2006) 014104. [cited at p. 66]

[96] V. Angelelli and S. Gordon, *Sanmartinite - a new zinc tungstate from Argentine*, *The Academy of Natural Sciences* (1948). [cited at p. 65]

[97] P. Dunn, *Sanmartinite: new data*, *Mineralogical Magazine* **4**2 (1978), no. 322 281–281. [cited at p. 65]

[98] A. W. Sleight, *Accurate cell dimentions for ABO4 molybdates and tungstates*, *Acta Cryst.* **B28** (1972) 2899–2902. [cited at p. 67]

[99] R. M. Hazen *et. al.*, *High-pressure crystal chemistry of scheelite-type tungstates and molybdates*, *J. Phys. Chem. Solids* **4**6 (1985), no. 253-263. [cited at p. 67]

[100] T. Hahn editor, *International tables for crystallography*, *D. Reidel, Boston* **A** (1987). [cited at p. 66, 67]

[101] J. D. Jackson and R. F. Fox, *Classical electrodynamics*, *American Journal of Physics* **6**7 (1999) 841. [cited at p. 68]

[102] Y. A. Borovlev *et. al.*, *Progress in growth of large sized BGO crystals by the low-thermal-gradient Czochralski technique*, *J. Cryst. Growth* **2**29 (2001) 305–311. [cited at p. 70]

[103] E. N. Galashov *et. al.*, *Growing of ZnWO4 single crystals from melt by the low thermal gradient Czochralski technique*, *Functional Materials* **1**6 (2009), no. 1 63–66. [cited at p. 70]

[104] K. Takagi *et. al.*, *Growth of high purity ZnWO4 single crystals*, *J. of Cryst. Growth* **5**2 (1981) 580–583. [cited at p. 70, 77]

[105] H. Kraus *et. al.*, *EURECA - setting the scene for scintillators*, in *Proceedings of RPScint'2008*, pp. 7–10, Institute for Nuclear Research, Kyiv, Ukraine, 2008. nucl-ex/0903.1539. [cited at p. 71, 152]

[106] A. A. Blistanov *et. al.*, *Luminescence of crystals of divalent tungstates*, *Crystallography Reports* **5**0 (2005), no. 2 284–290. [cited at p. 73, 84, 85]

[107] *Heraeus Quarzglas GmbH and Co. KG* . Homepage at http://corporate.heraeus.com/, 2008. [cited at p. 74]

[108] M. Kiefer *et. al.*, *Glued $CaWO_4$ detectors for the CRESST-II experiment*, *Optical Materials* **3**1 (2009). [cited at p. 74, 142]

[109] I. Bavykina *et. al.*, *Development of cryogenic phonon detectors based on CaMoO4 and ZnWO4 scintillating crystals for direct dark matter search experiments*, *Optical materials* **3**1 (2009) 1382–1387 [**0**811.1786]. [cited at p. 74, 152]

[110] S. Roth *et. al.*, *Cryogenic Composite Detectors for the Dark Matter Experiments CRESST and EURECA*, *Optical materials* **3**1 (2009) [**0**810.0423]. [cited at p. 74, 142]

[111] J. Ninkovic *et. al.*, *CaWO4 crystals as scintillators for cryogenic dark matter search*, *Nucl. Instrum. Meth.* **A**537 (2005) 339–343. [cited at p. 75]

[112] *ESK–Ceramics*. Homepage at http://www.esk.com/, 2008. [cited at p. 75]

[113] E. N. Galashov, *private communication*, 2008. [cited at p. 75]

[114] L. Stodolsky *et. al.*, *Some Practical Applications of Dark Matter Research*, *ArXiv e-prints* (2008) [0810.4446]. [cited at p. 75]

[115] Y. V. Vasiliev, *Big sized CdWO4 (CWO) scintillation crystals grown in NIIC by the LTG Cz technique*. Talk given at Max-Planck-Institute for Physics, 2008. [cited at p. 77]

[116] M. Korzhik, *Tungstate and molybdate based scintillators for experimental physics applications*. Talk given at Max-Planck-Institute for Physics, 2007. [cited at p. 77]

[117] I. Földvari *et. al.*, *The role of OH- ions in the charge compensation of impurities in ZnWO4 single crystals*, *Phys. Lett. A* **1**35 (1989), no. 6,7 363–367. [cited at p. 77, 78]

[118] I. Földvari *et. al.*, *Improvement of the quality of ZnWO4 single crystals for scintillation applications*, *J. of Cryst. Growth* **7**9 (1986) 714–719. [cited at p. 77]

[119] A. Watterich *et. al.*, *Point defects identified by spectroscopic methods in ZnWO4 single crystal*, *Rad. Prot. Dosimetry* **6**5 (1996) 97–100. [cited at p. 77, 78]

[120] A. Watterich *et. al.*, *Coloration, impurities and non-local charge compensation in ZnWO4*, *Solid State Commun.* **8**8 (1993) 619. [cited at p. 77]

[121] A. Watterich *et. al.*, *ESR of platinum impurity ions in ZnWO4 single crystals*, *J. Phys. Chem. Solids.* **5**2 (1991) 449. [cited at p. 77]

[122] L. F. Bencs *et. al.*, *Removal of iron, chromium and sodium impurities from zinc tungstate*, *J. of Cryst. Growth* **1**81 (1997) 455–458. [cited at p. 78]

[123] M. A. Green *et. al.*, *Optical properties of intrinsic silicon at 300 K*, *Progress in Photovoltaics* **3** (1995) 189–192. [cited at p. 81]

[124] *Ocean Optics Company*. Homepage at http://www.oceanoptics.com/, 2008. [cited at p. 82]

[125] T. Marrodan Undagoitia, *Measurement of light emission in organic liquid scintillators and studies towards the search for proton decay in the future large-scale detector LENA*. PhD thesis, Technische Universität München, 2008. [cited at p. 83]

[126] A. B. van Oosterhout, *An ab initio calculation on the WO6(6-) octahedron with an application to its luminescence*, *The Journal of Chemical Physics* **6**7 (1977), no. 6 2412–2418. [cited at p. 83]

[127] V. B. Mikhailik *et. al.*, *Luminescence of CaWO, CaMoO, and ZnWO scintillating crystals under different excitations*, *Journal of Applied Physics* **9**7 (2005) 083523. [cited at p. 83, 84]

[128] J. A. Groenink *et. al.*, *The luminescence of calcium molybdate*, *Physica Status Solidi (a)* **5**4 (1979), no. 1. [cited at p. 83, 84, 108]

[129] R. Grasser *et. al.*, *Optical properties of CaWO4 and CaMoO4 crystals in the 4 to 25 eV region*, *Physica Status Solidi (b)* **6**9 (1975), no. 2. [cited at p. 83]

[130] V. B. Mikhailik, *Radiative decay of self-trapped excitons in CaMoO4 and MgMoO4 crystals*, *J. of Phys. Condensed Matter* **1**7 (2005) 7209. [cited at p. 83]

[131] V. Nagirnyi *et. al.*, *Energy transfer in ZnWO4 and CdWO4 scintillators*, *Nucl. Instrum. Meth.* **4**86 (2002) 395–398. [cited at p. 84]

[132] A. E. Ovechkin *et. al.*, *Luminescence of ZnWO4 and CdWO4 Crystals*, *Physica Status Solidi (a)* **1**03 (1987), no. 1. [cited at p. 84]

[133] V. Babin *et. al.*, *Decay kinetics of the green emission in tungstates and molybdates*, *Rad. Meas.* **3**8 (2004) 533–537. [cited at p. 84, 108]

[134] *Technical data sheet of the XP3461B PMT*. [cited at p. 87]

[135] W. Swank *et. al.*, *Spectral effects in the comparison of scintillators and photomultipliers*, *Rev. Sci. Inst.* **2**9 (1958), no. 4 279. [cited at p. 87, 88]

[136] G. F. Knoll, *Radiation detection and measurement*. New York: Wiley, 2000. [cited at p. 89]

[137] P. C. F. Stefano *et. al.*, *Textured silicon calorimetric light detector*, *J. Appl. Phys.* **9**4 (2003), no. 10 6887–6891. [cited at p. 108, 112, 114]

[138] W. Westphal *et. al.*, *Detector calibration measurements in CRESST*, *NIM* **A**559 (2006) 372–374. [cited at p. 108]

[139] H. Kraus *et. al.*, *Multiple photon counting coincidence (MPCC) technique for scintillator characterization and its application to studies of CaWO4 and ZnWO4 scintillators*, *Nucl. Instrum. Meth.* **A**553 (2005) 522–534. [cited at p. 108]

[140] V. B. Mikhailik *et. al.*, *Scintillation studies of CaWO4 in the millikelvin temperature range*, *Phys. Rev.* **B**75 (2007) 184308. [cited at p. 108]

[141] G. Blasse and G. Bokkers, *Low-temperature decay-time measurements on the luminescence of calcium tungstate (CaWO4)*, *Journal of solid state chemistry(Print)* **4**9 (1983), no. 1 126–128. [cited at p. 108]

[142] W. W. Moses, *Current trends in scintillator detectors and materials*, *Nucl. Instrum. Meth.* **A**487 (2001) 123–128. [cited at p. 110, 111]

[143] I. Bavykina, *Investigation of ZnWO4 crystals as absorbers in the CRESST Dark Matter search*, Master's thesis, Universität Siegen, 2006. http://publications.mppmu.mpg.de/2006/MPP-2006-114/FullText.pdf. [cited at p. 111, 117]

[144] R. B. Murray and A. Meyer, *Scintillation response of activated inorganic crystals to various charged particles*, *Physical Review* **1**22 (1961), no. 3 815–826. [cited at p. 111]

[145] C. D. Zerby *et. al.*, *Intrinsic line broadening in NaI (Tl) gamma-ray spectrometers*, *Nucl. Instr. Meth* **1**2 (1961) 115. [cited at p. 111]

[146] P. Dorenbos *et. al.*, *Non-proportionality in the scintillation response and the energyresolution obtainable with scintillation crystals*, *IEEE Transactions on Nuclear Science* **4**2 (1995), no. 6 Part 2 2190–2202. [cited at p. 111]

[147] J. D. Valentine *et. al.*, *The light yield nonproportionality component of scintillator energyresolution*, *IEEE Transactions on Nuclear Science* **4**5 (1998), no. 3 Part 1 512–517. [cited at p. 111]

[148] W. W. Moses *et. al.*, *Scintillator non–proportionality: Present Understanding and Future Challengies*, *IEEE Trans. Nucl. Sci.* **5**5 (2008) 1049–1453. [cited at p. 111]

[149] W. Westphal, *Development and characterization of cryogenic detectors for the CRESST experiment*. PhD thesis, Technische Universität München, 2008. [cited at p. 114]

[150] *Technical data sheet of the Epo–Tek 301-2*, 2009. http://www.epotek.com/SSCDocs/datasheets/301-2.PDF. [cited at p. 118]

[151] J. Schmaler *et. al.*, *Status of the CRESST Dark Matter Search*, *proceedings on 13th International Workshop on Low Temperature Detectors* (2009). in press. [cited at p. 123, 127]

[152] K. Schäffner. PhD thesis, Technische Universität München, in preparation. [cited at p. 123]

[153] *National Nuclear Data Center*. Homepage at http://www.nndc.bnl.gov/qcalc/index.jsp, 2009. [cited at p. 127, 130, 131, 132, 179, 181, 183]

[154] J. Völkening *et. al.*, *Tungsten isotope ratio determinations by negative thermal ionization mass spectrometry*, *International Journal of Mass Spectrometry and Ion Processes* **1**07 (1991), no. 2 361–368. [cited at p. 130, 133]

[155] C. Cozzini *et. al.*, *Detection of the Natural Alpha Decay of Tungsten*, *Phys. Rev.* **C**70 (2004) 064606 [nucl-ex/0408006]. [cited at p. 129, 133]

[156] A. Tolhurst, *OxRop: Data Analysis Software for CRESST–II*. PhD thesis, University of Oxford, 2007. [cited at p. 134]

[157] M. Jelen, *The CRESST Dark Matter Search–Background Considirations and Data Analysis*, Master's thesis, Technische Universität München, 2006. [cited at p. 134]

[158] M. Kiefer *et. al.*, *Glued CaWO4 detectors for the CRESST-II experiment*, *proceedings on 13th International Workshop on Low Temperature Detectors* (2009). in press. [cited at p. 141, 150]

[159] S. Roth. PhD thesis, Technische Universität München, in preparation. [cited at p. 148]

[160] M. Kiefer. PhD thesis, Technische Universität München, in preparation. [cited at p. 148]

[161] V. Kornoukhov, *private communication*, 2009. [cited at p. 152]

[162] S. Nissi, *private communication*, 2008. [cited at p. 169]

[163] *NIST X-ray and gamma-ray attenuation coefficients and cross sections database*, 2008. Homepage at http://physics.nist.gov/PhysRefData/Xcom/Text. [cited at p. 173]

[164] B. B. Triplett *et. al.*, *Critical field for superconductivity and low-temperature normal-state heat capacity of tungsten*, *Journal of Low Temperature Physics* **1**2 (1973), no. 5 499–518. [cited at p. 176]

[165] Bardeen, J. and Cooper, L.N. and Schrieffer, J.R., *Theory of superconductivity*, *Physical Review* **108** (1957), no. 5 1175–1204. [cited at p. 176]

[166] *Argonne National Laboratory*. Homepage at http://www.anl.gov/, 2005. [cited at p. 177, 178, 180, 182]

Appendices

Appendix A

Results of the ICP–MS measurements

Inductively coupled plasma mass spectrometry (ICP–MS) measurements have been performed in the chemical laboratory at LNGS [162]. Firstly, small crystal samples are mechanically reduced to powder. The powder is then dissolved in an ultrasound bath at ~ 70 °C using a mixture of nitric (HNO_3) and hydrochloric (HCl) or HNO_3 acid diluted with H_2O. The composition of the mixture depends on the sample under test. In case of the $ZnWO_4$ sample, only partial dissolution was possible. Solutions of etched samples, obtained after centrifugation, have been analyzed in a semiquantitative mode using a standard single solution containing 10 ppb of Li, Y, Ce and Tl as calibration. The sensitivity of the ICP–MS device to the other elements is evaluated on the base of this single solution. The accuracy of the element concentration measurement reached in the semiquantitative mode is on the level of 20–30 %. However, for some elements (for example potassium) errors may be considerably higher. This is due to the carrier gas and matrix elements which may form oxides or double charged ions whose mass to charge ratio overlaps with that of some considered elements.

The results of the semiquantitative analysis performed with the help of the ICP–MS device for $CaMoO_4$, $ZnWO_4$, lead, and polyethylene samples are summarized in Table A.1, A.2, A.3, and A.4, respectively.

Element	Content in ppb (μg per kg)	Element	Content in ppb (μg per kg)
Li	<10	B	<100
Na	<10000	Mg	800
Al	<500	K	<10000
Sc	<30	Ti	<30000
Cr	<10000	Mn	<10
Fe	<20000	Co	<100
Ni	<100	Cu	<50
Zn	<50	Ga	<10
As	<1000	Se	<1000
Sr	3100	Y	700
Zr	<5	Te	<5000
I	<50	Cs	14
Ba	<2000	La	<3000
Ce	<50	Pr	<1
Nd	<20	Sm	<10
Eu	<5	Gd	<10
Er	<3	Yb	<5
Lu	230	Hf	<5
Pb	33	Th	2.5
U	1.5		

Table A.1: Results of the semiquantitative analysis performed with help of the ICP–MS device for the $CaMoO_4$ sample.

Element	Content in ppb (μg per kg)	Element	Content in ppb (μg per kg)
Li	<3	B	<200
Na	<5000	Mg	580
Al	1400	K	<10000
Sc	<10	Ti	<20
Cr	<100	Mn	130
Fe	<5000	Co	<1
Ni	<20	Cu	<100
Ga	<20	As	<10
Se	<1000	Sr	<50
Y	<1	Zr	<2
Te	<500	I	<50
Cs	<1	Ba	<5
La	<5	Ce	<5
Pr	<1	Nd	<10
Sm	<5	Eu	<1
Gd	<3	Er	<1
Yb	<2	Lu	<1
Hf	<2	Pb	58
Th	<0.2	U	0.2

Table A.2: Results of the semiquantitative analysis performed with help of the ICP–MS device for the $ZnWO_4$ sample.

Element	Content in ppb (μg per kg)
K	<10000
Ni	<30
Rb	<5
Cd	60
In	<5
Sm	<5
Pt	<20
Th	<0.2
U	<0.2

Table A.3: Results of the semiquantitative analysis performed with help of the ICP–MS device for a lead sample which is used as shielding material for the CRESST–II cryostat at LNGS.

Element	Content in ppb (μg per kg)	
	PE in granulas	PE solid
K	360	5300
Sr	2.6	200
Cs	0.025	0.46
Sm	<0.1	0.7
Pb	130	210
Bi	0.18	6
Th	0.05	1.3
U	0.03	0.5

Table A.4: Results of the semiquantitative analysis performed with the help of the ICP–MS device for polyethylene samples used as neutron shielding materials for the CRESST–II cryostat at LNGS.

Appendix B

Absorption of photons

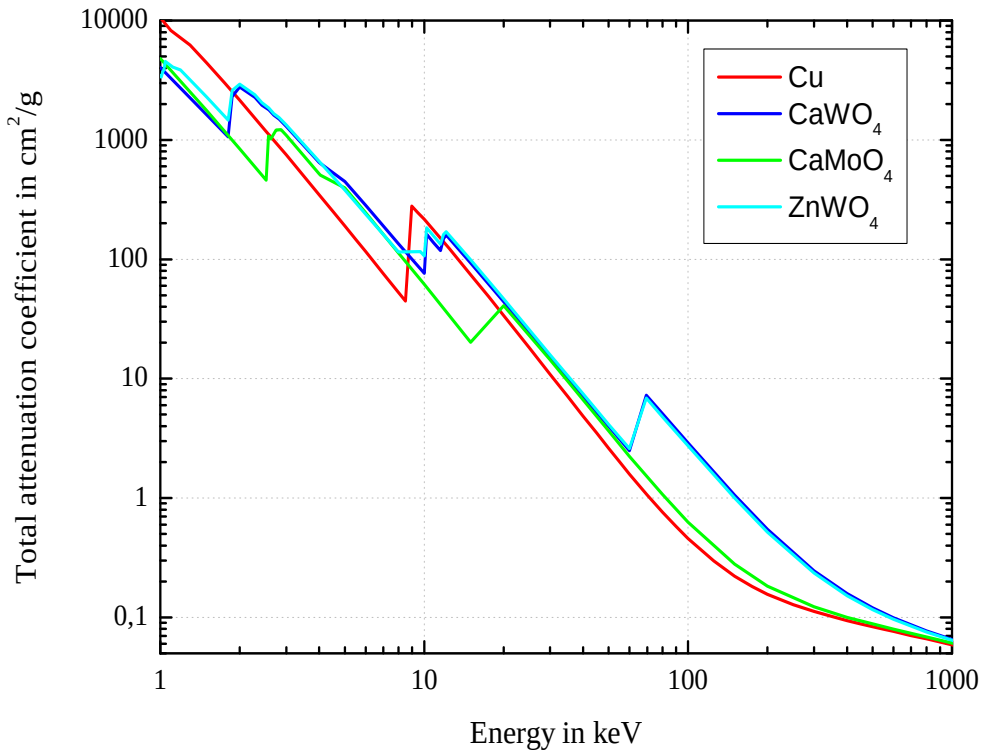

Figure B.1: The photon mass attenuation coefficient for Cu, $CaWO_4$, $CaMoO_4$ and $ZnWO_4$. The curves are produced with help of [163].

Appendix C

Heat capacity

The dependence of the heat capacity on temperature is different for various types of solids. In this appendix general information about the specific heat of dielectrics, metals, and superconductors is collected.

- In pure dielectrics the heat capacity is dominated by phonons. At low temperatures ($T \leq T_{Debye}$) it is well described by the Debye–model:

$$C_{ph} = \frac{12\pi^4}{5} n_a k_B \frac{T}{\Theta_D}^3 \propto T^3 \,. \tag{C.1}$$

  C_{ph} is the lattice specific heat, n_a is the number of lattice atoms per mole, k_B is the Boltzmann constant, and Θ_D is the Debye temperature of the material. In Debye theory, the Debye temperature is the temperature of a crystal's highest normal mode of vibration, i.e. the highest temperature that can be achieved due to a single normal vibration. The Debye temperature is given by

$$\Theta_D = \frac{h\nu_m}{k} \tag{C.2}$$

  where h is Planck's constant, k is Boltzmann's constant, and ν_m is the Debye frequency. At low temperatures, the same formula is valid for highly pure semiconductors. At T < 1 K all conducting electrons are frozen out. Due to the lack of free electrons there is no electronic contribution to the heat capacity of dielectrics at mK temperatures. Because of the T^3 dependence of the heat capacity it is very small at low temperatures. Therefore, dielectric crystals can be used as large calorimeters.

- In metals, the electronic part of the heat capacity dominates at low temperatures:

$$C_e = \frac{\pi^2}{2} n_e k_B \frac{T}{T_F} \propto T \,, \tag{C.3}$$

	Units	Tungsten	Gold	Aluminum
T_C	mK	15	-	1180
T_F	K	27000	63900	134900
Θ_D	K	400	165	428

Table C.1: T_C, T_F, and Θ_D of W, Au, and Al. The values are taken from [63, 164]

where n_e is the number of conduction electrons per mole and T_F is the Fermi temperature. The Fermi temperature is the temperature associated with the Fermi energy. The electronic specific heat depends linearly on the temperature. The phononic part is negligible at low temperatures. In Table C.1 the values for T_C, T_F, and Θ_D of tungsten, gold, and aluminum are given.

- In superconductors, the heat capacity has a discontinuity at the critical temperature T_c. At temperatures well below T_c the specific heat of a superconductor decreases exponentially. Below $T_c/2$ its behavior is described by the BCS–theory [165]:

$$C_e = 1.34\,\gamma\,T_c\left(\frac{\Delta}{k_B T}\right)^{\frac{3}{2}}\,\exp\left(\frac{-\Delta}{k_B T}\right), \tag{C.4}$$

where Δ is the superconducting energy gap and γ is a material specific constant. Below $T_c/10$ the heat capacity is dominated by the lattice specific heat. The vanishing of the electronic heat capacity in superconductors is important for the concept of the phonon collectors in the CRESST–II light detectors; see Section 2.3.3.

Appendix D

Natural decay chains

The radionuclides of the three natural decay series, headed by ^{238}U, ^{232}Th, and ^{235}U, are shown in Figure D.1, D.2, and D.3, respectively, along with the major radioactive decay mode for each.

In nature, the radionuclides of these three series are approximately in a state of secular equilibrium in which the activities of all radionuclides within each series are nearly equal. Two conditions are necessary for secular equilibrium: First, the parent radionuclide must have a half–life much longer than that of any other radionuclide in the series. Second, a sufficiently long time period must have elapsed, for example, ten half–lives of the decay product having the longest life time, to allow for ingrowth of the decay products [166]. Under secular equilibrium the activity of the parent radionuclide undergoes no appreciable changes during many half–lives of its decay products.

In general, the state of the secular equilibrium is sensitive to the time of the last disturbance. For synthetically grown crystals, the disturbance can happen either during the time of a crystal pulling or during purification of the raw materials. Therefore, in inorganic crystals, the secular equilibrium of ^{238}U/^{232}Th chains is usually broken.

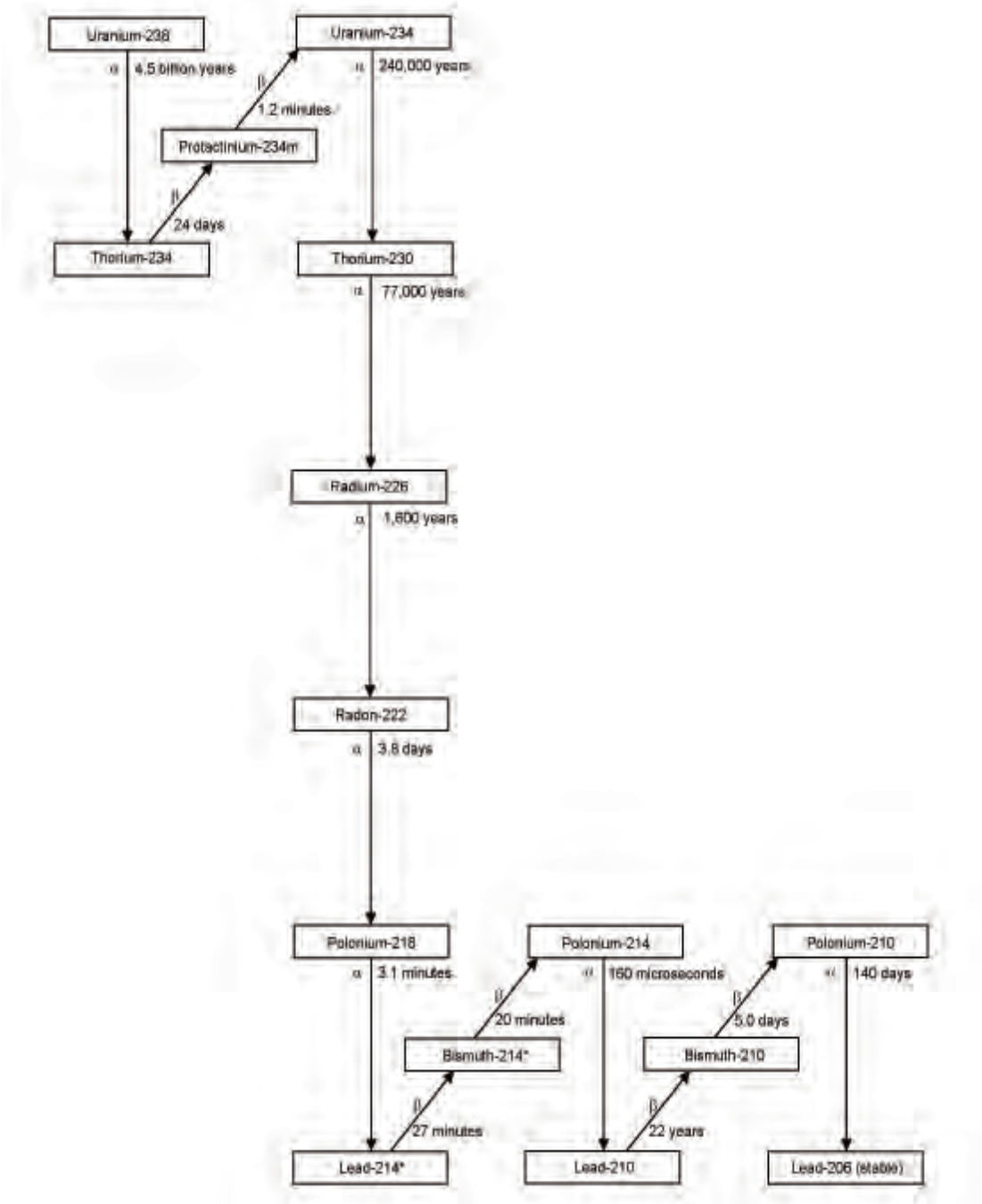

Figure D.1: Schematic representation of the natural ^{238}U decay chain. The times shown are half–lives. An asterisk indicates that the isotope is also a significant γ–emitter. ^{238}U also decays by spontaneous fission. Figure taken from [166].

Isotope	Half–life	Decay mode (B.R.)	Radiation energy in keV		
			Q–value	β (Intensity)	γ (Intensity)
^{238}U	4.5×10^9 yr	α	4270		
^{234}Th	24 d	β		199 (70 %) 107 (19 %)	
^{234}Pa^m	1 min	β		2269 (98 %)	
^{234}U	2.4×10^6 yr	α	4859		
^{230}Th	75.3×10^5 yr	α	4770		
^{226}Ra	1600 yr	α	4870		
^{222}Rn	4 d	α	5590		
^{218}Po	3 min	α	6115		
^{214}Pb	27 min	β		672 (49%) 729 (42%)	352 (38%) 295 (19 %)
^{214}Bi	20 min	β		3272 (18 %) 1542 (18%) 1508 (17%)	609 (49 %) 1764(15 %) 1120 (15 %)
^{214}Po	160 μs	α	7834		
^{210}Pb	22 yr	β		17 (84 %) 63.5 (16 %)	46.5 (4 %)
^{210}Bi	5 d	β		1162 (100 %)	
^{210}Po	138 d	α	5407		
^{206}Pb	stable				

Table D.1: Radioactive isotopes of the ^{238}U natural decay chain. Data taken from [30] and [153].

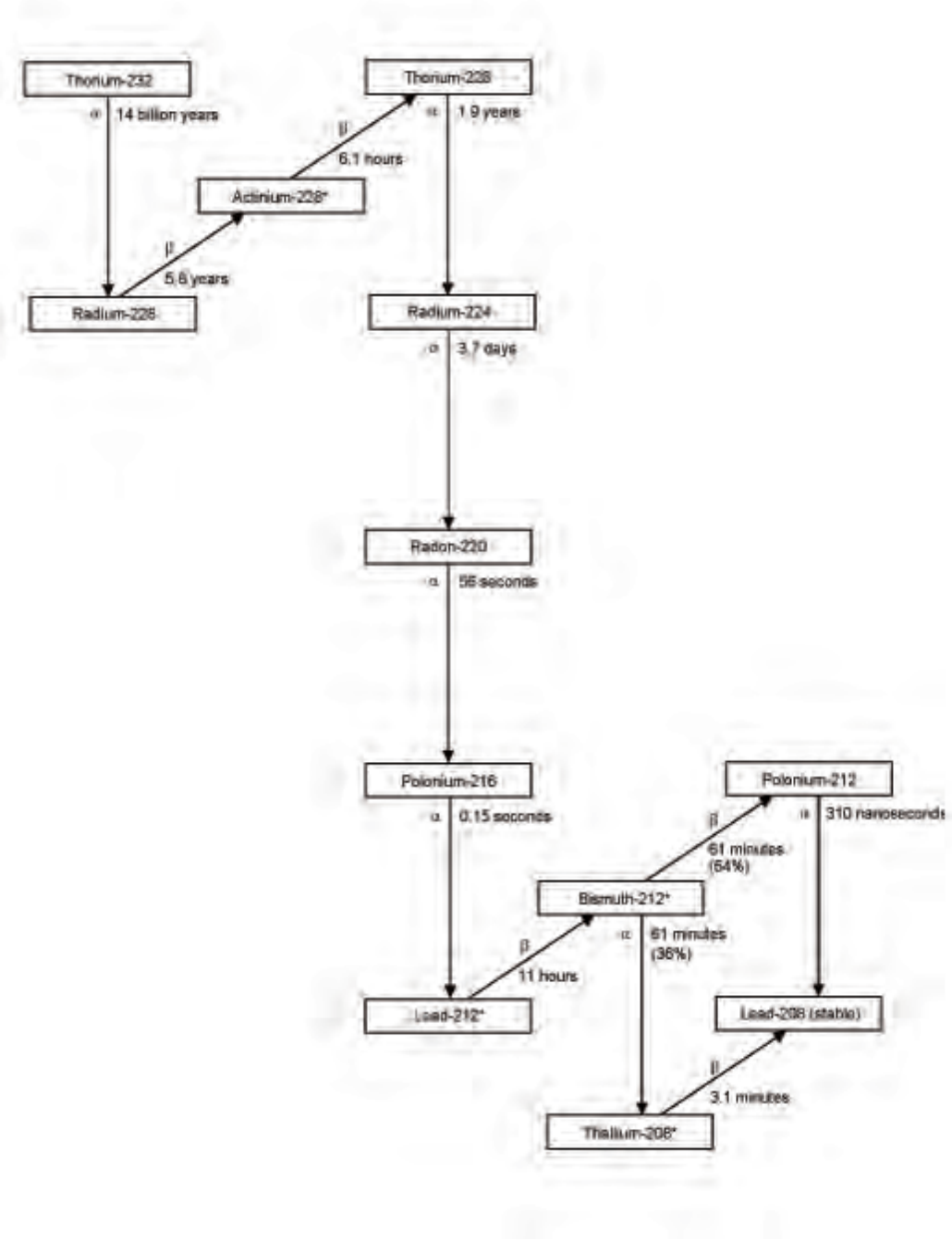

Figure D.2: As in Figure D.1 for the ^{232}Th chain. An asterisk indicates that the isotope is also a significant γ–emitter. Figure taken from [166].

Isotope	Half–life	Decay mode (B.R.)	Radiation energy in keV		
			Q–value	β (Intensity)	γ (Intensity)
^{232}Th	1.2×10^{10} yr	α	4082		
^{228}Ra	6 yr	β		39.2 (40 %)	
^{228}Ac	6 h	β		1158 (30 %) 1730(12 %)	911 (26 %) 969 (15 %) 338 (11 %)
^{228}Th	2 yr	α	5520		
^{224}Ra	4 d	α	5789		
^{220}Rn	56 s	α	6405		
^{216}Po	0.15 s	α	6907		
^{212}Pb	11 h	β		335.2 (83 %)	238 (43 %)
^{212}Bi	61 min	β (64 %); α (36 %)	6207	2254 (56 %)	727.3 (6.6 %)
^{212}Po	310 ns	α	8954		
^{208}Tl	3 min	β		1803 (40 %) 1293 (25 %) 1526 (21 %)	2625 (99 %) 583 (85 %) 511 (23 %) 861 (22 %)
^{208}Pb	stable				

Table D.2: Radioactive isotopes of the ^{232}Th natural decay chain. Data taken from [30] and [153].

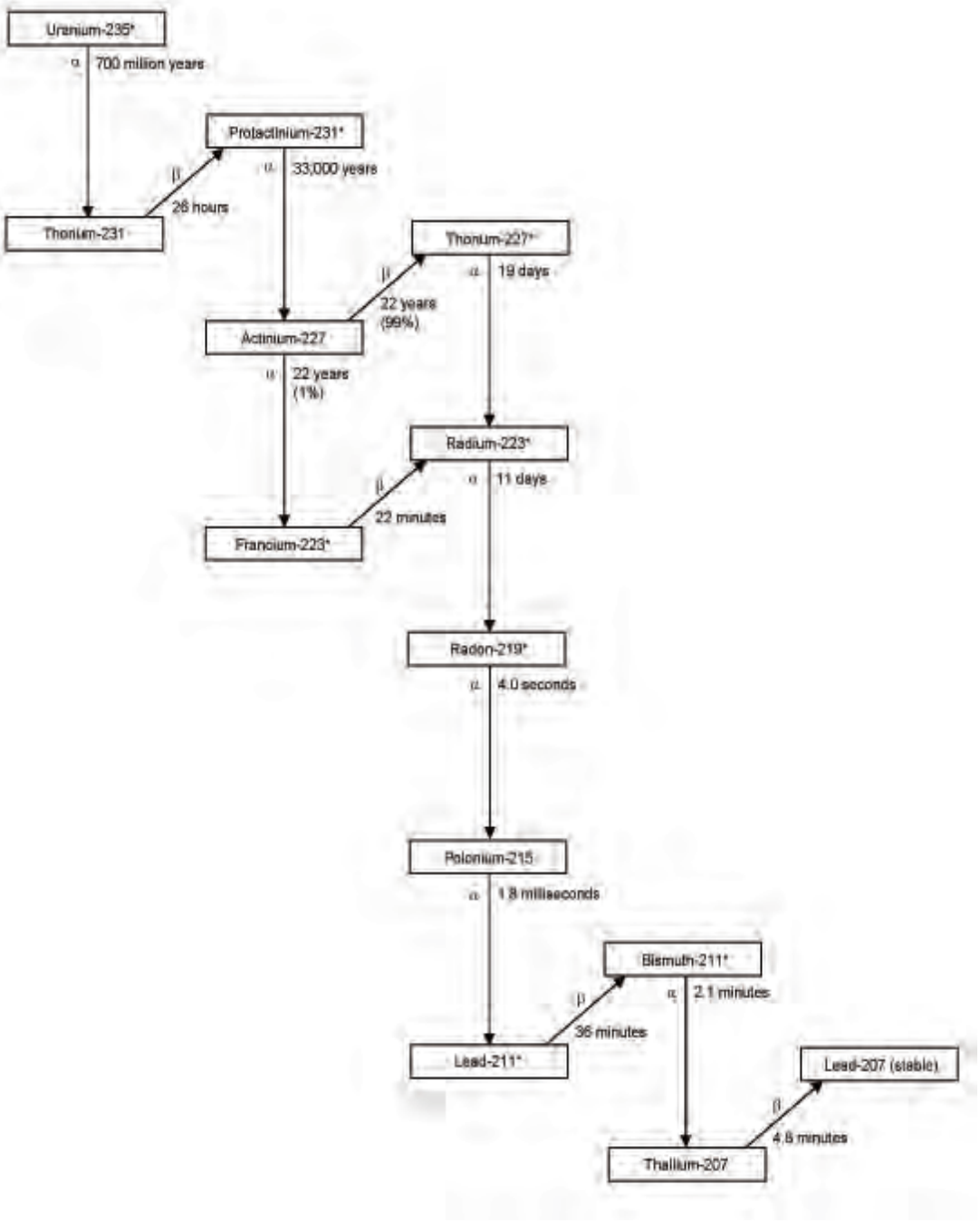

Figure D.3: As in Figure D.1 for the ^{235}U chain. Figure taken from [166].

Isotope	Half–life	Decay mode (B.R.)	Radiation energy in keV		
			Q–value	β (Intensity)	γ (Intensity)
^{235}U	703×10^6 yr	α	4679		
^{231}Th	26 h	β		288 (37 %) 305 (35 %) 287 (12 %)	
^{231}Pa	3.2×10^4 yr	α	5150		27 (10 %)
^{227}Ac	22 yr	β (98.62 %); α (1.38 %)	5042	45 (54 %) 36 (35 %) 20 (10 %)	
^{227}Th	19 d	α	6146		236 (12 %)
^{223}Ra	11 min	α	5979		270 (14 %)
^{219}Rn	4 s	α	6946		271 (11 %)
^{215}Po	2 ms	α	7526		
^{211}Pb	36 min	β		1372 (91 %)	
^{211}Bi	2 min	α	6751		351 (13 %)
^{207}Tl	5 min	β	1423		
^{207}Pb	stable				

Table D.3: Radioactive isotopes of the ^{235}U natural decay chain. Data taken from [30] and [153].